Andrés Prieto Aneiros

PhD Dissertation

SOME CONTRIBUTIONS IN TIME-HARMONIC DISSIPATIVE ACOUSTIC PROBLEMS

Departamento de Matemática Aplicada
Facultade de Matemáticas

¿Cómo me vas a explicar,
di, la dicha de esta tarde,
si no sabemos porqué
fue, ni cómo, ni de qué
ha sido,
si es pura dicha de nada?
En nuestros ojos visiones,
visiones y no miradas,
no percibían tamaños,
datos, colores, distancias.

Pedro Salinas

Contents

Preface

Nowadays the numerical methods have a fundamental role as a tool to reduce the design time and developed costs of new products in fields such as Aerospace, Mechanic, Naval Engineering, etc. From this point of view, sometimes the quick evolution of computers is not enough in all the cases to solve the real-life problems of engineering efficiently and in a practical time. Hence the computational capability of actual computers has to be completed with efficient and renewed numerical methods.

One of the problems which has become more relevant from a social point of view is the reduction of acoustic pollution produced by cars, planes, air-conditioned systems, etc., as it is reflected in national and European laws, which are more restrictive in the last years. In this context, it arises the necessity to solve more complex acoustic propagation problems which cannot be tackled with by numerical techniques based on classical methods.

Obviously, prototype essays are fundamental to asses the feasibility of the proposed technologies, nevertheless the high cost of prototype production makes necessary that this kind of experiments has to be done in an advanced phase of design, with a product close to the final one. These two factors are the reasons why computational acoustics becomes a scientific field of great importance nowadays and numerical simulation is a relevant tool to do analysis of products and to study innovative systems with comfortable acoustic properties with competitive cost and saving developing time.

The sophistication of the acoustic materials related with the real-life problems in the last decades have caused that the mathematical models used to solve acoustic propagation problems have been enriched from a mathematical point of view, and consequently they require the use of new advanced computational and numerical techniques.

Among these new models, we focus in this thesis on those derived from the porous materials and, from a computational point of view, on the Perfectly Matched Layer (PML) technique, which allows solving numerically acoustic propagation problems in unbounded domains.

In any case, the complexity of the acoustic models and the geometrical configuration of the problems require their resolution to be done by numerical methods as, for instance, the finite element methods. The study presented through this thesis is in the context of the frequency domain, i.e., under the assumption of time-harmonic dependency of the time variable of the acoustic fields. In fact, our attention is focused in acoustic propagation problems in the low range of frequencies, where the discretization by finite element methods is suitable and non excessively expensive from a numerical point of view.

In the present dissertation thesis, we distinguish three parts well defined and different but joined by a common topic: the study of acoustic propagation problems in bounded or unbounded domains which involves dissipative material. In some cases the main topic is the acoustic behavior of the porous material, but in other cases, the aim of our study is the use of dissipative materials as a numerical tool to deal with other problems, such as the truncation of unbounded computational domains. So, in the first part of this thesis, we focus our attention on the computation of the resonance frequencies and the frequency response of the porous material coupled with an acoustic fluid in bounded cavities. Then, the second part is devoted to the mathematical and numerical analysis of the PML technique, which can be understood as a special case of dissipative medium. Finally, the last part of this work shows some computational applications which involve porous media and the PML technique, to truncate the unbounded domain where the acoustic propagation problems are stated. In what follows, we describe every part and chapter in more detail.

The first part POROUS MATERIALS is devoted to the study of the time-harmonic acoustic propagation in porous materials. These kind of acoustic materials are widely used in several noise control applications and they are known for their ability to dissipate acoustic waves propagating along them. From an acoustic point of view, porous materials have relevant advantages as compared to other kind of materials, since they are light and absorbent at the same time, two characteristics which become fundamental in real-life applications.

In this first part we have two main goals. First, to revise the porous models attending to the physical properties of the materials (if they have rigid or elastic solid part), remarking the difference between the classical models and those more recent and derived by using homogenization techniques. Secondly, the numerical resolution of some of these models, proposing numerical tools which allow us to compute the resonance frequencies and the frequency response of acoustic systems that involve porous materials.

The first part is organized as follows:

- **Chapter 1. Porous models.** Different porous media models are considered through this chapter. The main difference between the models is the assumption done about the solid skeleton. First, the Darcy's like model and the Allard-Champoux models are described as the simplest and widest used models for rigid porous media. Then, an extensive revision of the porous models with elastic solid part is done. First, the classical Biot's model is presented. Secondly, a collection of models, obtained by homogenization techniques, are presented. More precisely, we consider different models for open pores (connected fluid part) or closed pores (isolated fluid part) geometries, and dissipative or non-dissipative materials. In these last cases, a brief outline of the homogenization technique is presented and the cell problems, which define the coefficients of the macroscopic equations, are also stated.

- **Chapter 2. Finite element solution of acoustic propagation in rigid porous media.** This chapter deals with the acoustical behavior of a rigid porous material. First, the time-harmonic acoustic propagation problem is stated, taking into account the Darcy's like model and the Allard-Champoux model. Both models are written in terms of the displacement field. For the Darcy's like model, the overdamped eigenvalues (pure complex resonance frequencies) are studied analytically in a coupled problem fluid/porous medium in a rigid rectangular cavity. Moreover, a finite element method to compute the response to a harmonic excitation and also the free vibrations of a three-dimensional finite multilayer system, consisting of a free fluid and a rigid porous material, are considered. The finite element used is the lowest order face element introduced by Raviart and Thomas, that eliminates the spurious or circulation modes with no physical meaning. With this finite element method we compute the response curve for the coupled system and also its complex eigenfrequencies. It is remarkable that some of these eigenfrequencies have a small imaginary part but there are also overdamped modes.

Part of the results presented in this chapter are contained in [27].

- **Chapter 3. Finite element solution of new displacement/pressure poroelastic models in acoustics.** This chapter deals with the acoustical behavior of porous materials having an elastic solid frame. First, we focus our attention on non-dissipative poroelastic materials with open pores, whose motion is modelled only by using the displacement and pressure field. Assuming periodic structure, we compute the coefficients in the model by using homogenization techniques, which require to solve boundary-value problems in the elementary cell. Secondly, we propose a finite element method to compute the response to a harmonic excitation of a three-dimensional enclosure containing a free fluid and a poroelastic material.

  As in the previous chapter, the finite element used to discretize the fluid displacement is the lowest order Raviart-Thomas face element that eliminates the spurious modes, whereas, for the displacements in the porous medium, the "MINI element" is used to achieve the stability of the method.

  Part of the results presented in this chapter are contained in [28].

The second part PERFECTLY MATCHED LAYERS is devoted to introduce the PML technique. First we introduce the partial differential equations which define its behavior, as it was stated by Berenger in [22], by using the artificial trick so-named "splitting" technique. Then a physical interpretation for the PML technique is done, understood as a dissipative medium which does not produce spurious reflections if it is coupled with an acoustic fluid. In fact, the PML technique is the numerical tool that will be used through all this work to truncate the computational domains of scattering problems stated in an unbounded medium, without perturbing too much the solution of the original problem.

However, the study of the PML is not reduced to a direct implementation of this technique. Through this part of the thesis, we propose a modification of the PML, which optimizes the numerical results obtained in the discrete problems. More precisely, until now the statement of the PML equations were based on a bounded absorbing function, which recovers a good accuracy from a theoretical point of view, but it presents some numerical drawbacks in the implementation of the discretized problem. As a way of solving these numerical problems, we propose a modified PML with a non integrable absorbing function, and study this alternative from both numerical and theoretical points of view.

The second part is organized as follows:

- **Chapter 4: A non reflecting porous material: the Perfectly Matched Layers.** This chapter is devoted to introduce the PML technique in the two-dimensional case using Cartesian coordinates. First, in the time domain, we consider the linear wave equation and then we modify it to obtain the PML equation by including some dissipative terms associated to the pressure and velocity fields. Besides, a physical interpretation is given by comparison with rigid porous materials and materials with memory.

  A preliminary analysis by using the fundamental solution of the Helmholtz problem is done to illustrate the advantages of using a non integrable absorbing function instead of a classical choice, as a quadratic or constant functions. With this purpose we compare the classical solution when a PML of unbounded thickness and the PML with a non integrable absorbing function are used. To complete the introduction to the PML technique, we perform an analysis in the context of plane waves with oblique incidence, showing the best accuracy of the PML when a non integrable absorbing function is used.

- **Chapter 5: An optimal PML in Cartesian coordinates.** Following the ideas presented for the fundamental solution of the Helmholtz problem in the previous chapter, we introduce an optimal bounded Perfectly Matched Layer (PML) technique, stated in Cartesian coordinates for the two-dimensional case, by choosing a particular absorbing function with unbounded integral. With this choice, as we have seen in the plane wave analysis, the spurious reflections are avoided, even though the thickness of the layer is finite. Different choices for the singular absorbing function are analyzed. Finally, we show that such choice is easy to implement in a finite element method and overcomes the dependency of parameters for the discrete problem. Finally, its efficiency and accuracy are illustrated with some numerical tests.

  Part of the results presented in this chapter are contained in [30].

- **Chapter 6: An exact bounded PML in radial coordinates.** The aim of this chapter is to study the uniqueness and existence of solution for the coupled fluid/PML problem, when the optimal PML, with a singular absorbing function is used. With this purpose we consider the two-dimensional PML equation written in polar coordinates.

  We prove that, in spite of the singularity of the absorbing function, the coupled fluid/PML problem is well posed when the solution is sought in an adequate weighted Sobolev space. Since the variational problem is not of Fredholm type, the steps followed in the proof are based on the series representation of a new Dirichlet-to-Neumman operator associated to the solution in the PML. This can be done since we are able to describe analytically the smooth solution of the PML even in the case of a non integrable absorbing function. Finally, the resulting variational formulation can be numerically dealt with standard finite elements. The high accuracy of this approach is numerically showed as compared with a classical PML technique.

Part of the results presented in this chapter are contained in [32] and [33].

In the third part COMPUTATIONAL APPLICATIONS ON DISSIPATIVE ACOUSTICS some numerical applications of the PML technique and the porous models are presented. First, we compare two different acoustic dissipative models: the Allard-Champoux model, which can be understood as an extensive reacting model (the pressure field depends on the physical properties of the whole porous medium) and the wall impedance condition, which is a local reacting model (the pressure field depends only on the properties of each spatial point). Both models are compared in some scattering problems stated in unbounded domains.

Finally, the last chapter is devoted to the computation of the absorption coefficient associated to an absorbing surface. The definition of this coefficient is analyzed in terms of the intensity and the sound power. A strategy consisting in two numerical experiments is described. To model the absorbing surface, we take into account four kind of local reacting panels. Let us remark that the PML technique, with a singular absorbing function, is used to truncate the computational domain of interest in all the problems. The third part is organized as follows:

- **Chapter 7: Validation of acoustic dissipative models.** The aim of this chapter is to study the time-harmonic scattering problem in a coupled fluid/porous medium system. We consider two different models for the treatment of porous materials: the Allard-Champoux equations and an approximate model based on a wall impedance condition. Both models are compared by computing analytically their respective solutions for unbounded planar obstacles, considering successively plane and spherical waves. A numerical method combining an optimal bounded PML and finite elements is introduced to compute the solutions of both problems for more general axisymmetric geometries. This method is used to compare the solutions for a spherical absorber.

  Part of the results presented in this chapter are contained in [31].

- **Chapter 8: Numerical simulation of local reacting panels.** As a simpler alternative to model thick porous panels with the models presented in the first part of this thesis, we introduce the local reacting models, which does not involve new partial differential equations in domains with small dimensions, that could imply numerical difficulties in the discretization. More precisely, four boundary conditions are introduced: wall impedance, porous veil, local reacting porous layer and local reacting multilayer condition. With each one of these boundary conditions a variational formulation is written for the coupled problem fluid/local reacting panel. As in the previous chapters, a finite element code, combined with the Cartesian PML technique, is used to compute the pressure field in arbitrary three-dimensional unbounded domains. After performing the validation code with five problems whose exact solution are well-known, some numerical results are showed for a real-life problem. Part of the results presented in this chapter are contained in the technical report [29].

Finally, the last part of the manuscript is devoted to the discussion on some future research lines and open problems. We also enclose the acknowledgments and a summary of this dissertation thesis in Galician language.

Part I

Porous materials

Chapter 1

Porous models

Contents

1.1 Introduction

The main goal of this chapter is to introduce various mathematical models which can be used to characterize the acoustic behavior of porous materials. By porous material we mean a material consisting of a solid matrix which is completely saturated by a fluid. The acoustical behavior of porous media depends not only on the fluid but also on the stiffness of its solid skeleton.

Acoustic behavior of porous media is of utmost importance because they exhibit good properties as sound absorbers. Such kind of materials, as glasswools or ceramic foams (see Figure 1.1) are used in isolation systems in buildings, vehicles or airplanes.

Figure 1.1: A particular porous material: ceramic foams.

When considering macroscopic models for porous media, they can be classified depending on whether the solid part is rigid or elastic:

A) **Rigid porous models.**
If the solid matrix is rigid, which is the simplest case, the porous material can be considered as an equivalent fluid, with complex mass density and bulk modulus. These parameters can be obtained through semi-empirical or experimental laws. Delany and Bazley [56] presented a first model in 1970, which has been widely used to describe sound propagation in fibrous materials. This model, was subsequently improved by Morse and Ingard [88], Attenborough [13] and Allard and Champoux [5], among others.

All models of this kind have a common characteristic: they are stated under the assumption of time-harmonic dependency. Hence, the coefficients that appear in the models depend on the frequency. Generally, the equations of these models can be derived from the classical compressible fluid equations with some slight modifications on the coefficients, for instance, adding a damping term or becoming the mass density or the bulk modulus complex valued.

B) **Poroelastic models.**
For the more realistic case when the elastic deformation of the skeleton is taken into account, the theoretical basis for the mechanical behavior was mainly established by Biot [38]. His theory describes the propagation of elastic waves in fluid-saturated porous media. Adaption of this theory to the acoustic context was done, for example, by Allard *et al.* [4] and Shiau [98] (see also the book by Allard [3] and the references therein).

In spite of the fact that the classical Biot's model was introduced in the time domain, it has been also adapted to the frequency domain by Broubard and Lafarge [76] among others, which allows writing a fluid-equivalent formulation for poroelastic materials.

One of the main drawbacks when Biot's model is analyzed is that the coefficients are not properly defined and, in general, their determination is not clear although several experimental procedures have been proposed, as can be seen in Biot and Willis [40].

This gives motivation to undertake a derivation of models, rigorously from a mathematical point of view, by using homogenization theory. It can be done for the both cases: rigid or elastic solid matrix. For rigid matrix, Darcy's model is obtained. Ene and Sanchez-Palencia [59] were the first who gave a derivation of this model from the Stokes system, using a formal multi-scale method, while Tartar [97] made that derivation rigorously in the case of 2D periodic porous media. This methodology allows obtaining not only the homogenized model but also the mathematical expression of the coefficients appearing in it.

Derivation of macroscopic models for poroelastic materials depends strongly on the connectivity of the fluid part. When the domain occupied by the fluid is connected, the material is named open pore material; otherwise, it is named closed pore material. Fundamental references are papers by Gilbert and Mikelić [65], and by Clopeau *et al.* [49], where the classical dissipative Biot's model was derived by homogenization, using two-scale convergence methods. They also contain a number of references to papers on the dissipative Biot's law. Moreover, the same procedure has been applied, for the first time, by Ferrín and Mikelić [62] to derive macroscopic models for non-dissipative poroelastic material with open or closed pore.

The outline of this chapter is as follows. In Section 1.2 we introduce the two rigid models that will be used through this work: the Darcy's like model (Subsection 1.2.1) and the Allard-Champoux model (Subsection 1.2.2). In the case of Darcy's like model, we also give a sketch of its derivation by homogenization techniques. In Section 1.3, we first introduce the classical Biot's model (Subsection 1.3.1) and then we recall three poroelastic models obtained by homogenization techniques through the Subsections 1.3.2-1.3.4: non-dissipative and open pore, non-dissipative and close pore, and dissipative and open pore. In every model the auxiliary cell problems which define the coefficients of the models are also detailed.

1.2 Rigid porous models

In the last decades, simplified models, where absorptive materials are characterized by normal wave impedance, were widely used to study wave propagation in rigid lined ducted systems. More recently, when the solid skeleton is assumed to be rigid, the porous material has been considered as an equivalent fluid, with complex mass density and bulk modulus. These parameters can be obtained through empirical or experimental laws. A first model, introduced by Delany and Bazley (see [56]), was presented for the first time in 1970; it has been widely used to describe sound propagation in fibrous materials. Subsequently, this model was improved by Morse and Ingard [88], Johnson *et al.* [73], Attenborough [12], Allard *et al.* [6], Champoux and Stinson [45] or Allard and Champoux [5], among others.

But models simulating a slow flow fluid through porous media can be also derived rigorously from a mathematical point of view by means of homogenization techniques. By doing so, if we consider a rigid porous medium, we obtain the Darcy's model.

To the best of our knowledge, Ene and Sanchez-Palencia [59] were the first who gave derivation of it from the Stokes system, using a formal multiscale method. This derivation was made rigorous in the case of 2D periodic rigid porous media by Tartar (see appendix in [97]) and subsequently generalized by Mikelić, among others (see [86] and references therein). As we have said in the introduction of this chapter, by means of this methodology we obtain not only the homogenized model but also the mathematical expression of the coefficients appearing in it. For instance, in the case of rigid porous media, the most important coefficient in Darcy's law is permeability, which can be computed by solving a boundary-value problem in a unit cell of the periodic porous medium. For poroelastic media, generalized Biot models were also derived from the first principles by using homogenization techniques (see Gilbert and Mikelić [65], Clopeau *et al.* [49] or Ferrín and Mikelić [62]).

Classically, from a macroscopic point of view, rigid porous media are characterized modifying the conservative mass and momentum laws that model compressible fluids (see [12] or [88] among others), in order to take into account the friction phenomena and the energy exchange between the walls of pores of the solid material and the enclosed fluid. From these modifications, a dissipative term arises in the momentum conservation law, which models the friction phenomena, while the conservative mass law is modified to take into account that the movement of the fluid is restricted to a part of the porous material.

Another fundamental feature consists in the isothermal character of the movement. Whereas, in non-dissipative acoustics, the motion is assumed to be isentropic, when a rigid porous material is modelled, we consider that the temperature is constant, i.e, we assume that the movement in the porous material produce a change in the entropy but not in the temperature.

Anyway, the pressure and velocity fields computed with these models must be understood in a macroscopic sense, i.e., both the displacement and the pressure fields are only averaged estimates in a control volume element of the real pressure and velocity inside the porous material.

Among the different models existing in the bibliography for rigid porous media, we focus on a Darcy's like model (obtained by homogenization techniques) and on another one obtained through empirical laws by Allard and Champoux [5], for harmonic motions. The latter generalizes the former, in the sense that both are equivalent for low frequencies when the porosity is near to one.

The first one is derived from Darcy's law, by adding the inertial effect (see for instance [13]). In fact, if the porous material have a periodic structure, the Darcy's model can be obtained by applying a two-scale homogenization technique to the Stokes equations (see [59] and [97]). In this case, the only parameter characterizing the porous media (named *flow resistivity*), can be related to the permeability tensor, which can be computed explicitly by solving a Stokes problem defined in the fluid part of the unit cell.

A finite element solution of the acoustic propagation in rigid porous media simulated with these two models has been carried out by Bermúdez *et al.* [27].

1.2.1 Darcy's like model

If the porous material is homogeneous from a macroscopic point of view (i.e, if the pores that compose the micro-structure of the material are distributed uniformly) then, according to Darcy's law, it is necessary to introduce two new parameters: the flux resistivity tensor, $\boldsymbol{\sigma}$, which gives information about the resistance to the fluid movement exerted by the rigid skeleton of the porous material, and the porosity coefficient ϕ, which is the ratio between the volume of the fluid part and the total volume of the porous material.

If we suppose that the fluid filling the pores of the material is compressible, homogeneous and isothermal, then the equations governing the movement of a porous material with rigid solid part are

$$\rho\frac{\partial \boldsymbol{V}}{\partial t} + \rho(\mathbf{grad}\,\boldsymbol{V})\boldsymbol{V} + \mathbf{grad}\,P + \boldsymbol{\sigma}\boldsymbol{V} = \mathbf{0}, \tag{1.1}$$

$$\frac{\partial \rho}{\partial t} + \boldsymbol{V}\cdot\mathbf{grad}\,\rho + \frac{\rho}{\phi}\operatorname{div}\boldsymbol{V} = 0, \tag{1.2}$$

$$P = \rho R\theta, \tag{1.3}$$

where $\boldsymbol{\sigma}$ is the flow resistivity tensor ($[\boldsymbol{\sigma}] = \mathrm{kg}/(\mathrm{m}^3\mathrm{s})$), ϕ is the porosity coefficient and θ, P, ρ and $\boldsymbol{V}$ are the temperature, the pressure, the mass density and the velocity averaged in the part occupied by the fluid in a control volume element, respectively.

If the acceleration term is negligible in comparison with the dissipative term (which depends on the flow resistivity), the linear momentum conservation law (1.1) becomes the Darcy's law (see [21])

$$\boldsymbol{V} = -\boldsymbol{\sigma}^{-1}\,\mathbf{grad}\,P. \tag{1.4}$$

Usually, some authors (see [91]) write the above model in terms of the permeability tensor $\boldsymbol{K}$ ($[\boldsymbol{K}] = \mathrm{m}^2$). The permeability tensor can be written in terms of the flow resistivity and the porosity coefficient as follows:

$$\boldsymbol{K} = \eta\phi\boldsymbol{\sigma}^{-1},$$

where η is the viscosity of the fluid filling the pores of the material. Since it is possible to check that $\boldsymbol{K}$ only depends on the geometry of the pores, if we assume that the structure of the solid part of the porous media is uniformly periodic, the permeability tensor can be computed applying homogenization techniques.

Now, if we write the pressure in terms of mass density, ρ, and entropy, s, since we are assuming that the flow of the fluid is isothermal, the value of the sound speed is given by

$$c = \sqrt{\frac{\partial P}{\partial \rho}(\rho, s)} = \sqrt{\gamma \frac{\partial P}{\partial \rho}(\rho, \theta_0)} = \sqrt{\gamma R \theta_0}, \tag{1.5}$$

where θ_0 is the constant temperature of the porous material and γ is the ratio of specific heats at constant pressure and constant volume.

Similar to the classical arguments used in the linearization of the equations which govern a compressible fluid (see for instance Section 11.2 in [25]), we are going to write the linearized equations for this rigid porous model. More precisely, we linearize the mass and momentum conservation laws in the neighborhood of a state at rest with constant mass density ρ_0 an pressure P_0.

Since the movement is isothermal,

$$P \approx P_0 + \frac{\partial P}{\partial \rho}(\rho_0, \theta_0)(\rho - \rho_0) + \frac{\partial P}{\partial \theta}(\rho_0, \theta_0)(\theta - \theta_0) = P_0 + \frac{c^2}{\gamma}(\rho - \rho_0). \tag{1.6}$$

If we neglect the term $\boldsymbol{V} \cdot \mathbf{grad}\, \rho$ and integrate (1.2) in time, we have

$$\rho = \rho_0 - \frac{\rho_0}{\phi} \operatorname{div} \boldsymbol{U},$$

where $\boldsymbol{U}$ is the displacement field. So, using (1.6) we can write the pressure in terms of the displacement,

$$P = P_0 - \frac{\rho_0 c^2}{\phi \gamma} \operatorname{div} \boldsymbol{U},$$

whereas, the displacement field satisfies the equation

$$\rho_0 \frac{\partial^2 \boldsymbol{U}}{\partial t^2} - \frac{\rho_0 c^2}{\phi \gamma} \mathbf{grad}(\operatorname{div} \boldsymbol{U}) + \boldsymbol{\sigma} \frac{\partial \boldsymbol{U}}{\partial t} = \mathbf{0}. \tag{1.7}$$

On one hand, if the porous material is isotropic from a macroscopic point of view, i.e, if the flow resistivity tensor $\boldsymbol{\sigma}$ is proportional to the identity, $\boldsymbol{\sigma} = \sigma \boldsymbol{I}$, then (1.7) can be rewritten as

$$\rho_0 \frac{\partial^2 \boldsymbol{U}}{\partial t^2} - \frac{\rho_0 c^2}{\phi \gamma} \mathbf{grad}(\operatorname{div} \boldsymbol{U}) + \sigma \frac{\partial \boldsymbol{U}}{\partial t} = \mathbf{0}.$$

On the other hand, if the porous material is fibrous, i.e., if the acoustic propagation in the parallel and orthogonal directions to the fibers have different characteristics, then the porous material would be modelled as an orthotropic medium. In this case, if we assume that the principal directions of $\boldsymbol{\sigma}$ match with the coordinates axes, then it is diagonal, i.e., $\boldsymbol{\sigma} = \sigma_1 \boldsymbol{e}_1 \otimes \boldsymbol{e}_1 + \sigma_2 \boldsymbol{e}_2 \otimes \boldsymbol{e}_2 + \sigma_3 \boldsymbol{e}_3 \otimes \boldsymbol{e}_3$.

Finally, in the frequency domain the governing equations of the movement in the Darcy's like model are

$$(\omega^2 \rho_0 \boldsymbol{I} + i\omega\boldsymbol{\sigma})\boldsymbol{u} + \frac{\rho_0 c^2}{\phi\gamma}\,\mathbf{grad}(\operatorname{div}\boldsymbol{u}) = \mathbf{0}, \tag{1.8}$$

$$p = P_0 - \frac{\rho_0 c^2}{\phi\gamma}\operatorname{div}\boldsymbol{u}, \tag{1.9}$$

where $\boldsymbol{u}$ and p are the phasors of the displacement and the pressure fields in the frequency domain, respectively. Let us remark that we are using $\mathrm{e}^{-\omega t}$ for the time convention of the harmonic dependency.

Computing the permeability tensor

To finish this subsection, we show how to compute the permeability tensor for the rigid porous media by using homogenization techniques. In fact, we summarize the main results of the classic two-scale technique to determine the permeability tensor in the Darcy's law, where the fluid is considered viscous and incompressible (see [86]).

Assuming that the porous media have rigid solid part, we have seen that the equations governing the movement involve the permeability tensor, which only depends on the geometry of the pores of the periodic solid structure. If the material can be constructed with a periodic pattern from a unique cell with size ϵ, the permeability tensor can be computed by solving a Stokes problem in only one of these cells.

We denote by $\Omega \subset \mathbb{R}^n$ ($n = 2$ or 3) the domain occupied by the porous material whereas Ω^ϵ is the domain occupied by its fluid part. Since the porous material has a periodic structure, if we denote by $Y = (0,1)^n$ the unit cell of reference and by Y_F and Y_S its fluid and solid part, respectively, both the fluid part Ω^ϵ and the solid part of the porous medium $\Omega \setminus \Omega^\epsilon$ can be rewritten as

$$\Omega^\epsilon = \bigcup_{j \in T_\epsilon} Y^\epsilon_{\mathrm{F}_j}, \qquad \Omega \setminus \Omega^\epsilon = \bigcup_{j \in T_\epsilon} Y^\epsilon_{\mathrm{S}_j},$$

where $Y^\epsilon_{\mathrm{F}_j}$ and $Y^\epsilon_{\mathrm{S}_j}$ are respectively the fluid and the solid part of the cell Y^ϵ_j of size ϵ and homeomorphic to Y (see Figure 1.2). The index set T_ϵ is defined by $T_\epsilon = \{k \in \mathbb{Z}^n : \epsilon\,(Y_\mathrm{S} + k) = Y^\epsilon_{\mathrm{S}_k} \subset \Omega\}$. For the sake of simplicity in the exposition, we avoid to treat mathematically the exterior boundaries and consider that $\Omega = (0,L)^n$ with periodic boundary conditions on $\partial\Omega$.

Since the geometrical structure of the porous medium is fixed, we are in a position to precise what is the macroscopic problem that governs the slow flow of a viscous incompressible flow through the porous medium. With this aim, we use the following steady Stokes

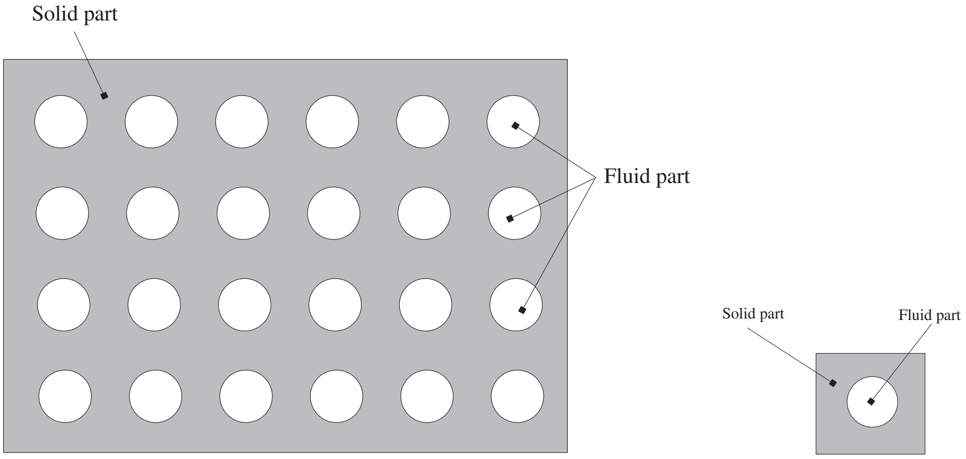

Figure 1.2: Rigid porous structure and unit cell.

system in Ω^ϵ (the fluid part of Ω):

$$\begin{aligned}
-\eta\Delta \boldsymbol{v}^\epsilon(\boldsymbol{x}) + \mathbf{grad}\, p^\epsilon(\boldsymbol{x}) &= \mathbf{0} && \text{in } \Omega^\epsilon, && (1.10)\\
\operatorname{div} \boldsymbol{v}^\epsilon(\boldsymbol{x}) &= 0 && \text{in } \Omega^\epsilon, && (1.11)\\
\boldsymbol{v}^\epsilon &= \mathbf{0} && \text{on } \partial\Omega^\epsilon \setminus \partial\Omega, && (1.12)\\
p^\epsilon \text{ and } \boldsymbol{v}^\epsilon & && \text{are } L-\text{periodic}, && (1.13)
\end{aligned}$$

where η is the dynamical viscosity, $\boldsymbol{v}^\epsilon$ the velocity and p^ϵ the pressure.

If we define the functional space $\mathbf{W}^\epsilon$ by

$$\mathbf{W}^\epsilon = \left\{ \boldsymbol{u} \in \mathrm{H}^1(\Omega^\epsilon)^n : \boldsymbol{u} = \mathbf{0} \text{ on } \partial\Omega^\epsilon \setminus \partial\Omega,\ \boldsymbol{u}^\epsilon \text{ is } L-\text{periodic} \right\},$$

then the weak formulation of the problem (1.10)-(1.13) is:

Find $\boldsymbol{v}^\epsilon \in \mathbf{W}^\epsilon$ *with* $\operatorname{div} \boldsymbol{v}^\epsilon = 0$ *in* Ω^ϵ *and* $p^\epsilon \in \mathrm{L}^2(\Omega^\epsilon)$ *such that*

$$\eta \int_{\Omega^\epsilon} \mathbf{grad}\, \boldsymbol{v}^\epsilon \cdot \mathbf{grad}\, \boldsymbol{\psi}\, dV_{\boldsymbol{x}} - \int_{\Omega^\epsilon} p^\epsilon \operatorname{div} \boldsymbol{\psi}\, dV_{\boldsymbol{x}} = 0,\ \forall \boldsymbol{\psi} \in \mathbf{W}^\epsilon. \tag{1.14}$$

On the one hand, the elemental theory of elliptic problems guarantees the existence and uniqueness of a velocity field solution of the above weak problem. On the other hand, the pressure field p^ϵ is unique up to a constant (see [86]), which is usually fixed such that the following condition holds:

$$\int_{\Omega^\epsilon} p^\epsilon\, dV_{\boldsymbol{x}} = 0.$$

Our aim is to take limits when $\epsilon \to 0$ in the system of equations (1.10)-(1.13). As a first step, we study the a priori estimates for the velocity $\boldsymbol{v}^\epsilon$ and the pressure p^ϵ. With this purpose, we extend $\boldsymbol{v}^\epsilon$ by zero in the rigid part of the porous medium and define an extension of the pressure as

$$\tilde{p}^\epsilon := \begin{cases} p^\epsilon & \text{in } \Omega^\epsilon, \\ \dfrac{1}{\left|Y^\epsilon_{\mathrm{F}_j}\right|} \displaystyle\int_{Y^\epsilon_{\mathrm{F}_j}} p^\epsilon \, dV_{\boldsymbol{x}} & \text{in } Y^\epsilon_{\mathrm{S}_j}, \text{ for each } j \in T_\epsilon, \end{cases}$$

where $Y^\epsilon_{\mathrm{F}_j}$ and $Y^\epsilon_{\mathrm{S}_j}$ are the fluid and solid part of the cell Y^ϵ_j, respectively. If we take into account these extensions for the pressure and the velocity, the following a priori estimates are satisfied (see [86]):

$$\|\boldsymbol{v}^\epsilon\|_{\mathrm{L}^2(\Omega^\epsilon)^n} \leq C\epsilon^2, \tag{1.15}$$

$$\|\mathbf{grad}\, \boldsymbol{v}^\epsilon\|_{\mathrm{L}^2(\Omega^\epsilon)^9} \leq C\epsilon, \tag{1.16}$$

$$\left\| \tilde{p}^\epsilon - \frac{1}{|\Omega|} \int_\Omega \tilde{p}^\epsilon \, dV_{\boldsymbol{x}} \right\|_{\mathrm{L}^2(\Omega)} \leq \frac{1}{|Y_{\mathrm{F}}|} \left\| p^\epsilon - \frac{1}{\Omega^\epsilon} \int_{\Omega^\epsilon} p^\epsilon \, dV_{\boldsymbol{x}} \right\|_{\mathrm{L}^2(\Omega^\epsilon)} \leq C, \tag{1.17}$$

where C is a positive constant not necessarily the same at each occurrence.

Because of these a priori estimates, we can assume that the pressure and the velocity fields have the asymptotic expansions

$$\boldsymbol{v}^\epsilon(\boldsymbol{x}, \boldsymbol{y}) = \epsilon^2 \boldsymbol{v}^0(\boldsymbol{x}, \boldsymbol{y}) + \epsilon^3 \boldsymbol{v}^1(\boldsymbol{x}, \boldsymbol{y}) + \epsilon^4 \boldsymbol{v}^2(\boldsymbol{x}, \boldsymbol{y}) + \ldots, \tag{1.18}$$

$$p^\epsilon(\boldsymbol{x}, \boldsymbol{y}) = p^0(\boldsymbol{x}, \boldsymbol{y}) + \epsilon p^1(\boldsymbol{x}, \boldsymbol{y}) + \epsilon^2 p^2(\boldsymbol{x}, \boldsymbol{y}) + \ldots, \tag{1.19}$$

where $\boldsymbol{y} = \boldsymbol{x}/\epsilon$. These expansions are written in two scales, i.e., taking into account the macroscopic and microscopic levels of the geometry. Moreover, since the geometry of the medium is periodic, it is natural to assume a periodic dependency in the scale of variable $\boldsymbol{y}$.

From the two scales of the expansions, the derivatives are transformed and, hence, the differential operators can be rewritten as

$$\mathbf{grad} = \mathbf{grad}_{\boldsymbol{x}} + \epsilon^{-1} \mathbf{grad}_{\boldsymbol{y}}, \tag{1.20}$$

$$\mathrm{div} = \mathrm{div}_{\boldsymbol{x}} + \epsilon^{-1} \mathrm{div}_{\boldsymbol{y}}, \tag{1.21}$$

$$\Delta = \Delta_{\boldsymbol{x}} + 2\epsilon^{-1} \mathrm{div}_{\boldsymbol{x}}\, \mathbf{grad}_{\boldsymbol{y}} + \epsilon^{-2} \Delta_{\boldsymbol{y}}, \tag{1.22}$$

where the subindexes denote the spatial variable involved in the differentiation.

If we substitute the expressions (1.18)-(1.19) in (1.10)-(1.13), the lower order terms satisfy the following equations:

- term $O(\epsilon^{-1})$,

$$\mathbf{grad}_{\boldsymbol{y}} p^0(\boldsymbol{x}, \boldsymbol{y}) = \mathbf{0} \qquad \text{in } \Omega \times Y_{\mathrm{F}}, \tag{1.23}$$

- term $O(1)$,

$$-\eta \Delta_{\boldsymbol{y}} \boldsymbol{v}^0(\boldsymbol{x}, \boldsymbol{y}) + \mathbf{grad}_{\boldsymbol{y}} p^1(\boldsymbol{x}, \boldsymbol{y}) + \mathbf{grad}_{\boldsymbol{x}} p^0(\boldsymbol{x}, \boldsymbol{y}) = \mathbf{0} \qquad \text{in } \Omega \times Y_{\mathrm{F}},$$

- term $O(\epsilon)$,

$$\begin{aligned} \operatorname{div}_{\boldsymbol{y}} \boldsymbol{v}^0(\boldsymbol{x},\boldsymbol{y}) &= 0 && \text{in } \Omega \times Y_{\mathrm{F}}, \\ -\eta \Delta_{\boldsymbol{y}} \boldsymbol{v}^1(\boldsymbol{x},\boldsymbol{y}) + \mathbf{grad}_{\boldsymbol{y}} p^2(\boldsymbol{x},\boldsymbol{y}) + \mathbf{grad}_{\boldsymbol{x}} p^1(\boldsymbol{x},\boldsymbol{y}) &= \mathbf{0} && \text{in } \Omega \times Y_{\mathrm{F}}, \end{aligned}$$

- term $O(\epsilon^2)$,

$$\begin{aligned} \operatorname{div}_{\boldsymbol{x}} \boldsymbol{v}^0(\boldsymbol{x},\boldsymbol{y}) + \operatorname{div}_{\boldsymbol{y}} \boldsymbol{v}^1(\boldsymbol{x},\boldsymbol{y}) &= 0 && \text{in } \Omega \times Y_{\mathrm{F}}, \qquad (1.24) \\ \boldsymbol{v}^0(\boldsymbol{x},\boldsymbol{y}) &= \mathbf{0} && \text{in } \Omega \times (\partial Y_{\mathrm{F}} \setminus \partial Y), \\ \boldsymbol{v}^0(\boldsymbol{x},\boldsymbol{y}) \text{ and } p^1(\boldsymbol{x},\boldsymbol{y}) & && \text{are } 1-\text{periodic in } \boldsymbol{y}, \\ -\eta \Delta_{\boldsymbol{y}} \boldsymbol{v}^2(\boldsymbol{x},\boldsymbol{y}) + \mathbf{grad}_{\boldsymbol{y}} p^3(\boldsymbol{x},\boldsymbol{y}) + \mathbf{grad}_{\boldsymbol{x}} p^2(\boldsymbol{x},\boldsymbol{y}) &= \mathbf{0} && \text{in } \Omega \times Y_{\mathrm{F}}. \end{aligned}$$

Equation (1.23) is equivalent to $p^0 = p^0(\boldsymbol{x})$, whereas $\boldsymbol{v}^1$ satisfies (1.24) if and only if

$$\operatorname{div}_{\boldsymbol{x}} \int_{Y_{\mathrm{F}}} \boldsymbol{v}^0(\boldsymbol{x},\boldsymbol{y})\, dV_{\boldsymbol{y}} = 0 \qquad \text{in } \Omega.$$

In summary, the equations which are satisfied by $\boldsymbol{v}^0$, p^0 and p^1 are condensed in the following system:

$$\begin{aligned} -\eta \Delta_{\boldsymbol{y}} \boldsymbol{v}^0(\boldsymbol{x},\boldsymbol{y}) + \mathbf{grad}_{\boldsymbol{y}} p^1(\boldsymbol{x},\boldsymbol{y}) + \mathbf{grad}_{\boldsymbol{x}} p^0(\boldsymbol{x}) &= \mathbf{0} && \text{in } \Omega \times Y_{\mathrm{F}}, \\ \operatorname{div}_{\boldsymbol{y}} \boldsymbol{v}^0(\boldsymbol{x},\boldsymbol{y}) &= 0 && \text{in } \Omega \times Y_{\mathrm{F}}, \\ \boldsymbol{v}^0(\boldsymbol{x},\boldsymbol{y}) &= \mathbf{0} && \text{in } \Omega \times (\partial Y_{\mathrm{F}} \setminus \partial Y), \\ \boldsymbol{v}^0(\boldsymbol{x},\boldsymbol{y}) \text{ and } p^1(\boldsymbol{x},\boldsymbol{y}) & && \text{are } 1-\text{periodic in } \boldsymbol{y}, \\ p^0(\boldsymbol{x}) \text{ and } \int_{Y_{\mathrm{F}}} \boldsymbol{v}^0(\boldsymbol{x},\boldsymbol{y})\, dV_{\boldsymbol{y}} & && \text{are } L-\text{periodic in } \boldsymbol{x}, \\ \operatorname{div}_{\boldsymbol{x}} \int_{Y_{\mathrm{F}}} \boldsymbol{v}^0(\boldsymbol{x},\boldsymbol{y})\, dV_{\boldsymbol{y}} &= 0, \end{aligned}$$

where, in the above system of equations, we have added the condition of periodicity in the spatial variable $\boldsymbol{x}$ (see [86]). For each $j = 1, \dots, n$, let us introduce the following auxiliary problem in Y_{F}, whose solution is sought in $\mathrm{H}^1_{\mathrm{per}}(Y_{\mathrm{F}})^n$, i.e., periodic vector fields in $\mathrm{H}^1(Y_{\mathrm{F}})^n$:

Find $\boldsymbol{w}^j \in \mathrm{H}^1_{\mathrm{per}}(Y_F)^n$ *and* $\pi^j \in \mathrm{L}^2(Y_F)$ *such that:*

$$\begin{aligned} -\Delta_{\boldsymbol{y}} \boldsymbol{w}^j(\boldsymbol{y}) + \mathbf{grad}_{\boldsymbol{y}} \pi^j(\boldsymbol{y}) &= \boldsymbol{e}_j && \text{in } Y_{\mathrm{F}}, \\ \operatorname{div}_{\boldsymbol{y}} \boldsymbol{w}^j(\boldsymbol{y}) &= 0 && \text{in } Y_{\mathrm{F}}, \\ \boldsymbol{w}^j(\boldsymbol{y}) &= \mathbf{0} && \text{on } \partial Y_{\mathrm{F}} \setminus \partial Y, \\ \int_{Y_{\mathrm{F}}} \pi^j(\boldsymbol{y})\, dV_{\boldsymbol{y}} &= 0, \end{aligned}$$

where $\boldsymbol{e}_j$ is the j-th vector of the canonical basis. For each fixed j, this problem has a unique solution.

From $\boldsymbol{w}^j = \sum_{k=1}^n w_k^j \boldsymbol{e}_k,\ 1 \le j \le n$, if we define the permeability tensor $\boldsymbol{K}$ as

$$K_{lm} := \int_{Y_{\mathrm{F}}} w_m^l \, dV_{\boldsymbol{y}}, \qquad 1 \le l, m \le n,$$

$\boldsymbol{v}^0$ and p^1 are rewritten as

$$\boldsymbol{v}_0(\boldsymbol{x},\boldsymbol{y}) = -\frac{1}{\eta}\sum_{j=1}^n \boldsymbol{w}^j(\boldsymbol{y})\frac{\partial p^0}{\partial x_j}(\boldsymbol{x}), \qquad \boldsymbol{x} \in \Omega,\ \boldsymbol{y} \in Y_{\mathrm{F}},$$

$$p^1(\boldsymbol{x}) = -\sum_{j=1}^n \pi^j(\boldsymbol{y})\frac{\partial p^0}{\partial x_j}(\boldsymbol{x}), \qquad \boldsymbol{x} \in \Omega,\ \boldsymbol{y} \in Y_{\mathrm{F}},$$

and we obtain the relation between $\boldsymbol{v}^0$ and $\mathbf{grad}_{\boldsymbol{x}} p^0$:

$$\int_{Y_{\mathrm{F}}} \boldsymbol{v}^0(\boldsymbol{x},\boldsymbol{y})\, dV_{\boldsymbol{y}} = -\frac{\boldsymbol{K}}{\eta}\mathbf{grad}_{\boldsymbol{x}} p^0(\boldsymbol{x}), \qquad \boldsymbol{x} \in \Omega. \tag{1.25}$$

Finally, if we take into account that porosity is the measure of Y_{F}, i.e., $\phi = |Y_{\mathrm{F}}|$, we identify the macroscopic pressure p with p^0 and define the averaged velocity $\boldsymbol{v}$ as

$$\boldsymbol{v}(\boldsymbol{x}) := \frac{1}{|Y_{\mathrm{F}}|}\int_{Y_{\mathrm{F}}} \boldsymbol{v}^0(\boldsymbol{x},\boldsymbol{y})\, dV_{\boldsymbol{y}},$$

then equation (1.25) recovers the classical Darcy's law (1.4) stated at the beginning of this subsection.

1.2.2 Allard-Champoux model

In the previous Darcy's like model, we have characterized the pressure and the displacement of rigid porous media, by linearizing the conservative mass and momentum equations and using, implicitly, that the relations between pressure and density are given by

$$c^2(\rho - \rho_0) = \gamma(p - P_0). \tag{1.26}$$

Moreover, Darcy's like model includes a dissipative term which depends on the flow resistivity tensor. In the first case, the state equation (1.26) guarantees that the fluid expands isothermally inside the pores when it moves through them. However, some authors have suggested that thermal effects in real-life materials depend on frequency. In order to take into account these phenomena, it is obvious that both, the bulk modulus $\rho_0 c^2/\phi\gamma$ and the flow resistivity tensor $\boldsymbol{\sigma}$, have to be frequency dependent.

Under this assumption, there are several semi-empirical models (see [12], [56] or [73]) which take into account this dependency with respect to frequency. In spite of this variety, we focus our attention on one of the most recent and used ones: the Allard-Champoux model (see [5]).

The governing equations of the movement in the porous Allard-Champoux model are written, in the frequency domain:

$$\omega^2\boldsymbol{\rho}(\omega)\boldsymbol{u} + \mathbf{grad}(\mathrm{div}\boldsymbol{\mu}(\omega)\boldsymbol{u}) = \mathbf{0}, \tag{1.27}$$

$$p = P_0 - \mathrm{div}\,\boldsymbol{\mu}(\omega)\boldsymbol{u}, \tag{1.28}$$

where $\boldsymbol{\rho}(\omega)$ is the dynamic mass density and $\boldsymbol{\mu}(\omega)$ is the dynamic bulk modulus.

If the material is isotropic, $\boldsymbol{\rho}(\omega)$ and $\boldsymbol{\mu}(\omega)$ are isotropic tensors, i.e., $\boldsymbol{\rho}(\omega) = \rho(\omega)\boldsymbol{I}$ and $\boldsymbol{\mu}(\omega) = \mu(\omega)\boldsymbol{I}$. Following the Allard-Champoux formulas (see [5]), the dynamic mass density ($[\rho(\omega)] = \mathrm{kg/m^3}$) is computed by the expression

$$\rho(\omega) = \rho_0\left(1 - i\left(\frac{\sigma}{\rho_0\omega}\right)G_1\left(\frac{\rho_0\omega}{\sigma}\right)\right), \tag{1.29}$$

whereas the dynamic bulk modulus ($[\mu(\omega)] = \mathrm{N/m^2}$) is given by

$$\mu(\omega) = \gamma P_0\left(\gamma - \frac{\gamma - 1}{1 - \left(\frac{i}{4N_{pr}}\right)\left(\frac{\sigma}{\rho_0\omega}\right)G_2\left(\frac{\rho_0\omega}{\sigma}\right)}\right)^{-1}. \tag{1.30}$$

Functions G_1 and G_2 are

$$G_1\left(\frac{\rho_0\omega}{\sigma}\right) = \sqrt{1 + \frac{i}{2}\left(\frac{\rho_0\omega}{\sigma}\right)}, \tag{1.31}$$

$$G_2\left(\frac{\rho_0\omega}{\sigma}\right) = G_1\left(4N_{pr}\left(\frac{\rho_0\omega}{\sigma}\right)\right), \tag{1.32}$$

where P_0 is the fluid pressure at rest, ρ_0 is the mass density at rest, N_{pr} the Prandtl's number and γ the rate of specific heats at constant pressure and volume.

From the expressions of G_1 and G_2, both the dynamic mass density and the dynamic bulk modulus are functions of the ratio $\rho_0\omega/\sigma$. If we assume that $\rho_0\omega \ll \sigma$, then we obtain

$$\rho(\omega) \simeq \rho_0\left(O(1) + \frac{\sigma}{i\omega\rho_0}\right),$$

$$\lim_{\frac{\rho_0\omega}{\sigma}\to 0}\mu(\omega) = P_0 = \frac{\rho_0 c^2}{\gamma} \simeq \frac{\rho_0 c^2}{\phi\gamma}.$$

Hence, if the porosity is close to one ($\phi \simeq 1$) and the frequency range is small enough, when compared to the flow resistivity values, the Allard-Champoux model reduces to the Darcy's like model.

If the porous material is orthotropic (for instance, in the case of fibrous materials), and we assume that the principal directions match with the coordinate axes and that $\boldsymbol{e}_1$ is the direction parallel to the fibers, then tensors $\boldsymbol{\rho}(\omega)$ and $\boldsymbol{\mu}(\omega)$ are diagonal, $\boldsymbol{\rho}(\omega) = \rho_1(\omega)\boldsymbol{e}_1 \otimes$

$\boldsymbol{e}_1 + \rho_2(\omega)\,(\boldsymbol{e}_2 \otimes \boldsymbol{e}_2 + \boldsymbol{e}_3 \otimes \boldsymbol{e}_3)$ and $\boldsymbol{\mu}(\omega) = \mu_1(\omega)\boldsymbol{e}_1 \otimes \boldsymbol{e}_1 + \mu_2(\omega)\,(\boldsymbol{e}_2 \otimes \boldsymbol{e}_2 + \boldsymbol{e}_3 \otimes \boldsymbol{e}_3)$, where $\mu_j(\omega), \rho_j(\omega),\ j = 1, 2$, are given by (1.29) and (1.30), respectively. The terms σ_j are the flow resistivity coefficients in each principal direction. In this case, the equations satisfied by the displacement are

$$\omega^2 \rho_1(\omega) u_1 + \frac{\partial}{\partial x_1} (\operatorname{div} \boldsymbol{\mu}(\omega)\boldsymbol{u}) = 0,$$
$$\omega^2 \rho_2(\omega) u_j + \frac{\partial}{\partial x_2} (\operatorname{div} \boldsymbol{\mu}(\omega)\boldsymbol{u}) = 0, \qquad j = 2, 3,$$

where $\boldsymbol{u}(\boldsymbol{x}) = u_1(\boldsymbol{x})\boldsymbol{e}_1 + u_2(\boldsymbol{x})\boldsymbol{e}_2 + u_3(\boldsymbol{x})\boldsymbol{e}_3$. It can be seen that, even in this case, it is not possible to decouple the three displacement components.

1.3 Poroelastic models

In the previous section we have presented two models for porous media where the solid part is assumed to be rigid. Now we deal with the more general case of a porous medium with elastic solid part, so that the displacement field in the solid part is not negligible.

The theoretical basis for the mechanical behavior of poroelastic materials has been established by Biot (see [38]). He describes the propagation of elastic waves in fluid-saturated elastic porous media. Adaption of Biot's theory to the acoustic propagation can be seen in Allard's book [3]. The resulting model, named below as "classical" Biot's model, is the basis for most of the numerical studies involving poroelastic materials. However, the fact that macroscopic coefficients appearing in this model can only be obtained from empirical experiments (see Biot and Willis [40]) and that it involves the two displacements fields (for solid and fluid parts, respectively) are unsuitable features of this model. These are some of the reasons why a rigorous derivation of Biot-like models, starting from the first principles and using homogenization techniques, is an interesting task. This work has been done by Mikelić and coworkers in several papers and we shall refer to the obtained models as generalized Biot's models.

In the following subsection, as a first step, we study the classical Biot's model. Then, the rest of the subsections are devoted to introduce three new poroelastic models attending to different geometries of the pores (open or closed) and to whether they are dissipative or not. The main advantange of these new models, which are obtained by homogenization techniques, lies in the fact that they can be described in terms of a pressure field and a unique displacement field, whereas the Biot's model needs two displacements fields to be written.

1.3.1 Classical Biot's model

The description of the acoustic model of a porous medium with elastic solid part was stated originally by Biot [38] involving two displacements, $\boldsymbol{U}_{\mathrm{S}}$ and $\boldsymbol{U}_{\mathrm{F}}$, which are the macroscopic displacement of the solid and fluid parts of the porous medium, respectively.

If we suppose that the porous medium is homogeneous and isotropic from a macroscopic point of view (i.e., pores are uniformly distributed and such that in each direction the material properties are equal) then the constitutive laws defining the stress tensors, in the solid part, $\boldsymbol{S}_{\mathrm{S}}$, and in the fluid part, $\boldsymbol{S}_{\mathrm{F}}$, are, respectively,

$$\begin{aligned}
\boldsymbol{S}_{\mathrm{S}} &= (P-2N)\,(\operatorname{tr}(\boldsymbol{E}[\boldsymbol{U}_{\mathrm{S}}]))\,\boldsymbol{I} + Q\,(\operatorname{tr}(\boldsymbol{E}[\boldsymbol{U}_{\mathrm{F}}]))\,\boldsymbol{I} + 2N\boldsymbol{E}[\boldsymbol{U}_{\mathrm{S}}],\\
\boldsymbol{S}_{\mathrm{F}} &= Q\,(\operatorname{tr}(\boldsymbol{E}[\boldsymbol{U}_{\mathrm{S}}]))\,\boldsymbol{I} + R\,(\operatorname{tr}(\boldsymbol{E}[\boldsymbol{U}_{\mathrm{F}}]))\,\boldsymbol{I},
\end{aligned}$$

where $\boldsymbol{E}[\boldsymbol{U}] = \frac{1}{2}\left(\mathbf{grad}\,\boldsymbol{U} + \mathbf{grad}\,\boldsymbol{U}^t\right)$, ϕ is the porosity coefficient, and P, N, Q, and R are scalar coefficients which are empirically determined through the so-called *gedanke experiments* suggested initially by Biot (see [3] or [40]). In fact, this coefficients can be rewritten in terms of the bulk modulus of the fluid and solid parts,

$$\begin{aligned}
P &= \frac{(1-\phi)\left(1-\phi-\dfrac{\mu_{\mathrm{B}}}{\mu_{\mathrm{S}}}\right)\mu_{\mathrm{S}} + \phi\dfrac{\mu_{\mathrm{S}}}{\mu_{\mathrm{F}}}\mu_{\mathrm{B}}}{1-\phi-\dfrac{\mu_{\mathrm{B}}}{\mu_{\mathrm{S}}}+\phi\dfrac{\mu_{\mathrm{S}}}{\mu_{\mathrm{F}}}} + \frac{4}{3}N,\\
Q &= \frac{\left(1-\phi-\dfrac{\mu_{\mathrm{B}}}{\mu_{\mathrm{S}}}\right)\phi\mu_{\mathrm{S}}}{1-\phi-\dfrac{\mu_{\mathrm{B}}}{\mu_{\mathrm{S}}}+\phi\dfrac{\mu_{\mathrm{S}}}{\mu_{\mathrm{F}}}},\\
R &= \frac{\phi^2\mu_{\mathrm{S}}}{1-\phi-\dfrac{\mu_{\mathrm{B}}}{\mu_{\mathrm{S}}}+\phi\dfrac{\mu_{\mathrm{S}}}{\mu_{\mathrm{F}}}},
\end{aligned}$$

where N is the shear coefficient of the porous medium and $\mu_{\mathrm{B}}, \mu_{\mathrm{S}}$, and μ_{F} are, respectively, the bulk modulus of the porous medium, the solid part and the fluid part.

If we assume the following hypotheses for the porosity coefficient and the bulk modulus of the solid and of the porous medium:

$$\phi \approx 1, \qquad \mu_{\mathrm{B}} \ll \mu_{\mathrm{S}},$$

then we obtain simpler expressions for the above coefficients:

$$\begin{aligned}
P &= \mu_{\mathrm{B}} + \frac{4}{3}N + \frac{(1-\phi)^2}{\phi}\mu_{\mathrm{F}},\\
Q &= (1-\phi)\mu_{\mathrm{F}},\\
R &= \phi\mu_{\mathrm{F}}.
\end{aligned}$$

The system of equations governing the motion is a coupled system where the unknown fields are the displacements $\boldsymbol{u}_{\mathrm{S}}$ and $\boldsymbol{u}_{\mathrm{F}}$. Taking into account the dissipative effects of the displacement inside the pores, this system of equations can be written as

$$\rho_{11}\frac{\partial^2 \boldsymbol{U}_{\mathrm{S}}}{\partial t^2} + \rho_{12}\frac{\partial^2 \boldsymbol{U}_{\mathrm{F}}}{\partial t^2} - (P-N)\,\mathbf{grad}(\operatorname{div}\boldsymbol{U}_{\mathrm{S}}) - N\,\Delta\boldsymbol{U}_{\mathrm{S}} - Q\,\mathbf{grad}(\operatorname{div}\boldsymbol{U}_{\mathrm{F}}) + \boldsymbol{F} = \mathbf{0}, \tag{1.33}$$

$$\rho_{22}\frac{\partial^2 \boldsymbol{U}_{\mathrm{F}}}{\partial t^2} + \rho_{12}\frac{\partial^2 \boldsymbol{U}_{\mathrm{S}}}{\partial t^2} - R\,\mathbf{grad}(\operatorname{div}\boldsymbol{U}_{\mathrm{F}}) - Q\,\mathbf{grad}(\operatorname{div}\boldsymbol{U}_{\mathrm{S}}) - \boldsymbol{F} = \mathbf{0}, \tag{1.34}$$

where $\boldsymbol{F}$ is the force due to the viscosity effects produced by the fluid inside the porous medium. This force is proportional to the flow resistivity coefficient σ. In fact, we have

$$\boldsymbol{F} = \phi\sigma\frac{\partial}{\partial t}\left(\boldsymbol{U}_{\mathrm{S}} - \boldsymbol{U}_{\mathrm{F}}\right),$$

and coefficients $\rho_{ij}, 1 \leq i, j \leq 2$ are given by

$$\begin{aligned}
\rho_{11} &= \phi(\alpha_\infty - 1)\rho_{\mathrm{F}} + (1-\phi)\rho_{\mathrm{S}},\\
\rho_{12} &= -\phi(\alpha_\infty - 1)\rho_{\mathrm{F}},\\
\rho_{22} &= \phi\alpha_\infty\rho_{\mathrm{F}},
\end{aligned}$$

where ρ_{F} and ρ_{S} are respectively the mass densities of the fluid and solid part, and ϕ is the porosity coefficient and α_∞ the tortuosity coefficient.

Finally, in the frequency domain, i.e., if we assume a time-harmonic dependence with respect to time and we take into account that

$$\Delta\boldsymbol{u} = \mathbf{grad}(\operatorname{div}\,\boldsymbol{u}) - \operatorname{rot}(\operatorname{rot}\,\boldsymbol{u}),$$

then the Biot system (1.33)-(1.34) becomes

$$\begin{aligned}
&\omega^2(\tilde{\rho}_{11}\boldsymbol{u}_{\mathrm{S}} + \tilde{\rho}_{12}\boldsymbol{u}_{\mathrm{F}}) + P\,\mathbf{grad}(\operatorname{div}\boldsymbol{u}_{\mathrm{S}}) - N\operatorname{rot}(\operatorname{rot}\,\boldsymbol{u}_{\mathrm{S}}) + Q\,\mathbf{grad}(\operatorname{div}\boldsymbol{u}_{\mathrm{F}}) = \mathbf{0},\\
&\omega^2(\tilde{\rho}_{22}\boldsymbol{u}_{\mathrm{F}} + \tilde{\rho}_{12}\boldsymbol{u}_{\mathrm{S}}) + R\,\mathbf{grad}(\operatorname{div}\boldsymbol{u}_{\mathrm{F}}) + Q\,\mathbf{grad}(\operatorname{div}\boldsymbol{u}_{\mathrm{S}}) = \mathbf{0},
\end{aligned}$$

where $\boldsymbol{u}_{\mathrm{F}}$ and $\boldsymbol{u}_{\mathrm{S}}$ are, respectively, the fluid and solid displacement fields in the frequency domain and

$$\tilde{\rho}_{11} = \rho_{11} - i\frac{\sigma\phi}{\omega}, \quad \tilde{\rho}_{12} = \rho_{12} + i\frac{\sigma\phi}{\omega}, \quad \tilde{\rho}_{22} = \rho_{22} - i\frac{\sigma\phi}{\omega}.$$

From a computational point of view, the main drawback of the classical Biot's model consists in the use of two displacements fields for describing the behavior of a porous medium with elastic solid part. Moreover, from a modelling point of view, the coefficients of this model are not properly defined. These disadvantage can be avoided by using models obtained by homogenization techniques. In this case, it is possible to state models which involve only a pressure field and a unique displacement field as unknowns.

In fact, we have to distinguish two kinds of models attending to the geometrical configuration of the pores in the material: the first one when the fluid part is disconnected (media with closed pores), and the second one when the fluid part is connected (media with open pores). Besides, according to the different treatment of the dissipative effects in the models, we can also derive two different kind of them named dissipative and non-dissipative models.

Firstly we focus our attention in the description of the non-dissipative model with closed pores, following the ideas presented by Ferrín and Mikelic in [49] and [62].

1.3.2 Non-dissipative poroelastic model (closed pores)

If we again assume that the porous medium is homogeneous and isotropic from a macroscopic point of view, then the equations governing the pressure field, P, and the displacement field, $\boldsymbol{U}$, in the porous medium are

$$\rho \frac{\partial^2 \boldsymbol{U}}{\partial t^2} - \operatorname{div}\left(\mathsf{A}\left[\boldsymbol{E}(\boldsymbol{U})\right]\right) + \frac{1}{\hat{c}}\left(\boldsymbol{B} - \phi \boldsymbol{I}\right) \mathbf{grad}\left(\operatorname{div}\left(\boldsymbol{B} - \phi \boldsymbol{I}\right) \boldsymbol{U}\right) = \mathbf{0}, \tag{1.35}$$

$$P = -\frac{1}{\hat{c}} \operatorname{div}\left(\boldsymbol{B} - \phi \boldsymbol{I}\right) \boldsymbol{U}. \tag{1.36}$$

We recall that ϕ is the porosity, ρ_{F} and ρ_{S} are, respectively, the density of the fluid and of the solid part, and the coefficient $\hat{c}$, the symmetric tensor $\boldsymbol{B}$, and the linear operator A depend on the geometrical shape of the pores of the porous material, but not on the spatial variables.

Derivation of the model by two-scale homogenization technique

For the sake of completeness in the exposition, in this subsection we describe how to obtain the systems of equations (1.35)-(1.36) by using a two-scale homogenization technique. Moreover, we also state the cell problems which define the coefficients that arise in this model.

In the case of periodic porous media with elastic solid part and closed pores, we apply the same homogenization technique reviewed in Section 1.2.1 for porous media with rigid solid part. With this technique we obtain a model with a unique unknown displacement field to describe the motion in the porous material (see [48], [49] or [50]). In what follows, we use the same technique to derive the equations (1.35)-(1.36).

Firstly, we use the same notation used for the fluid and solid domains and the cells as the ones introduced in Subsection 1.2.1. We only recall that $\Omega_{\mathrm{F}}^{\epsilon}$ and $\Omega_{\mathrm{S}}^{\epsilon}$ are, respectively, the fluid and solid part of the porous domain.

Under the small deformations assumption, the macroscopic problem is given by the following fluid-structure problem, where the displacements are described in terms of the linearized equations in the fluid and solid domains:

$$\begin{aligned}
\rho_{\mathrm{S}}\frac{\partial^2 \boldsymbol{w}^\epsilon}{\partial t^2} - \operatorname{div}(\boldsymbol{S}(\boldsymbol{w}^\epsilon)) &= \boldsymbol{0} && \text{in } \Omega_{\mathrm{S}}^\epsilon \times (0,T), && (1.37)\\
\boldsymbol{S}(\boldsymbol{w}^\epsilon) := \mathsf{C}[\boldsymbol{E}(\boldsymbol{w}^\epsilon)] = 2\mu\boldsymbol{E}(\boldsymbol{w}^\epsilon) + \lambda(\operatorname{tr}(\boldsymbol{E}(\boldsymbol{w}^\epsilon)))\boldsymbol{I} & && \text{in } \Omega_{\mathrm{S}}^\epsilon \times (0,T), && (1.38)\\
\rho_{\mathrm{F}}\frac{\partial^2 \boldsymbol{u}^\epsilon}{\partial t^2} + \mathbf{grad}\, p^\epsilon &= \boldsymbol{0} && \text{in } \Omega_{\mathrm{F}}^\epsilon \times (0,T), && (1.39)\\
p^\epsilon &= -\rho_{\mathrm{F}} c^2 \operatorname{div} \boldsymbol{u}^\epsilon && \text{in } \Omega_{\mathrm{F}}^\epsilon \times (0,T), && (1.40)\\
\boldsymbol{u}^\epsilon \cdot \boldsymbol{\nu} &= \boldsymbol{w}^\epsilon \cdot \boldsymbol{\nu} && \text{on } \Gamma_\epsilon \times (0,T), && (1.41)\\
\boldsymbol{S}(\boldsymbol{w}^\epsilon)\boldsymbol{\nu} &= -p^\epsilon \boldsymbol{\nu} && \text{on } \Gamma_\epsilon \times (0,T), && (1.42)\\
\boldsymbol{w}^\epsilon = \frac{\partial \boldsymbol{w}^\epsilon}{\partial t} &= \boldsymbol{0} && \text{in } \Omega_{\mathrm{S}}^\epsilon \times \{0\}, && (1.43)\\
\boldsymbol{u}^\epsilon = \frac{\partial \boldsymbol{u}^\epsilon}{\partial t} &= \boldsymbol{0} && \text{in } \Omega_{\mathrm{F}}^\epsilon \times \{0\}, && (1.44)\\
p^\epsilon, \boldsymbol{w}^\epsilon, \text{ and } \boldsymbol{u}^\epsilon & && \text{are } L-\text{periodic}. && (1.45)
\end{aligned}$$

Here, $\boldsymbol{u}^\epsilon$ and p^ϵ are, respectively, the fluid displacement and pressure fields, $\boldsymbol{w}^\epsilon$ is the solid displacement field, $\boldsymbol{S}(\boldsymbol{w}^\epsilon)$ is the linear approximation of the Piola-Kirchhoff stress tensor and $\boldsymbol{E}(\boldsymbol{w}^\epsilon) = \frac{1}{2}(\mathbf{grad}\,\boldsymbol{w}^\epsilon + (\mathbf{grad}\,\boldsymbol{w}^\epsilon)^t)$ is the infinitesimal strain tensor associated to the solid displacement field. Finally ρ_{F} and ρ_{S} are the mass densities in the fluid and in the solid part, respectively, λ and μ are the Lamé coefficients of the solid part, and c is the sound speed in the fluid part of the porous material.

Now we describe the construction of the homogenized problem using the two-scale method. We recall that $\boldsymbol{x}$ is the slow spatial variable whereas $\boldsymbol{y}$ is the fast one. Since we have two scales, the spatial derivatives are transformed by Eqs. (1.20)-(1.22), introduced in Subsection 1.2.1, in terms of operators $\mathbf{grad}_{\boldsymbol{x}}$, $\mathbf{grad}_{\boldsymbol{y}}$, $\operatorname{div}_{\boldsymbol{x}}$, and $\operatorname{div}_{\boldsymbol{y}}$, where the subscripts denote the spatial variable involved in the differential operator.

Following the ideas presented by Ferrín & Mikelić [62], as a first step, we extend the fluid and solid displacement field to a unique field $\tilde{\boldsymbol{u}}^\epsilon$ defined in Ω by the expression

$$\tilde{\boldsymbol{u}}^\epsilon(\boldsymbol{x},t) = \begin{cases} \boldsymbol{u}^\epsilon(\boldsymbol{x},t) & \text{if } \boldsymbol{x} \in \Omega_{\mathrm{F}}^\epsilon, \\ \boldsymbol{w}^\epsilon(\boldsymbol{x},t) & \text{if } \boldsymbol{x} \in \Omega_{\mathrm{S}}^\epsilon, \end{cases} \tag{1.46}$$

and, analogously, a pressure field $\tilde{p}^\epsilon$ defined as

$$\tilde{p}^\epsilon(\boldsymbol{x},t) = \begin{cases} -\rho_{\mathrm{F}} c^2 \operatorname{div} \boldsymbol{u}^\epsilon(\boldsymbol{x},t) + \dfrac{\rho_{\mathrm{F}} c^2}{|\Omega|} \displaystyle\int_{\Omega_F^\epsilon} \operatorname{div} \boldsymbol{u}^\epsilon(\boldsymbol{x},t)\, dV_{\boldsymbol{x}} & \text{if } \boldsymbol{x} \in \Omega_{\mathrm{F}}^\epsilon, \\ \dfrac{\rho_{\mathrm{F}} c^2}{|\Omega|} \displaystyle\int_{\Omega_F^\epsilon} \operatorname{div} \boldsymbol{u}^\epsilon(\boldsymbol{x},t)\, dV_{\boldsymbol{x}} & \text{if } \boldsymbol{x} \in \Omega_{\mathrm{S}}^\epsilon. \end{cases} \tag{1.47}$$

If we denote by $\boldsymbol{u}^0(\boldsymbol{x},t)$ and $\tilde{p}^0(\boldsymbol{x},\boldsymbol{y},t)$ the limit fields when ϵ tends to zero for the displacement $\tilde{\boldsymbol{u}}^\epsilon$ and the pressure $\tilde{p}^\epsilon$, respectively, and we define $P(\boldsymbol{x},t)$ such that

$$\tilde{p}^0(\boldsymbol{x},\boldsymbol{y},t) = \chi_{Y_{\mathrm{F}}}(\boldsymbol{y}) P(\boldsymbol{x},t) + B(t),$$

where $B(t)$ only depends on time $t \in (0,T)$, then $\boldsymbol{u}^0(\boldsymbol{x},t)$ and $P(\boldsymbol{x},t)$ satisfy the limit problem

$$\rho \frac{\partial^2 \boldsymbol{u}^0}{\partial t^2} - \operatorname{div}_{\boldsymbol{x}} \left(\mathsf{A} \left[\boldsymbol{E}(\boldsymbol{u}^0) \right] \right) - \operatorname{div}_{\boldsymbol{x}} (P \boldsymbol{B}) + |Y_{\mathrm{F}}| \, \mathbf{grad}_{\boldsymbol{x}} P = \mathbf{0}, \tag{1.48}$$

$$-\frac{|Y_{\mathrm{F}}|}{\rho_{\mathrm{F}} c^2} \frac{\partial P}{\partial t} = |Y_{\mathrm{F}}| \operatorname{div}_{\boldsymbol{x}} \left(\frac{\partial \boldsymbol{u}^0}{\partial t} \right) - \boldsymbol{B} : \frac{\partial}{\partial t} \left(\boldsymbol{E}_{\boldsymbol{x}}(\boldsymbol{u}^0) \right) - \frac{\partial P}{\partial t} \int_Y \operatorname{div}_{\boldsymbol{y}} \boldsymbol{w}^0 \, dV_{\boldsymbol{y}}, \tag{1.49}$$

where $\rho = \rho_{\mathrm{F}} |Y_{\mathrm{F}}| + \rho_{\mathrm{S}} |Y_{\mathrm{S}}|$. Vector field $\boldsymbol{w}^0$, and tensor $\boldsymbol{B}$ and linear operator A are defined from problems stated in only one of the cells of the porous medium. More precisely, let $\boldsymbol{w}^0$ be the solution of the following problem in the solid part of the cell Y:

$$-\operatorname{div}_{\boldsymbol{y}} \left(\mathsf{C} \left[\boldsymbol{E}_{\boldsymbol{y}}(\boldsymbol{w}^0) \right] \right) = \mathbf{0} \qquad \text{in } Y_{\mathrm{S}}, \tag{1.50}$$

$$-\mathsf{C} \left[\boldsymbol{E}_{\boldsymbol{y}}(\boldsymbol{w}^0) \right] \boldsymbol{\nu} = \boldsymbol{\nu} \qquad \text{on } \partial Y_{\mathrm{S}} \setminus \partial Y, \tag{1.51}$$

$$\int_Y \boldsymbol{w}^0 \, dV_{\boldsymbol{y}} = \mathbf{0}, \tag{1.52}$$

where $\boldsymbol{\nu}$ is the unit normal vector to $\partial Y_{\mathrm{S}} \setminus \partial Y$ exterior to Y_{S}. Moreover, if for each $1 \le i,j \le n$, we define the vector $\boldsymbol{w}^{ij}$ as the solution of the following problem:

$$\operatorname{div}_{\boldsymbol{y}} \left(\mathsf{C} \left[\frac{\boldsymbol{e}_i \otimes \boldsymbol{e}_j + \boldsymbol{e}_j \otimes \boldsymbol{e}_i}{2} + \boldsymbol{E}_{\boldsymbol{y}} \left(\boldsymbol{w}^{ij} \right) \right] \right) = \mathbf{0} \qquad \text{in } Y_{\mathrm{S}}, \tag{1.53}$$

$$\mathsf{C} \left[\frac{\boldsymbol{e}_i \otimes \boldsymbol{e}_j + \boldsymbol{e}_j \otimes \boldsymbol{e}_i}{2} + \boldsymbol{E}_{\boldsymbol{y}}(\boldsymbol{w}^{ij}) \right] \boldsymbol{\nu} = \mathbf{0} \qquad \text{on } \partial Y_{\mathrm{S}} \setminus \partial Y, \tag{1.54}$$

$$\int_{Y_{\mathrm{S}}} \boldsymbol{w}^{ij} \, dV_{\boldsymbol{y}} = \mathbf{0}, \tag{1.55}$$

then the symmetric tensor $\boldsymbol{B}$ is given by

$$\boldsymbol{B} = \int_{Y_{\mathrm{S}}} \mathsf{C} \left[\boldsymbol{E}_{\boldsymbol{y}} \left(\boldsymbol{w}^0 \right) \right] \, dV_{\boldsymbol{y}}, \tag{1.56}$$

whereas every component A_{klij} of the linear operator A ($(\mathsf{A}[\boldsymbol{E}])_{kl} = \mathsf{A}_{klij} E_{ij}$), is given by

$$\mathsf{A}_{klij} = \left(\int_{Y_{\mathrm{S}}} \mathsf{C} \left[\frac{\boldsymbol{e}_i \otimes \boldsymbol{e}_j + \boldsymbol{e}_j \otimes \boldsymbol{e}_i}{2} + \boldsymbol{E}_{\boldsymbol{y}} \left(\boldsymbol{w}^{ij} \right) \right] \, dV_{\boldsymbol{y}} \right)_{kl}, \quad 1 \le i,j,k,l \le n. \tag{1.57}$$

We can easily check that $\mathsf{A}_{klij} = \mathsf{A}_{lkij} = \mathsf{A}_{lkji}$.

Hence, if $\boldsymbol{U} = \boldsymbol{u}^0$ denotes the macroscopic displacement and we integrate (1.49) with respect to time, we obtain

$$\rho \frac{\partial^2 \boldsymbol{U}}{\partial t^2} - \operatorname{div} \left(\mathsf{A} \left[\boldsymbol{E}(\boldsymbol{U}) \right] \right) - (\boldsymbol{B} - \phi \boldsymbol{I}) \, \mathbf{grad} \, P = \mathbf{0}, \tag{1.58}$$

$$\phi \operatorname{div} \boldsymbol{U} = \boldsymbol{B} : \boldsymbol{E}(\boldsymbol{U}) + \hat{c} P, \tag{1.59}$$

where the differential operators are assumed to be written with respect to the macroscopic variable $\boldsymbol{x}$ and

$$\hat{c} = -\frac{\phi}{\rho_{\mathrm{F}} c^2} + \int_{Y_{\mathrm{S}}} \mathrm{div}_{\boldsymbol{y}} \boldsymbol{w}^0 \, dV_{\boldsymbol{y}}. \tag{1.60}$$

If we rewrite the terms arising in the equations, taking into account that $\boldsymbol{B} : \boldsymbol{E}(\boldsymbol{U}) = \mathrm{div}\, \boldsymbol{B}\boldsymbol{U}$, and we eliminate the pressure in (1.48), then we have

$$\rho \frac{\partial^2 \boldsymbol{U}}{\partial t^2} - \mathrm{div}\left(\mathsf{A}\left[\boldsymbol{E}(\boldsymbol{U})\right]\right) + \frac{1}{\hat{c}} \left(\boldsymbol{B} - \phi \boldsymbol{I}\right) \mathbf{grad}\left(\mathrm{div}\left(\boldsymbol{B} - \phi \boldsymbol{I}\right) \boldsymbol{U}\right) = \boldsymbol{0}, \tag{1.61}$$

$$P = -\frac{1}{\hat{c}} \mathrm{div}\left(\boldsymbol{B} - \phi \boldsymbol{I}\right) \boldsymbol{U}. \tag{1.62}$$

1.3.3 Non-dissipative poroelastic model (open pores)

Now, we consider a porous medium with elastic solid part and open pores. We apply the same homogenization technique that we have used in the previous section to obtain other new model.

If we again assume that the porous medium is homogeneous and isotropic, from a macroscopic point of view, then the equations satisfied by the pressure field P and the displacement $\boldsymbol{U}$ in the porous medium are

$$\left(\rho \boldsymbol{I} - \rho_{\mathrm{F}} \boldsymbol{A}\right) \frac{\partial^2 \boldsymbol{U}}{\partial t^2} - \mathrm{div}\left(\mathsf{A}\left[\boldsymbol{E}(\boldsymbol{U})\right]\right) - \left(\boldsymbol{A} + \boldsymbol{B} - \phi \boldsymbol{I}\right) \mathbf{grad}\, P = \boldsymbol{0}, \tag{1.63}$$

$$\hat{c} \frac{\partial^2 P}{\partial t^2} + \frac{1}{\rho_{\mathrm{F}}} \mathrm{div}\left(\boldsymbol{A}\, \mathbf{grad}\, P\right) = -\mathrm{div}\left(\left(\boldsymbol{A} + \boldsymbol{B} - \phi \boldsymbol{I}\right) \frac{\partial^2 \boldsymbol{U}}{\partial t^2}\right), \tag{1.64}$$

where we recall that ϕ is the porosity coefficient, ρ_{F} and ρ_{S} are, respectively, the mass density of the fluid and solid part, $\rho = \rho_{\mathrm{F}} |Y_{\mathrm{F}}| + \rho_{\mathrm{S}} |Y_{\mathrm{S}}|$.

As we have made in the previous subsection, we are going to summarize how to obtain this model by using the two-scale homogenization technique. If we state the same fluid-structure problem as in (1.37)-(1.45) and define the same extended pressure, $\tilde{p}^\epsilon$, and displacement field $\tilde{u}^\epsilon$, given by (1.47) and (1.46), respectively, then $\boldsymbol{u}^0(\boldsymbol{x}, t)$ and $P(\boldsymbol{x}, t)$ satisfy the limit problem

$$\rho \frac{\partial^2 \boldsymbol{u}^0}{\partial t^2} - \boldsymbol{A}\left(\mathbf{grad}_{\boldsymbol{x}} P + \rho_{\mathrm{F}} \frac{\partial^2 \boldsymbol{u}^0}{\partial t^2}\right) = \mathrm{div}_{\boldsymbol{x}}\left(\mathsf{A}\left[\boldsymbol{E}(\boldsymbol{u}^0)\right]\right) + \mathrm{div}_{\boldsymbol{x}}\left(P \boldsymbol{B}\right) - |Y_{\mathrm{F}}|\, \mathbf{grad}_{\boldsymbol{x}} P, \tag{1.65}$$

$$\begin{aligned} -\frac{|Y_{\mathrm{F}}|}{\rho_{\mathrm{F}} c^2} \frac{\partial P}{\partial t} =& \mathrm{div}_{\boldsymbol{x}}\left(\left(|Y_{\mathrm{F}}|\, \boldsymbol{I} - \boldsymbol{A}\right) \frac{\partial \boldsymbol{u}^0}{\partial t} - \frac{1}{\rho_{\mathrm{F}}} \boldsymbol{A} \int_0^t \mathbf{grad}_{\boldsymbol{x}} P(\boldsymbol{x}, \tau) d\tau\right) \\ & -\boldsymbol{B} : \frac{\partial}{\partial t}\left(\boldsymbol{E}_{\boldsymbol{x}}(\boldsymbol{u}^0)\right) - \frac{\partial P}{\partial t} \int_Y \mathrm{div}_{\boldsymbol{y}} \boldsymbol{w}^0 \, dV_{\boldsymbol{y}}, \end{aligned} \tag{1.66}$$

where we recall that $\rho = \rho_{\mathrm{F}}\, |Y_{\mathrm{F}}| + \rho_{\mathrm{S}}\, |Y_{\mathrm{S}}|$.

Tensor $\boldsymbol{B}$ and linear operator A are defined by (1.56) and (1.57), respectively, also using the same cell problems (1.50)-(1.52) and (1.53)-(1.55) stated in the previous subsection. We recall that the coefficient $\hat{c}$, the tensors $\boldsymbol{A}$ and $\boldsymbol{B}$, and the operator A depend on the geometrical shape of the pores of the material and on the properties of the fluid and solid parts, but not on the spatial variables.

In order to define tensor $\boldsymbol{A}$, we need to introduce a new cell problem. For each $1 \leq j \leq n$, we define the scalar field ξ^j as the solution of the following problem in the fluid part of the unit cell:

$$-\Delta_{\boldsymbol{y}} \xi^j = 0 \qquad \text{in } Y_{\mathrm{F}}, \tag{1.67}$$

$$\frac{\partial \xi^j}{\partial \boldsymbol{\nu}} = \boldsymbol{e}_j \cdot \boldsymbol{\nu} \qquad \text{on } \partial Y_{\mathrm{F}} \setminus \partial Y, \tag{1.68}$$

$$\xi^j \qquad \text{is } 1-\text{periodic in } Y, \tag{1.69}$$

$$\int_{Y_{\mathrm{F}}} \xi^j \, dV_{\boldsymbol{y}} = 0, \tag{1.70}$$

then each component A_{ij} of tensor $\boldsymbol{A}$ is given by

$$A_{ij} = \int_{Y_{\mathrm{F}}} \left(\delta_{ij} - \frac{\partial \xi^j}{\partial y_i} \right) dV_{\boldsymbol{y}}, \ 1 \leq i, j \leq n.$$

If $\boldsymbol{U} = \boldsymbol{u}^0$ denotes the macroscopic displacement and we integrate equation (1.66) with respect to time, we obtain

$$\rho \frac{\partial^2 \boldsymbol{U}}{\partial t^2} - \boldsymbol{A} \left(\mathbf{grad}\, P + \rho_{\mathrm{F}} \frac{\partial^2 \boldsymbol{U}}{\partial t^2} \right) - \operatorname{div} \left(\mathsf{A} \left[\boldsymbol{E}(\boldsymbol{U}) \right] \right) - (\boldsymbol{B} - \phi \boldsymbol{I})\, \mathbf{grad}\, P = \mathbf{0}, \tag{1.71}$$

$$\operatorname{div} \left(\phi \frac{\partial^2 \boldsymbol{U}}{\partial t^2} - \frac{1}{\rho_{\mathrm{F}}} \boldsymbol{A}\, \mathbf{grad}\, P - \boldsymbol{A} \frac{\partial^2 \boldsymbol{U}}{\partial t^2} \right) = \boldsymbol{B} : \boldsymbol{E} \left(\frac{\partial^2 \boldsymbol{U}}{\partial t^2} \right) + \hat{c} \frac{\partial^2 P}{\partial t^2}. \tag{1.72}$$

where the differential operators are assumed to be written with respect to the macroscopic variable $\boldsymbol{x}$ and $\hat{c}$ is again given by (1.60). If we rewrite the terms which arise in the equations taking into account that $\boldsymbol{B} : \boldsymbol{E}(\boldsymbol{U}) = \operatorname{div} \boldsymbol{B}\boldsymbol{U}$, and eliminate the pressure in the first of these equations, we finally obtain the system of equations (1.63)-(1.64).

In spite of the fact that this model only uses a unique displacement field $\boldsymbol{U}$, which is an advantage with respect to the classical Biot's model, the inclusion of the pressure gradient in equation (1.64) does not allow decoupling the equations as we have done in the model for closed pores.

For the sake of completeness in the exposition we also summarize the model when a dissipative behavior is assumed in a porous medium with open pores.

1.3.4 Dissipative poroelastic model (open pore)

The dissipative generalized Biot model has been derived, by using homogenization techniques, in Clopeau *et al.* [49] for the case where fluid viscosity η is of order $O(\varepsilon^2)$, ε being the size of the elementary cell. The equations are given by

$$\rho\boldsymbol{I}\frac{\partial^2\boldsymbol{U}}{\partial t^2} - \frac{d}{dt}\int_0^t \boldsymbol{A}(t-\tau)\left(\mathbf{grad}\,P(\boldsymbol{x},\tau) + \rho_{\mathrm{F}}\frac{\partial^2\boldsymbol{U}}{\partial\tau^2}(\boldsymbol{x},\tau)\right)d\tau \\ - \operatorname{div}\left(\mathsf{A}\left[\boldsymbol{E}(\boldsymbol{U})\right]\right) - (\boldsymbol{B} - \phi\boldsymbol{I})\,\mathbf{grad}\,P = \mathbf{0},$$

and

$$\operatorname{div}\left(\phi\frac{\partial\boldsymbol{U}}{\partial t} - \int_0^t \boldsymbol{A}(t-\tau)\left(\frac{1}{\rho_{\mathrm{F}}}\,\mathbf{grad}\,P(\boldsymbol{x},\tau) + \frac{\partial^2\boldsymbol{U}}{\partial\tau^2}(\boldsymbol{x},\tau)\right)d\tau\right) = \operatorname{div}\boldsymbol{B}\frac{\partial\boldsymbol{U}}{\partial t} + \hat{c}\frac{\partial P}{\partial t},$$

where we recall that ρ_{F} is the fluid density, ρ_{S} is the density of the solid skeleton, $\rho = \phi\rho_{\mathrm{F}} + (1-\phi)\rho_{\mathrm{S}}$ and

$$\begin{aligned} \mathsf{A}_{klij} &:= \left(\int_{Y_{\mathrm{S}}} \mathsf{C}\left[\frac{\boldsymbol{e}_i\otimes\boldsymbol{e}_j + \boldsymbol{e}_j\otimes\boldsymbol{e}_i}{2} + \boldsymbol{E}_{\boldsymbol{y}}\left(\boldsymbol{w}^{ij}\right)\right]\,dV_{\boldsymbol{y}}\right)_{kl}, \\ \boldsymbol{B} &:= \int_{Y_{\mathrm{S}}} \mathsf{C}\left[\boldsymbol{E}_{\boldsymbol{y}}(\boldsymbol{w}^0)\right]\,dV_{\boldsymbol{y}}, \\ \hat{c} &:= \int_{Y_{\mathrm{S}}} \operatorname{div}_{\boldsymbol{y}}\boldsymbol{w}^0\,dV_{\boldsymbol{y}}, \\ A_{ij}(t) &:= \int_{Y_{\mathrm{F}}} \boldsymbol{w}^{ij}\left(\boldsymbol{y}, \frac{\rho_{\mathrm{F}}}{\eta}t\right)\,dV_{\boldsymbol{y}}, \end{aligned}$$

which implies, in particular, $A_{ij}(0) = \int_{Y_{\mathrm{F}}} \boldsymbol{w}^{ij}(\boldsymbol{y},0)\,dV_{\boldsymbol{y}} = \phi\delta_{ij}$.

Let us remark that tensor $\boldsymbol{B}$, linear operator A, and coefficient $\hat{c}$ coincide with the expressions given for the non-dissipative models, since the vector fields $\boldsymbol{w}^0$ and $\boldsymbol{w}^{ij}$ are solution of the same boundary-value problems (1.50)-(1.52) and (1.53)-(1.55), respectively.

Chapter 2

Finite element solution of acoustic propagation in rigid porous media

Contents

2.1 Introduction

In this chapter, only the case of rigid frame porous material will be considered. Two models will be taken into account: the above mentioned sort of Darcy's model and the Allard-Champoux model (see [5]), both presented in Section 1.2. As we have shown in the previous chapter, the main difference between them lies in the frequency dependence of the coefficients, namely, the mass density and bulk modulus.

In fact, through this chapter we will focus our attention on the numerical computation of the resonance frequencies and the frequency response of some acoustic problems which involve these two models, which will be always stated in bounded domains. With this purpose we have implemented a finite element method. Because its easy implementation and its effectiveness in handling complex geometries, the finite element method has become popular to solve such problems. Some examples of the finite element method applied to sound propagation in poroelastic media are in the papers by Easwaran *et al* [58], Panneton and Atalla [92], Göransson [68] or Atalla *et al* [11]. All of them, take Biot's general theory as the starting point. Other kind of problems concerning porous materials, related to vibration modes, were solved by Bermúdez *et al* [36].

More precisely, a finite element method introduced by Raviart and Thomas [96] will be used to solve numerically the two models which are formulated in displacements. In fact, if we consider a tetrahedron partition of the computational domain, the degrees of freedom of the Raviart-Thomas elements are the normal displacement in each face of the tetrahedra. So the divergence of the displacement field is conserved in the continuous and discrete problem and, as it has been proven in Bermúdez *et al* [26] (see also [35] and references therein), these finite elements do not produce spurious modes.

Numerical experiments using both models will be presented for different three-dimensional examples. More precisely, we solve the source problem associated with an external harmonic excitation which allows us to know the response of the porous material. We also solve the nonlinear spectral problem associated with it.

The outline of this chapter is as follows. In Section 2.2 we present the two models associated with the problem consisting of a finite two-layer system with rigid porous materials. They will be stated in the frequency domain leading to the response problem and to a nonlinear eigenvalue problem. In Section 2.3 the free vibration problem associated with this nonlinear eigenvalue problem is analyzed in order to obtain a deeper insight of the overdamped vibration frequencies. In Section 2.4 weak formulations for both problems are presented and an analysis of overdamped vibration frequencies is made. In Section 2.5 the finite element method is introduced, whereas in Section 2.6 the corresponding matrix description is shown. Finally, in Section 2.7, numerical results for some 3D examples are given for both the response and the spectral problems.

2.2 Models for fluid-porous vibrations

Let us consider a coupled system consisting of an acoustic fluid (i.e. compressible barotropic inviscid) and a porous medium contained in a three-dimensional cavity. Let Ω_{F} and Ω_{A} be the domains occupied by the fluid and the porous medium, respectively (see Figure 2.1). The boundary of $\overline{\Omega}_{\mathrm{F}} \cup \overline{\Omega}_{\mathrm{A}}$, denoted by Γ, is the union of two parts, Γ_{D} and Γ_{E}. Γ_{D} denotes the rigid walls of the cavity. Let $\boldsymbol{\nu}$ the outward unit normal vector to Γ. We assume the interface between the fluid and the porous media, denoted by Γ_{I}, is the union of surfaces, $\Gamma_0, \Gamma_1, \ldots, \Gamma_J$. Let $\boldsymbol{n}$ be the unit normal vector to this interface pointing outwards Ω_{A}. Figure 2.1 shows a vertical cut of the domain for a better understanding of the notation.

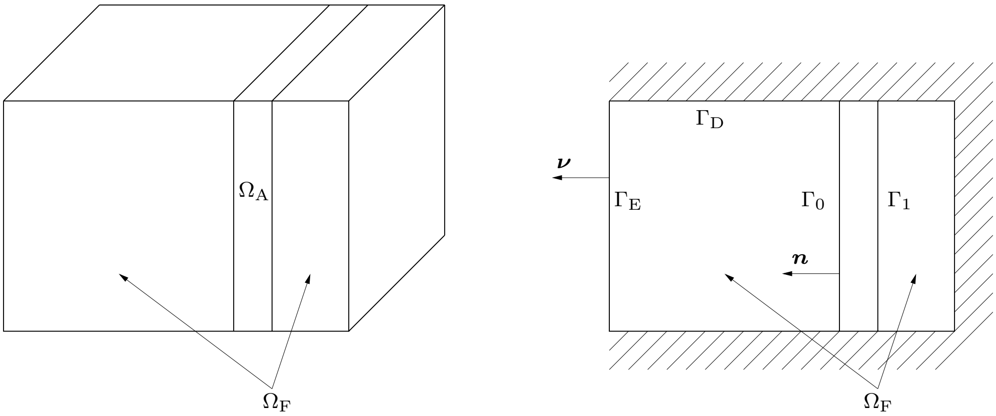

Figure 2.1: 3D domain and vertical cut.

For studying the response of the coupled system (fluid-porous medium), subject to harmonic forces acting on Γ_{E}, we consider two different models for the vibrations in the porous medium: Darcy's like model and Allard-Champoux model. Both models assume the skeleton of the porous media is rigid.

Firstly, the governing equations for free small amplitude motions of an acoustic fluid filling Ω_{F} are given in terms of displacement and pressure fields by

$$\rho_{\mathrm{F}} \frac{\partial^2 \boldsymbol{U}_{\mathrm{F}}}{\partial t^2} + \mathbf{grad}\, P_{\mathrm{F}} = \mathbf{0} \qquad \text{in } \Omega_{\mathrm{F}}, \tag{2.1}$$

$$P_{\mathrm{F}} = -\rho_{\mathrm{F}} c^2 \operatorname{div} \boldsymbol{U}_{\mathrm{F}} \qquad \text{in } \Omega_{\mathrm{F}}, \tag{2.2}$$

where P_{F} is the pressure, $\boldsymbol{U}_{\mathrm{F}}$ the displacement field, ρ_{F} the density and c the acoustic speed in the fluid.

Secondly, let us recall the rigid porous models introduced in Section 1.2 of the previous chapter. The Darcy's like model only has slight differences with respect to the above fluid model. One of them consists of an additional damping term, named Darcy's term (see [3]). Moreover, the interstitial fluid flow is supposed to be isothermal, a standard assumption in porous media acoustics. If $\boldsymbol{U}_{\mathrm{A}}$ is the displacement field and P_{A} is the pressure in the porous medium, the Darcy's like model is described by the following equations,

$$\begin{aligned} \rho_{\mathrm{F}} \frac{\partial^2 \boldsymbol{U}_{\mathrm{A}}}{\partial t^2} + \mathbf{grad}\, P_{\mathrm{A}} + \boldsymbol{\sigma} \frac{\partial \boldsymbol{U}_{\mathrm{A}}}{\partial t} &= \mathbf{0} \qquad \text{in } \Omega_{\mathrm{A}}, \\ P_{\mathrm{A}} &= -\frac{\rho_{\mathrm{F}} c^2}{\phi \gamma} \operatorname{div} \boldsymbol{U}_{\mathrm{A}} \qquad \text{in } \Omega_{\mathrm{A}}, \end{aligned}$$

where $\boldsymbol{\sigma}$ is the flow resistivity tensor, ϕ is the porosity, γ is the ratio of specific heats of fluid and, again, ρ_{F} is the density and c the acoustic speed of the fluid filling the porous medium.

Since we neglect viscosity in the fluid and shear stresses in the porous media, only the normal component of the displacement vanishes on the part Γ_{D} of the cavity boundary,

$$\begin{aligned} \boldsymbol{U}_{\mathrm{F}} \cdot \boldsymbol{\nu} &= 0 \qquad \text{on } \Gamma_{\mathrm{D}} \cap \partial\Omega_{\mathrm{F}}, \\ \boldsymbol{U}_{\mathrm{A}} \cdot \boldsymbol{\nu} &= 0 \qquad \text{on } \Gamma_{\mathrm{D}} \cap \partial\Omega_{\mathrm{A}}. \end{aligned}$$

Similarly, on the interface Γ_{I} between the fluid and the porous medium we consider the usual kinematic and kinetic interface conditions, i.e., $\boldsymbol{U}_{\mathrm{F}} \cdot \boldsymbol{n} = \boldsymbol{U}_{\mathrm{A}} \cdot \boldsymbol{n}$ and $P_{\mathrm{F}} = P_{\mathrm{A}}$.

If a displacement F is applied on Γ_{E}, the equations describing the motion of the coupled system can be written, when we use the above model, as follows (see [3]):

$$\begin{aligned} \rho_{\mathrm{F}} \frac{\partial^2 \boldsymbol{U}_{\mathrm{F}}}{\partial t^2} + \mathbf{grad}\, P_{\mathrm{F}} &= \mathbf{0} \qquad \text{in } \Omega_{\mathrm{F}}, && (2.3) \\ \rho_{\mathrm{F}} \frac{\partial^2 \boldsymbol{U}_{\mathrm{A}}}{\partial t^2} + \mathbf{grad}\, P_{\mathrm{A}} + \boldsymbol{\sigma} \frac{\partial \boldsymbol{U}_{\mathrm{A}}}{\partial t} &= \mathbf{0} \qquad \text{in } \Omega_{\mathrm{A}}, && (2.4) \\ P_{\mathrm{F}} &= -\rho_{\mathrm{F}} c^2 \operatorname{div} \boldsymbol{U}_{\mathrm{F}} \qquad \text{in } \Omega_{\mathrm{F}}, && (2.5) \\ P_{\mathrm{A}} &= -\frac{\rho_{\mathrm{F}} c^2}{\phi\gamma} \operatorname{div} \boldsymbol{U}_{\mathrm{A}} \qquad \text{in } \Omega_{\mathrm{A}}, && (2.6) \\ P_{\mathrm{F}} &= P_{\mathrm{A}} \qquad \text{on } \Gamma_{\mathrm{I}}, && (2.7) \\ \boldsymbol{U}_{\mathrm{F}} \cdot \boldsymbol{n} &= \boldsymbol{U}_{\mathrm{A}} \cdot \boldsymbol{n} \qquad \text{on } \Gamma_{\mathrm{I}}, && (2.8) \\ \boldsymbol{U}_{\mathrm{F}} \cdot \boldsymbol{\nu} &= 0 \qquad \text{on } \Gamma_{\mathrm{D}} \cap \partial\Omega_{\mathrm{F}}, && (2.9) \\ \boldsymbol{U}_{\mathrm{A}} \cdot \boldsymbol{\nu} &= 0 \qquad \text{on } \Gamma_{\mathrm{D}} \cap \partial\Omega_{\mathrm{A}}, && (2.10) \\ \boldsymbol{U}_{\mathrm{F}} \cdot \boldsymbol{\nu} &= F \qquad \text{on } \Gamma_{\mathrm{E}}. && (2.11) \end{aligned}$$

We are interested in harmonic vibrations. Thus, we suppose the displacement is of the form $F(x_1, x_2, x_3, t) = \operatorname{Re}\left(\mathrm{e}^{i\omega t} f(x_1, x_2, x_3)\right)$. Then, all fields are harmonic, i.e.,

$$\begin{aligned} \boldsymbol{U}_{\mathrm{F}}(x_1, x_2, x_3, t) &= \operatorname{Re}\left(\mathrm{e}^{i\omega t} \boldsymbol{u}_{\mathrm{F}}(x_1, x_2, x_3)\right), \quad \boldsymbol{U}_{\mathrm{A}}(x_1, x_2, x_3, t) = \operatorname{Re}\left(\mathrm{e}^{i\omega t} \boldsymbol{u}_{\mathrm{A}}(x_1, x_2, x_3)\right), \\ P_{\mathrm{F}}(x_1, x_2, x_3, t) &= \operatorname{Re}\left(\mathrm{e}^{i\omega t} p_{\mathrm{F}}(x_1, x_2, x_3)\right), \quad P_{\mathrm{A}}(x_1, x_2, x_3, t) = \operatorname{Re}\left(\mathrm{e}^{i\omega t} p_{\mathrm{A}}(x_1, x_2, x_3)\right). \end{aligned}$$

By replacing these expressions into the above equations, we can define a harmonic source problem associated with the evolutionary source problem (2.3)-(2.11), namely,

$$-\omega^2\rho_{\mathrm{F}}\boldsymbol{u}_{\mathrm{F}} + \mathbf{grad}\, p_{\mathrm{F}} = \mathbf{0} \qquad \text{in } \Omega_{\mathrm{F}}, \tag{2.12}$$

$$-\omega^2\rho_{\mathrm{F}}\left(1 + \frac{\boldsymbol{\sigma}}{i\omega\rho_{\mathrm{F}}}\right)\boldsymbol{u}_{\mathrm{A}} + \mathbf{grad}\, p_{\mathrm{A}} = \mathbf{0} \qquad \text{in } \Omega_{\mathrm{A}}, \tag{2.13}$$

$$p_{\mathrm{F}} = -\rho_{\mathrm{F}}c^2 \operatorname{div} \boldsymbol{u}_{\mathrm{F}} \qquad \text{in } \Omega_{\mathrm{F}}, \tag{2.14}$$

$$p_{\mathrm{A}} = -\frac{\rho_{\mathrm{F}}c^2}{\phi\gamma} \operatorname{div} \boldsymbol{u}_{\mathrm{A}} \qquad \text{in } \Omega_{\mathrm{A}}, \tag{2.15}$$

$$p_{\mathrm{F}} = p_{\mathrm{A}} \qquad \text{on } \Gamma_{\mathrm{I}}, \tag{2.16}$$

$$\boldsymbol{u}_{\mathrm{F}} \cdot \boldsymbol{n} = \boldsymbol{u}_{\mathrm{A}} \cdot \boldsymbol{n} \qquad \text{on } \Gamma_{\mathrm{I}}, \tag{2.17}$$

$$\boldsymbol{u}_{\mathrm{F}} \cdot \boldsymbol{\nu} = 0 \qquad \text{on } \Gamma_{\mathrm{D}} \cap \partial\Omega_{\mathrm{F}}, \tag{2.18}$$

$$\boldsymbol{u}_{\mathrm{A}} \cdot \boldsymbol{\nu} = 0 \qquad \text{on } \Gamma_{\mathrm{D}} \cap \partial\Omega_{\mathrm{A}}, \tag{2.19}$$

$$\boldsymbol{u}_{\mathrm{F}} \cdot \boldsymbol{\nu} = f \qquad \text{on } \Gamma_{\mathrm{E}}. \tag{2.20}$$

In this context, i.e., looking for harmonic motions, we can also consider the Allard-Champoux model (see [5]) for rigid frame fibrous materials (a particular case of porous medium with rigid solid part). In this case, not only the Darcy's term is included in a new generalized form but also the thermal exchange between the air and the fibers of the porous medium is considered in the model. The new equations replacing (2.13) and (2.15) are

$$-\omega^2\boldsymbol{\rho}(\omega)\boldsymbol{u}_{\mathrm{A}} + \mathbf{grad}\, p_{\mathrm{A}} = \mathbf{0} \qquad \text{in } \Omega_{\mathrm{A}}, \tag{2.21}$$

$$p_{\mathrm{A}} = -\operatorname{div}\left(\boldsymbol{\mu}(\omega)\boldsymbol{u}_{\mathrm{A}}\right) \qquad \text{in } \Omega_{\mathrm{A}}, \tag{2.22}$$

where $\boldsymbol{\rho}(\omega)$ and $\boldsymbol{\mu}(\omega)$ are the so called dynamic density tensor and dynamic bulk modulus tensor, respectively (see [5]) which was described in the previous chapter.

Drawing an analogy with the harmonic source problem (2.12)-(2.20), we can establish a similar one using the Allard-Champoux model (1.27):

$$-\omega^2\rho_{\mathrm{F}}\boldsymbol{u}_{\mathrm{F}} + \mathbf{grad}\, p_{\mathrm{F}} = \mathbf{0} \qquad \text{in } \Omega_{\mathrm{F}}, \tag{2.23}$$

$$-\omega^2\boldsymbol{\rho}(\omega)\boldsymbol{u}_{\mathrm{A}} + \mathbf{grad}\, p_{\mathrm{A}} = \mathbf{0} \qquad \text{in } \Omega_{\mathrm{A}}, \tag{2.24}$$

$$p_{\mathrm{F}} = -\rho_{\mathrm{F}}c^2 \operatorname{div} \boldsymbol{u}_{\mathrm{F}} \qquad \text{in } \Omega_{\mathrm{F}}, \tag{2.25}$$

$$p_{\mathrm{A}} = -\operatorname{div}\left(\boldsymbol{\mu}(\omega)\boldsymbol{u}_{\mathrm{A}}\right) \qquad \text{in } \Omega_{\mathrm{A}}, \tag{2.26}$$

$$p_{\mathrm{F}} = p_{\mathrm{A}} \qquad \text{on } \Gamma_{\mathrm{I}}, \tag{2.27}$$

$$\boldsymbol{u}_{\mathrm{F}} \cdot \boldsymbol{n} = \boldsymbol{u}_{\mathrm{A}} \cdot \boldsymbol{n} \qquad \text{on } \Gamma_{\mathrm{I}}, \tag{2.28}$$

$$\boldsymbol{u}_{\mathrm{F}} \cdot \boldsymbol{\nu} = 0 \qquad \text{on } \Gamma_{\mathrm{D}} \cap \partial\Omega_{\mathrm{F}}, \tag{2.29}$$

$$\boldsymbol{u}_{\mathrm{A}} \cdot \boldsymbol{\nu} = 0 \qquad \text{on } \Gamma_{\mathrm{D}} \cap \partial\Omega_{\mathrm{A}}, \tag{2.30}$$

$$\boldsymbol{u}_{\mathrm{F}} \cdot \boldsymbol{\nu} = f \qquad \text{on } \Gamma_{\mathrm{E}}. \tag{2.31}$$

2.3 Associated nonlinear eigenvalue problems

We can define a nonlinear eigenvalue problem, associated with the above source problem (2.23)-(2.31), which corresponds to determining the free vibrations of the fluid-porous system. More precisely, if we assume that $f = 0$ in the system (2.23)-(2.31), we can define the following problem:

Find a complex angular frequency ω *and complex amplitudes of pressure and displacement fields* (p_F, p_A) *and* $(\boldsymbol{u}_F, \boldsymbol{u}_A)$*, respectively, not all identically zero, satisfying*

$$-\omega^2\rho_{\mathrm{F}}\boldsymbol{u}_{\mathrm{F}} + \mathbf{grad}\, p_{\mathrm{F}} = \mathbf{0} \qquad \text{in } \Omega_{\mathrm{F}}, \tag{2.32}$$

$$-\omega^2\boldsymbol{\rho}(\omega)\boldsymbol{u}_{\mathrm{A}} + \mathbf{grad}\, p_{\mathrm{A}} = \mathbf{0} \qquad \text{in } \Omega_{\mathrm{A}}, \tag{2.33}$$

$$p_{\mathrm{F}} = -\rho_{\mathrm{F}}c^2 \operatorname{div} \boldsymbol{u}_{\mathrm{F}} \qquad \text{in } \Omega_{\mathrm{F}}, \tag{2.34}$$

$$p_{\mathrm{A}} = -\operatorname{div}\left(\boldsymbol{\mu}(\omega)\boldsymbol{u}_{\mathrm{A}}\right) \qquad \text{in } \Omega_{\mathrm{A}}, \tag{2.35}$$

$$p_{\mathrm{F}} = p_{\mathrm{A}} \qquad \text{on } \Gamma_{\mathrm{I}}, \tag{2.36}$$

$$\boldsymbol{u}_{\mathrm{F}} \cdot \boldsymbol{n} = \boldsymbol{u}_{\mathrm{A}} \cdot \boldsymbol{n} \qquad \text{on } \Gamma_{\mathrm{I}}, \tag{2.37}$$

$$\boldsymbol{u}_{\mathrm{F}} \cdot \boldsymbol{\nu} = 0 \qquad \text{on } \Gamma \cap \partial\Omega_{\mathrm{F}}, \tag{2.38}$$

$$\boldsymbol{u}_{\mathrm{A}} \cdot \boldsymbol{\nu} = 0 \qquad \text{on } \Gamma \cap \partial\Omega_{\mathrm{A}}. \tag{2.39}$$

On the other hand, if we used the Darcy's like model (2.3)-(2.11), we still obtain the above eigenvalue problem but the expressions for the dynamic density and the bulk modulus change. In this case, they are $\boldsymbol{\rho}(\omega) = \rho_{\mathrm{F}}\mathbf{I} + \boldsymbol{\sigma}/(i\omega)$ and $\boldsymbol{\mu}(\omega) = \rho_{\mathrm{F}}c^2/(\phi\gamma)\mathbf{I}$.

The solutions ω to this nonlinear eigenvalue problem (2.32)-(2.39) are expected to be complex numbers with non-null real and imaginary parts due to the dissipative terms. The real part corresponds to the angular frequency of the damped vibration mode, whereas the imaginary part corresponds to its decay rate and should be strictly positive. However, as the example below shows, overdamped modes corresponding to purely imaginary positive values of ω also exist.

To gain a deeper insight into these overdamped modes, let us introduce a simpler model problem for which these eigenvalues can be computed analytically. Let us take $\Omega_{\mathrm{F}} = (-a_{\mathrm{F}}, 0) \times (0, b) \times (0, d)$, $\Omega_{\mathrm{A}} = (0, a_{\mathrm{A}}) \times (0, b) \times (0, d)$, $\Gamma_{\mathrm{D}} = \Gamma$ and $\Gamma_{\mathrm{E}} = \emptyset$ (see Figure 2.2). If we consider an isotropic porous medium, modelled by the Darcy's equations, the eigenvalue problem can be solved by separation of variables.

For this purpose, it is convenient to write the problem in terms of pressure. This can be done by eliminating $\boldsymbol{u}_{\mathrm{F}}$ and $\boldsymbol{u}_{\mathrm{A}}$ in equations (2.32)-(2.33) by using (2.34) and (2.35). Thus

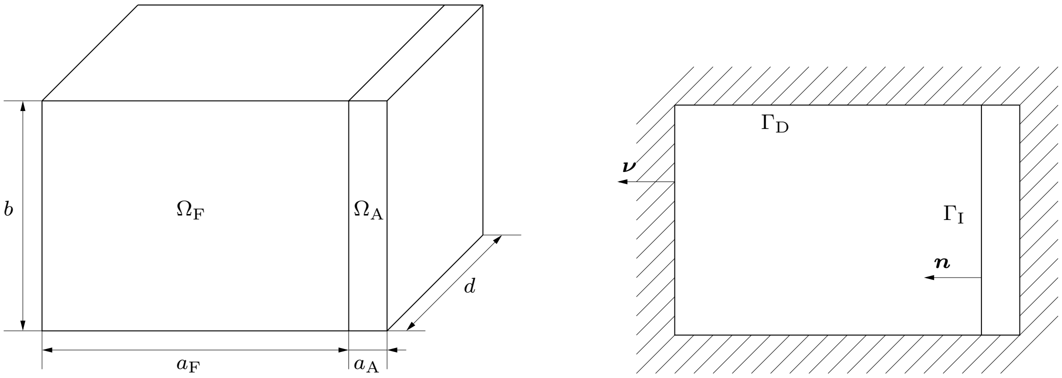

Figure 2.2: Fluid and rigid porous medium in a cavity with rigid walls.

we obtain:

$$\begin{aligned}
\omega^2 p_\mathrm{F} + c^2 \Delta p_\mathrm{F} &= 0 && \text{in } \Omega_\mathrm{F}, && (2.40)\\
\omega^2 \left(1 + \frac{\sigma}{i\omega\rho_\mathrm{F}}\right) p_\mathrm{A} + \frac{c^2}{\phi\gamma}\Delta p_\mathrm{A} &= 0 && \text{in } \Omega_\mathrm{A}, && (2.41)\\
p_\mathrm{F} &= p_\mathrm{A} && \text{on } \Gamma_\mathrm{I}, && (2.42)\\
\frac{1}{\rho_\mathrm{F}}\frac{\partial p_\mathrm{F}}{\partial \boldsymbol{n}} &= \frac{1}{\rho_\mathrm{F} + \frac{\sigma}{i\omega}}\frac{\partial p_\mathrm{A}}{\partial \boldsymbol{n}} && \text{on } \Gamma_\mathrm{I}, && (2.43)\\
\frac{\partial p_\mathrm{F}}{\partial \boldsymbol{\nu}} &= 0 && \text{on } \Gamma_\mathrm{D} \cap \partial\Omega_\mathrm{F}, && (2.44)\\
\frac{\partial p_\mathrm{A}}{\partial \boldsymbol{\nu}} &= 0 && \text{on } \Gamma_\mathrm{D} \cap \partial\Omega_\mathrm{A}. && (2.45)
\end{aligned}$$

If we look for non-trivial solutions of this problem of the form

$$\begin{aligned}
p_\mathrm{F}(x_1, x_2, x_3) &= X_\mathrm{F}(x_1) Y_\mathrm{F}(x_2) Z_\mathrm{F}(x_3),\\
p_\mathrm{A}(x_1, x_2, x_3) &= X_\mathrm{A}(x_1) Y_\mathrm{A}(x_2) Z_\mathrm{A}(x_3),
\end{aligned}$$

standard calculations show that:

$$\begin{aligned}
Y_\mathrm{F}(x_2) &= \cos\frac{j\pi x_2}{b},\ Y_\mathrm{A}(x_2) = \cos\frac{j\pi x_2}{b}, && j = 0, \pm 1, \pm 2, \dots\\
Z_\mathrm{F}(x_3) &= \cos\frac{k\pi x_3}{d},\ Z_\mathrm{A}(x_3) = \cos\frac{k\pi x_3}{d}, && k = 0, \pm 1, \pm 2, \dots
\end{aligned}$$

Furthermore, for any pair of integers j and k, we must have

$$\begin{aligned}
X_{\mathrm{F}}'' &= \beta_{\mathrm{F}}^2 X_{\mathrm{F}}, \qquad -a_{\mathrm{F}} < x_1 < 0, && (2.46)\\
X_{\mathrm{A}}'' &= \beta_{\mathrm{A}}^2 X_{\mathrm{A}}, \qquad 0 < x_1 < a_{\mathrm{A}}, && (2.47)\\
X_{\mathrm{F}}(0) &= X_{\mathrm{A}}(0), && (2.48)\\
\frac{1}{\rho_{\mathrm{F}}} X_{\mathrm{F}}'(0) &= \frac{1}{\rho_{\mathrm{F}} + \frac{\sigma}{i\omega}} X_{\mathrm{A}}'(0), && (2.49)\\
X_{\mathrm{F}}'(-a_{\mathrm{F}}) &= 0, && (2.50)\\
X_{\mathrm{F}}'(a_{\mathrm{A}}) &= 0, && (2.51)
\end{aligned}$$

with

$$\begin{aligned}
\beta_{\mathrm{F}}^2 + \frac{\omega^2}{c^2} &= \frac{\pi^2}{b^2} j^2 + \frac{\pi^2}{d^2} k^2, && (2.52)\\
\beta_{\mathrm{A}}^2 + \omega^2 \frac{\phi\gamma}{c^2}\left(1 + \frac{\sigma}{i\rho_{\mathrm{F}}\omega}\right) &= \frac{\pi^2}{b^2} j^2 + \frac{\pi^2}{d^2} k^2. && (2.53)
\end{aligned}$$

The general solutions of (2.46) and (2.47) are $X_{\mathrm{F}}(x_1) = C_{\mathrm{F},1}\,\mathrm{e}^{\beta_{\mathrm{F}} x_1} + C_{\mathrm{F},2}\,\mathrm{e}^{-\beta_{\mathrm{F}} x_1}$ and $X_{\mathrm{A}}(x_1) = C_{\mathrm{A},1}\,\mathrm{e}^{\beta_{\mathrm{A}} x_1} + C_{\mathrm{A},2}\,\mathrm{e}^{-\beta_{\mathrm{A}} x_1}$. By replacing these expressions in (2.48)-(2.51) and after some calculations, we obtain the following dispersion relation:

$$\beta_{\mathrm{F}}\left(\rho_{\mathrm{F}} + \frac{\sigma}{i\omega}\right)\cosh(a_{\mathrm{A}}\beta_{\mathrm{A}})\sinh(a_{\mathrm{F}}\beta_{\mathrm{F}}) + \beta_{\mathrm{A}}\rho_{\mathrm{F}}\sinh(a_{\mathrm{A}}\beta_{\mathrm{A}})\cosh(a_{\mathrm{F}}\beta_{\mathrm{F}}) = 0. \qquad (2.54)$$

For any pair of integers j and k, this equation together with (2.52) and (2.53) constitute a nonlinear system which has complex solutions $(\omega, \beta_{\mathrm{F}}) \in \mathbb{C}^2$ if we consider β_{A} as an expression that depends on ω and β_{F} via

$$\beta_A = \sqrt{\beta_{\mathrm{F}}^2 + \frac{i\omega}{c^2}\frac{\phi\gamma\sigma}{\rho} - \frac{\omega^2}{c^2}(1 - \phi\gamma)},$$

which is obtained from (2.52) and (2.53).

As we show below, for some of these solutions ω is a purely imaginary positive number. To see this, we plot in figures 2.3 and 2.4 the curves obtained from equations (2.52)-(2.54) for positive real values of β_{F} and $\lambda = -i\omega$ (i.e., purely imaginary positive values of $\omega = i\lambda$).

If we assume that $a_{\mathrm{F}} > a_{\mathrm{A}}$, it can be seen that the resulting curves intersect differently in case of $a_{\mathrm{A}} < \pi\frac{\rho_{\mathrm{F}} c}{\sigma}\sqrt{\frac{1}{3-\phi\gamma}}$ or $a_{\mathrm{A}} > \pi\frac{\rho_{\mathrm{F}} c}{\sigma}\sqrt{\frac{1}{3-\phi\gamma}}$. More precisely, the following alternative holds:

- If $a_{\mathrm{A}} < \pi\frac{\rho_{\mathrm{F}} c}{\sigma}\sqrt{\frac{1}{3-\phi\gamma}}$, then for any pair of integers $j, k = 0, 1, 2, \ldots$, there exists a solution $(\omega_{jk}, \beta_{\mathrm{F},jk})$ of (2.52)-(2.54), with $\omega_{jk} = i\lambda_{jk}$ satisfying

$$\frac{\sigma}{2\rho_{\mathrm{F}}} < \lambda_{jk} \le \max\left\{\frac{\sigma}{\rho_{\mathrm{F}}}, \frac{\sigma}{\rho_{\mathrm{F}}\phi\gamma}\right\} \text{ and } \lambda_{jk} \to \frac{\sigma}{2\rho_{\mathrm{F}}} \text{ as } \frac{j^2}{b^2} + \frac{k^2}{d^2} \to \infty.$$

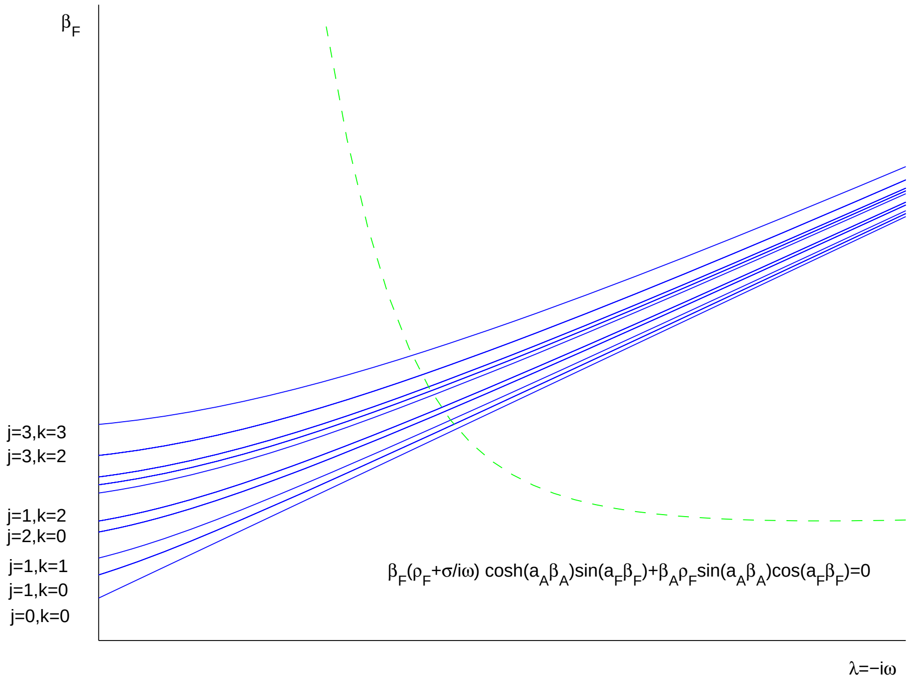

Figure 2.3: Curves (2.52) and (2.54) for real values of β_{F} and $\lambda = -i\omega$; case $a_{\mathrm{A}} < \pi \frac{\rho_{\mathrm{F}} c}{\sigma} \sqrt{\frac{1}{3-\phi\gamma}}$.

- If $a_{\mathrm{A}} > \pi \frac{\rho_{\mathrm{F}} c}{\sigma} \sqrt{\frac{1}{3-\phi\gamma}}$, then for any pair of integers $j, k = 0, 1, 2, \ldots$, there exists a solution $(\omega_{jk}, \beta_{\mathrm{F},jk})$ of (2.52)-(2.54), with $\omega_{jk} = i\lambda_{jk}$ satisfying

$$0 < \lambda_{jk} \leq \max \left\{ \frac{\sigma}{\rho_{\mathrm{F}}}, \frac{\sigma}{\rho_{\mathrm{F}} \phi\gamma} \right\} \text{ and } \lambda_{jk} \to \frac{\sigma}{2\rho_{\mathrm{F}}} \text{ as } \frac{j^2}{b^2} + \frac{k^2}{d^2} \to \infty.$$

Each of these solutions $(\omega_{jk}, \beta_{\mathrm{F},jk})$ yields an eigenmode of (2.40)-(2.45) with

$$\begin{aligned}
p_{\mathrm{F},jk}(x_1, x_2, x_3) &= \cos\frac{j\pi x_2}{a} \cos\frac{k\pi x_3}{d} \left(C_{\mathrm{F},1}\, \mathrm{e}^{\beta_{\mathrm{F},jk} x_1} + C_{\mathrm{F},2}\, \mathrm{e}^{-\beta_{\mathrm{F},jk} x_1} \right), \qquad -a_{\mathrm{F}} < x_1 < 0, \\
p_{\mathrm{A},jk}(x_1, x_2, x_3) &= \cos\frac{j\pi x_2}{a} \cos\frac{k\pi x_3}{d} \left(C_{\mathrm{A},1}\, \mathrm{e}^{\beta_{\mathrm{A},jk} x_1} + C_{\mathrm{A},2}\, \mathrm{e}^{-\beta_{\mathrm{A},jk} x_1} \right), \qquad 0 < x_1 < a_{\mathrm{A}},
\end{aligned}$$

where

$$\beta_{\mathrm{A},jk} = \sqrt{\beta_{\mathrm{F},jk}^2 - \frac{\lambda_{jk}}{c^2} \frac{\phi\gamma\sigma}{\rho} + \frac{\lambda_{jk}^2}{c^2}(\phi\gamma - 1)}.$$

For real porous-fluid configuration, the thickness of porous layer typically satisfies $a_{\mathrm{A}} < \pi \frac{\rho_{\mathrm{F}} c}{\sigma} \sqrt{\frac{1}{3-\phi\gamma}}$ and, in this case, the overdamped eigenvalues are always between $\frac{\sigma}{2\rho_{\mathrm{F}}}$ and $\frac{\sigma}{\rho_{\mathrm{F}}}$.

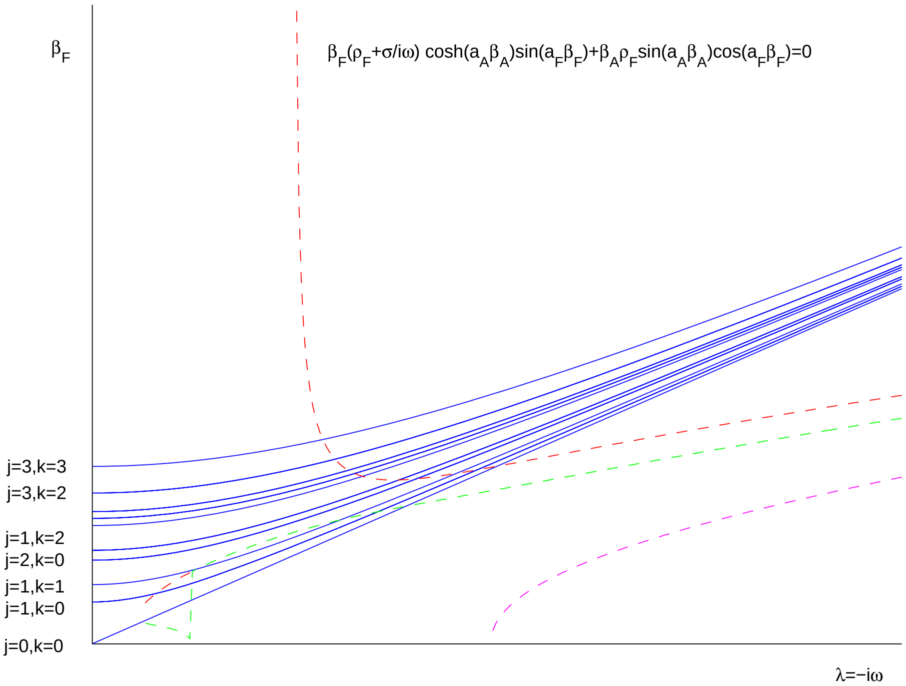

Figure 2.4: Curves (2.52) and (2.54) for real values of β_{F} and $\lambda = -i\omega$; case $a_{\mathrm{A}} > \pi \frac{\rho_{\mathrm{F}} c}{\sigma} \sqrt{\frac{1}{3-\phi\gamma}}$.

2.4 Statement of the weak formulation

For the sake of simplicity, we restrict our attention to the case where the porous medium is isotropic, i.e., $\boldsymbol{\mu}(\omega) = \mu(\omega)\boldsymbol{I}$. Let us define the set $\mathbf{V}$ of kinematically admissible virtual displacements,

$$\mathbf{V} = \{(\boldsymbol{v}_{\mathrm{F}}, \boldsymbol{v}_{\mathrm{A}}) \in \mathbf{H} : \boldsymbol{v}_{\mathrm{F}} \cdot \boldsymbol{n} = \boldsymbol{v}_{\mathrm{A}} \cdot \boldsymbol{n} \text{ on } \Gamma_{\mathrm{I}}\},$$

where

$$\begin{aligned}\mathbf{H} = \{(\boldsymbol{v}_{\mathrm{F}}, \boldsymbol{v}_{\mathrm{A}}) \in \mathbf{H}(\mathrm{div}, \Omega_{\mathrm{F}}) \times \mathbf{H}(\mathrm{div}, \Omega_{\mathrm{A}}) \ : \ & \boldsymbol{v}_{\mathrm{F}} \cdot \boldsymbol{\nu} = 0 \text{ on } \Gamma \cap \partial\Omega_{\mathrm{F}}, \\ & \boldsymbol{v}_{\mathrm{A}} \cdot \boldsymbol{\nu} = 0 \text{ on } \Gamma \cap \partial\Omega_{\mathrm{A}}\},\end{aligned}$$

and

$$\mathrm{H}(\mathrm{div}, \Omega) = \left\{ \mathbf{v} \in (\mathrm{L}^2(\Omega))^3 : \ \mathrm{div}\, \mathbf{v} \in \mathrm{L}^2(\Omega) \right\},$$

where $\mathrm{L}^2(\Omega)$ denotes the space of square integrable functions. To get a weak formulation of the eigenvalue problem (2.32)-(2.39), equation (2.32) is multiplied by the conjugate of a virtual fluid displacement $\bar{\boldsymbol{v}}_{\mathrm{F}}$ satisfying the Dirichlet condition (2.38) and then integrated in Ω_{F}. By using a Green's formula and equation (2.34), we obtain

$$\int_{\Omega_{\mathrm{F}}} \rho_{\mathrm{F}} c^2 \,\mathrm{div}\, \boldsymbol{u}_{\mathrm{F}} \ \mathrm{div}\, \bar{\boldsymbol{v}}_{\mathrm{F}} - \int_{\Gamma_{\mathrm{I}}} p_{\mathrm{F}} \bar{\boldsymbol{v}}_{\mathrm{F}} \cdot \boldsymbol{n} = \omega^2 \int_{\Omega_{\mathrm{F}}} \rho_{\mathrm{F}} \boldsymbol{u}_{\mathrm{F}} \cdot \bar{\boldsymbol{v}}_{\mathrm{F}}.$$

In an analogous way, equations (2.33), (2.35) and (2.39) yield

$$\int_{\Omega_\mathrm{A}} \mu(\omega)\,\mathrm{div}\,\boldsymbol{u}_\mathrm{A}\ \ \mathrm{div}\,\bar{\boldsymbol{v}}_\mathrm{A} + \int_{\Gamma_\mathrm{I}} p_\mathrm{A}\bar{\boldsymbol{v}}_\mathrm{A}\cdot\boldsymbol{n} = \omega^2 \int_{\Omega_\mathrm{A}} \rho(\omega)\boldsymbol{u}_\mathrm{A}\cdot\bar{\boldsymbol{v}}_\mathrm{A}.$$

Now, by adding both equations and using the kinetic constraint (2.37), we can write the following pure displacement eigenvalue problem:

Find a complex angular frequency ω *and a pair of displacements* $(\boldsymbol{u}_\mathrm{F},\boldsymbol{u}_\mathrm{A})\in\mathbf{V}$, *with* $\boldsymbol{u}_\mathrm{F}$ *and* $\boldsymbol{u}_\mathrm{A}$ *not both identically zero, satisfying*

$$\int_{\Omega_\mathrm{F}} \rho_\mathrm{F} c^2\,\mathrm{div}\,\boldsymbol{u}_\mathrm{F}\ \ \mathrm{div}\,\bar{\boldsymbol{v}}_\mathrm{F} + \int_{\Omega_\mathrm{A}} \mu(\omega)\,\mathrm{div}\,\boldsymbol{u}_\mathrm{A}\,\mathrm{div}\,\bar{\boldsymbol{v}}_\mathrm{A} = \omega^2\left(\int_{\Omega_\mathrm{F}} \rho_\mathrm{F}\boldsymbol{u}_\mathrm{F}\cdot\bar{\boldsymbol{v}}_\mathrm{F} + \int_{\Omega_\mathrm{A}} \rho(\omega)\boldsymbol{u}_\mathrm{A}\cdot\bar{\boldsymbol{v}}_\mathrm{A}\right), \tag{2.55}$$

for all $(\boldsymbol{v}_\mathrm{F},\boldsymbol{v}_\mathrm{A})\in\mathbf{V}$.

As it is typical in displacement formulations (see [26]), $\omega = 0$ is an eigenfrequency of this problem in both the Darcy's like model and the Allard-Champoux model, with an infinite-dimensional eigenspace given by

$$\mathbf{Z} = \left\{(\boldsymbol{u}_\mathrm{F},\boldsymbol{u}_\mathrm{A})\in\mathbf{V}\ :\ \mathrm{div}\,\boldsymbol{u}_\mathrm{F} = 0 \text{ in } \Omega_\mathrm{F},\ \mathrm{div}\,\boldsymbol{u}_\mathrm{A} = 0 \text{ in } \Omega_\mathrm{A}\right\}.$$

This eigenspace consists of pure rotational fluid motions inducing neither variations of pressure in the fluid nor in the porous medium. They are mathematical solutions of the eigenvalue problem with no physical entity because they do not correspond to vibration modes of the coupled system. They arise because no irrotational constraint is imposed to the fluid and porous displacements (see [26]).

2.5 Finite element discretization

Fluid and porous displacements belong to the same class of functional spaces, $\mathbf{H}(\mathrm{div},\Omega_\mathrm{F})$ and $\mathbf{H}(\mathrm{div},\Omega_\mathrm{A})$, respectively; hence the same type of finite elements should be used for each of them to discretize the variational problem (2.55).

Let $\mathcal{T}_h$ be a regular tetrahedral partition of $\Omega_\mathrm{F}\cup\Omega_\mathrm{A}$ such that every tetrahedra is completely contained either in Ω_F or in Ω_A. We also assume that the faces of tetrahedra lying on $\Gamma_\mathrm{D}\cup\Gamma_\mathrm{E}$ are completely contained either in Γ_D or in Γ_E.

To approximate the fluid and porous displacements, the lowest order Raviart-Thomas elements (see [96]) are used to avoid spurious modes typical of displacement formulations (see [74]). They consist of vector valued functions which, when restricted to each tetrahedron, are incomplete linear polynomials of the form

$$\boldsymbol{u}^h(x_1,x_2,x_3) = (a+dx_1, b+dx_2, c+dx_3), \qquad a,b,c,d\in\mathbb{C}.$$

These vector fields have constant normal components on each of the four faces of a tetrahedron (Figure 2.5) which define a unique polynomial function of this type. Moreover, the global discrete displacement field $\boldsymbol{u}^h$ is allowed to have discontinuous tangential components on the faces of the tetrahedra of the partition $\mathcal{T}_h$. Instead, its constant normal components must be continuous through these faces (these constant values being the degrees of freedom defining $\boldsymbol{u}^h$). Because of this, $\operatorname{div}\boldsymbol{u}^h$ is globally well defined in the domain, $\Omega_{\mathrm{F}} \cup \Omega_{\mathrm{A}}$.

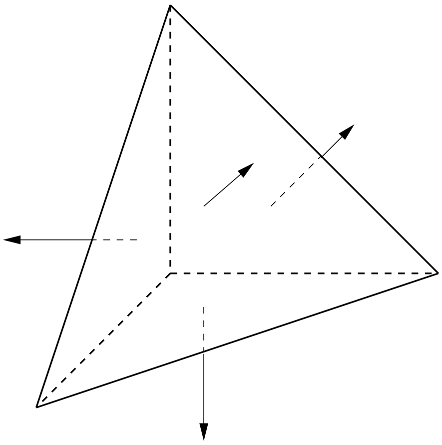

Figure 2.5: Raviart-Thomas finite element.

Then, for fluid displacements we use the Raviart-Thomas space (see [96])

$$\mathbf{R}_h(\Omega_{\mathrm{F}}) := \{\boldsymbol{u} \in \mathrm{H}(\operatorname{div}, \Omega_{\mathrm{F}}) \ : \ \boldsymbol{u}|_T \in \mathcal{R}_0(T),\ \forall T \in \mathcal{T}_h,\ T \subset \Omega_{\mathrm{F}}\},$$

and an analogous space for porous medium displacements:

$$\mathbf{R}_h(\Omega_{\mathrm{A}}) := \{\boldsymbol{u} \in \mathrm{H}(\operatorname{div}, \Omega_{\mathrm{A}}) \ : \ \boldsymbol{u}|_T \in \mathcal{R}_0(T),\ \forall T \in \mathcal{T}_h,\ T \subset \Omega_{\mathrm{A}}\},$$

where

$$\mathcal{R}_0(T) := \left\{\boldsymbol{u} \in \mathcal{P}_1(T)^3 : \boldsymbol{u}(x_1, x_2, x_3) = (a + dx_1, b + dx_2, c + dx_3),\ a, b, c, d \in \mathbb{C}\right\}.$$

Then, the discrete analogue of $\mathbf{V}$ is

$$\begin{aligned}\mathbf{V}_h := \{(\boldsymbol{u}_{\mathrm{F}}, \boldsymbol{u}_{\mathrm{A}}) \in \mathbf{R}_h(\Omega_{\mathrm{F}}) \times \mathbf{R}_h(\Omega_{\mathrm{A}}) \ : \ \boldsymbol{u}_{\mathrm{F}} \cdot \boldsymbol{n} = \boldsymbol{u}_{\mathrm{A}} \cdot \boldsymbol{n} \ \text{ for each} \\ \text{face on } \Gamma_{\mathrm{I}},\ \boldsymbol{u}_{\mathrm{F}} \cdot \boldsymbol{\nu} = 0 \text{ on } \Gamma \cap \partial\Omega_{\mathrm{F}},\ \boldsymbol{u}_{\mathrm{A}} \cdot \boldsymbol{\nu} = 0 \text{ on } \Gamma \cap \partial\Omega_{\mathrm{A}}\}.\end{aligned}$$

With this finite element space we define an approximate problem to (2.55):

Find a complex number ω_h *and a pair of displacements* $(\boldsymbol{u}_{\mathrm{F}}^h, \boldsymbol{u}_{\mathrm{A}}^h) \in \mathbf{V}_h$ *not both identically zero, such that*

$$\begin{aligned}\int_{\Omega_{\mathrm{F}}} \rho_{\mathrm{F}} c^2 \operatorname{div}\boldsymbol{u}_{\mathrm{F}}^h \ \operatorname{div}\bar{\boldsymbol{v}}_{\mathrm{F}}^h + \int_{\Omega_{\mathrm{A}}} \mu(\omega_h) \operatorname{div}\boldsymbol{u}_{\mathrm{A}}^h \ \operatorname{div}\bar{\boldsymbol{v}}_{A}^h = \\ \omega_h^2 \left(\int_{\Omega_{\mathrm{F}}} \rho_{\mathrm{F}} \boldsymbol{u}_{\mathrm{F}}^h \cdot \bar{\boldsymbol{v}}_{\mathrm{F}}^h + \int_{\Omega_{\mathrm{A}}} \rho(\omega_h) \boldsymbol{u}_{\mathrm{A}}^h \cdot \bar{\boldsymbol{v}}_{\mathrm{A}}^h\right),\end{aligned} \quad (2.56)$$

for all $(\boldsymbol{v}_{\mathrm{F}}^h, \boldsymbol{v}_{\mathrm{A}}^h) \in \mathbf{V}_h$.

2.6 Matrix description

In the previous section, a discrete formulation of our eigenvalue problem has been stated. Now a matrix description is given and it is shown that it is a well posed symmetric nonlinear generalized eigenvalue problem involving sparse matrices.

Let u_{F}^h and v_{F}^h denote the column vectors of components of $\boldsymbol{u}_{\mathrm{F}}^h$ and $\boldsymbol{v}_{\mathrm{F}}^h$, respectively, in the standard finite element basis associated with $\mathbf{R}_h(\Omega_{\mathrm{F}})$. Similarly, let u_{A}^h and v_{A}^h denote the column vectors of components of $\boldsymbol{u}_{\mathrm{A}}^h$ and $\boldsymbol{v}_{\mathrm{A}}^h$, respectively, in the standard finite element basis associated with $\mathbf{R}_h(\Omega_{\mathrm{A}})$. Then the problem (2.56) can be written in matrix form as

$$\begin{pmatrix} R_{\mathrm{F}} & 0 \\ 0 & R_{\mathrm{A}}(\omega_h) \end{pmatrix} \begin{pmatrix} u_{\mathrm{F}}^h \\ u_{\mathrm{A}}^h \end{pmatrix} = \omega_h^2 \begin{pmatrix} M_{\mathrm{F}} & 0 \\ 0 & M_{\mathrm{A}}(\omega_h) \end{pmatrix} \begin{pmatrix} u_{\mathrm{F}}^h \\ u_{\mathrm{A}}^h \end{pmatrix}, \tag{2.57}$$

where

$$\begin{aligned} {v_{\mathrm{F}}^h}^* R_{\mathrm{F}} u_{\mathrm{F}}^h &= \int_{\Omega_{\mathrm{F}}} \rho_{\mathrm{F}} c^2 \operatorname{div} \boldsymbol{u}_{\mathrm{F}}^h \ \operatorname{div} \bar{\boldsymbol{v}}_{\mathrm{F}}^h, \\ {v_{\mathrm{A}}^h}^* R_{\mathrm{A}}(\omega_h) u_{\mathrm{A}}^h &= \int_{\Omega_{\mathrm{A}}} \mu(\omega_h) \operatorname{div} \boldsymbol{u}_{\mathrm{A}}^h \ \operatorname{div} \bar{\boldsymbol{v}}_{A}^h, \\ {v_{\mathrm{F}}^h}^* M_{\mathrm{F}} u_{\mathrm{F}}^h &= \int_{\Omega_{\mathrm{F}}} \rho_{\mathrm{F}} \boldsymbol{u}_{\mathrm{F}}^h \cdot \bar{\boldsymbol{v}}_{\mathrm{F}}^h, \\ {v_{\mathrm{A}}^h}^* M_{\mathrm{A}}(\omega_h) u_{\mathrm{A}}^h &= \int_{\Omega_{\mathrm{A}}} \rho(\omega_h) \boldsymbol{u}_{\mathrm{A}}^h \cdot \bar{\boldsymbol{v}}_{\mathrm{A}}^h. \end{aligned}$$

R_{F} and M_{F} are the standard stiffness and mass matrices of the fluid, respectively, while $R_{\mathrm{A}}(\omega_h)$ and $M_{\mathrm{A}}(\omega_h)$ are the corresponding ones for the porous medium. Notice that every matrix is highly sparse because only a maximum of seven entries per row can be different from zero (this corresponds to the number of faces of two adjacent tetrahedra).

Matrices R_{F} and $R_{\mathrm{A}}(\omega_h)$ in the eigenvalue problem (2.57) are singular; however, by performing a translation in the eigenvalues, it can be written in an equivalent more convenient way:

$$\begin{pmatrix} R_{\mathrm{F}} + M_{\mathrm{F}} & 0 \\ 0 & R_{\mathrm{A}}(\omega_h) + M_{\mathrm{A}}(\omega_h) \end{pmatrix} \begin{pmatrix} u_{\mathrm{F}}^h \\ u_{\mathrm{A}}^h \end{pmatrix} = (\omega_h^2 + 1) \begin{pmatrix} M_{\mathrm{F}} & 0 \\ 0 & M_{\mathrm{A}}(\omega_h) \end{pmatrix} \begin{pmatrix} u_{\mathrm{F}}^h \\ u_{\mathrm{A}}^h \end{pmatrix}.$$

Now, matrix $R_{\mathrm{F}} + M_{\mathrm{F}}$ is clearly positive definite, hence non-singular and symmetric. However, the matrix $R_{\mathrm{A}}(\omega_h) + M_{\mathrm{A}}(\omega_h)$ is singular if there exists ω_h such that $\rho(\omega_h)$ is null. When we use the Darcy's like model, the dynamic density is null only if $\omega_h = i\frac{\sigma}{\rho_{\mathrm{F}}}$ (which is an eigenvalue associated to null divergence displacements in the porous medium) while the bulk modulus is positive. In the case of Allard-Champoux model, there exists a frequency ω_h such that $\mu(\omega_h)$ is null but this is not true for $\rho(\omega_h)$.

Thus, except for this special case, the matrix on the left hand side is non-singular and, consequently, it can be used to build a well posed generalized eigenvalue problem to help us to solve the non-linear eigenvalue problem (2.57). With this aim, we can define a function

$S : \mathbb{C} \to \mathbb{C}$ such that $S(\omega_h) = \lambda_h$, where λ_h is the least modulus eigenvalue of the following problem,

$$\begin{pmatrix} R_{\mathrm{F}} + M_{\mathrm{F}} & 0 \\ 0 & R_{\mathrm{A}}(\omega_h) + M_{\mathrm{A}}(\omega_h) \end{pmatrix} \begin{pmatrix} u_{\mathrm{F}}^h \\ u_{\mathrm{A}}^h \end{pmatrix} = \lambda_h \begin{pmatrix} M_{\mathrm{F}} & 0 \\ 0 & M_{\mathrm{A}}(\omega_h) \end{pmatrix} \begin{pmatrix} u_{\mathrm{F}}^h \\ u_{\mathrm{A}}^h \end{pmatrix}.$$

The function S is well defined because the generalized eigenvalue problem is well posed. Furthermore, both matrices of this problem are symmetric and highly sparse and, hence, convenient for computational purposes. Finally, calculation of the eigenvalues of the problem (2.57) is equivalent to find the roots ω_h of the nonlinear equation,

$$S(\omega_h) - (\omega_h^2 + 1) = 0.$$

A similar problem arising from finite element analysis of dissipative acoustic models can be found in [36].

2.7 Numerical results

In this section we present some numerical results obtained with a computer code implementing the numerical method given in this chapter. This code allows us to compute the response diagram of enclosures as those in Figures 2.1 and 2.2, consisting of several layers of fluids and porous media, and also to solve the nonlinear eigenvalue problem (2.55) by means of a secant method combined with an inverse power method. This type of method has been already used in other works devoted to solve nonlinear eigenvalues problems (see [36]).

In order to validate our method, we have considered the following data: fluid is air with density $\rho_{\mathrm{F}} = 1.225$ kg/m^3, $c = 343$ m/s whereas properties of the porous material are summarized in $\sigma = 10^4$ kg/(m^{3}s), $\phi = 0.71$, $\gamma = 1.4$, $N_{pr} = 0.702$ and $P_0 = 101320$ Pa. Concerning dimensions of enclosures shown in Figures 2.1 and 2.2, they are as follows: length and width are 4 m whereas height is 2 m for the first layer of free fluid, 0.05 m for the second layer of porous material and 0.1 m for the third layer of free fluid in the case of the enclosure in Figure 2.1.

These two enclosures have been decomposed in tetrahedra (see Figure 2.6). Depending on which one is considered and on the degree of mesh refinement (parameter n refers to the number of divisions introduced for each layer of the enclosure in Figure 2.6), the meshes are denoted as it is shown in Table 2.1.

Firstly we consider the enclosure in Figure 2.2. In Table 2.2 we show the first complex eigenfrequencies (in Hz) for three different meshes: mesh 2, mesh 3 and mesh 4. One can see that they have a small imaginary part and a real part "close" to the response peaks. We also include the extrapolated complex eigenfrequencies computed by the least square method, and the exact ones corresponding to both Darcy's like model and Allard-Champoux model, obtained by solving their respective nonlinear system of equations, for any pair of integers

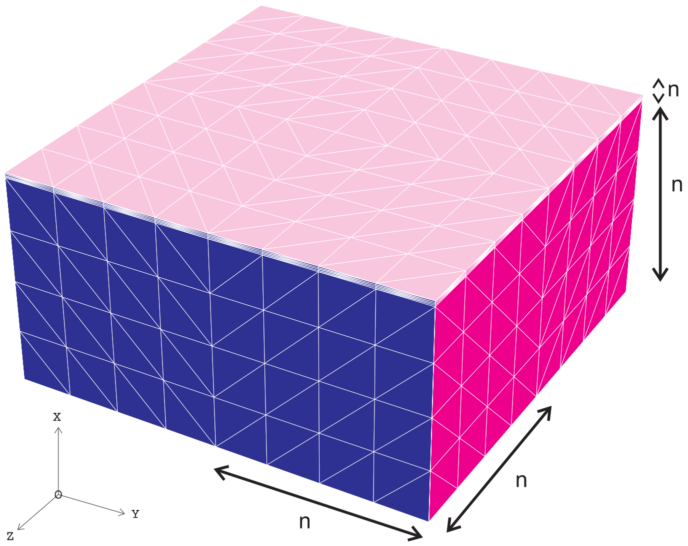

Figure 2.6: Mesh 2 corresponding to the enclosure shown in Figure 2.2

	Mesh 0	Mesh 1	Mesh 2	Mesh 3	Mesh 4
Sample	Figure 2.1	Figure 2.1	Figure 2.2	Figure 2.2	Figure 2.2
n	2	4	6	8	10
d.o.f	1072	8128	21600	50688	98400

Table 2.1: Name and degrees of freedom for the different meshes.

j and k, namely,

$$\begin{aligned}\beta_{\mathrm{F}}^2+\frac{\omega^2}{c^2} &= \frac{\pi^2}{b^2}j^2+\frac{\pi^2}{d^2}k^2,\\ \beta_{\mathrm{A}}^2+\frac{\omega^2\rho(\omega)}{K(\omega)} &= \frac{\pi^2}{b^2}j^2+\frac{\pi^2}{d^2}k^2,\\ \beta_{\mathrm{F}}\rho(\omega)\cosh(a_{\mathrm{A}}\beta_{\mathrm{A}})\sinh(a_{\mathrm{F}}\beta_{\mathrm{F}}) &= -\beta_{\mathrm{A}}\rho_{\mathrm{F}}\sinh(a_{\mathrm{A}}\beta_{\mathrm{A}})\cosh(a_{\mathrm{F}}\beta_{\mathrm{F}}).\end{aligned}$$

An excellent agreement can be observed between exact and computed values, even for the coarser mesh. This shows the effectiveness of the method. From this Table we have calculated the order of convergence of the method and found that it is approximately $O(h^2)$, h being a parameter associated with the mesh size, which is optimal for the lowest order Raviart-Thomas finite elements we have used.

On the other hand, according to the analysis in Section 2.3, there exist overdamped modes. In spite of the fact that these overdamped modes are not the magnitudes of interest, from the numerical point of view it is important to know if they are well approximated by the finite element method. Otherwise they could be a source of spectral pollution. Table 2.3 includes the computed and exact purely imaginary eigenfrequencies of higher modulus for the same three meshes described above.

Mode	Mesh 2	Mesh 3	Mesh 4	Extrapolated	Exact
ω^F_{100}	265.791+0.382 i	265.891+0.287 i	265.961+0.242 i	266.708+0.162 i	266.026+0.164 i
ω^F_{110}	375.722+0.786 i	375.894+0.593 i	375.977+0.502 i	376.144+0.338 i	376.132+0.342 i
ω^F_{001}	523.913+1.943 i	524.685+1.284 i	525.038+0.965 i	525.644+0.332 i	525.656+0.389 i
ω^F_{200}	531.251+1.704 i	531.418+1.284 i	531.506+1.087 i	531.733+0.772 i	531.680+0.737 i
ω^F_{020}	528.894+1.684 i	530.052+1.273 i	530.622+1.081 i	531.807+0.730 i	531.680+0.737 i

Table 2.2: Rigid porous medium and air. Darcy's like model.

Mode	Mesh 2	Mesh 3	Mesh 4	Extrapolated	Exact
ω^F_{00}	8163.265 i	8163.265 i	8163.265 i	8163.265 i	8163.265 i
ω^F_{10}	8156.630 i	8157.003 i	8157.277 i	8163.163 i	8158.435 i
ω^F_{11}	8149.990 i	8150.735 i	8151.285 i	8163.382 i	8153.605 i

Table 2.3: Rigid porous medium and air. Darcy's like model. Overdamped modes.

When the Allard-Champoux model is used we obtain similar results to those previously obtained for the Darcy's like model. They are shown in Tables 2.4 and 2.5.

Mode	Mesh 2	Mesh 3	Mesh 4	Extrapolated	Exact
ω^F_{100}	264.498+0.768 i	264.545+0.582 i	264.570+0.495 i	264.641+0.336 i	264.622+0.340 i
ω^F_{110}	373.830+1.586 i	373.915+1.212 i	373.968+1.033 i	374.195+0.692 i	374.082+0.712 i
ω^F_{001}	519.622+4.457 i	519.968+3.274 i	520.166+2.687 i	520.829+1.440 i	520.584+1.606 i
ω^F_{200}	528.662+3.436 i	528.559+2.652 i	528.550+2.266 i	528.535+1.461 i	528.598+1.561 i
ω^F_{020}	526.277+3.395 i	527.194+2.630 i	527.670+2.254 i	528.816+1.475 i	528.598+1.561 i

Table 2.4: Rigid porous medium and air. Allard-Champoux model.

Nevertheless, when calculating overdamped modes with the Allard-Champoux model some difficulties appear due to the highly oscillating eigenfunction associated with it. This means that a very refined mesh must be used in order to get a suitable approximation. In fact, only with mesh 4 a good accuracy has been achieved. Figure 2.7 shows the oscillation in the eigenvector in a plane near the interface between the fluid and the porous material.

Finally, we consider the enclosure shown in Figure 2.1. The response curves are drawn in Figure 2.8 when the model is solved with mesh 0 and mesh 1. In these curves $\log_{10}||p||_{\mathrm{L}^2}$ is plotted for frequencies ranging from 50 to 1000 Hz.

Several response peaks can be observed in these curves depending on the refinement of the mesh. We notice that the finer the mesh, the smaller the number of peaks in the response diagram. Moreover, Table 2.6 shows the computed (complex) resonance frequencies for the damped coupled system shown in Figure 2.1 and the (real) eigenfrequencies of a similar undamped enclosure where the porous material has been replaced with air. As one can see, all are quite similar.

Mode	Mesh 2	Mesh 3	Mesh 4	Exact
ω^F_{100}	4983.698 i	4439.175 i	4439.603 i	4438.380 i
ω^F_{110}	4979.907 i		4436.174 i	4436.828 i
ω^F_{001}	4976.004 i	4435.718 i	4435.633 i	4435.279 i

Table 2.5: Rigid porous medium and air. Allard - Champoux model. Overdamped modes.

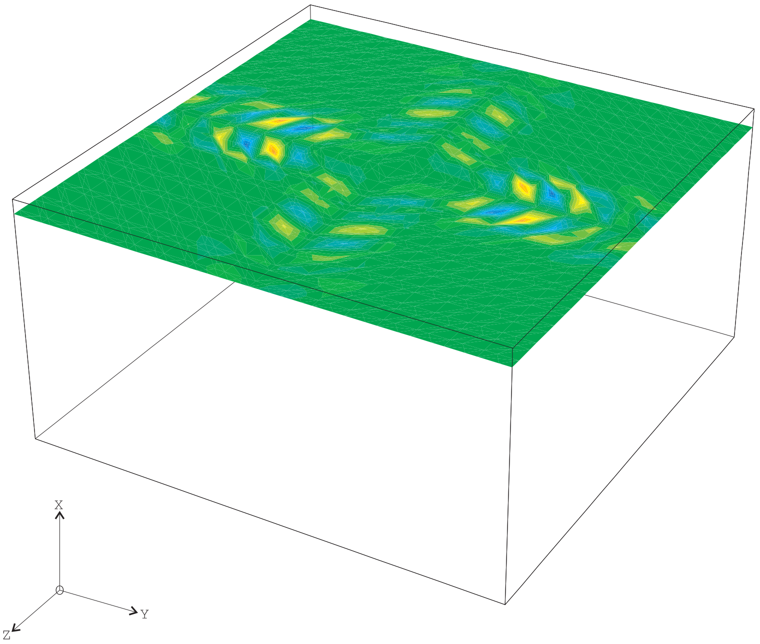

Figure 2.7: Eigenvector for an overdamped mode with Allard-Champoux model

2.8 Conclusions

In this chapter a three-dimensional finite element method has been implemented to solve the system of equations modelling the macroscopic behavior of a porous material with rigid solid frame. It allows us to compute both the response to a harmonic excitation and the free vibrations of a three-dimensional multilayer system consisting of different layers composed of free fluids and rigid porous media. The finite element used is the lowest order face element introduced by Raviart and Thomas, with the advantage of eliminating the spurious modes.

For rigid porous media we have considered two models: a Darcy's like model and the Allard-Champoux model. These two models are equivalent when frequency is much lower than flow resistivity.

When solving the problem of free vibrations, the computer program predicts very well the exact complex eigenfrequencies for the Darcy's like model in the case of a test example. This is true even for the overdamped modes. On the other hand, when using the Allard-Champoux model, the eigenfrequencies with non-null real part are well approximated whereas calculation of overdamped modes is much more complicated due to the highly os-

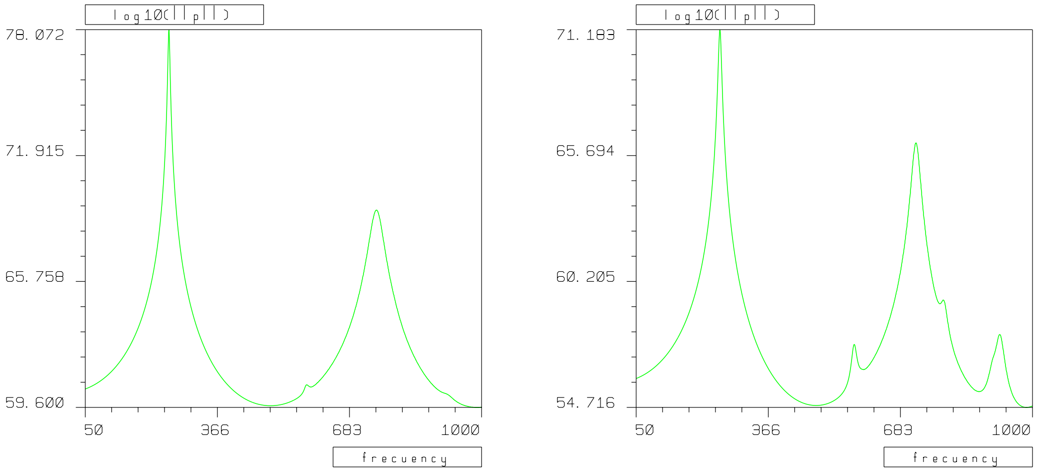

Figure 2.8: Response curve with Mesh 0 (left) and Mesh 1 (right)

Undamped peaks	Complex eigenfrequencies	Damped peaks Mesh 0	Damped peaks Mesh 1
269.392	266.189+1.495 i	250.5	250.5
588.840	594.737+8.535 i	572.5	581.0
751.297	751.811+1.506 i	720.5	748.0
808.175	797.242+1.750 i	785.5	-
924.519	936.395+5.309 i	921.0	-

Table 2.6: Resonance vibration frequencies and complex eigenfrequencies

cillating eigenfunction associated with them, as observed in Figure 2.7. This forces us to use very fine meshes.

Chapter 3

Finite element solution of new displacement/pressure poroelastic models in acoustics

Contents

3.1 Introduction

In this chapter, we consider the case of elastic frame porous material. The non-dissipative model that we shall take into account has already been presented in Section 1.3.3. The advantages exhibited by this model with respect to classical Biot's model (see Section 1.3.1) lies in that we know mathematical expressions allowing us to compute their coefficients.

We will focus our attention on the numerical computation of the frequency response of some acoustic problems which involve the non-dissipative open-pores model (see Eqs. (1.63)-(1.64)), which will be always stated in bounded domains. With this purpose we have implemented a finite element method based on different types of elements for each pressure and displacement fields in the acoustic source problems.

More precisely, to approximate fluid displacements, the lowest order Raviart-Thomas finite element (see [96] and [37]) is used in order to avoid spurious modes typical of displacement formulations when they are discretized by standard Lagrange finite elements (see [74]). To approximate displacements in the porous medium, we use the so called "MINI element" in order to achieve stability in the discrete problem (see [8]) and finally, the porous medium pressure is approximated using continuous piecewise linear finite elements.

Numerical experiments presented in this chapter concerns the solution of a source problem associated with an external harmonic excitation in some three-dimensional examples. Besides, the optimal order of convergence of the discrete problem is also showed for a problem where the exact solution is known.

The outline of the chapter is as follows. In Section 3.2 we recall several models of porous media associated with an elastic solid skeleton. In Section 3.3 we consider the model for open poroelastic materials introduced by Ferrín and Mikelić [62] coupled with the model for acoustic propagation in a fluid written in terms of displacements. Then both are specialized for harmonic waves in order to obtain the frequency response of the system. In Section 3.4 a weak formulation for this coupled model is presented. Numerical solution by finite element approximation is addressed in Section 3.5 and a matrix description of the discrete problem is given in Section 3.6. Section 3.7 is devoted to the computation of coefficients in the model by solving cell problems. Finally, in Section 3.8, some numerical results are shown both for academic tests and for enclosures containing a real life porous material and air.

3.2 Statement of the problem

We consider a coupled system consisting of an acoustic fluid (i.e. inviscid compressible barotropic) in contact with a poroelastic medium. Both are enclosed in a three-dimensional cavity with rigid walls except one on which a harmonic excitation is applied. Let Ω_{F} and Ω_{A} be the domains occupied by the fluid and the porous medium, respectively (see Figure 3.1). The boundary of $\overline{\Omega}_{\mathrm{F}} \cup \overline{\Omega}_{\mathrm{A}}$, denoted by Γ, is the union of two parts, Γ_{W} and Γ_{E}, where Γ_{W} denotes the rigid walls of the cavity. Let $\boldsymbol{\nu}$ be the outward unit normal vector to Γ.

The interface between the fluid and the porous medium is denoted by Γ_{I} and $\boldsymbol{n}$ is the unit normal vector to this interface pointing outwards Ω_{A}. Figure 3.1 includes a vertical cut of the domain for a better understanding of notations.

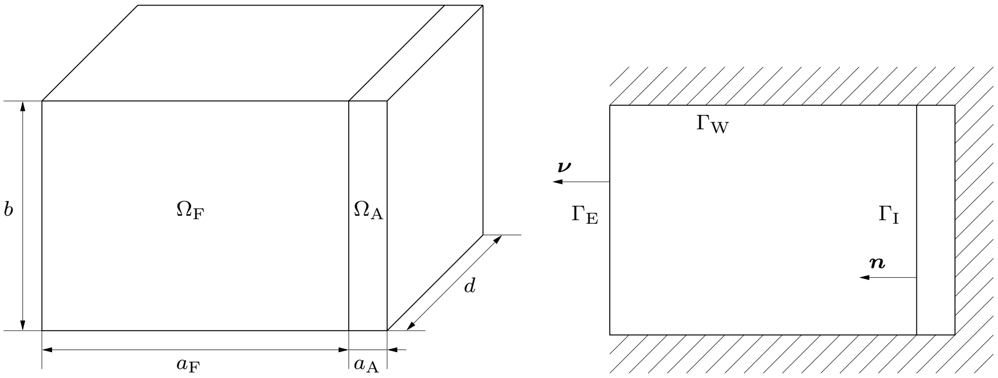

Figure 3.1: 3D domain and vertical cut.

In order to study the response of the fluid-porous coupled system subject to a harmonic excitation acting on Γ_{E}, we assume that the skeleton of the porous medium is elastic and consider the model for open pore non-dissipative poroelastic media given in Chapter 1.

First, we recall that, as we have considered in Chapter 2, the governing equations for free small amplitude motions of an acoustic fluid filling Ω_{F} are given, in terms of displacement and pressure fields, by

$$\rho_{\mathrm{F}}\frac{\partial^2\boldsymbol{U}_{\mathrm{F}}}{\partial t^2}+\mathbf{grad}\,P_{\mathrm{F}}=\mathbf{0} \qquad \text{in } \Omega_{\mathrm{F}}, \tag{3.1}$$

$$P_{\mathrm{F}}=-\rho_{\mathrm{F}}c^2\mathrm{div}\,\boldsymbol{U}_{\mathrm{F}} \qquad \text{in } \Omega_{\mathrm{F}}, \tag{3.2}$$

where P_{F} is pressure, $\boldsymbol{U}_{\mathrm{F}}$ is displacement field, ρ_{F} is density and c is acoustic speed.

Secondly, we denote by $\boldsymbol{U}_{\mathrm{A}}$ and P_{A} the macroscopic displacement and pressure fields in the porous medium. The governing equations of the small amplitud motion are given by (1.63)-(1.64), i.e.,

$$(\rho\boldsymbol{I}-\rho_{\mathrm{F}}\boldsymbol{A})\frac{\partial^2\boldsymbol{U}_{\mathrm{A}}}{\partial t^2}-\ \mathrm{div}\left(\mathsf{A}\left[\boldsymbol{E}(\boldsymbol{U}_{\mathrm{A}})\right]\right)-(\boldsymbol{A}+\boldsymbol{B}-\phi\boldsymbol{I})\,\mathbf{grad}\,P_{\mathrm{A}}=\mathbf{0} \qquad \text{in } \Omega_{\mathrm{A}}, \tag{3.3}$$

$$\hat{c}\frac{\partial^2 P_{\mathrm{A}}}{\partial t^2}+\frac{1}{\rho_{\mathrm{F}}}\mathrm{div}\left(\boldsymbol{A}\,\mathbf{grad}\,P_{\mathrm{A}}\right)=-\mathrm{div}\left((\boldsymbol{A}+\boldsymbol{B}-\phi\boldsymbol{I})\frac{\partial^2\boldsymbol{U}_{\mathrm{A}}}{\partial t^2}\right) \qquad \text{in } \Omega_{\mathrm{A}}, \tag{3.4}$$

where $\boldsymbol{E}(\boldsymbol{U})=\frac{1}{2}(\mathbf{grad}\,\boldsymbol{U}+(\mathbf{grad}\,\boldsymbol{U})^t)$ and coefficient $\hat{c}$, tensors $\boldsymbol{A},\boldsymbol{B}$, and linear operator A depend on the geometry of the cells composing the poroelastic material and also on physical properties of its solid and fluid parts. In fact, one can check that $\boldsymbol{B}$ is a symmetric linear operator and tensor A ($(\mathsf{A}[\boldsymbol{E}])_{kl}=A_{klij}E_{ij}$) satisfies $\mathsf{A}_{klij}=\mathsf{A}_{lkij}=\mathsf{A}_{lkji}$.

Since the fluid is supposed to be inviscid, only the normal component of displacements vanishes on Γ_{W}, namely,

$$\boldsymbol{U}_{\mathrm{F}}\cdot\boldsymbol{\nu}=0 \qquad \text{on } \Gamma_{\mathrm{W}}\cap\partial\Omega_{\mathrm{F}}, \tag{3.5}$$

whereas for boundary displacement of porous medium we suppose

$$\boldsymbol{U}_{\mathrm{A}} = \mathbf{0} \qquad \text{on } \Gamma_{\mathrm{W}} \cap \partial\Omega_{\mathrm{A}}. \tag{3.6}$$

Similarly, on interface Γ_{I} between fluid and porous medium we consider the usual interface conditions of continuity of forces and normal displacements, that is,

$$-P_{\mathrm{F}}\boldsymbol{n} = \mathsf{A}\left[\boldsymbol{E}(\boldsymbol{U}_{\mathrm{A}})\right]\boldsymbol{n} + P_{\mathrm{A}}\left(\boldsymbol{A}+\boldsymbol{B}-\phi\boldsymbol{I}\right)\boldsymbol{n} \qquad \text{on } \Gamma_{\mathrm{I}}, \tag{3.7}$$

$$\boldsymbol{U}_{\mathrm{F}}\cdot\boldsymbol{n} = \boldsymbol{U}_{\mathrm{A}}\cdot\boldsymbol{n} \qquad \text{on } \Gamma_{\mathrm{I}}. \tag{3.8}$$

If a normal displacement F is imposed on Γ_{E}, the above equations describing the motion of coupled system (3.1)-(3.8) must be completed with boundary condition

$$\boldsymbol{U}_{\mathrm{F}}\cdot\boldsymbol{\nu} = F \qquad \text{on } \Gamma_{\mathrm{E}}. \tag{3.9}$$

Finally, in order to close the model (see [11]), we are going to assume that

$$\boldsymbol{A}\,\mathbf{grad}\,p_{\mathrm{A}}\cdot\boldsymbol{\nu} = \mathbf{0} \qquad \text{on } \Gamma_{\mathrm{W}} \cap \partial\Omega_{\mathrm{A}}, \tag{3.10}$$

$$\boldsymbol{A}\,\mathbf{grad}\,p_{\mathrm{A}}\cdot\boldsymbol{n} = \mathbf{0} \qquad \text{on } \Gamma_{\mathrm{I}}. \tag{3.11}$$

We are interested in harmonic vibrations so let us suppose excitation F to be of the form, $F(x_1,x_2,x_3,t) = \mathrm{Re}\,(\mathrm{e}^{i\omega t}f(x_1,x_2,x_3))$. Then all fields are also harmonic:

$$\boldsymbol{U}_{\mathrm{F}}(x_1,x_2,x_3,t) = \mathrm{Re}\left(\mathrm{e}^{i\omega t}\boldsymbol{u}_{\mathrm{F}}(x_1,x_2,x_3)\right), \quad \boldsymbol{U}_{\mathrm{A}}(x_1,x_2,x_3,t) = \mathrm{Re}\left(\mathrm{e}^{i\omega t}\boldsymbol{u}_{\mathrm{A}}(x_1,x_2,x_3)\right),$$
$$P_{\mathrm{F}}(x_1,x_2,x_3,t) = \mathrm{Re}\left(\mathrm{e}^{i\omega t}p_{\mathrm{F}}(x_1,x_2,x_3)\right), \quad P_{\mathrm{A}}(x_1,x_2,x_3,t) = \mathrm{Re}\left(\mathrm{e}^{i\omega t}p_{\mathrm{A}}(x_1,x_2,x_3)\right).$$

By replacing these expressions in equations (3.1)-(3.11), we can define a harmonic source problem associated with the evolutionary source problem, namely,

$$\omega^2\rho_{\mathrm{F}}\boldsymbol{u}_F - \mathbf{grad}\,p_{\mathrm{F}} = \mathbf{0} \ \text{ in } \Omega_{\mathrm{F}}, \tag{3.12}$$

$$p_{\mathrm{F}} = -\rho_{\mathrm{F}}c^2\mathrm{div}\,\boldsymbol{u}_{\mathrm{F}} \ \text{ in } \Omega_{\mathrm{F}}, \tag{3.13}$$

$$\omega^2\left(\rho\boldsymbol{I}-\rho_{\mathrm{F}}\boldsymbol{A}\right)\boldsymbol{u}_{\mathrm{A}} + \mathrm{div}\left(\mathsf{A}[\boldsymbol{E}(\boldsymbol{u}_{\mathrm{A}})]\right) + \left(\boldsymbol{A}+\boldsymbol{B}-\phi\boldsymbol{I}\right)\mathbf{grad}\,p_{\mathrm{A}} = \mathbf{0} \ \text{ in } \Omega_{\mathrm{A}}, \tag{3.14}$$

$$-\omega^2\hat{c}p_{\mathrm{A}} + \frac{1}{\rho_{\mathrm{F}}}\,\mathrm{div}(\boldsymbol{A}\,\mathbf{grad}\,p_{\mathrm{A}}) = \omega^2\mathrm{div}\left(\left(\boldsymbol{A}+\boldsymbol{B}-\phi\boldsymbol{I}\right)\boldsymbol{u}_{\mathrm{A}}\right) \ \text{ in } \Omega_{\mathrm{A}}, \tag{3.15}$$

$$-p_{\mathrm{F}}\boldsymbol{n} = \mathsf{A}\left[\boldsymbol{E}(\boldsymbol{u}_{\mathrm{A}})\right]\boldsymbol{n} + p_{\mathrm{A}}\left(\boldsymbol{A}+\boldsymbol{B}-\phi\boldsymbol{I}\right)\boldsymbol{n} \ \text{ on } \Gamma_{\mathrm{I}}, \tag{3.16}$$

$$\boldsymbol{u}_{\mathrm{F}}\cdot\boldsymbol{n} = \boldsymbol{u}_{\mathrm{A}}\cdot\boldsymbol{n} \ \text{ on } \Gamma_{\mathrm{I}}, \tag{3.17}$$

$$\boldsymbol{u}_{\mathrm{F}}\cdot\boldsymbol{\nu} = 0 \ \text{ on } \Gamma_{\mathrm{W}} \cap \partial\Omega_{\mathrm{F}}, \tag{3.18}$$

$$\boldsymbol{u}_{\mathrm{A}} = \mathbf{0} \ \text{ on } \Gamma_{\mathrm{W}} \cap \partial\Omega_{\mathrm{A}}, \tag{3.19}$$

$$\boldsymbol{A}\,\mathbf{grad}\,p_{\mathrm{A}}\cdot\boldsymbol{\nu} = \mathbf{0} \ \text{ on } \Gamma_{\mathrm{W}} \cap \partial\Omega_{\mathrm{A}}, \tag{3.20}$$

$$\boldsymbol{A}\,\mathbf{grad}\,p_{\mathrm{A}}\cdot\boldsymbol{n} = \mathbf{0} \ \text{ on } \Gamma_{\mathrm{I}}, \tag{3.21}$$

$$\boldsymbol{u}_{\mathrm{F}}\cdot\boldsymbol{\nu} = f \ \text{ on } \Gamma_{\mathrm{E}}. \tag{3.22}$$

3.3 Weak formulation

In order to use finite element methods for numerical solution of (3.12)-(3.22), we write a weak formulation. For this purpose, we first introduce appropriate functional spaces. Let $\mathbf{V}$ be the Hilbert space

$$\mathbf{V} = \mathbf{H}(\mathrm{div}, \Omega_{\mathrm{F}}) \times \mathrm{L}^2(\Gamma_{\mathrm{I}}) \times \mathrm{H}^1(\Omega_{\mathrm{A}})^3 \times \mathrm{H}^1(\Omega_{\mathrm{A}})$$

and $\mathbf{V}_0$ its closed subspace

$$\mathbf{V}_0 = \{(\boldsymbol{v}_{\mathrm{F}}, q_{\mathrm{F}}, \boldsymbol{v}_{\mathrm{A}},\ q_{\mathrm{A}}) \in \mathbf{V}\ :\ \boldsymbol{v}_{\mathrm{F}} \cdot \boldsymbol{\nu} = 0 \text{ on } (\Gamma_{\mathrm{W}} \cup \Gamma_{\mathrm{E}}) \cap \partial\Omega_{\mathrm{F}},\ \boldsymbol{v}_{\mathrm{A}} = \mathbf{0} \text{ on } \Gamma_{\mathrm{W}} \cap \partial\Omega_{\mathrm{A}}\}\,.$$

Because of the choice of this functional framework and due to a trace Theorem for space $\mathbf{H}(\mathrm{div}, \Omega_{\mathrm{F}})$, we are led to assume that Dirichlet data function f belongs to functional space $\mathrm{H}_{00}^{-\frac{1}{2}}(\Gamma_{\mathrm{E}})$.

In order to get a weak formulation of source problem (3.12)-(3.22), we first multiply equation (3.12) by the complex conjugate of a virtual fluid displacement $\boldsymbol{v}_{\mathrm{F}} \in \mathbf{H}(\mathrm{div}, \Omega_{\mathrm{F}})$ satisfying Dirichlet condition (3.18), and then integrate in Ω_{F}. By using a Green's formula and equation (3.13) we obtain

$$-\omega^2 \int_{\Omega_{\mathrm{F}}} \rho_{\mathrm{F}} \boldsymbol{u}_{\mathrm{F}} \cdot \bar{\boldsymbol{v}}_{\mathrm{F}} + \int_{\Omega_{\mathrm{F}}} \rho_{\mathrm{F}} c^2 \mathrm{div} \boldsymbol{u}_{\mathrm{F}}\ \mathrm{div} \bar{\boldsymbol{v}}_{\mathrm{F}} - \int_{\Gamma_{\mathrm{I}}} p_{\mathrm{F}} \bar{\boldsymbol{v}}_{\mathrm{F}} \cdot \boldsymbol{n} = 0.$$

In an analogous way, equations (3.14) and (3.15), when multiplied by the complex conjugate of a virtual porous medium displacement $\bar{\boldsymbol{v}}_{\mathrm{A}}$ satisfying Dirichlet condition (3.19) and a virtual pressure $\bar{q}_{\mathrm{A}}$ and then integrated in Ω_{A} yield

$$\begin{aligned} -\omega^2 \int_{\Omega_{\mathrm{A}}} (\rho \boldsymbol{I} - \rho_{\mathrm{F}} \boldsymbol{A})\, \boldsymbol{u}_{\mathrm{A}} \cdot \bar{\boldsymbol{v}}_{\mathrm{A}} + \int_{\Omega_{\mathrm{A}}} \mathsf{A}[\boldsymbol{E}(\boldsymbol{u}_{\mathrm{A}})] : \boldsymbol{E}(\bar{\boldsymbol{v}}_{\mathrm{A}}) + & \\ \int_{\Omega_{\mathrm{A}}} \mathrm{div}\left((\boldsymbol{A} + \boldsymbol{B} - \phi \boldsymbol{I})^t \bar{\boldsymbol{v}}_{\mathrm{A}}\right) p_{\mathrm{A}} = \int_{\Gamma_{\mathrm{I}}} \mathsf{A}\,[\boldsymbol{E}(\boldsymbol{u}_{\mathrm{A}})]\, \boldsymbol{n} \cdot \bar{\boldsymbol{v}}_{\mathrm{A}} + & \\ \int_{\Gamma_{\mathrm{I}}} (\boldsymbol{A} + \boldsymbol{B} - \phi \boldsymbol{I})^t \bar{\boldsymbol{v}}_{\mathrm{A}} \cdot \boldsymbol{n} p_{\mathrm{A}}, & \end{aligned}$$

and

$$\begin{aligned} \int_{\Omega_{\mathrm{A}}} \hat{c} p_{\mathrm{A}} \bar{q}_{\mathrm{A}} + \int_{\Omega_{\mathrm{A}}} \frac{1}{\rho_{\mathrm{F}} \omega^2} \boldsymbol{A}\, \mathbf{grad}\, p_{\mathrm{A}} \cdot \mathbf{grad}\, \bar{q}_{\mathrm{A}} + \int_{\Omega_{\mathrm{A}}} \mathrm{div}\left((\boldsymbol{A} + \boldsymbol{B} - \phi \boldsymbol{I}) \boldsymbol{u}_{\mathrm{A}}\right) \bar{q}_{\mathrm{A}} = & \\ \int_{\Gamma_{\mathrm{I}}} \frac{1}{\rho_{\mathrm{F}} \omega^2} \bar{q}_{\mathrm{A}} \boldsymbol{A}\, \mathbf{grad}\, p_{\mathrm{A}} \cdot \boldsymbol{n} + \int_{\Gamma_{\mathrm{D}} \cap \partial\Omega_{\mathrm{A}}} \frac{1}{\rho_{\mathrm{F}} \omega^2} \bar{q}_{\mathrm{A}} \boldsymbol{A}\, \mathbf{grad}\, p_{\mathrm{A}} \cdot \boldsymbol{\nu}, & \end{aligned}$$

respectively.

Now, by adding the last three equations and using interface and boundary conditions (3.16), (3.20) and (3.21), we obtain

$$\begin{aligned}\int_{\Omega_{\mathrm{F}}} \rho_{\mathrm{F}} c^2 \operatorname{div} \boldsymbol{u}_{\mathrm{F}}\ \operatorname{div} \bar{\boldsymbol{v}}_{\mathrm{F}} - \omega^2 \int_{\Omega_{\mathrm{F}}} \rho_{\mathrm{F}} \boldsymbol{u}_{\mathrm{F}} \cdot \bar{\boldsymbol{v}}_{\mathrm{F}} - \omega^2 \int_{\Omega_{\mathrm{A}}} \left(\rho \boldsymbol{I} - \rho_{\mathrm{F}} \boldsymbol{A}\right) \boldsymbol{u}_{\mathrm{A}} \cdot \bar{\boldsymbol{v}}_{\mathrm{A}} + \\ \int_{\Omega_{\mathrm{A}}} \mathsf{A}[\boldsymbol{E}(\boldsymbol{u}_{\mathrm{A}})] : \boldsymbol{E}(\bar{\boldsymbol{v}}_{\mathrm{A}}) + \int_{\Omega_{\mathrm{A}}} \operatorname{div}\left((\boldsymbol{A} + \boldsymbol{B} - \phi \boldsymbol{I})^t \bar{\boldsymbol{v}}_{\mathrm{A}}\right) p_{\mathrm{A}} + \int_{\Omega_{\mathrm{A}}} \hat{c} p_{\mathrm{A}} \bar{q}_{\mathrm{A}} + \\ \int_{\Omega_{\mathrm{A}}} \frac{1}{\rho_{\mathrm{F}} \omega^2} \boldsymbol{A} \,\mathbf{grad}\, p_{\mathrm{A}} \cdot \mathbf{grad}\, \bar{q}_{\mathrm{A}} + \int_{\Omega_{\mathrm{A}}} \operatorname{div}\left((\boldsymbol{A} + \boldsymbol{B} - \phi \boldsymbol{I}) \boldsymbol{u}_{\mathrm{A}}\right) \bar{q}_{\mathrm{A}} = \\ \int_{\Gamma_{\mathrm{I}}} p_{\mathrm{F}} (\bar{\boldsymbol{v}}_{\mathrm{F}} \cdot \boldsymbol{n} - \bar{\boldsymbol{v}}_{\mathrm{A}} \cdot \boldsymbol{n}).\end{aligned}$$

Finally, kinematic constraint (3.17) is weakly imposed on the interface between the fluid and the porous medium by integrating this equation multiplied by any test function q_{F} defined on Γ_{I}:

$$\int_{\Gamma_{\mathrm{I}}} \bar{q}_{\mathrm{F}} (\boldsymbol{u}_{\mathrm{A}} \cdot \boldsymbol{n} - \boldsymbol{u}_{\mathrm{F}} \cdot \boldsymbol{n}) = 0.$$

All together allow us to write the following source problem:

For fixed angular frequency ω*, find* $(\boldsymbol{u}_{\mathrm{F}}, p_{\mathrm{F}}, \boldsymbol{u}_{\mathrm{A}}, p_{\mathrm{A}}) \in \mathbf{V}$ *satisfying (3.18), (3.19), (3.22) and furthermore,*

$$\begin{aligned}\int_{\Omega_{\mathrm{F}}} \rho_{\mathrm{F}} c^2 \operatorname{div} \boldsymbol{u}_{\mathrm{F}}\ \operatorname{div} \bar{\boldsymbol{v}}_{\mathrm{F}} - \omega^2 \int_{\Omega_{\mathrm{F}}} \rho_{\mathrm{F}} \boldsymbol{u}_{\mathrm{F}} \cdot \bar{\boldsymbol{v}}_{\mathrm{F}} - \omega^2 \int_{\Omega_{\mathrm{A}}} \left(\rho \boldsymbol{I} - \rho_{\mathrm{F}} \boldsymbol{A}\right) \boldsymbol{u}_{\mathrm{A}} \cdot \bar{\boldsymbol{v}}_{\mathrm{A}} + \\ \int_{\Omega_{\mathrm{A}}} \mathsf{A}[\boldsymbol{E}(\boldsymbol{u}_{\mathrm{A}})] : \boldsymbol{E}(\bar{\boldsymbol{v}}_{\mathrm{A}}) + \int_{\Omega_{\mathrm{A}}} \operatorname{div}\left((\boldsymbol{A} + \boldsymbol{B} - \phi \boldsymbol{I})^t \bar{\boldsymbol{v}}_{\mathrm{A}}\right) p_{\mathrm{A}} + \int_{\Omega_{\mathrm{A}}} \hat{c} p_{\mathrm{A}} \bar{q}_{\mathrm{A}} + \\ \int_{\Omega_{\mathrm{A}}} \frac{1}{\rho_{\mathrm{F}} \omega^2} \boldsymbol{A} \,\mathbf{grad}\, p_{\mathrm{A}} \cdot \mathbf{grad}\, \bar{q}_{\mathrm{A}} + \int_{\Omega_{\mathrm{A}}} \operatorname{div}\left((\boldsymbol{A} + \boldsymbol{B} - \phi \boldsymbol{I}) \boldsymbol{u}_{\mathrm{A}}\right) \bar{q}_{\mathrm{A}} = \\ \int_{\Gamma_{\mathrm{I}}} p_{\mathrm{F}} (\bar{\boldsymbol{v}}_{\mathrm{F}} \cdot \boldsymbol{n} - \bar{\boldsymbol{v}}_{\mathrm{A}} \cdot \boldsymbol{n}),\end{aligned} \tag{3.23}$$

$$\int_{\Gamma_{\mathrm{I}}} \bar{q}_{\mathrm{F}} (\boldsymbol{u}_{\mathrm{A}} \cdot \boldsymbol{n} - \boldsymbol{u}_{\mathrm{F}} \cdot \boldsymbol{n}) = 0, \tag{3.24}$$

for all $(\boldsymbol{v}_{\mathrm{F}}, q_{\mathrm{F}}, \boldsymbol{v}_{\mathrm{F}}, q_{\mathrm{A}}) \in \mathbf{V}_0$.

3.4 Finite element discretization

Fluid and porous displacement fields belong to different functional spaces, $\mathbf{H}(\operatorname{div}, \Omega_{\mathrm{F}})$ and $\mathrm{H}^1(\Omega_{\mathrm{A}})^3$, respectively, hence it is quite natural to use different types of finite elements for each of them in order to discretize weak problem (3.23)-(3.24).

Let $\mathcal{T}_h$ be a regular family of tetrahedral partitions of $\Omega_{\mathrm{F}} \cup \Omega_{\mathrm{A}}$ such that every tetrahedra is completely contained either in Ω_{F} or in Ω_{A}. We also assume that faces of tetrahedra lying on $\Gamma_{\mathrm{W}} \cup \Gamma_{\mathrm{E}} \cup \Gamma_{\mathrm{I}}$ are completely contained either in Γ_{W}, or in Γ_{E} or in Γ_{I}.

As we have considered in Chapter 2, lowest order Raviart-Thomas finite elements have been used to approximate fluid displacements. They consist of vector valued functions which, when restricted to each tetrahedron, are incomplete linear polynomials of the form

$$\boldsymbol{u}^h(x_1, x_2, x_3) = (a + dx_1, b + dx_2, c + dx_3), \ a, b, c, d \in \mathbb{C}.$$

These vector fields have constant normal components on each of the four faces of a tetrahedron (see Figure 3.2) which define a unique polynomial function of this type. Moreover, the global discrete displacement field $\boldsymbol{u}^h$ is allowed to have discontinuous tangential components on the faces of tetrahedra of partition $\mathcal{T}_h$. Instead, its constant normal components must be continuous through these faces (these constant values being the degrees of freedom defining $\boldsymbol{u}^h$). Because of this, $\operatorname{div} \boldsymbol{u}^h$ is globally well defined in Ω_{F}.

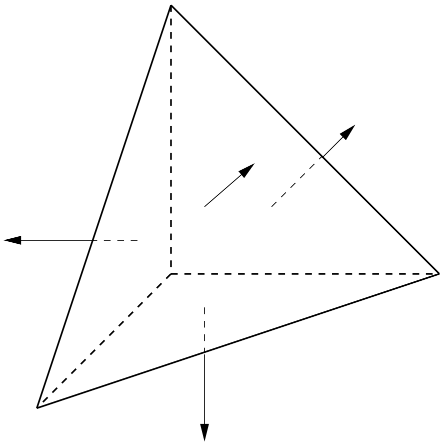

Figure 3.2: Raviart-Thomas finite element.

Thus, for fluid displacements we use the Raviart-Thomas space (see [96])

$$\mathbf{R}_h(\Omega_{\mathrm{F}}) := \{\boldsymbol{u} \in \mathbf{H}(\operatorname{div}, \Omega_{\mathrm{F}}) \ : \ \boldsymbol{u}|_T \in \mathcal{R}_0(T), \ \forall T \in \mathcal{T}_h, \ T \subset \Omega_{\mathrm{F}}\},$$

where

$$\mathcal{R}_0(T) := \left\{\boldsymbol{u} \in \mathcal{P}_1(T)^2 \ : \ \boldsymbol{u}(x_1, x_2, x_3) = (a + dx_1, b + dx_2, c + dx_3), \ a, b, c, d \in \mathbb{C}\right\}.$$

To approximate displacements in the porous medium, we use the so called "MINI element" in order to achieve stability in the discrete problem (see [8]). We recall definition of the corresponding discrete space by first defining bubble functions. For fixed $T \in \mathcal{T}_h$, we denote by $\lambda_1^T, \dots, \lambda_4^T$ barycentric coordinates in tetrahedron T. Then bubble function α, associated with T, is defined by the product

$$\alpha = 256 \prod_{i=1}^{4} \lambda_i^T.$$

This bubble function is a polynomial of degree four, null on the surface of tetrahedron T and taking value one at barycenter of T. The approximating space associated with the MINI element consists of continuous vector valued functions whose components, restricted to each tetrahedron, are sum of a bubble function and a polynomial of degree one, i.e.,

$$\boldsymbol{u}_i^h(x_1, x_2, x_3)|_T = ax_1 + bx_2 + cx_3 + d + e\alpha(x_1, x_2, x_3),\ a, b, c, d, e \in \mathbb{C}.$$

The degrees of freedom for functions in this space are the values of the vector field at vertices and barycenters of tetrahedra (see Figure 3.3).

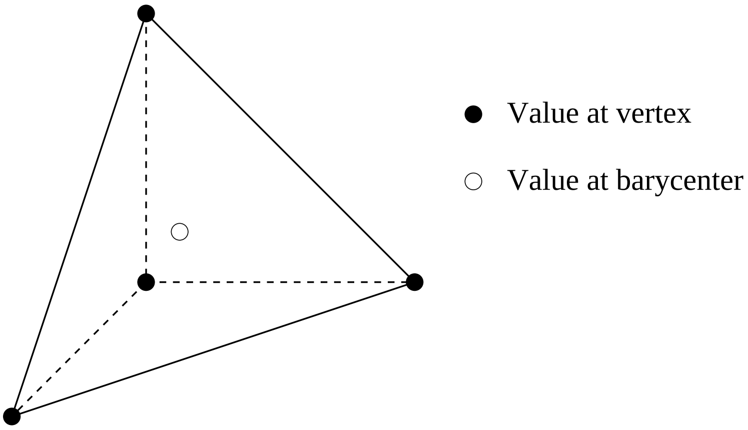

Figure 3.3: MINI finite element.

Then, for porous displacements, we use the MINI space

$$\mathbf{M}_h\left(\Omega_{\mathrm{A}}\right) := \left\{\boldsymbol{u} \in \mathrm{H}^1(\Omega_{\mathrm{A}})^3\ :\ \boldsymbol{u}|_T \in (\mathcal{P}_1(T) \oplus \mathcal{P}^b(T))^3,\ \forall T \in \mathcal{T}_h,\ T \subset \Omega_{\mathrm{A}}\right\},$$

where

$$\mathcal{P}^b(T) = \{a\alpha : a \in \mathbb{C}\}.$$

To approximate porous medium pressure, continuous piecewise linear finite elements are used. They consist of scalar valued functions which, when restricted to each tetrahedron, are polynomials of the form

$$p^h(x_1, x_2, x_3)|_T = ax_1 + bx_2 + cx_3 + d,\ a, b, c, d \in \mathbb{C}.$$

Thus, the porous medium pressure is approximated in the finite-dimensional space,

$$\mathbf{L}_h\left(\Omega_{\mathrm{A}}\right) := \left\{p \in \mathrm{H}^1(\Omega_{\mathrm{A}})\ :\ p|_T \in \mathcal{P}_1(T),\ \forall T \in \mathcal{T}_h,\ T \subset \Omega_{\mathrm{A}}\right\}.$$

We recall that the degrees of freedom defining p^h are its values at vertices of tetrahedra.

Finally, in order to approximate the interface pressure we use piecewise constant functions on the triangles of the mesh lying on the interface Γ_I. In other words, for interface pressure we use the space

$$\mathbf{C}_h\left(\Gamma_{\mathrm{I}}\right) := \left\{p \in \mathrm{L}^2(\Gamma_{\mathrm{I}})\ :\ p|_{\partial T} \in \mathcal{P}_0(\partial T),\ \forall T \in \mathcal{T}_h,\ \partial T \cap \Gamma_{\mathrm{I}} \neq \emptyset\right\}.$$

The degrees of freedom of this finite element space are the (constant) values on triangles in Γ_{I}.

Consequently, the discrete analogue to $\mathbf{V}$ is

$$\mathbf{V}_h = \mathbf{R}_h\left(\Omega_{\mathrm{F}}\right) \times \mathbf{M}_h\left(\Omega_{\mathrm{A}}\right) \times \mathbf{L}_h\left(\Omega_{\mathrm{A}}\right) \times \mathbf{C}_h\left(\Gamma_{\mathrm{I}}\right)$$

while the corresponding to $\mathbf{V}_0$ is

$$\begin{aligned}\mathbf{V}_{0h} = \{(\boldsymbol{v}_{\mathrm{F}}, q_{\mathrm{F}}, \boldsymbol{v}_{\mathrm{A}}, q_{\mathrm{A}}) \in \mathbf{R}_h\left(\Omega_{\mathrm{F}}\right) \times \mathbf{M}_h\left(\Omega_{\mathrm{A}}\right) \times \mathbf{L}_h\left(\Omega_{\mathrm{A}}\right) \times \mathbf{C}_h\left(\Gamma_{\mathrm{I}}\right)\ :& \\ \boldsymbol{v}_{\mathrm{F}} \cdot \boldsymbol{\nu} = 0 \text{ on } (\Gamma_{\mathrm{D}} \cup \Gamma_{\mathrm{E}}) \cap \partial\Omega_{\mathrm{F}}, \boldsymbol{v}_{\mathrm{A}} = \mathbf{0} \text{ on } \Gamma_{\mathrm{D}} \cap \partial\Omega_{\mathrm{A}}\}\,.&\end{aligned}$$

With these finite element spaces we can define the approximate problem to (3.23)-(3.24) by

For an angular frequency ω fixed, find $(\boldsymbol{u}_{\mathrm{F}}^h, p_{\mathrm{F}}^h, \boldsymbol{u}_{\mathrm{A}}^h, p_{\mathrm{A}}^h) \in \mathbf{V}_h$ satisfying

$$\begin{aligned}\boldsymbol{u}_{\mathrm{F}}^h \cdot \boldsymbol{\nu} &= 0 \ \textit{ on faces in } \Gamma_{\mathrm{W}} \cap \partial\Omega_{\mathrm{F}},\\ \boldsymbol{u}_{\mathrm{A}}^h &= \mathbf{0} \ \textit{ at vertices in } \Gamma_{\mathrm{W}} \cap \partial\Omega_{\mathrm{A}},\\ \boldsymbol{u}_{\mathrm{F}}^h \cdot \boldsymbol{\nu} &= f \ \textit{ on faces in } \Gamma_{\mathrm{E}},\end{aligned}$$

and furthermore,

$$\begin{aligned}&\int_{\Omega_{\mathrm{F}}} \rho_{\mathrm{F}} c^2 \operatorname{div} \boldsymbol{u}_{\mathrm{F}}^h \ \operatorname{div} \bar{\boldsymbol{v}}_{\mathrm{F}}^h - \omega^2 \int_{\Omega_{\mathrm{F}}} \rho_{\mathrm{F}} \boldsymbol{u}_{\mathrm{F}}^h \cdot \bar{\boldsymbol{v}}_{\mathrm{F}}^h - \omega^2 \int_{\Omega_{\mathrm{A}}} \left(\rho \mathbf{I} - \rho_{\mathrm{F}} \boldsymbol{A}\right) \boldsymbol{u}_{\mathrm{A}}^h \cdot \bar{\boldsymbol{v}}_{\mathrm{A}}^h + \\ &\quad \int_{\Omega_{\mathrm{A}}} A^H[D(\boldsymbol{u}_{\mathrm{A}}^h)] : D(\bar{\boldsymbol{v}}_{\mathrm{A}}^h) + \int_{\Omega_{\mathrm{A}}} \operatorname{div}\left((\boldsymbol{A} + \boldsymbol{B}^H - \phi \mathbf{I})^t \bar{\boldsymbol{v}}_{\mathrm{A}}^h\right) p_{\mathrm{A}}^h + \int_{\Omega_{\mathrm{A}}} \hat{c} p_{\mathrm{A}}^h \bar{q}_{\mathrm{A}}^h + \\ &\qquad \int_{\Omega_{\mathrm{A}}} \frac{1}{\rho_{\mathrm{F}} \omega^2} \boldsymbol{A} \, \mathbf{grad}\, p_{\mathrm{A}}^h \cdot \mathbf{grad}\, \bar{q}_{\mathrm{A}}^h + \int_{\Omega_{\mathrm{A}}} \operatorname{div}\left((\boldsymbol{A} + \boldsymbol{B}^H - \phi \mathbf{I}) \boldsymbol{u}_{\mathrm{A}}^h\right) \bar{q}_{\mathrm{A}}^h = \\ &\qquad\qquad \int_{\Gamma_{\mathrm{I}}} p_{\mathrm{F}}^h (\bar{\boldsymbol{v}}_{\mathrm{F}}^h \cdot \mathbf{n} - \bar{\boldsymbol{v}}_{\mathrm{A}}^h \cdot \mathbf{n}) \qquad (3.25)\end{aligned}$$

and

$$\int_{\Gamma_{\mathrm{I}}} \bar{q}_{\mathrm{F}}^h (\boldsymbol{u}_{\mathrm{A}}^h \cdot \mathbf{n} - \boldsymbol{u}_{\mathrm{F}}^h \cdot \mathbf{n}) = 0, \qquad (3.26)$$

for all $(\boldsymbol{v}_{\mathrm{F}}^h, q_{\mathrm{F}}^h, \boldsymbol{v}_{\mathrm{F}}^h, q_{\mathrm{A}}^h) \in \mathbf{V}_{0h}$.

3.5 Matricial description

In the previous Section, a discrete formulation of our source problem has been established. Now a matrix description is given and, assuming that it is well posed, we show that it is equivalent to a reduced linear system whose unknowns are the degrees of freedom of the interface pressure.

Let U_{F}^h and V_{F}^h denote the column vectors of nodal components of fluid displacement fields $\boldsymbol{u}_{\mathrm{F}}^h$ and $\boldsymbol{v}_{\mathrm{F}}^h$, in the standard finite element basis associated with $\mathbf{R}_h(\Omega_{\mathrm{F}})$, excluding those corresponding to faces on $(\Gamma_{\mathrm{W}} \cup \Gamma_{\mathrm{E}}) \cap \partial\Omega_{\mathrm{F}}$. Similarly, let $(U_{\mathrm{A}}^h, P_{\mathrm{A}}^h)$ and $(V_{\mathrm{A}}^h, Q_{\mathrm{A}}^h)$ denote the column vectors of nodal components of the pair fields $(\boldsymbol{u}_{\mathrm{A}}^h, p_{\mathrm{A}}^h)$ and $(\boldsymbol{v}_{\mathrm{A}}^h, q_{\mathrm{A}}^h)$, in the standard finite element basis associated with $\mathbf{M}_h(\Omega_{\mathrm{A}}) \times \mathbf{L}_h(\Omega_{\mathrm{A}})$, excluding those corresponding to vertices in $\Gamma_{\mathrm{W}} \cap \partial\Omega_{\mathrm{A}}$ for U_{A}^h and V_{A}^h. Lastly, let us call P_{F}^h and Q_{F}^h the vectors of nodal components of the interface pressure fields p_{F}^h and q_{F}^h, in the space of finite elements $\mathbf{C}_h(\Gamma_{\mathrm{I}})$.

Then the discretization problem can be written in matrix form as

$$\begin{pmatrix} R_{\mathrm{F}} - \omega^2 M_{\mathrm{F}} & 0 & 0 & -D_{\mathrm{F}} \\ 0 & R_{u,\mathrm{A}} - \omega^2 M_{u,\mathrm{A}} & C^* & D_{\mathrm{A}} \\ 0 & C & \omega^{-2} R_{p,\mathrm{A}} + M_{p,\mathrm{A}} & 0 \\ -D_{\mathrm{F}}^* & D_{\mathrm{A}}^* & 0 & 0 \end{pmatrix} \begin{pmatrix} U_{\mathrm{F}}^h \\ U_{\mathrm{A}}^h \\ P_{\mathrm{A}}^h \\ P_{\mathrm{F}}^h \end{pmatrix} = \begin{pmatrix} B^h \\ 0 \\ 0 \\ 0 \end{pmatrix} \tag{3.27}$$

where

$$\begin{aligned}
(V_{\mathrm{F}}^h)^* R_{\mathrm{F}} U_{\mathrm{F}}^h &= \int_{\Omega_{\mathrm{F}}} \rho_{\mathrm{F}} c^2 \operatorname{div} \boldsymbol{u}_{\mathrm{F}}^h \ \operatorname{div} \bar{\boldsymbol{v}}_{\mathrm{F}}^h, \\
(V_{\mathrm{A}}^h)^* R_{u,\mathrm{A}} U_{\mathrm{A}}^h &= \int_{\Omega_{\mathrm{A}}} \mathsf{A}[\boldsymbol{E}(\boldsymbol{u}_{\mathrm{A}}^h)] : \boldsymbol{E}(\bar{\boldsymbol{v}}_{\mathrm{A}}^h), \\
(Q_{\mathrm{A}}^h)^* R_{p,\mathrm{A}} P_{\mathrm{A}}^h &= \int_{\Omega_{\mathrm{A}}} \frac{1}{\rho_{\mathrm{F}}} \boldsymbol{A} \,\mathbf{grad}\, p_{\mathrm{A}}^h \cdot \mathbf{grad}\, \bar{q}_{\mathrm{A}}^h, \\
(V_{\mathrm{F}}^h)^* M_{\mathrm{F}} U_{\mathrm{F}}^h &= \int_{\Omega_{\mathrm{F}}} \rho_{\mathrm{F}} \boldsymbol{u}_{\mathrm{F}}^h \cdot \bar{\boldsymbol{v}}_{\mathrm{F}}^h, \\
(V_{\mathrm{A}}^h)^* M_{u,\mathrm{A}} U_{\mathrm{A}}^h &= \int_{\Omega_{\mathrm{A}}} (\rho \mathbf{I} - \rho_{\mathrm{F}} \boldsymbol{A})\, \boldsymbol{u}_{\mathrm{A}}^h \cdot \bar{\boldsymbol{v}}_{\mathrm{A}}^h, \\
(Q_{\mathrm{A}}^h)^* M_{p,\mathrm{A}} P_{\mathrm{A}}^h &= \int_{\Omega_{\mathrm{A}}} \hat{c} p_{\mathrm{A}}^h \bar{q}_{\mathrm{A}}^h, \\
(Q_{\mathrm{A}}^h)^* C U_{\mathrm{A}}^h &= \int_{\Omega_{\mathrm{A}}} \operatorname{div} \left((\boldsymbol{A} + \boldsymbol{B} - \phi \mathbf{I}) \boldsymbol{u}_{\mathrm{A}}^h \right) \bar{q}_{\mathrm{A}}^h, \\
(V_{\mathrm{F}}^h)^* D_{\mathrm{F}} P_{\mathrm{F}}^h &= \int_{\Gamma_{\mathrm{I}}} p_{\mathrm{F}}^h \bar{\boldsymbol{v}}_{\mathrm{F}}^h \cdot \mathbf{n}, \\
(V_{\mathrm{F}}^h)^* D_{\mathrm{A}} P_{\mathrm{F}}^h &= \int_{\Gamma_{\mathrm{I}}} p_{\mathrm{F}}^h \bar{\boldsymbol{v}}_{\mathrm{A}}^h \cdot \mathbf{n},
\end{aligned}$$

and the right hand side B^h comes from boundary data f. R_{F} and M_{F} are the standard stiffness and mass matrices of the fluid, while $R_{u,\mathrm{A}}$, $M_{u,\mathrm{A}}$ and $R_{p,\mathrm{A}}$, $M_{p,\mathrm{A}}$ are the corresponding ones for the porous medium in the case of displacement and pressure, respectively. Notice that every matrix depending on fluid fields is highly sparse because only a maximum of seven entries per row can be different from zero (this corresponds to the number of faces of two adjacent tetrahedra).

Now, we are going to choose ω such that it is not an eigenvalue of the discrete problem. Specifically, we assume that the entire matrix of linear system (3.27) and matrices $R_{\mathrm{F}} - \omega^2 M_{\mathrm{F}}$ and

$$K_{\mathrm{A}} = \begin{pmatrix} R_{u,\mathrm{A}} - \omega^2 M_{u,\mathrm{A}} & C^* \\ C & \omega^{-2} R_{p,\mathrm{A}} + M_{p,\mathrm{A}} \end{pmatrix} \tag{3.28}$$

are non-singular. On the other hand, we notice that matrix $\omega^{-2} R_{p,\mathrm{A}} + M_{p,\mathrm{A}}$ is clearly positive definite and hence non-singular.

In order to improve the resolution of linear system (3.27), we are going to take into account the non-singularity of diagonal matrices. Firstly, we can rewrite this system as

$$(R_{\mathrm{F}} - \omega^2 M_{\mathrm{F}}) U_{\mathrm{F}}^h - D_{\mathrm{F}} P_{\mathrm{F}}^h = B^h, \tag{3.29}$$

$$(R_{u,\mathrm{A}} - \omega^2 M_{u,\mathrm{A}}) U_{\mathrm{A}}^h + C^* P_{\mathrm{A}}^h + D_{\mathrm{A}} P_{\mathrm{F}}^h = 0, \tag{3.30}$$

$$C U_{\mathrm{A}}^h + (\omega^{-2} R_{p,\mathrm{A}} + M_{p,\mathrm{A}}) P_{\mathrm{A}}^h = 0, \tag{3.31}$$

$$-D_{\mathrm{F}}^* U_{\mathrm{F}}^h + D_{\mathrm{A}}^* U_{\mathrm{A}}^h = 0. \tag{3.32}$$

Since matrix $R_{\mathrm{F}} - \omega^2 M_{\mathrm{F}}$ is non-singular, because of the choice of frequency ω, and $\omega^{-2} R_{p,\mathrm{A}} + M_{p,\mathrm{A}}$ is positive definite, we can obtain from (3.29) and (3.31)

$$U_{\mathrm{F}}^h = (R_{\mathrm{F}} - \omega^2 M_{\mathrm{F}})^{-1} (B^h + D_{\mathrm{F}} P_{\mathrm{F}}^h), \tag{3.33}$$

$$P_{\mathrm{A}}^h = -(\omega^{-2} R_{p,\mathrm{A}} + M_{p,\mathrm{A}})^{-1} C U_{\mathrm{A}}^h. \tag{3.34}$$

If we take into account that K_{A} is non-singular and $\omega^{-2} R_{p,\mathrm{A}} + M_{p,\mathrm{A}}$ is positive definite, we can conclude that matrix $R_{u,\mathrm{A}} - \omega^2 M_{u,\mathrm{A}} - C^* (\omega^{-2} R_{p,\mathrm{A}} + M_{p,\mathrm{A}})^{-1} C$ is also non-singular. Then, it results from (3.30) and (3.34) that

$$U_{\mathrm{A}}^h = -(R_{u,\mathrm{A}} - \omega^2 M_{u,\mathrm{A}} - C^* (\omega^{-2} R_{p,\mathrm{A}} + M_{p,\mathrm{A}})^{-1} C)^{-1} D_{\mathrm{A}} P_{\mathrm{F}}^h. \tag{3.35}$$

Collecting equations (3.33) and (3.35), we can write a simple linear system from (3.32) whose unique unknown is the nodal interface pressure vector P_{F}^h, namely,

$$\begin{aligned} \big\{ D_{\mathrm{A}}^* (R_{u,\mathrm{A}} - \omega^2 M_{u,\mathrm{A}} - C^* (\omega^{-2} R_{p,\mathrm{A}} + M_{p,\mathrm{A}})^{-1} C)^{-1} D_{\mathrm{A}} & \\ + D_{\mathrm{F}}^* (R_{\mathrm{F}} - \omega^2 M_{\mathrm{F}})^{-1} D_{\mathrm{F}} \big\} P_{\mathrm{F}}^h &= D_{\mathrm{F}}^* (R_{\mathrm{F}} - \omega^2 M_{\mathrm{F}})^{-1} B^h, \end{aligned}$$

where the involved matrix is non-singular because this system is equivalent to the full system (3.27) which has unique solution.

3.6 Numerical solution of cell problems

In this section we solve the cell problems allowing us to obtain values of the macroscopic coefficients for the poroelastic model considered in this chapter. More precisely, we are going to solve problems (1.50)-(1.52), (1.53)-(1.55) and (1.67)-(1.70) presented in Chapter 1 for the fluid and solid cells shown in Figure 3.4. This is a first step to determine the components of operator A, matrices $\boldsymbol{A}$ and $\boldsymbol{B}$, and scalar $\hat{c}$ appearing in the poroelastic model (3.3)-(3.4).

We use a finite element method to solve these boundary-value problems. More precisely, we employ continuous piecewise linear finite elements on tetrahedral meshes to approximate w^{ij}, w^0 and ξ^i. These meshes can be seen in Figure 3.4.

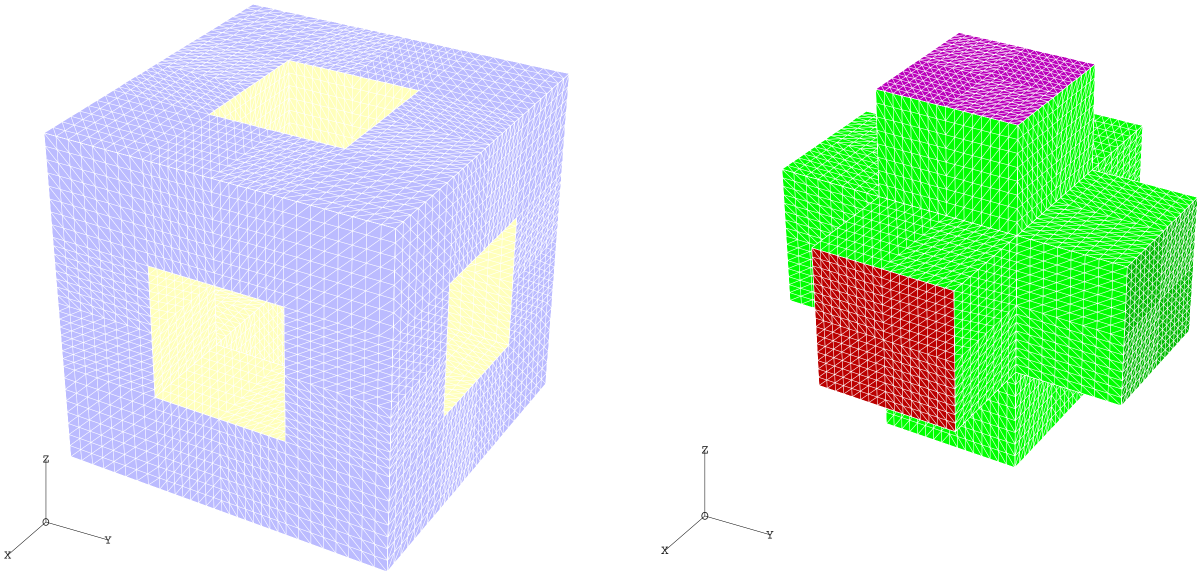

Figure 3.4: Meshes of the fluid and solid part of the unit cell (Y_{F} and Y_{S}, respectively)

We assume that the solid part of the poroelastic material is glasswool of type R, with the following properties:

Young modulus	8.7×10^{10} N/m^2
Poisson coefficient	0.15
Density	2500 kg/m^3

Assuming that the poroelastic material is completely saturated by air, we have obtained the following macroscopic coefficients for generalized Biot model (3.3)-(3.4):

$$\boldsymbol{A} = \begin{pmatrix} 0.7576 & 0.3222\text{E-}4 & 0.8560\text{E-}4 \\ 0.8526\text{E-}4 & 0.7581 & 0.8646\text{E-}4 \\ 0.5362\text{E-}4 & 0.2928\text{E-}4 & 0.7573 \end{pmatrix},$$

$$\hat{c} = \text{-}0.4955\text{E-}11,$$

$$\boldsymbol{B} = \begin{pmatrix} \text{-0.2050} & \text{-0.1385E-3} & \text{-0.5167E-3} \\ \text{-0.1385E-3} & \text{-0.2061} & \text{0.4572E-3} \\ \text{-0.5167E-3} & \text{0.4572E-3} & \text{-0.2047} \end{pmatrix},$$

$$\mathsf{A} = 10^{11} \times \begin{pmatrix} M_{11} & M_{12} & M_{13} \\ M_{12} & M_{22} & M_{23} \\ M_{13} & M_{23} & M_{33} \end{pmatrix},$$

where

$$M_{11} = \begin{pmatrix} \text{0.1589} & \text{-0.3337E-4} & \text{-0.8505E-4} \\ \text{-0.3337E-4} & \text{0.1195E-1} & \text{-0.1311E-3} \\ \text{-0.8505E-4} & \text{-0.1311E-3} & \text{0.1213E-1} \end{pmatrix},$$

$$M_{12} = \begin{pmatrix} \text{-0.1057E-4} & \text{0.1813E-1} & \text{-0.5855E-4} \\ \text{0.1813E-1} & \text{-0.2185E-4} & \text{-0.1051E-5} \\ \text{-0.5855E-4} & \text{-0.1051E-5} & \text{0.2270E-4} \end{pmatrix},$$

$$M_{13} = \begin{pmatrix} \text{0.1115E-5} & \text{-0.1254E-4} & \text{0.1834E-1} \\ \text{-0.1254E-4} & \text{0.8837E-6} & \text{0.1045E-5} \\ \text{0.1834E-1} & \text{0.1045E-5} & \text{0.4812E-5} \end{pmatrix},$$

$$M_{22} = \begin{pmatrix} \text{0.1190E-1} & \text{-0.1144E-3} & \text{0.2185E-3} \\ \text{-0.1144E-3} & \text{0.1586} & \text{0.7522E-5} \\ \text{0.2185E-3} & \text{0.7522E-5} & \text{0.1204E-1} \end{pmatrix},$$

$$M_{23} = \begin{pmatrix} \text{0.1190E-5} & \text{0.4927E-4} & \text{-0.1044E-3} \\ \text{0.4927E-4} & \text{-0.1069E-5} & \text{0.1851E-1} \\ \text{-0.1044E-3} & \text{0.1851E-1} & \text{-0.1966E-5} \end{pmatrix},$$

$$M_{33} = \begin{pmatrix} \text{0.1212E-1} & \text{0.5964E-2} & \text{-0.1349E-3} \\ \text{0.5964E-2} & \text{0.1203E-1} & \text{-0.2908E-3} \\ \text{-0.1349E-3} & \text{-0.2908E-3} & \text{0.1584} \end{pmatrix}.$$

Moreover, porosity of the porous sample is $\phi = 0.648$.

Finally, by progressive refinement of meshes one can see that matrices of macroscopic parameters $\boldsymbol{A}$ and $\boldsymbol{B}$ tend to isotropic matrices. Similarly, tensor A has the same structure as the elasticity tensor for isotropic elastic materials. Thus, due to the symmetry properties of the cell, the macroscopic behavior of the studied porous medium is isotropic.

3.7 Numerical results

In this Section we present some numerical results obtained with a computer code developed by us which implements the numerical methods proposed in this chapter. This code allows us to compute the response diagram of the enclosure shown in Figure 3.1, consisting of a fluid and a poroelastic medium.

In order to validate our method, we are going to build a simple example which can be reduced to a one-dimensional problem and then solved exactly. We recall that equations satisfied by pressure and displacement fields in the poroelastic media are

$$\begin{aligned} \omega^2\left(\rho\mathbf{I}-\rho_{\mathrm{F}}\boldsymbol{A}\right)\boldsymbol{u}_{\mathrm{A}}+\ \operatorname{div}\left(\mathsf{A}[D(\boldsymbol{u}_{\mathrm{A}})]\right)+\left(\boldsymbol{A}+\boldsymbol{B}-\phi\mathbf{I}\right)\mathbf{grad}\,p_{\mathrm{A}}&=\mathbf{0} && \text{in } \Omega_{\mathrm{A}},\\ -\omega^2\hat{c}p_{\mathrm{A}}+\frac{1}{\rho_{\mathrm{F}}}\operatorname{div}(\boldsymbol{A}\,\mathbf{grad}\,p_{\mathrm{A}})&=\omega^2\operatorname{div}\left(\left(\boldsymbol{A}+\boldsymbol{B}-\phi\mathbf{I}\right)\boldsymbol{u}_{\mathrm{A}}\right) && \text{in } \Omega_{\mathrm{A}}. \end{aligned}$$

If we assume that every linear operator is a multiple of the identity operator, we can find a solution $(\boldsymbol{u}_{\mathrm{A}}, p_{\mathrm{A}})$ of the form $\boldsymbol{u}_{\mathrm{A}}(x_1,x_2,x_3)=u_{\mathrm{A}}(x_3)\boldsymbol{e}_3$, $p_{\mathrm{A}}(x_1,x_2,x_3)=p_{\mathrm{A}}(x_3)$, and rewrite the above three-dimensional problem as a one-dimensional problem, namely,

$$\begin{aligned} \omega^2\left(\rho-\rho_{\mathrm{F}}a\right)u_{\mathrm{A}}+su_{\mathrm{A}}''+\left(a+b-\phi\right)p_{\mathrm{A}}'&=0 && \text{in } (0,a_{\mathrm{A}}),\\ -\omega^2\hat{c}p_{\mathrm{A}}+\frac{a}{\rho_{\mathrm{F}}}p_{\mathrm{A}}''&=\omega^2\left(a+b-\phi\right)u_{\mathrm{A}}' && \text{in } (0,a_{\mathrm{A}}), \end{aligned}$$

where the prime denotes derivative with respect to z and we have supposed that $\mathsf{A}\left[\boldsymbol{E}(\boldsymbol{u}_{\mathrm{A}})\right]\boldsymbol{e}_3 = su_{\mathrm{A}}'\boldsymbol{e}_3$, $\boldsymbol{A}=a\mathbf{I}$, $\boldsymbol{B}=b\mathbf{I}$. After some algebraic manipulations, we obtain

$$\begin{aligned} \frac{a}{\omega^2\rho_{\mathrm{F}}}p_{\mathrm{A}}''''-\left(\hat{c}-\frac{(a+b-\phi)^2}{s}-\frac{a(\rho-\rho_{\mathrm{F}}a)}{\omega^2 s\rho_{\mathrm{F}}}\right)p_{\mathrm{A}}''-\frac{\omega^2(\rho-\rho_{\mathrm{F}}a)\hat{c}}{s}p_{\mathrm{A}}&=0 && \text{in } (0,a_{\mathrm{A}}),\\ u_{\mathrm{A}}=\frac{s}{\omega^2(a+b-\phi)(\rho-\rho_{\mathrm{F}}a)}\left(-\frac{a}{\omega^2\rho_{\mathrm{F}}}p_{\mathrm{A}}'''+\left(\hat{c}-\frac{(a+b-\phi)^2}{s}\right)p_{\mathrm{A}}'\right)& && \text{in } (0,a_{\mathrm{A}}). \end{aligned}$$

Let us assume a similar assumption for fluid displacement and interface pressure, i.e., $\boldsymbol{u}_{\mathrm{F}}(x_1,x_2,x_3)=u_{\mathrm{F}}(x_3)\boldsymbol{e}_3$ and $p_{\mathrm{F}}(x_1,x_2,x_3)=p_{\mathrm{F}}(x_3)$. We also suppose that $\Omega_{\mathrm{F}}=(0,b)\times(0,d)\times(\tilde{a}_{\mathrm{F}},0)$, being $\tilde{a}_{\mathrm{F}}=-a_{\mathrm{F}}$, and $\Omega_{\mathrm{A}}=(0,b)\times(0,d)\times(0,a_{\mathrm{A}})$. Then the coupled fluid-poroelastic problem can be written as

$$-\omega^2\rho_{\mathrm{F}}u_F+p_{\mathrm{F}}'=0 \text{ in } (\tilde{a}_{\mathrm{F}},0), \tag{3.36}$$

$$p_{\mathrm{F}}=-\rho_{\mathrm{F}}c^2u_{\mathrm{F}}' \text{ in } (\tilde{a}_{\mathrm{F}},0), \tag{3.37}$$

$$\frac{a}{\omega^2\rho_{\mathrm{F}}}p_{\mathrm{A}}''''-\left(\hat{c}-\frac{(a+b-\phi)^2}{s}-\frac{a(\rho-\rho_{\mathrm{F}}a)}{\omega^2 s\rho_{\mathrm{F}}}\right)p_{\mathrm{A}}''-\frac{\omega^2(\rho-\rho_{\mathrm{F}}a)\hat{c}}{s}p_{\mathrm{A}}=0 \text{ in } (0,a_{\mathrm{A}}), \tag{3.38}$$

$$u_{\mathrm{A}}=\frac{s}{\omega^2(a+b-\phi)(\rho-\rho_{\mathrm{F}}a)}\left(-\frac{a}{\omega^2\rho_{\mathrm{F}}}p_{\mathrm{A}}'''+\left(\hat{c}-\frac{(a+b-\phi)^2}{s}\right)p_{\mathrm{A}}'\right) \text{ in } (0,a_{\mathrm{A}}), \tag{3.39}$$

$$-p_{\mathrm{F}}(0)=su_{\mathrm{A}}'(0)+\left(a+b-\phi\right)p_{\mathrm{A}}(0), \tag{3.40}$$

$$u_{\mathrm{F}}(0)=u_{\mathrm{A}}(0), \tag{3.41}$$

$$u_{\mathrm{F}}(\tilde{a}_{\mathrm{F}})=0, \tag{3.42}$$

$$u_{\mathrm{A}}(a_{\mathrm{A}})=0, \tag{3.43}$$

$$ap_{\mathrm{A}}'(a_{\mathrm{A}})=0, \tag{3.44}$$

$$ap_{\mathrm{A}}'(0)=0, \tag{3.45}$$

$$u_{\mathrm{F}}(\tilde{a}_{\mathrm{F}})=f. \tag{3.46}$$

The general solution of the ordinary differential system (3.36)-(3.38) is

$$u_{\mathrm{F}}(x_3) = C_1 e^{-ik_{\mathrm{F}}x_3} + C_2 e^{ik_{\mathrm{F}}x_3}, \qquad x_3 \in (-a_{\mathrm{F}}, 0), \tag{3.47}$$

$$p_{\mathrm{A}}(x_3) = C_3 e^{-ik_{\mathrm{A},1}x_3} + C_4 e^{ik_{\mathrm{A},1}x_3} + C_5 e^{-ik_{\mathrm{A},2}x_3} + C_6 e^{ik_{\mathrm{A},2}x_3}, \qquad x_3 \in (0, a_{\mathrm{A}}), \tag{3.48}$$

where $k_{\mathrm{F}} = \frac{\omega}{c}$ and $\{k_{\mathrm{A},1}, -k_{\mathrm{A},1}, k_{\mathrm{A},2}, -k_{\mathrm{A},2}\}$ are the four roots of the polynomial equation

$$-\frac{a}{\omega^2 \rho_{\mathrm{F}}} k_{\mathrm{A}}^4 + \left(\hat{c} - \frac{(a+b-\phi)^2}{s} - \frac{a(\rho - \rho_{\mathrm{F}} a)}{\omega^2 s \rho_{\mathrm{F}}} \right) k_{\mathrm{A}}^2 + \frac{\omega^2 (\rho - \rho_{\mathrm{F}} a)\hat{c}}{s} = 0.$$

If we take into account boundary and interface conditions (3.40)-(3.46) and expressions (3.47) and (3.48), amplitudes $C_j,\ 1 \le j \le 6$ can be calculated by solving a linear system of equations.

We have considered that fluid is air with $\rho_{\mathrm{F}} = 1.225$ kg/m^3 and $c = 343$ m/s, whereas properties of the porous material are summarized in $s = 9.18633 \times 10^{10}$N/m^2, $\phi = 0.95$, $a = 0.67857$, $b = -0.05$, $\hat{c} = -6.59172 \times 10^{-6}$ms^2/kg and $\rho = 1.26163 \times 10^2$ kg/m^3. With respect to the dimensions of the enclosure, length and width are 1 m while height is 1 m for the first layer of free fluid and 1 m for the second layer of porous material whereas the normal displacement on Γ_{E} is $f = 60$.

We have computed the solution to this problem with three different uniform meshes, named mesh 1, mesh 2 and mesh 3 of 2548, 8140 and 18788 degrees of freedom, respectively. In Figure 3.5, we show the L^2-norm of the relative errors for fluid displacement, $\left\|u_{\mathrm{F}}^h - u_{\mathrm{F}}\right\|_{0,\Omega_{\mathrm{F}}} / \left\|u_{\mathrm{F}}\right\|_{0,\Omega_{\mathrm{F}}}$, porous displacement, $\left\|u_{\mathrm{A}}^h - u_{\mathrm{A}}\right\|_{0,\Omega_{\mathrm{A}}} / \left\|u_{\mathrm{A}}\right\|_{0,\Omega_{\mathrm{A}}}$, porous pressure, $\left\|p_{\mathrm{A}}^h - p_{\mathrm{A}}\right\|_{0,\Omega_{\mathrm{A}}} / \left\|p_{\mathrm{A}}\right\|_{0,\Omega_{\mathrm{A}}}$, and interface pressure, $\left\|p_{\mathrm{F}}^h - p_{\mathrm{F}}\right\|_{0,\Omega_{\mathrm{F}}} / \left\|p_{\mathrm{F}}\right\|_{0,\Omega_{\mathrm{F}}}$, against mesh-size, h. As it can be seen, convergence of order 2 is achieved for poroelastic fields and interface pressure. In addition, convergence of order 1 is achieved for fluid displacement.

As a real life test, we are going to compute the solution of the coupled problem, using the data obtained in the previous Section by solving cell problems. Figure 3.6 shows the *response curves* for enclosure in Figure 3.1, when solved with mesh 1 having 2548 degrees of freedom. In this curve the logarithm of "energy",

$$\log_{10}\left(\frac{1}{2} \int_{\Omega_{\mathrm{F}}} \rho_{\mathrm{F}} c^2 |\operatorname{div} \boldsymbol{u}_{\mathrm{F}}|^2 + \int_{\Omega_{\mathrm{A}}} \mathsf{A}[\boldsymbol{E}(\boldsymbol{u}_{\mathrm{A}})] : \boldsymbol{E}(\bar{\boldsymbol{u}}_{\mathrm{A}}) + \int_{\Omega_{\mathrm{A}}} \operatorname{div}\left((\boldsymbol{A} + \boldsymbol{B} - \phi \mathbf{I}) \boldsymbol{u}_{\mathrm{A}} \right) \bar{p}_{\mathrm{A}} \right),$$

is plotted for angular frequencies ω ranging from 50 to 2000 rad/s. Several response peaks can be observed in this curve. In fact, response peaks of the curve shows the resonance frequencies for the coupled system shown in Figure 3.1.

3.8 Conclusions

We have considered a mathematical model for acoustic propagation in periodic non-dissipative porous media with elastic solid frame and open pore. Parameters of this model have been computed by solving some partial differential equations in the unit cell obtained

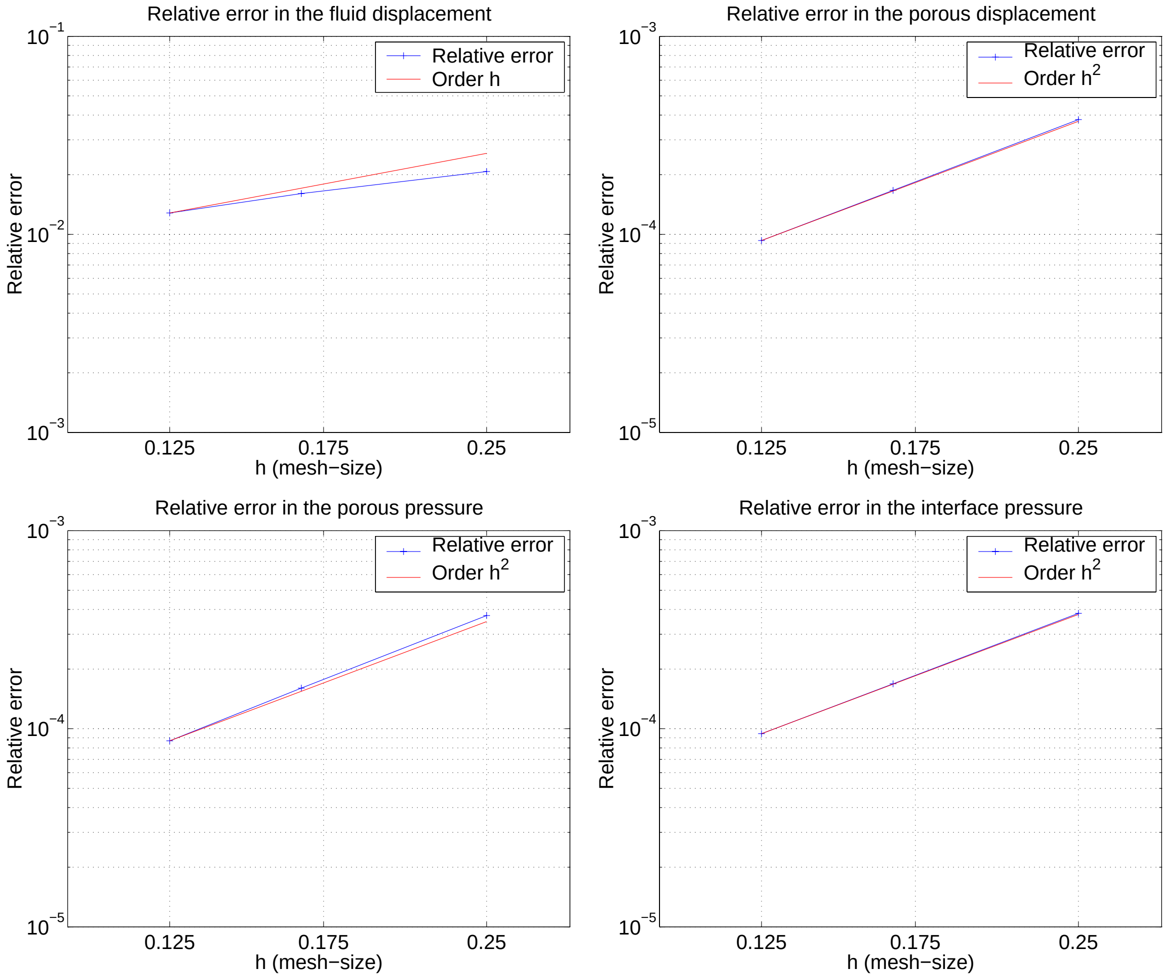

Figure 3.5: Curves of convergence for fluid and porous fields.

by homogenization methods. Then a three-dimensional finite element method has been proposed and implemented for numerical solution of the coupling between a fluid and the above porous medium. In order to validate the proposed methodology and to assess convergence properties, the computer code has been used for a test example having analytical solution. Then, as an application, we have computed the response curve for an enclosure containing air and a layer of porous material.

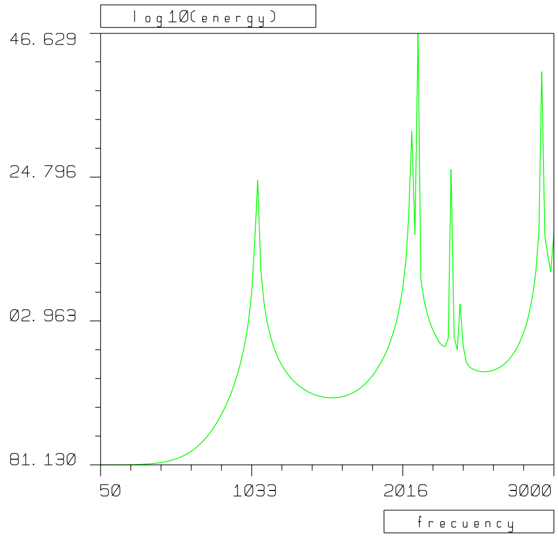

Figure 3.6: Response curve.

Part II

Perfectly Matched Layers

Chapter 4

A non reflecting porous material: the Perfectly Matched Layers

Contents

4.1 Introduction

The first problem to be tackled for the numerical solution of any scattering problem in an unbounded domain is truncating the computational domain without perturbing too much the solution of the original problem. In an ideal framework, the method should satisfy, at least, three properties: efficiency, easiness of implementation, and robustness.

In fact, the typical first step for the numerical solution of any scattering problem in an unbounded domain, by either finite elements or finite differences, entails an inherent difficulty: *to choose boundary conditions to replace the Sommerfeld radiation condition at infinity* (see, for instance, [66]).

Several numerical techniques have been developed with this purpose: boundary element methods, infinite element methods, Dirichlet-to-Neumann operators based on truncating Fourier expansions, absorbing boundary conditions, etc. The potential advantages of each of them have been widely studied in the literature (see, for instance, [9, 57, 72, 90], and [66] for a classical review on this subject).

We focus our attention on the last mentioned technique: local absorbing boundary conditions (ABCs) can be used to preserve the computational efficiency of the numerical method. Those of Bayliss and Turkel [15], Engquist and Majda [60], and Feng [61] are among the most widely used. However, in spite of the simple implementation of lowest order ABCs, good accuracy is only achieved for higher order ones [99], because these conditions are not fully non-reflecting on the truncated boundary of the computational domain. As a consequence, high accuracy using ABCs leads to a substantial computational cost and increases the difficulty of implementation. Recently, a promising way has been open: high order ABCs not involving high derivatives (see [67, 102]).

Let us remark that if the domain of the original problem is truncated with a sphere, then the Dirichlet-to-Neumann (DtN) boundary condition is exactly known (see [66, 84]). However, this boundary condition involves an infinite series which must be truncated for its numerical use. Moreover, the exact DtN condition is non local, leading to dense blocks in the linear system to be solved when a finite element method is used.

An alternative approach to deal with the truncation of unbounded domains is the so called *Perfectly Matched Layer* (PML) method, which was introduced by Berenger [22, 23, 24]. It is based on simulating an absorbing layer of anisotropic damping material surrounding the domain of interest, like a thin sponge which absorbs the scattered field radiated to the exterior of this domain. This method is known as 'perfectly matched' because the interface between the physical domain and the absorbing layer does not produce spurious reflections inside the domain of interest, as it is the case with ABCs.

This method has been applied to different problems. It was initially settled for Maxwell's equations in electromagnetism [18, 22] and subsequently used for the scalar Helmholtz equation [69, 94, 101], advective acoustics [1, 16, 71], shallow water waves [89], elasticity [14, 53], poroelastic media [105], and other hyperbolic problems (see for instance [82] among many other papers). We focus our attention on wave propagation time-harmonic scattering problems in linear acoustics, i.e., on the scalar Helmholtz equation.

In the deduction of the PML [22], Berenger used an artificial splitting of the physical unknowns, to force the tangential components of both velocities (in the acoustic medium and in the PML layer) to coincide on the interface for any frequency and any angle of incidence, thus guaranteeing the absence of spurious reflections [72]. However, from a mathematical point of view, this non physical splitting has been shown unnecessary to state the PML equations. In fact, Chew and Weedon [47] and Rappaport [95] showed that the PML equations can be obtained using a complex-valued coordinate stretching, in the framework of time-harmonic wave propagation. Related to this, Lassas *et al.* [79, 77] showed that the PML, and in general a family of absorbing conditions, can be obtained by using complex Riemannian metric tensors.

Furthermore, in spite of the fact that the PML has been originally settled in Cartesian coordinates, Collino and Monk [52] proposed a similar complex-valued change of coordinates to build a PML on curvilinear coordinates, as we show in Chapter 6.

In practice, since the PML has to be truncated at a finite distance of the domain of interest, its external boundary produces artificial reflections. Theoretically, these reflections are of minor importance because of the exponential decay of the acoustic waves inside the PML. In fact, for Helmholtz-type scattering problems, Lassas and Somersalo [78] proved, using boundary integral equation techniques, that the approximate solution obtained by the PML method converges exponentially to the exact solution in the computational domain as the thickness of the layer tends to infinity. This result was generalized by Hohage *et al.* [70] using techniques based on the pole condition. Similarly, Bécache *et al.* proved an analogous result for the convected Helmholtz equation [16] and for the Galbrun's equation [17].

When the problem is discretized to be numerically solved, the approximation error typically becomes larger. Increasing the thickness of the PML may be a remedy, but not always available because of computational cost. An alternative is to take larger values for the absorbing function involved in the complex-valued coordinate stretching. However, Collino and Monk [51] showed that this methodology may produce an error growth in the discretized problem. Consequently, an optimization problem arises: given a data set and a mesh, to choose the optimal absorbing function to minimize the error.

In this framework, Asvadurov *et al.* [10] proposed a pure imaginary stretching to optimize the PML error. They recovered exponential error estimates using finite-difference grid optimization. However, to the best of the authors' knowledge, the optimization problem is still open in that there is no optimal criterion to choose the absorbing function independently of data and meshes.

In the following three chapters we propose (see [32, 33, 30]) an alternative procedure to avoid this drawback: to use an absorbing function with unbounded integral on the PML.

The outline of this introductory chapter on the PML technique is as follows. In Section 4.2 a two-dimensional acoustic scattering problem is stated in an unbounded domain and the solution is written explicitly under the assumption of time-harmonic dependency in the case of a monopole source. In Section 4.3, we derive the time domain formulation of the perfectly matched layer for the linear acoustic equations in Cartesian coordinates and show the exact solution of the PML equations when the domain remains unbounded or when a singular absorbing function is used in the construction of the perfectly matched layer. Finally, in Section 4.4 we consider a simple problem: the propagation of plane waves with oblique incidence in a two-dimensional unbounded domain. We show that a PML method based on a non-integrable absorbing function allows recovering the exact solution in the domain of interest.

4.2 Wave equation

For the sake of completeness, the derivation of the two-dimensional linear wave equation is outlined, since the same steps will be done for the PML equation.

4.2.1 Time domain equations

First, we state the system of equations of the wave motion in terms of the pressure and the velocity fields.

Find the velocity field $\boldsymbol{V}$ *and pressure field* P *in the whole space* $\mathbb{R}^2$ *which satisfy the system of equations:*

$$\begin{aligned} \frac{\partial \rho}{\partial t} + \rho_0 \operatorname{div} \boldsymbol{V} &= 0, && (4.1)\\ \rho_0 \frac{\partial \boldsymbol{V}}{\partial t} + \mathbf{grad}\, P &= \mathbf{0}, && (4.2)\\ P &= \tilde{P}(\rho), && (4.3) \end{aligned}$$

where ρ_0 *is the fluid mass density at rest, which is supposed to be a constant, and* ρ *is the mass density.*

From the fluid constitutive equation (4.3), we deduce that

$$\frac{\partial P}{\partial t} = c^2 \frac{\partial \rho}{\partial t},$$

where c is the sound speed. By using (4.1), we obtain

$$\frac{1}{c^2}\frac{\partial P}{\partial t} + \rho_0 \operatorname{div} \boldsymbol{V} = 0. \tag{4.4}$$

If we derive with respect to the time variable, then we have

$$\frac{1}{c^2}\frac{\partial^2 P}{\partial t^2} + \rho_0 \operatorname{div} \frac{\partial \boldsymbol{V}}{\partial t} = 0.$$

Now, by applying the divergence operator in (4.2),

$$\rho_0 \operatorname{div} \frac{\partial \boldsymbol{V}}{\partial t} + \Delta P = 0,$$

and replacing this expression in (4.4), it results

$$\frac{1}{c^2}\frac{\partial^2 P}{\partial t^2} - \Delta P = 0. \tag{4.5}$$

4.2.2 Time-harmonic equations

We take into account a simple toy problem which illustrates the construction of perfectly matched layers in Cartesian coordinates. If there exists an acoustical source in the fluid domain, a non-null right-hand term F arises in the above equation. If we assume that F is time-harmonic, i.e., $F(\boldsymbol{x},t) = \mathrm{Re}\left(\mathrm{e}^{-i\omega t} f(\boldsymbol{x})\right)$, then $P(\boldsymbol{x},t) = \mathrm{Re}\left(\mathrm{e}^{-i\omega t} p(\boldsymbol{x})\right)$ is a solution of equation (4.5) provided

$$-\frac{\omega^2}{c^2} p - \Delta p = f. \tag{4.6}$$

Moreover, from a physical point of view, if we postulate that no waves are reflected from infinity, p must satisfy the Sommerfeld's radiation condition uniformly in all the directions (see [72]). Hence, the source problem stated in the whole space $\mathbb{R}^2$ and using the pressure field as unique unknown is:

Given an acoustical source f, find the pressure field p satisfying

$$-\frac{\omega^2}{c^2} p - \Delta p = f \qquad \text{in } \mathbb{R}^2, \tag{4.7}$$

$$\lim_{r\to\infty} r^{\frac{1}{2}} \left(\frac{\partial p}{\partial r} - ikp \right) = 0, \tag{4.8}$$

where $r = |\boldsymbol{x}|$ and $k = \dfrac{\omega}{c}$ is the wave number.

If the harmonic excitation inside the fluid domain is a monopole supported in $\boldsymbol{d} = (d_1, d_2)$, then the right-hand term is $f = -i\omega\rho_0 Q \delta_{\boldsymbol{d}}$, where Q is the volume velocity and $\delta_{\boldsymbol{d}}$ is the Dirac's delta (see [63]). In this case the solution of problem (4.7)-(4.8) is

$$p(\boldsymbol{x}) = \frac{\omega\rho_0 Q}{4}\,\mathrm{H}_0^{(1)}(k|\boldsymbol{x} - \boldsymbol{d}|), \tag{4.9}$$

where $\mathrm{H}_0^{(1)}$ is the Hankel function of first kind and order zero.

4.3 Cartesian Perfectly Matched Layers

Now we are going to introduce the Cartesian perfectly matched layers to deal with the same problem. As a first step, we assume that the domain filled by the PML is unbounded. In spite that this fact does not avoid to state a problem in a bounded domain, it allows us to illustrate the derivation of the PML problem.

4.3.1 Time-domain equations

We assume that the equations of linear acoustics (4.1)-(4.3) are satisfied in

$$\Omega_{\mathrm{F}} = (-a, a) \times (-b, b),$$

whereas the perfectly matched layers are situated in $\Omega_{\mathrm{A}} = \mathbb{R}^2 \setminus \overline{\Omega}_{\mathrm{F}}$.

The two-dimensional Cartesian PML equations involve absorbing coefficients σ_j defined for each $1 \leq j \leq 2$, such that they are monotonically increasing, non negative, smooth in Ω_{A} and null inside the fluid domain Ω_{F}. Moreover σ_j only depends on the spatial variable x_j.

Next, we state which are the equations governing the pressure field inside Ω_{A}. With this aim, we use the 'splitting' technique developed originally by Berenger ([22], [72]). First, we suppose that the pressure field in Ω_{A} is the addition of two terms which involve two new unknowns without any physical meaning, P_j, $1 \leq j \leq 2$, such that Eq. (4.1) can be rewritten in terms of the pressure and the velocity fields as

$$\frac{\partial P_j}{\partial t} + \rho_0 c^2 \frac{\partial V_j}{\partial x_j} = 0, \qquad 1 \leq j \leq 2, \tag{4.10}$$
$$P = P_1 + P_2,$$

where V_j denotes the j-th component of the velocity field. Analogously, if we write every component of Eq. (4.2), we obtain

$$\rho_0 \frac{\partial V_j}{\partial t} + \frac{\partial P}{\partial x_j} = 0, \qquad 1 \leq j \leq 2. \tag{4.11}$$

Inside the domain Ω_A, where the PML is situated, we rewrite the equations adding a dissipative or damping term involving the fictitious pressure component P_j and the velocity field V_j, modifying (4.10)-(4.11). Consequently, the system to be solved in Ω_A is

$$\frac{\partial P_j}{\partial t} + \sigma_j P_j + \rho_0 c^2 \frac{\partial V_j}{\partial x_j} = 0, \qquad 1 \leq j \leq 2, \tag{4.12}$$

$$\rho_0 \left(\frac{\partial V_j}{\partial t} + \sigma_j V_j \right) + \frac{\partial P}{\partial x_j} = 0, \qquad 1 \leq j \leq 2, \tag{4.13}$$

$$P = \sum_{j=1}^{2} P_j. \tag{4.14}$$

4.3.2 A physical interpretation

If we denote by $\boldsymbol{\sigma}$ the diagonal tensor of coefficients σ_j, $j = 1, 2$, associated with the j-th component, equation (4.13) can be rewritten as

$$\rho_0 \left(\frac{\partial \boldsymbol{V}}{\partial t} + \boldsymbol{\sigma} \boldsymbol{V} \right) = -\,\mathbf{grad}\, P, \tag{4.15}$$

which is equal to the equation introduced in Chapter 1 for the Darcy's like model in the porous media (where $\boldsymbol{\sigma}$ was the flux resistivity tensor). The unique difference between that model and the system of equations of the PML is the absorbing functions introduced for the pressure field in (4.12).

Integrating (4.12) in time, we obtain

$$P_j = -\rho_0 c^2 \int_0^t \mathrm{e}^{\sigma_j(s-t)} \frac{\partial V_j}{\partial x_j}\, ds.$$

Adding P_1 and P_2, we obtain an explicit expression for the pressure P,

$$P = -\rho_0 c^2 \int_0^t \sum_{j=1}^{2} \left(\mathrm{e}^{\sigma_j(s-t)} \frac{\partial V_j}{\partial x_j} \right) ds. \tag{4.16}$$

If we derive the previous equality two times respect to the time variable, we obtain

$$\frac{\partial^2 P}{\partial t^2} = -\rho_0 c^2 \left(\operatorname{div}\left(\frac{\partial \boldsymbol{V}}{\partial t} + \boldsymbol{\sigma}\boldsymbol{V} \right) + \int_0^t \sum_{j=1}^{2} \left(\sigma_j^2\, \mathrm{e}^{\sigma_j(s-t)} \frac{\partial V_j}{\partial x_j} \right) ds - 2\sum_{j=1}^{2} \sigma_j \frac{\partial V_j}{\partial x_j} \right). \tag{4.17}$$

Finally, if we take into account (4.15)-(4.17), we obtain a time-formulation of the PML in terms of the pressure field,

$$\begin{aligned} \frac{\partial^2 P}{\partial t^2} - c^2 \Delta P - c^2 \int_0^t \sum_{j=1}^{2} \left(\sigma_j^2 e^{\sigma_j(s-t)} \frac{\partial}{\partial x_j} \left(\int_0^s e^{\sigma_j(\tau-s)} \frac{\partial P}{\partial x_j}\, d\tau \right) \right) ds & \\ + 2c^2 \sum_{j=1}^{2} \left(\sigma_j \frac{\partial}{\partial x_j} \left(\int_0^t e^{\sigma_j(s-t)} \frac{\partial P}{\partial x_j}\, ds \right) \right) &= 0. \end{aligned}$$

As a particular case, if the absorbing functions are constant and equal, i.e., if $\sigma_1(x_1) = \sigma_2(x_2) = \sigma$, in the domains where they are not null, then we can rewrite the previous PML equation in terms of the pressure field in a simpler form. In fact, the system of equations (4.12)-(4.14) leads to

$$\rho_0 \left(\frac{\partial \boldsymbol{V}}{\partial t} + \sigma \boldsymbol{V} \right) = -\,\mathbf{grad}\, P, \tag{4.18}$$

$$\frac{\partial P}{\partial t} + \sigma P = -\rho_0 c^2 \operatorname{div} \boldsymbol{V}. \tag{4.19}$$

Integrating (4.18) with respect to the time variable, we have

$$\boldsymbol{V} = -\frac{1}{\rho_0} \int_0^t \mathrm{e}^{\sigma(s-t)}\, \mathbf{grad}\, P\, ds, \tag{4.20}$$

and, substituting this expression in (4.19) and deriving with respect to time,

$$\frac{\partial^2 P}{\partial t^2} + \sigma \frac{\partial P}{\partial t} - c^2 \Delta P + \operatorname{div}\left(c^2 \sigma \int_0^t \mathrm{e}^{\sigma(s-t)} \, \mathbf{grad}\, P \; ds \right) = 0. \tag{4.21}$$

As a conclusion, we observe that the PML equation written in terms of the pressure has a damping term depending linearly on σ and, as in the case of materials with memory, the pressure field at time $t = T$ depends on the pressure fields in the interval $0 \le t < T$. Moreover, let us remark that, obviously, if $\sigma = 0$ then we recover the wave equation.

4.3.3 Time-harmonic equations

Now we rewrite the system of equations (4.12)-(4.14) in the frequency domain. If we assume that

$$P(\boldsymbol{x}, t) = \operatorname{Re}(p(\boldsymbol{x}) \, \mathrm{e}^{-i\omega t}), \;\; P_j(\boldsymbol{x}, t) = \operatorname{Re}(p_j(\boldsymbol{x}) \, \mathrm{e}^{-i\omega t}), \boldsymbol{V}(\boldsymbol{x}, t) = \operatorname{Re}(\boldsymbol{v}(\boldsymbol{x}) \, \mathrm{e}^{-i\omega t}),$$

then the PML equations (4.12)-(4.14) turn into

$$p_j = -\frac{\rho_0 c^2}{\sigma_j - i\omega} \frac{\partial v_j}{\partial x_j}, \tag{4.22}$$

$$v_j = \frac{1}{\rho_0(\sigma_j - i\omega)} \frac{\partial p}{\partial x_j}, \tag{4.23}$$

$$p = p_1 + p_2. \tag{4.24}$$

By substituting (4.23) in (4.22),

$$p_j = -c^2 \frac{1}{\sigma_j - i\omega} \frac{\partial}{\partial x_j} \left[\frac{1}{\sigma_j - i\omega} \frac{\partial p}{\partial x_j} \right], \qquad 1 \le j \le 2,$$

and then, using this expression in (4.24), we obtain

$$-\frac{\omega^2}{c^2} p - \sum_{j=1}^{2} \frac{i\omega}{\sigma_j - i\omega} \frac{\partial}{\partial x_j} \left[\frac{i\omega}{\sigma_j - i\omega} \frac{\partial p}{\partial x_j} \right] = 0. \tag{4.25}$$

Following the ideas introduced in [47], we can define the complex change of variable

$$\hat{x}_j(x_j) = x_j + \frac{i}{\omega} \int_0^{x_j} \sigma_j(s) ds, \qquad 1 \le j \le 2, \tag{4.26}$$

so that formally we recover the weights that arise in (4.25) using its derivatives, i.e.,

$$\frac{\partial x_j}{\partial \hat{x}_j} = \frac{-i\omega}{\sigma_j(x_j) - i\omega}.$$

Hence the PML equation (4.25) can be seen as the Helmholtz equation in a new complex coordinate system $\hat{\boldsymbol{x}} = (\hat{x}_1, \hat{x}_2)$, since we can rewrite Eq. (4.25) formally as

$$-\frac{\omega^2}{c^2} p - \sum_{j=1}^{2} \frac{\partial^2 p}{\partial \hat{x}_j^2} = 0.$$

So, the construction of the PML equation can be understood as a complex stretching of coordinates. However, let us remark that we will not use this formal property for any derivation of the theoretical results on PML through this thesis.

Finally, we introduce some notation for the weights of the PML equation that will be used through the next chapters. We define $\gamma(x_j),\ 1 \leq j \leq 2$ as

$$\gamma_j(x_j) := \frac{\sigma_j(x_j) - i\omega}{-i\omega} = 1 + \frac{i}{\omega}\sigma_j(x_j).$$

Now, if we assume an external harmonic source, $F(\boldsymbol{x}, t) = \operatorname{Re}(f(\boldsymbol{x})\,\mathrm{e}^{-i\omega t})$, such that $\operatorname{supp} f \subset \Omega_{\mathrm{F}}$, the equation to solve in the PML domain as well as in the fluid domain is

$$-\frac{\omega^2}{c^2} p - \sum_{j=1}^{2} \frac{1}{\gamma_j} \frac{\partial}{\partial x_j} \left[\frac{1}{\gamma_j} \frac{\partial p}{\partial x_j} \right] = f \qquad \text{in } \mathbb{R}^2. \tag{4.27}$$

Infinite thickness layer with a bounded absorbing function

In order to close the system of equations of the time-harmonic source problem with PML layers, (4.27), we need a radiation boundary condition, uniform in all the directions, which substitutes the classical Sommerfeld's condition. We take a homogeneous Dirichlet condition at infinity. Hence, the source problem stated in the whole space $\mathbb{R}^2$ written in terms of the pressure field is the following:

Given an acoustic source f, with compact support contained in Ω_{F}, find the pressure field p that satisfies

$$-k^2 p - \sum_{j=1}^{2} \frac{1}{\gamma_j} \frac{\partial}{\partial x_j} \left[\frac{1}{\gamma_j} \frac{\partial p}{\partial x_j} \right] = f \qquad \text{in } \mathbb{R}^2, \tag{4.28}$$

$$\lim_{|\boldsymbol{x}| \to \infty} p(\boldsymbol{x}) = 0, \tag{4.29}$$

where $k = \omega / c$ is the wavenumber.

For example, if we suppose that the source is a monopole supported at the point $\boldsymbol{d} = (d_1, d_2) \in \Omega_{\mathrm{F}}$, then $f = -i\omega\rho_0 Q \delta_{\boldsymbol{d}}$. Straightforward computations show that a solution of (4.28)-(4.29) is

$$p(\boldsymbol{x}) = \frac{\omega \rho_0 Q}{4} \, \mathrm{H}_0^{(1)}(k \hat{r}_{\boldsymbol{d}}(\boldsymbol{x})), \tag{4.30}$$

where $\hat{r}_{\boldsymbol{d}}(\boldsymbol{x}) = \sqrt{(\hat{x}_1(x_1) - d_1)^2 + (\hat{x}_2(x_2) - d_2)^2}$.

From the complex stretching of coordinates, since $\hat{x}_1(x_1) = x_1$ if $x_1 \in (-a, a)$ and $\hat{x}_2(x_2) = x_2$ if $x_2 \in (-b, b)$, it is immediate to check that the fundamental solutions given by (4.9) and (4.30) coincide in the fluid domain Ω_{F}.

In general, the exact solution of the original scattering problem is recovered from the PML problem if the physical domain of interest is surrounded by an unbounded PML layer (see [52]).

Finite-thickness layer with a singular absorbing function

Now we consider the more realistic case of a bounded PML domain.

We assume that the linear acoustic equations (4.1)-(4.3) are satisfied in

$$\Omega_{\mathrm{F}} = (-a, a) \times (-b, b),$$

whereas the PML is situated in the bounded domain

$$\Omega_{\mathrm{A}} = [-a^\star, a^\star] \times [-b^\star, b^\star] \setminus \Omega_{\mathrm{F}},$$

where $a < a^\star$ and $b < b^\star$. We denote by $\Gamma_{\mathrm{D}} = \partial\Omega_{\mathrm{A}} \setminus \partial\Omega_{\mathrm{F}}$ the exterior artificial boundary where the PML domain is truncated (see Figure 4.1).

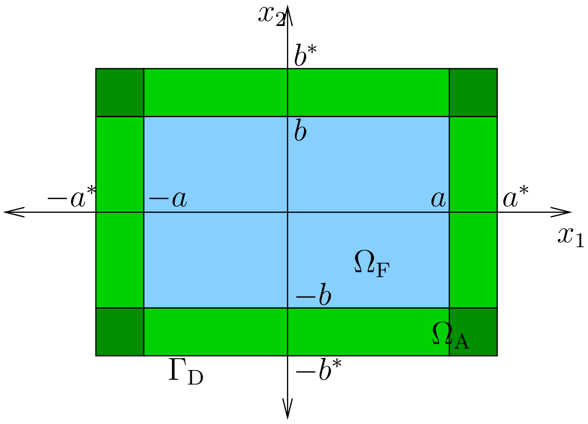

Figure 4.1: Cartesian PML stated in a two-dimensional bounded domain.

In this case the analogous to problem (4.28)-(4.29) is the following:

Given an acoustic source f with compact support in Ω_{F}, find the pressure filed p that satisfies

$$-k^2 p - \sum_{j=1}^{2} \frac{1}{\gamma_j} \frac{\partial}{\partial x_j} \left[\frac{1}{\gamma_j} \frac{\partial p}{\partial x_j} \right] = f \qquad \mathit{in}\ \Omega_{\mathrm{A}} \cup \Omega_{\mathrm{F}}, \tag{4.31}$$

$$p = 0 \qquad \mathit{on}\ \Gamma_{\mathrm{D}}. \tag{4.32}$$

It is well-known that since the PML domain has been truncated, spurious reflections arise in the solution of the classical PML problem with standard bounded absorbing functions. So it does not coincide any more with the original solution of the Helmholtz problem stated in the unbounded domain. This drawback can be avoided by using singular absorbing functions.

More precisely, we state the same two-dimensional Cartesian PML equations involving the absorbing coefficients σ_j. But now, besides assuming that the absorbing functions are non negative, smooth, monotonically increasing and null in Ω_{F}, we suppose that they are not integrable, so that

$$\lim_{|x_1|\to|a^\star|} \sigma_1(x_1) = +\infty,$$
$$\lim_{|x_2|\to|b^\star|} \sigma_2(x_2) = +\infty,$$

Through the rest of this part of the thesis, we will focus our attention on PMLs based on this kind of singular absorbing functions.

In this case, using the same source as in the previous section, namely $f = -i\omega\rho_0 Q\delta_{\boldsymbol{d}}$, then it is easy to check that a solution of problem (4.31)-(4.32) is

$$p(\boldsymbol{x}) = \frac{\omega\rho_0 Q}{4}\,\mathrm{H}_0^{(1)}(k\hat{r}_{\boldsymbol{d}}(\boldsymbol{x})), \tag{4.33}$$

where $\hat{r}_{\boldsymbol{d}}(\boldsymbol{x}) = \sqrt{(\hat{x}_1(x_1) - d_1)^2 + (\hat{x}_2(x_2) - d_2)^2}$.

As in the previous case where the PML domain was unbounded, since $\hat{x}_1(x_1) = x_1$ if $x_1 \in (-a, a)$ and $\hat{x}_2(x_2) = x_2$ if $x_2 \in (-b, b)$, it is immediate to check that the fundamental solutions given by (4.9) and (4.33) coincide in the fluid domain Ω_{F}. This kind of results are proved theoretically in Chapter 6 (see also [33]) for the PML equation written in radial coordinates for time-harmonic scattering problems.

4.4 Plane wave analysis of the PMLs

We consider a simple problem which will provide valuable information for the design of an efficient PML method: the propagation of two-dimensional acoustic plane waves with oblique incidence. With this problem, we also illustrate the ideas introduced in the previous subsection.

Consider the following time-harmonic problem posed in the right half-space:

$$\begin{cases} \Delta p + k^2 p = 0, & x_1 > 0,\ x_2 \in \mathbb{R}, \\ p(0, x_2) = \mathrm{e}^{ik_2 x_2}, & x_2 \in \mathbb{R}, \\ \displaystyle\lim_{x_1\to+\infty}\left(\frac{\partial p}{\partial x_1} - ik_1 p\right) = 0, & \end{cases} \tag{4.34}$$

where $k = \omega/c$ is the wave number, $k_1 = k\cos\theta$ and $k_2 = k\sin\theta$, with θ being the incidence angle. It is well-known that the solution of this problem is the plane wave

$$p(x_1, x_2) = \mathrm{e}^{i(k_1 x_1 + k_2 x_2)}.$$

We introduce a PML in the vertical strip $a < x_1 < a^*$, to truncate the unbounded domain in the x_1-direction (see Figure 4.2). The strip $0 < x_1 < a$ is the so called 'physical domain', i.e., the domain where we are interested in computing the solution of problem (4.34).

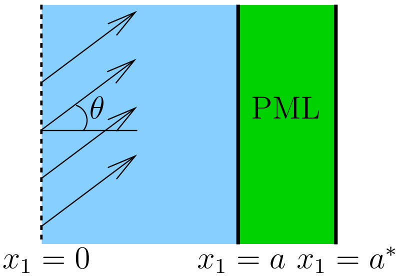

Figure 4.2: PML in the x_1-direction for plane waves with oblique incidence.

We consider a variable absorption coefficient σ in the PML. This coefficient is allowed to be a function of the variable x_1; constant, linear or quadratic 'absorbing functions' are the typical choices (see, for instance, [16, 22, 52]). In this case, we allow for any arbitrary non-negative absorbing function.

In order to solve the problem with PML layers, we distinguish two pressure fields: we denote by p_{F} and p_{A} the restriction of the pressure field to the fluid domain and to the PML, respectively. This approach allows us to write explicitly the spurious reflection that the bounded PML domain produces in the fluid domain.

Thus, the amplitudes of the pressure waves in the physical domain, p_{F}, and in the PML, p_{A}, are the solution of the following equations:

$$\begin{cases} \Delta p_{\mathrm{F}} + k^2 p_{\mathrm{F}} = 0, \qquad 0 < x_1 < a, \\ \dfrac{1}{\gamma_1}\dfrac{\partial}{\partial x_1}\left(\dfrac{1}{\gamma_1}\dfrac{\partial p_{\mathrm{A}}}{\partial x_1}\right) + \dfrac{\partial^2 p_{\mathrm{A}}}{\partial x_2^2} + k^2 p_{\mathrm{A}} = 0, \qquad a < x_1 < a^*, \\ p_{\mathrm{F}}(0, x_2) = \mathrm{e}^{ik_2x_2}, \\ p_{\mathrm{F}}(a, x_2) = p_{\mathrm{A}}(a, x_2), \\ \dfrac{\partial p_{\mathrm{F}}}{\partial x_1}(a, x_2) = \dfrac{1}{\gamma_1(a)}\dfrac{\partial p_{\mathrm{A}}}{\partial x_1}(a, x_2), \\ p_{\mathrm{A}}(a^*, x_2) = 0, \end{cases}$$

with, as it was defined in Section 4.3.3,

$$\gamma_1(x_1) := \begin{cases} 1, & \text{if } 0 < x_1 < a, \\ 1 + \dfrac{i}{\omega}\sigma_1(x_1), & \text{if } a \le x_1 < a^*. \end{cases}$$

As we have already shown in the previous subsection, if we introduce the complex change of variable

$$\widetilde{x}_1(x_1) = \int_0^{x_1} \gamma_1(s) = x_1 + \frac{i}{\omega}\int_a^{x_1} \sigma_1(s), \qquad x_1 \in [a, a^*), \tag{4.35}$$

then

$$\frac{\partial \widetilde{x}_1}{\partial x_1} = \gamma_1 \qquad \text{and} \qquad \frac{\partial}{\partial \widetilde{x}_1} = \frac{1}{\gamma_1}\frac{\partial}{\partial x_1},$$

and hence, if we denote $\hat{p}_{\mathrm{A}}(\widetilde{x}_1, x_2) = p_{\mathrm{A}}(x_1, x_2)$, then we have

$$\frac{1}{\gamma_1}\frac{\partial}{\partial x_1}\left(\frac{1}{\gamma_1}\frac{p_{\mathrm{A}}}{\partial x_1}\right) + \frac{\partial^2 p_{\mathrm{A}}}{\partial x_2^2} + k^2 p_{\mathrm{A}} = 0 \quad \Longleftrightarrow \quad \frac{\partial^2 \hat{p}_{\mathrm{A}}}{\partial \widetilde{x}_1^2} + \frac{\partial^2 \hat{p}_{\mathrm{A}}}{\partial x_2^2} + k^2 \hat{p}_{\mathrm{A}} = 0.$$

Since we have recovered formally the Helmholtz equation, the solution of the PML problem can be written as superposition of plane waves:

$$\begin{cases} p_{\mathrm{F}}(x_1, x_2) = \left(I\, \mathrm{e}^{ik_1 x_1} + R\, \mathrm{e}^{-ik_1 x_1}\right) \mathrm{e}^{ik_2 x_2}, & x_1 \in (0, a), \\ \hat{p}_{\mathrm{A}}(\widetilde{x}_1, x_2) = \left(T\, \mathrm{e}^{ik_1 \widetilde{x}_1} + R_{\mathrm{A}}\, \mathrm{e}^{-ik_1 \widetilde{x}_1}\right) \mathrm{e}^{ik_2 x_2}, & x_1 \in [a, a^*), \end{cases}$$

where I is the amplitude of the incident wave, T that of the wave transmitted to the PML, and R and R_{A} are the amplitudes of the reflected waves in the physical domain and in the absorbing layer, respectively.

By substituting (4.35) in the last equation, we can write the solution in the absorbing layer in the following equivalent form:

$$p_{\mathrm{A}}\left(x_1, x_2\right) = \left[T\, \mathrm{e}^{ik_1 x_1}\, \mathrm{e}^{-\frac{\cos\theta}{c}\int_a^{x_1}\sigma_1(s)} + R_{\mathrm{A}}\, \mathrm{e}^{-ik_1 x_1}\, \mathrm{e}^{\frac{\cos\theta}{c}\int_a^{x_1}\sigma_1(s)}\right] \mathrm{e}^{ik_2 x_2}.$$

Hence, from the boundary condition at $x_1 = 0$, we obtain

$$I = 1 - R,$$

and, from the transmission conditions at $x_1 = a$,

$$R = R_{\mathrm{A}} \qquad \text{and} \qquad I = T.$$

Notice that the latter implies that no spurious reflections arise at $x_1 = a$ (which is the main feature of the PML technique); the terms involving R and R_{A} arise as a consequence of the waves reflected at $x_1 = a^*$. Finally, the homogeneous Dirichlet boundary condition at $x_1 = a^*$ yields

$$R = R_{\mathrm{A}} = \frac{\mathrm{e}^{2ik_1 a^*}}{\mathrm{e}^{2ik_1 a^*} - \mathrm{e}^{\frac{2\cos\theta}{c}\int_a^{a^*}\sigma_1(s)}}. \tag{4.36}$$

Summarizing, we have obtained the following analytical expression for the solution to the PML problem above:

$$\begin{cases} p_{\mathrm{F}}(x_1, x_2) = \left[(1 - R_{\mathrm{A}})\, \mathrm{e}^{ik_1 x_1} + R_{\mathrm{A}}\, \mathrm{e}^{-ik_1 x_1}\right] \mathrm{e}^{ik_2 x_2}, & x_1 \in (0, a), \\ p_{\mathrm{A}}(x_1, x_2) = \left[(1 - R_{\mathrm{A}})\, \mathrm{e}^{ik_1 x_1}\, \mathrm{e}^{-\frac{\cos\theta}{c}\int_a^{x_1}\sigma_1(s)} + R_{\mathrm{A}}\, \mathrm{e}^{-ik_1 x_1}\, \mathrm{e}^{\frac{\cos\theta}{c}\int_a^{x_1}\sigma_1(s)}\right] \mathrm{e}^{ik_2 x_2}, & \\ & x_1 \in [a, a^*). \end{cases}$$

Expression (4.36) for R_{A} shows that the larger the integral $\int_a^{a^*} \sigma_1(s)$ the closer R_{A} to zero and, consequently, the closer p_{F} to the solution, p, of problem (4.34) in the physical domain. Indeed, straightforward computations lead to

$$\int_0^a |p(x_1,x_2) - p_{\mathrm{F}}(x_1,x_2)|^2 \, dx_1 = |R_{\mathrm{A}}|^2 \, \frac{2k_1 a - \sin(2k_1 a)}{k_1}.$$

Classical PML techniques rely on taking a bounded absorbing function σ, such that its integral be sufficiently large. We propose instead to use an unbounded σ such that

$$\int_a^{a^*} \sigma(s) = +\infty.$$

In this case, $R_{\mathrm{A}} = 0$ and, consequently, the resulting p_{F} will coincide exactly with the solution p of problem (4.34) in the physical domain.

In order to illustrate this behavior we take the following parameters: $a = 0.5$ m, $a^* = 0.6$ m, $\omega = 1200$ rad/s, $c = 340$ m/s, and $\theta = \frac{3\pi}{8}$ rad. We compare two examples of the above mentioned absorbing functions: a classical choice, namely the quadratic function taking the value σ^* at $x_1 = a^*$,

$$\sigma_1(x_1) = \sigma^{(\mathrm{Q})}(x_1) = \frac{\sigma^*}{(a^*-a)^2}(x_1 - a)^2, \qquad x_1 \in [a, a^*), \tag{4.37}$$

and the following unbounded function with unbounded integral in $[a, a^*)$,

$$\sigma_1(x_1) = \sigma^{(\mathrm{U})}(x_1) = \frac{c}{a^* - x_1}, \qquad x_1 \in [a, a^*). \tag{4.38}$$

In Figures 4.3 and 4.4 we can see that, when choosing the quadratic function, p_{F} approximates the exact solution p when σ^* becomes large. The reflection coefficient is, in this case, $R_{\mathrm{A}} = 0.26$ for $\sigma^* = 50c$, and $R_{\mathrm{A}} = 2.88 \times 10^{-6}$ for $\sigma^* = 500c$. In the same Figure we can see that the error is 0 when choosing the unbounded absorbing function, $\sigma^{(\mathrm{U})}$.

In Figure 4.5 we show the dependence of the reflection coefficient R_{A}, with respect to the angle of incidence of the plane wave, when $\sigma^{(\mathrm{Q})}$ is used. It is important to emphasize that, in this case, the reflection coefficient (and hence the error) increases when taking a larger angle of incidence, whereas the error is null, for any angle of incidence, when $\sigma^{(\mathrm{U})}$ is used.

Analogously, we show in Figure 4.6 the dependency of R_{A} with respect to the frequency ω when $\sigma^{(\mathrm{Q})}$ is used. For this test we have taken $\theta = 0.99\frac{\pi}{2}$ as angle of incidence (very close to the critical value $\frac{\pi}{2}$). We observe that R_{A} achieves periodically maximum values for certain high frequencies. Again, we want to remark that, taking the unbounded absorbing function $\sigma^{(\mathrm{U})}$ in the PML, we recover $R_{\mathrm{A}} = 0$, for any value of the frequency.

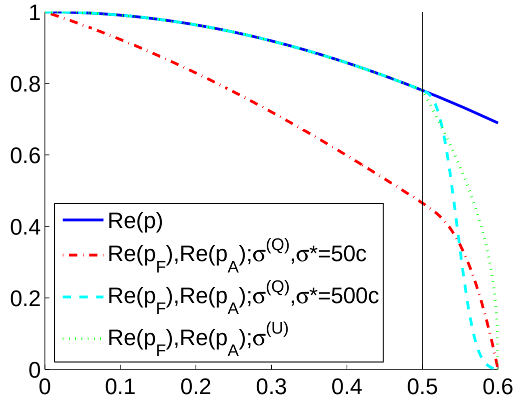

Figure 4.3: Real part of exact and approximated pressures for $\theta = 3\pi/8$.

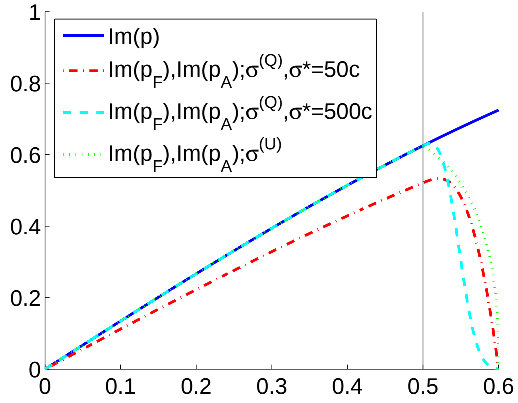

Figure 4.4: Imaginary part of exact and approximated pressures for $\theta = 3\pi/8$.

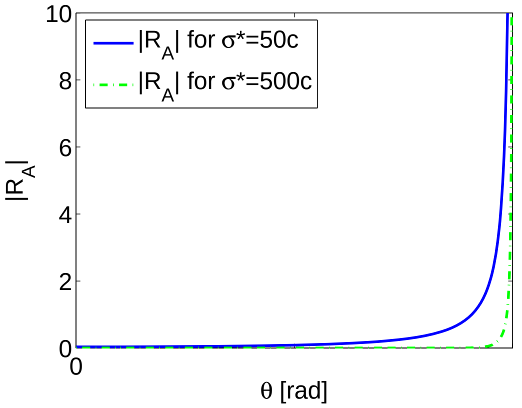

Figure 4.5: Absolute value of the reflection coefficient for $\sigma^{(\mathrm{Q})}$ versus incidence angle.

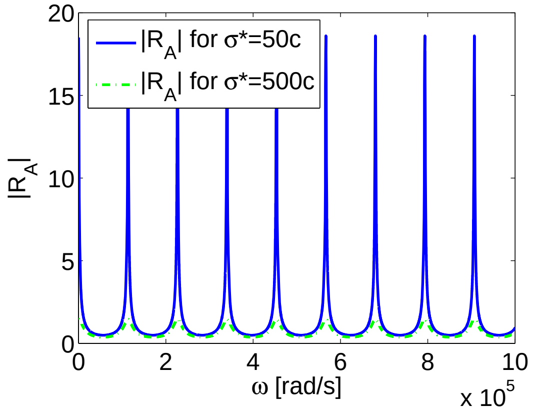

Figure 4.6: Absolute value of the reflection coefficient for $\sigma^{(\mathrm{Q})}$ versus frequency.

Chapter 5

An optimal PML in Cartesian coordinates

Contents

5.1 Introduction

We have shown in Chapter 4, in the plane wave analysis of a bounded PML and also for the fundamental solution of the Helmholtz equations that we can recover the solution of the original source problem with a bounded PML layer with singular absorbing functions. Now, through this chapter we are going to use the same ideas to check that we also recover accurate numerical results for time-harmonic scattering problems using an absorbing function with unbounded integral on the PML.

In this chapter, we consider Cartesian perfectly matched layers. We report numerical evidence that allows us to choose a particularly convenient non-integrable absorbing function. This function only depends on the sound speed of the fluid. We show that this choice leads to a robust PML method, easy to implement in a finite element code. We assess the efficiency of our choice by comparing it with classical bounded absorbing functions in some test problems. We also report the numerical results obtained for some realistic examples.

The outline of this chapter is as follows. In Section 5.2 we recall the classical two-dimensional scattering problem with Cartesian perfectly matched layers. In Section 5.3 we describe a finite element method to solve this problem. We show that for the resulting finite element problem to be well posed, it is necessary to impose some constraints on the absorbing function. In Section 5.4 we report the results of some numerical tests which show us how to choose the most convenient non-integrable absorbing function. In Section 5.5 we point out the advantages of our choice as compared with classical PMLs based on quadratic absorbing functions. In Section 5.6 we report the numerical results obtained with our PML technique applied to some realistic wave propagation problems. Finally, in an appendix, we show how the element matrices can be computed either by explicit integration or by means of quadrature rules.

5.2 The time-harmonic acoustic scattering problem

We deal with the time-harmonic acoustic scattering problem in an unbounded exterior 2D domain. Let Ω be a bounded domain of $\mathbb{R}^2$ occupied by an obstacle to the propagation of acoustic waves; we assume the obstacle has a totally reflecting boundary Γ, with outer normal unit vector $\boldsymbol{n}$ (see Figure 5.1). Our goal is to solve the following exterior Helmholtz problem with Neumann boundary data:

$$\begin{cases} \Delta p + k^2 p = 0 \qquad \text{in } \mathbb{R}^2 \setminus \Omega, \\ \dfrac{\partial p}{\partial \boldsymbol{n}} = g \qquad \text{on } \Gamma, \\ \displaystyle\lim_{r\to\infty} \sqrt{r}\left(\frac{\partial p}{\partial r} - ikp\right) = 0. \end{cases} \tag{5.1}$$

Once more, p is the unknown amplitude of the pressure wave and $k = \omega/c$ is the wave number, with ω being the angular frequency of the waves and c the sound speed of the fluid in the exterior domain.

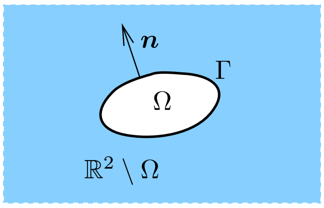

Figure 5.1: Two-dimensional unbounded domain.

We introduce perfectly matched layers (PML) on the x_1 and x_2 directions to truncate the unbounded domain, as shown in Figure 5.2. The inner rectangle contains the obstacle Ω as well as the physical domain Ω_{F}, i.e., the subdomain occupied by the fluid surrounding the obstacle where we are interested in computing the solution of (5.1).

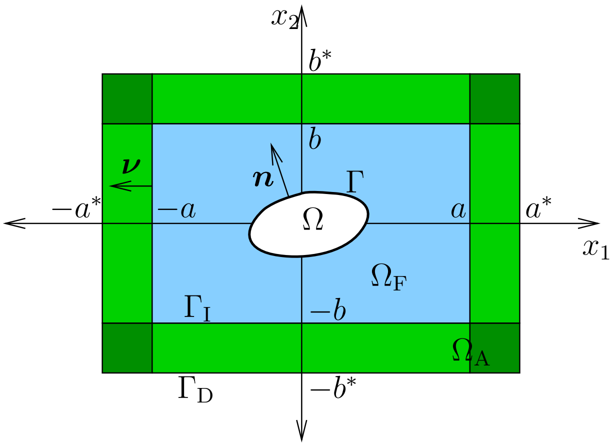

Figure 5.2: Cartesian PML on a two-dimensional domain.

We use the notation introduced in Figure 5.2. In particular, Ω_{A} denotes the absorbing layer, Γ_{I} the interface between the physical domain and the layer, Γ_{D} the outer boundary, and $\boldsymbol{\nu} = (\nu_1, \nu_2)$ the unit normal vector to Γ_{I} outward to Ω_{F}.

As we have done for the plane wave analysis of the PMLs in Subsection 4.4, we consider now variable absorption coefficients, σ_1 and σ_2, acting on the vertical and horizontal layers, respectively; moreover, both absorption coefficients act in the corner layers. These coefficients, σ_1 and σ_2, are allowed to be functions of x_1 and x_2, respectively. Although constant, linear or quadratic functions are the typical choices, we proceed as in the previous section, and allow for arbitrary non-negative absorbing functions $\sigma_1(|x_1|)$ and $\sigma_2(|x_2|)$.

The amplitudes of the pressure waves in the physical domain, p_{F}, and in the PML, p_{A}, are solution of the following equations (see, for instance, [52]):

$$\left\{\begin{array}{ll}\Delta p_{\mathrm{F}} + k^2 p_{\mathrm{F}} = 0 \qquad \text{in } \Omega_{\mathrm{F}}, & \\ \dfrac{1}{\gamma_1}\dfrac{\partial}{\partial x}\left(\dfrac{1}{\gamma_1}\dfrac{\partial p_{\mathrm{A}}}{\partial x}\right) + \dfrac{1}{\gamma_2}\dfrac{\partial}{\partial y}\left(\dfrac{1}{\gamma_2}\dfrac{\partial p_{\mathrm{A}}}{\partial y}\right) + k^2 p_{\mathrm{A}} = 0 & \text{in } \Omega_{\mathrm{A}}, \\ \dfrac{\partial p_{\mathrm{F}}}{\partial \boldsymbol{n}} = g \qquad \text{on } \Gamma, & \\ p_{\mathrm{F}} = p_{\mathrm{A}} \qquad \text{on } \Gamma_{\mathrm{I}}, & \\ \dfrac{\partial p_{\mathrm{F}}}{\partial \nu_x} + \dfrac{\partial p_{\mathrm{F}}}{\partial \nu_y} = \dfrac{1}{\gamma_1}\dfrac{\partial p_{\mathrm{A}}}{\partial \nu_x} + \dfrac{1}{\gamma_2}\dfrac{\partial p_{\mathrm{A}}}{\partial \nu_y} \qquad \text{on } \Gamma_{\mathrm{I}}, & \\ p_{\mathrm{A}} = 0 \qquad \text{on } \Gamma_{\mathrm{D}}, & \end{array}\right. \tag{5.2}$$

where

$$\gamma_1(x_1) = \begin{cases} 1, & \text{if } |x_1| < a, \\ 1 + \dfrac{i}{\omega}\sigma_1\left(|x_1|\right), & \text{if } a \leq |x_1| < a^*, \end{cases}$$

and

$$\gamma_2(x_2) = \begin{cases} 1, & \text{if } |x_2| < b, \\ 1 + \dfrac{i}{\omega}\sigma_2\left(|y|\right), & \text{if } b \leq |x_2| < b^*. \end{cases}$$

The main goal of this chapter is to determine how to choose the absorbing functions σ_1 and σ_2, so that p_{F} be an approximation as close as possible to the solution p of problem (5.1) in the physical domain. According to the results of the previous section, the natural candidates are unbounded functions σ_1 and σ_2 such that

$$\int_a^{a^*} \sigma_1(s) = +\infty \qquad \text{and} \qquad \int_b^{b^*} \sigma_2(s) = +\infty.$$

5.3 Finite element discretization.

In this section we describe a finite element method for the numerical solution of (5.2) and show that the resulting discrete problem is well posed only for certain unbounded absorbing functions. This will lead to additional constraints on σ_1 and σ_2.

We consider a partition in triangles of the physical domain Ω_{F} and a partition in rectangles of the absorbing layer Ω_{A}, matching on the common interface Γ_{I} as shown in Figure 5.3. As usual, h denotes the mesh-size.

The reason why we use such hybrid meshes is that triangles are more adequate to fit the boundary of the obstacle, whereas rectangles will allow us to compute explicitly the integrals involving the absorbing function appearing in the elements in the layer. This is not strictly necessary, since these integrals can also be efficiently computed by means of standard quadrature rules as shown in the appendix. However, in this chapter, we will mainly consider exact integration to be able to assess the accuracy of the proposed PML independently of quadrature errors.

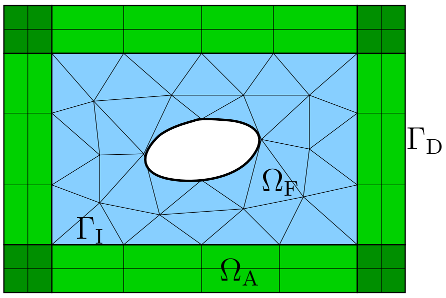

Figure 5.3: Hybrid mesh on PML and physical domain.

We will compute approximations p_F^h and p_A^h of the pressure amplitudes in the physical domain and in the absorbing layer, respectively, by using linear triangular finite elements for the former and bilinear rectangular finite elements for the latter. The degrees of freedom defining the finite element solution are the values of p_F^h and p_A^h at the vertices of the elements. Notice that because of the transmission condition $p_\mathrm{F} = p_\mathrm{A}$ on Γ_I, the values of p_F^h and p_A^h must coincide at the vertices on the interface.

Moreover, we impose the Dirichlet boundary condition $p_\mathrm{A}^h = 0$ on Γ_D to the finite element solution. Hence, p_A^h does not have degrees of freedom on the outer boundary. This fact will be essential for the resulting discrete problem to be well posed.

Standard arguments in this finite element framework lead to the following discretization of problem (5.2)written in weak form:

$$\int_{\Omega_\mathrm{F}} \nabla p_\mathrm{F}^h \cdot \nabla \bar{q}^h \, dx_1 \, dx_2 - \int_{\Omega_\mathrm{F}} k^2 p_\mathrm{F}^h \bar{q}^h \, dx_1 \, dx_2 + \int_{\Omega_\mathrm{A}} \frac{\gamma_2}{\gamma_1} \frac{\partial p_\mathrm{A}^h}{\partial x_1} \frac{\partial \bar{q}^h}{\partial x_1} \, dx_1 \, dx_2$$
$$+ \int_{\Omega_\mathrm{A}} \frac{\gamma_1}{\gamma_2} \frac{\partial p_\mathrm{A}^h}{\partial x_2} \frac{\partial \bar{q}^h}{\partial x_2} \, dx_1 \, dx_2 - \int_{\Omega_\mathrm{A}} k^2 \gamma_1 \gamma_2 p_\mathrm{A}^h \bar{q}^h \, dx_1 \, dx_2 = \int_\Gamma g \bar{q}^h,$$

for all function q^h, continuous in $\Omega_\mathrm{F} \cup \Omega_\mathrm{A}$, piecewise linear in Ω_F, piecewise bilinear in Ω_A, and vanishing on Γ_D.

Once the discrete problem is written in matrix form, it yields a system of linear equations whose unknowns are the nodal values of p_F^h and p_A^h. The entries of the matrix are computed by assembling the element matrices; in particular, the following terms involve the unbounded absorbing functions:

$$\int_K \frac{\gamma_2}{\gamma_1} \frac{\partial N_i}{\partial x_1} \frac{\partial N_j}{\partial x_1} \, dx_1 \, dx_2, \quad \int_K \frac{\gamma_1}{\gamma_2} \frac{\partial N_i}{\partial x_2} \frac{\partial N_j}{\partial x_2} \, dx_1 \, dx_2, \quad \text{and} \quad \int_K k^2 \gamma_1 \gamma_2 N_i N_j \, dx_1 \, dx_2, \tag{5.3}$$

with K being a rectangular element in Ω_A and $\{N_i\}$ the nodal finite element basis.

For the discrete problem to be well posed, it is necessary that all the integrals above be finite, what is not trivial since they involve singular functions, whenever K is a rectangle with one edge lying on the outer boundary Γ_D.

For instance, consider the element K shown in Figure 5.4 (the forthcoming arguments and conclusions hold also true for all other elements with edges lying on Γ_D). Notice that,

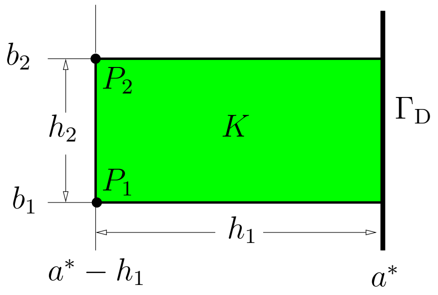

Figure 5.4: Finite element with an edge lying on Γ_{D}.

since p_{A}^h vanishes at the vertices on Γ_{D}, in this element we only need to compute the integrals (5.3) for the nodal functions N_1 and N_2 associated with the vertices denoted by P_1 and P_2, respectively.

These functions are given by

$$N_1(x_1,x_2)=\frac{(x_1-a^*)(x_2-b_2)}{h_1h_2},\qquad N_2(x_1,x_2)=-\frac{(x_1-a^*)(x_2-b_1)}{h_1h_2},$$

and their partial derivatives by

$$\begin{aligned}\frac{\partial N_1}{\partial x_1}(x_1,x_2)&=\frac{x_2-b_2}{h_1h_2}, & \frac{\partial N_2}{\partial x_1}(x_1,x_2)&=-\frac{x_2-b_1}{h_1h_2},\\ \frac{\partial N_1}{\partial x_2}(x_1,x_2)&=\frac{x_1-a^*}{h_1h_2}, & \frac{\partial N_2}{\partial x_2}(x_1,x_2)&=-\frac{x_1-a^*}{h_1h_2}.\end{aligned}$$

Therefore, the integrals in (5.3) can be written as follows:

$$\int_K \frac{\gamma_2}{\gamma_1}\frac{\partial N_i}{\partial x_1}\frac{\partial N_j}{\partial x_1}\,dx_1\,dx_2=\pm\frac{1}{h_1^2h_2^2}\int_{b_1}^{b_2}\gamma_2(x_2)(x_2-b_j)(x_2-b_i)\,dx_2\int_{a^*-h_1}^{a^*}\frac{dx_1}{\gamma_1(x_1)},\tag{5.4}$$

$$\int_K \frac{\gamma_1}{\gamma_2}\frac{\partial N_i}{\partial x_2}\frac{\partial N_j}{\partial x_2}\,dx_1\,dx_2=\pm\frac{1}{h_1^2h_2^2}\int_{b_1}^{b_2}\frac{dx_2}{\gamma_2(x_2)}\int_{a^*-h_1}^{a^*}\gamma_1(x_1)(x_1-a^*)^2\,dx_1,\tag{5.5}$$

$$\begin{aligned}&\int_K \gamma_1\gamma_2 N_iN_j\,dx_1\,dx_2\\ &\quad=-\frac{1}{h_1^2h_2^2}\int_{b_1}^{b_2}\gamma_2(x_2)(x_2-b_j)(x_2-b_i)\,dx_2\int_{a^*-h_1}^{a^*}\gamma_1(x_1)(x_1-a^*)^2\,dx_1.\end{aligned}\tag{5.6}$$

We assume singularities of power type for the absorbing functions:

$$\sigma_1(x_1)=\mathcal{O}\left((a^*-x_1)^{-\alpha}\right)\text{ as } x_1\to a^*,\quad \sigma_2(x_2)=\mathcal{O}\left((b^*-x_2)^{-\alpha}\right)\text{ as } x_2\to b^*.\tag{5.7}$$

Notice that the constraint that σ_1 and σ_2 have unbounded integrals holds true if and only if $\alpha\geq 1$.

From the definitions of γ_1 and γ_2 we have that $\gamma_1(x_1) = \mathcal{O}\left((a^* - |x_1|)^{-\alpha}\right)$ and $\gamma_2(x_2) = \mathcal{O}\left((b^* - |x_2|)^{-\alpha}\right)$. Moreover, $|\gamma_1| \geq 1$ and $|\gamma_2| \geq 1$ and, hence, the integrals of $1/\gamma_1(x_1)$ and $1/\gamma_2(x_2)$ are always finite.

For an element K as that in Figure 5.4, γ_2 is bounded in the interval $[b_1, b_2]$ and, consequently, the integrals involving $\gamma_2(x_2)$ are also finite. Finally, for the integral involving $\gamma_1(x_1)$ we have

$$\int_{a^*-h}^{a^*} \gamma_1(x_1)(x_1 - a^*)^2 \, dx_1 = \int_{a^*-h}^{a^*} \mathcal{O}\left((a^* - x_1)^{2-\alpha}\right) dx_1 < \infty \qquad \Longleftrightarrow \qquad \alpha < 3.$$

As a consequence of this analysis, we will restrict our choice of σ_1 and σ_2 satisfying (5.7) to exponents α such that $1 \leq \alpha < 3$.

5.4 Determination of the absorbing function

In this section we report the numerical experimentation performed to determine the most convenient unbounded absorbing functions. With this purpose, we have applied our PML method with different σ_1 and σ_2 to a scattering problem with known analytical solution and compared the accuracy of the numerical results.

Consider problem (5.1) where the obstacle Ω is the unit circle centered at the origin. Given any inner point (x_1^0, x_2^0) of this circle, it is well known that the function

$$p(x_1, x_2) = \frac{i}{4} \mathrm{H}_0^{(1)} \left(k \sqrt{(x_1 - x_1^0)^2 + (x_2 - x_2^0)^2} \right)$$

satisfies the first and third equations of (5.1). Therefore, if we take $g = \partial p / \partial \boldsymbol{n}$, then p is the unique solution of this problem.

In our experiments we have taken $x_1^0 = 0.5\,\mathrm{m}$, $x_2^0 = 0$, and $k = \omega/c$, with $c = 340\,\mathrm{m/s}$ and different values of the frequency ω. For our computational domain we have taken $a = b = 2.0\,\mathrm{m}$ and $a^* = b^* = 2.25\,\mathrm{m}$ (see Figure 5.5).

We have used uniform refinements of the mesh shown in Figure 5.5; the number N of elements through the thickness of the PML is used to label each mesh.

To measure the accuracy we have computed the relative error in the L^2-norm in Ω_{F}:

$$\mathrm{Error} = \frac{\left(\displaystyle\int_{\Omega_{\mathrm{F}}} \left| p_{\mathrm{F}}^h - p \right|^2 dx_1 \, dx_2 \right)^{1/2}}{\left(\displaystyle\int_{\Omega_{\mathrm{F}}} |p|^2 \, dx_1 \, dx_2 \right)^{1/2}}, \tag{5.8}$$

where p_{F}^h is the numerical solution in the physical domain and p the exact solution.

According to the results of the previous section, it is enough to restrict the analysis to absorbing functions satisfying (5.7) with $1 \leq \alpha < 3$. We have considered the integer powers: $\alpha = 1$ and $\alpha = 2$. In particular, we have tested functions of the following type, where β is a free parameter to be fitted:

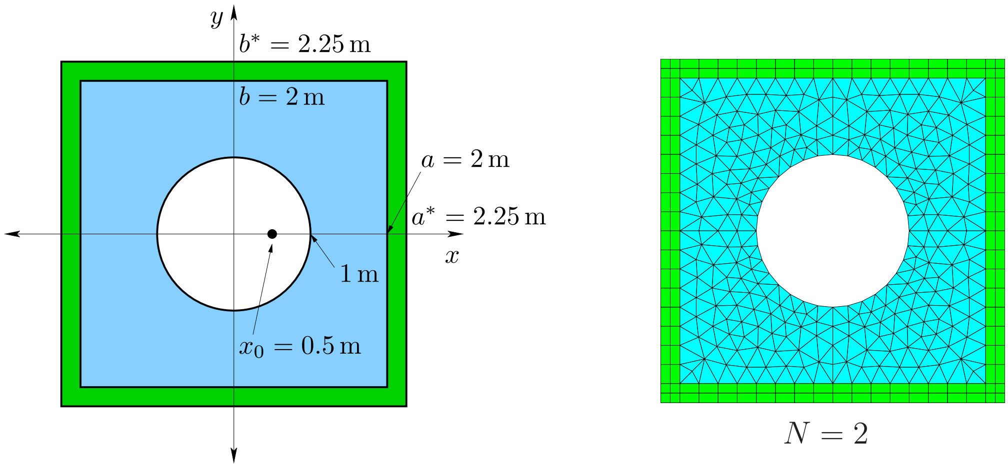

$N = 2$

Figure 5.5: Domains and mesh in the scattering problem.

- **A.**

$$\sigma_1(x_1) = \frac{\beta}{a^* - x_1}, \qquad \sigma_2(x_2) = \frac{\beta}{b^* - x_2};$$

- **B.**

$$\sigma_1(x_1) = \frac{\beta}{(a^* - x_1)^2}, \qquad \sigma_2(x_2) = \frac{\beta}{(b^* - x_2)^2}.$$

Notice that, in both cases, $\sigma_1(a) \neq 0$ and $\sigma_2(b) \neq 0$. Hence, the corresponding coefficients γ_1 and γ_2 will be discontinuous. To avoid eventual side effects of these discontinuities in the coupling conditions on Γ_{I}, we have also considered functions of the following type, which yield continuous γ_1 and γ_2:

- **C.**

$$\sigma_1(x_1) = \frac{\beta}{a^* - x_1} - \frac{\beta}{a^* - a}, \qquad \sigma_2(x_2) = \frac{\beta}{b^* - x_2} - \frac{\beta}{b^* - b},$$

- **D.**

$$\sigma_1(x_1) = \frac{\beta}{(a^* - x_1)^2} - \frac{\beta}{(a^* - a)^2}, \qquad \sigma_2(x_2) = \frac{\beta}{(b^* - x_2)^2} - \frac{\beta}{(b^* - b)^2}.$$

In each case, we have fitted the parameter β so as to minimize the error. Figs. 5.6 to 5.11 show the results obtained with each type of absorbing functions and a range of values of β. We have used three meshes with refinement levels $N = 2$, 4, and 8, which have 464, 1720, and 6768 vertices, respectively. We report the results obtained with two frequencies: $\omega = 250\,\mathrm{rad/s}$ and $\omega = 750\,\mathrm{rad/s}$.

We report, in Table 5.1, the minimal relative errors and the optimal values of β determined for each type of absorbing function and each of the three meshes. It can be clearly seen from this table that the smallest errors are always attained for a function of **A** type

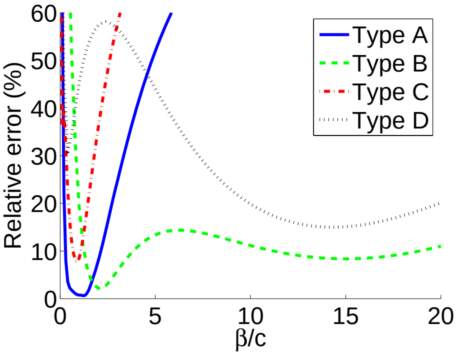

Figure 5.6: Relative errors for PML with different unbounded absorbing functions. Mesh: $N = 2$; $\omega = 250\,\mathrm{rad/s}$.

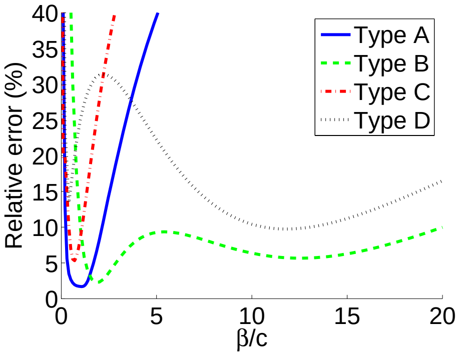

Figure 5.7: Relative errors for PML with different unbounded absorbing functions. Mesh: $N = 2$; $\omega = 750\,\mathrm{rad/s}$.

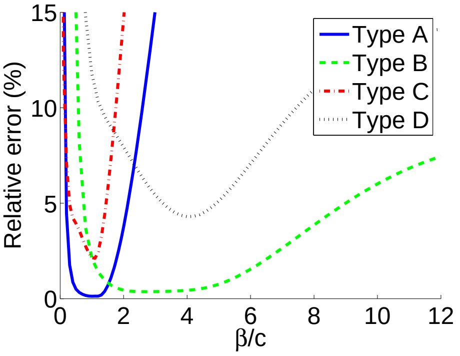

Figure 5.8: Relative errors for PML with different unbounded absorbing functions. Mesh: $N = 4$; $\omega = 250\,\mathrm{rad/s}$.

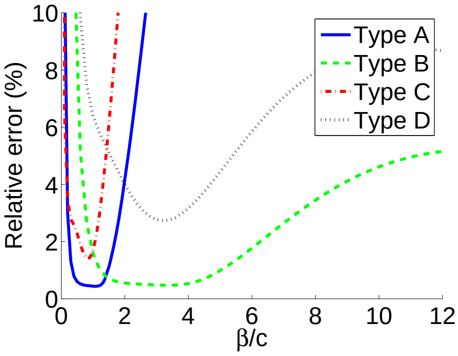

Figure 5.9: Relative errors for PML with different unbounded absorbing functions. Mesh: $N = 4$; $\omega = 750\,\mathrm{rad/s}$.

with the parameter $\beta \approx c$. To allow for comparison, we also include in the table the errors for this choice; namely,

$$\sigma_1(x_1) = \frac{c}{a^* - x_1}, \qquad \sigma_2(x_2) = \frac{c}{b^* - x_2}. \tag{5.9}$$

Let us remark that, for each mesh, the CPU time needed to solve the problem is essentially the same for the four types of absorbing functions. The condition numbers of the system matrices remain basically of the same order of magnitude for all of the choices, too.

As a definite conclusion of this experimentation, we propose to use the absorbing functions (5.9). Notice that an additional advantage of this proposal is that the resulting PML method does not need any parameter to be determined.

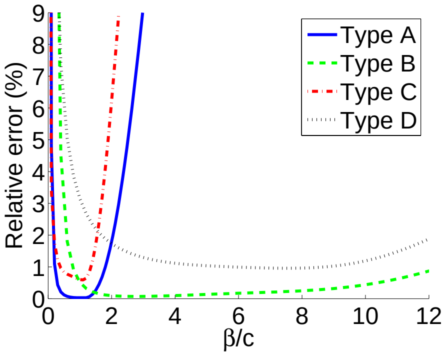

Figure 5.10: Relative errors for PML with different unbounded absorbing functions. Mesh: $N = 8$; $\omega = 250\,\mathrm{rad/s}$.

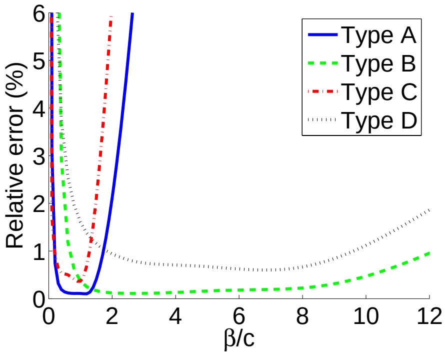

Figure 5.11: Relative errors for PML with different unbounded absorbing functions. Mesh: $N = 8$; $\omega = 750\,\mathrm{rad/s}$.

Table 5.1: Minimal errors and optimal values of the parameter β for PML with different unbounded absorbing functions.

		$\omega = 250\,\mathrm{rad/s}$		$\omega = 750\,\mathrm{rad/s}$	
Mesh	Type	β	Error(%)	β	Error(%)
$N = 2$	**A**	$1.2\,c$	0.646	$1.1\,c$	1.696
	B	$2.2\,c$	2.160	$1.8\,c$	2.305
	C	$0.9\,c$	7.646	$0.7\,c$	5.318
	D	$14.4\,c$	14.995	$11.8\,c$	9.739
	(5.9)	c	0.763	c	1.700
$N = 4$	**A**	$1.0\,c$	0.131	$1.1\,c$	0.437
	B	$2.6\,c$	0.367	$3.4\,c$	0.474
	C	$1.1\,c$	2.113	$0.8\,c$	1.411
	D	$4.0\,c$	4.297	$3.2\,c$	2.729
	(5.9)	c	0.131	c	0.447
$N = 8$	**A**	$1.0\,c$	0.029	$1.2\,c$	0.101
	B	$2.8\,c$	0.070	$2.6\,c$	0.111
	C	$1.1\,c$	0.589	$0.9\,c$	0.365
	D	$7.6\,c$	0.957	$6.8\,c$	0.602
	(5.9)	c	0.029	c	0.109

To assess the order of convergence of the proposed numerical method, we show in Figure 5.12 the error curves (log-log plots of errors versus mesh-size) for $\omega = 250\,\mathrm{rad/s}$ and $\omega = 750\,\mathrm{rad/s}$. It can be seen from this figure that an order of convergence $\mathcal{O}(h^2)$ is achieved. Let us recall that this is the optimal order for the used finite elements in L^2-norm.

To end this section, we show in Figure 5.13 the real and imaginary parts of the solution computed with the proposed PML method for the mesh corresponding to $N = 8$ and $\omega = 750\,\mathrm{rad/s}$. The solution is plotted in the physical domain and in the PML.

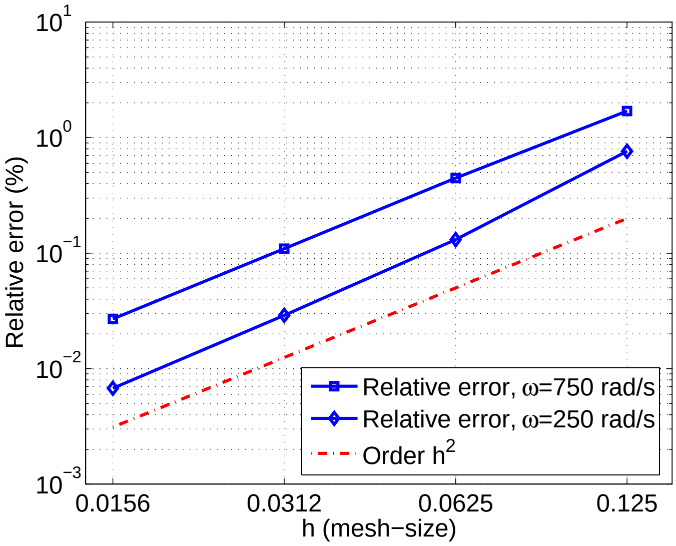

Figure 5.12: Error curves of the PML method with absorbing functions (5.9).

5.5 Comparison with classical absorbing functions

The aim of this section is to compare the proposed unbounded absorbing function (5.9) with the most standard classical choice: quadratic functions of the form

$$\sigma_1(x_1) = \sigma^*(x_1 - a)^2 \qquad \text{and} \qquad \sigma_2(x_2) = \sigma^*(x_2 - b)^2, \tag{5.10}$$

where σ^* is a parameter to be determined. For the comparison we have used the same numerical test as in the previous section.

When these quadratic absorbing functions are used, the standard procedure to minimize the spurious reflections produced at the outer boundary of the PML consists of taking large values for σ^*. Notice that this agrees with the analysis in Section 4.4. However, larger values of σ^* lead to larger discretization errors. Therefore, σ^* cannot be chosen arbitrarily large because, otherwise, the discretization errors would be dominant, deteriorating the overall accuracy of the method.

As shown in [51], for a given problem and a given mesh there is an optimal value of σ^* leading to minimal errors. Unfortunately, such optimal value depends strongly on the problem data as well as on the particular mesh. Thus, in practice, it is necessary to find in advance a reasonable value of σ^*. No theoretical procedure to tune this parameter is known

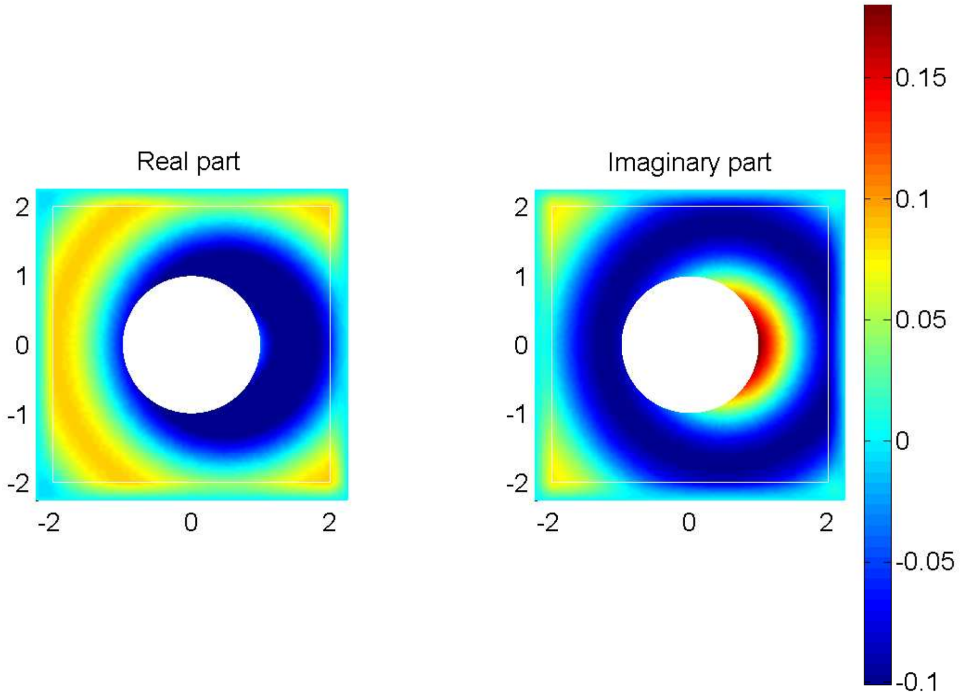

Figure 5.13: Solution of the scattering problem computed by the PML method with absorbing functions (5.9). Mesh $N = 8$, $\omega = 750\,\mathrm{rad/s}$.

to date. Some efforts have been done in [100], but the dependency of σ^* with respect to the mesh has not been avoided.

Let us emphasize that a benefit of our proposed PML strategy is that it does not need of any parameter to be fitted.

In Table 5.2 we compare the errors of the PML method with the unbounded absorbing functions (5.9) and with the quadratic absorbing functions (5.10). For the latter, we have used the optimal value of σ^*, which is also reported in the table. We also include in the table the condition number κ of the system matrix for each discrete problem.

A significant advantage of the proposed unbounded absorbing functions (5.9) can be clearly appreciated from this table. This is particularly remarkable for lowest frequencies, but the errors with the quadratic absorbing functions are larger in all cases, even though the optimal value of σ^* has been used. On the other hand, in spite of the singular character of the unbounded functions, the condition numbers of the resulting system matrices are essentially of the same order as those of the quadratic functions.

On the other hand, Table 5.2 also shows that the optimal value of σ^* strongly depends on the problem data (the frequency ω in this case) and the mesh. The errors and the condition numbers would be significantly larger if any other value than the optimal σ^* were

Table 5.2: Comparison of PML methods with unbounded and quadratic absorbing functions.

		Unbounded (5.9)		Quadratic (5.10)		
ω(rad/s)	Mesh	Error(%)	κ	σ^*	Error(%)	κ
250	$N = 2$	0.763	6.7e+02	$22.28\,c$	11.644	4.7e+02
	$N = 4$	0.131	5.1e+03	$29.57\,c$	3.675	5.0e+03
	$N = 8$	0.029	4.1e+04	$38.37\,c$	1.134	4.6e+04
750	$N = 2$	1.700	1.1e+02	$27.67\,c$	7.602	1.1e+02
	$N = 4$	0.447	7.0e+02	$35.52\,c$	2.291	9.4e+02
	$N = 8$	0.109	5.6e+03	$43.49\,c$	0.698	8.2e+03
1250	$N = 2$	6.958	2.7e+02	$27.89\,c$	11.620	2.9e+02
	$N = 4$	1.946	1.1e+03	$36.94\,c$	3.336	1.7e+03
	$N = 8$	0.430	9.7e+03	$45.70\,c$	0.919	1.5e+03

used. This can be appreciated from Figure 5.14 and 5.15, where the relative error and the condition number are respectively plotted as functions of σ^*, for the mesh corresponding to $N = 4$ and $\omega = 750\,\text{rad/s}$.

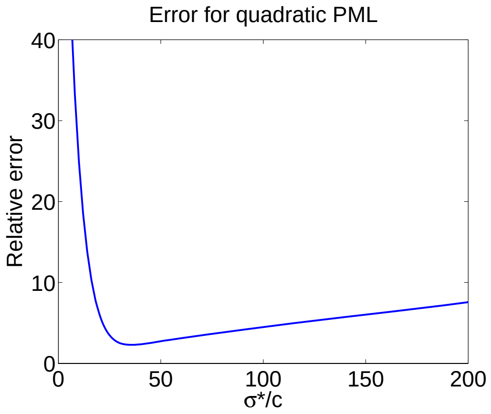

Figure 5.14: Relative error for quadratic absorbing functions with varying σ^*. Mesh: $N = 4$; $\omega = 750\,\text{rad/s}$.

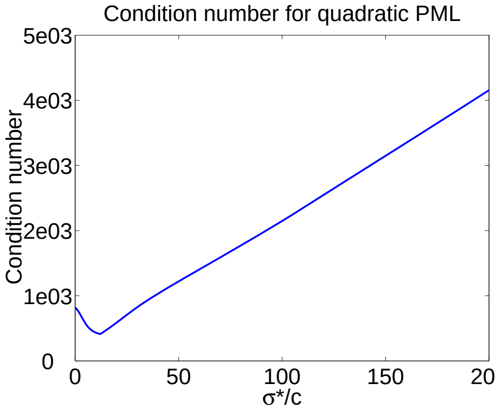

Figure 5.15: Condition number for quadratic absorbing functions with varying σ^*. Mesh: $N = 4$; $\omega = 750\,\text{rad/s}$.

As a conclusion, the proposed PML method with unbounded absorbing function (5.9) clearly beats the classical choice of bounded absorbing functions. Moreover, it overcomes the problem of determining optimal parameters.

5.6 Numerical tests

In this section we report the results obtained by applying the proposed PML strategy based on the non-integrable absorbing function (5.9) to solve two 'real life' Helmholtz problems.

The first test is the scattering of an incident plane wave on the annular obstacle shown in Figure 5.16. The wave number has been taken $k = 2\pi$ and the acoustic speed $c = 340\,\mathrm{m/s}$.

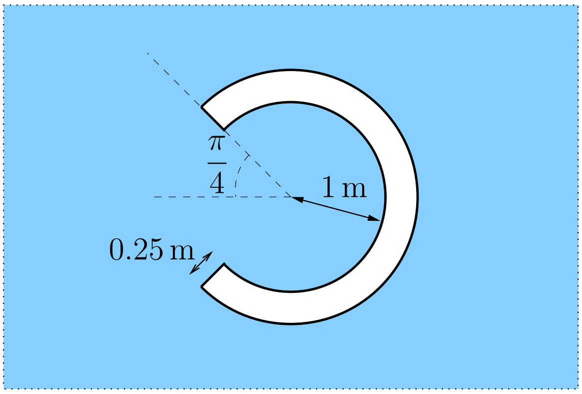

Figure 5.16: Annular obstacle of the scattering problem.

We have used our PML method on the two embedded square domains shown in Figs. 5.17 and 5.18. Therefore, we have been able to compare the numerical results as a mean of assessing the accuracy of the method, since an analytical solution of this problem is not available.

We have used uniform refinements of the meshes shown in Figs. 5.17 and 5.18, with 21160 triangles and 3328 rectangles, for the smaller domain, and with 64680 triangles and 5888 rectangles for the larger.

In Figs. 5.19 and 5.20 we show the real and imaginary parts, respectively, of the computed solutions in both domains. It can be seen that both solutions are almost identical on the common part of the physical domains. Indeed, the relative difference in L^2-norm (which is defined analogously to (5.8)) is only 0.233%. Therefore, the solution computed in the smaller domain (and consequently with less computational effort) can be safely used.

In the second test we have simulated the scattering of waves generated by a monopole (i.e., a Dirac's delta source term). We have used the same annular obstacle and square domains as in the previous test, with the monopole located at the center of the squares. We have also used the same meshes, wave number, and acoustic speed.

The computed solutions are shown in Figs. 5.21 and 5.22. Once more, both solutions are practically indistinguishable in the common part of the physical domains. In this case, the relative difference in L^2-norm is only 0.184%.

Obviously we can change the geometry of the obstacle. For instance, we also consider a diapason whose thickness is 0.2 m, its interior aperture 1 m, and its length 4.1 m (see

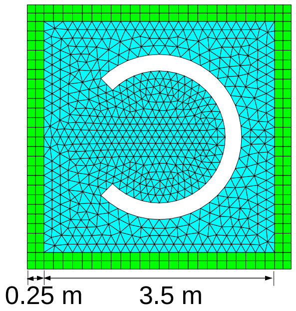

Figure 5.17: Smaller domain and coarse mesh for the scattering problem.

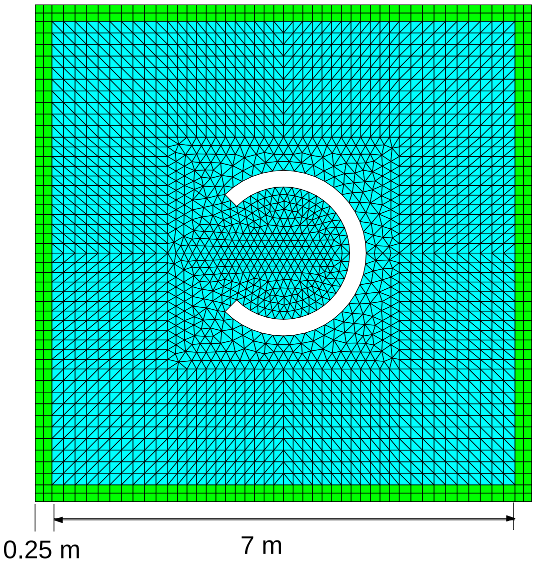

Figure 5.18: Larger domain and coarse mesh for the scattering problem.

Figure 5.23).

First, we suppose that a plane wave in the positive x-direction is scattered by the diapason. The mesh corresponds to the physical domain $\Omega_\mathrm{F} = [-3.6, 3.6]^2 \setminus \overline{\Omega}$ and to PML layers with thickness 0.5 m. We use two meshes, which are refinements of the mesh in Figure 5.23. Mesh $N = 4$ has 9140 triangles in Ω_F and 3120 rectangles in the PML layers, whereas mesh $N = 8$ has 36610 triangles in the fluid domain and 12480 in the PML.

In Figures 5.24 and 5.25 we show the results that we have obtained for the reflected pressure field by the diapason, for a wave number $k = 2\pi\,\mathrm{m}^{-1}$, using the mesh $N = 4$.

Figures 5.26 and 5.27 show the same numerical problem with a higher wave number, $k = 10\pi\,\mathrm{m}^{-1}$. In this case we have used the mesh $N = 8$.

Now we keep the same geometry of the diapason with the same meshes, but simulate a Dirac's delta (monopole) acting at the point $(0.5, 0)\,\mathrm{m}$ (inside the arc of the diapason). In Figures 5.28 to 5.31 we show the real and the imaginary part of the reflected pressure fields generated by a monopole for the wave numbers $k = 2\pi\,\mathrm{m}^{-1}$ (with the mesh $N = 4$) and $k = 10\pi\,\mathrm{m}^{-1}$ (with the mesh $N = 8$).

Finally, the last example resembles the well-known double-slit interference experiment stated originally by Thomas Young in 1801 to infer the wave-like nature of light. This model mimics the plane-wave excitation with two waveguides leading to slits in a screen and computes the diffraction pattern in a domain surrounding the apertures.

We have used the domain shown in Figure 5.32 and a refinement of the mesh plotted in the same figure, with 51424 triangles and 6656 rectangles. We have taken a wave number

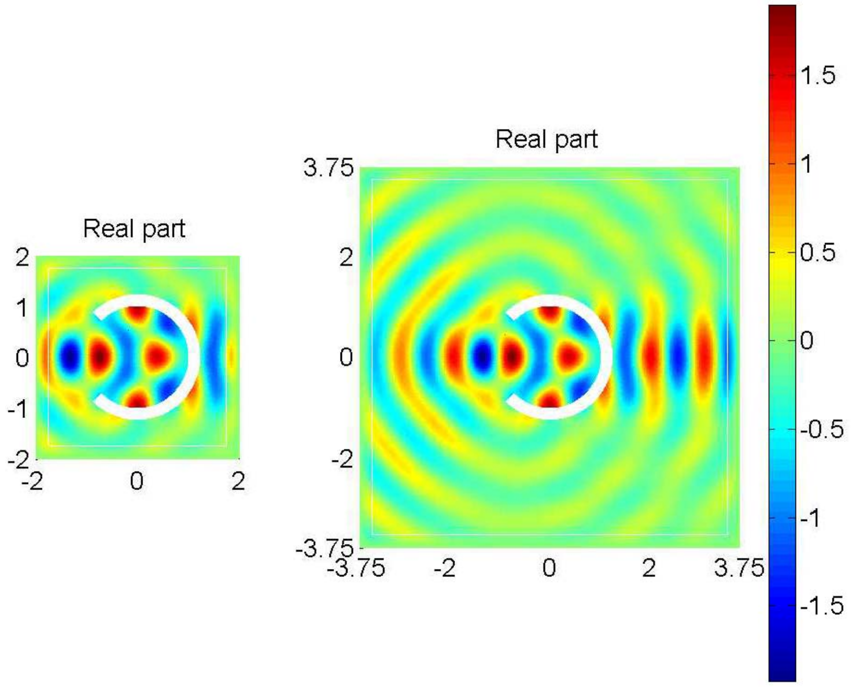

Figure 5.19: Reflected wave field generated by an incident plane wave. Real part.

$k = 8\pi$ and an acoustic speed $c = 340\,\mathrm{m/s}$.

Figure 5.33 shows the wave field near the double-slit.

When the Fresnel number is small enough, classical theory predicts a phenomenon of destructive interference which depends only on the angular coordinate θ (see for instance [41]). The interference lines are $\theta = \pm ka$, being k the wave number and a the radius of the aperture in the slits. It can be checked in Figure 5.34 that the numerical results achieve a good accuracy with respect to the approximated classical theory of Fraunhofer diffraction.

5.7 Conclusions

We have introduced a PML method based on a non-integrable absorbing function for the numerical solution of time-harmonic problems in unbounded domains. We have shown that this method is able to absorb plane waves with arbitrary incidence angle without any spurious reflection.

We have compared the performance of different non-integrable absorbing functions leading to well posed finite element discretizations. The comparison allow us to choose a particularly simple one, which only depends on the acoustic speed. Therefore, we have obtained a PML method free of parameters with no physical meaning.

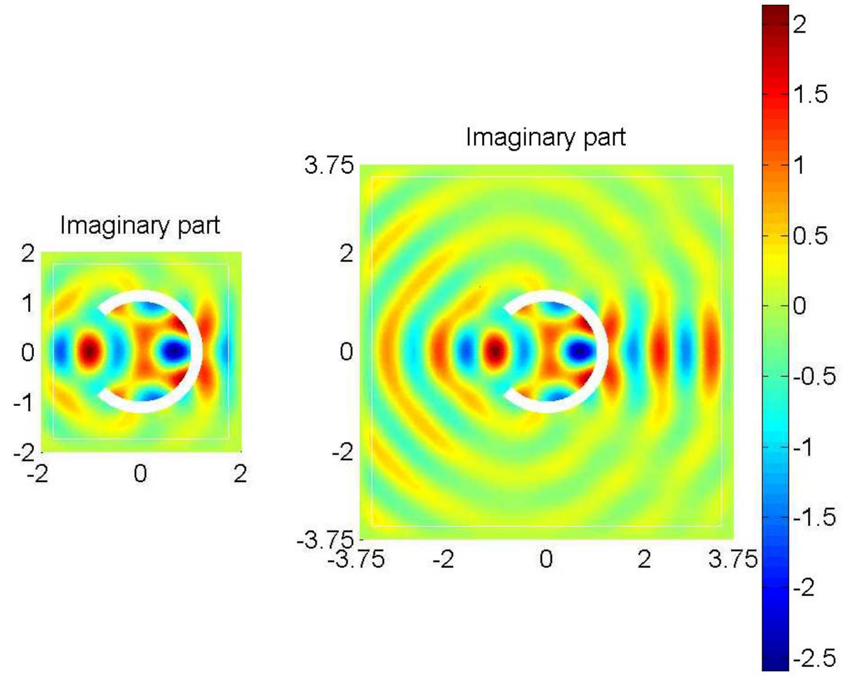

Figure 5.20: Reflected wave field generated by an incident plane wave. Imaginary part.

We have shown that the proposed method leads to significantly smaller errors than the classical ones based on bounded absorbing functions. To assess the efficiency of our approach, we have applied it to solve some realistic problems, obtaining very good results even with thin absorbing layers close to the obstacles.

As shown in the forthcoming appendix, the method is very easy to implement. The integrals in the PML involving the unbounded absorbing function can be computed either explicitly or by means of standard quadrature rules. Let us emphasize that, if quadrature rules are chosen, then there is no need of using hybrid meshes with triangles in the region of interest and rectangles in the PML. A thorough numerical experimentation to validate the proposed PML method on purely triangular meshes will be reported somewhere else.

5.8 Computation of the element matrices

Our choice of absorbing functions,

$$\sigma_1(x_1) = \frac{c}{a^* - x_1}, \qquad \sigma_2(x_2) = \frac{c}{b^* - x_2},$$

allows the explicit computation of integrals like those in (5.3). Although such explicit computation is not indispensable, it avoids the use of quadrature rules and their inherent

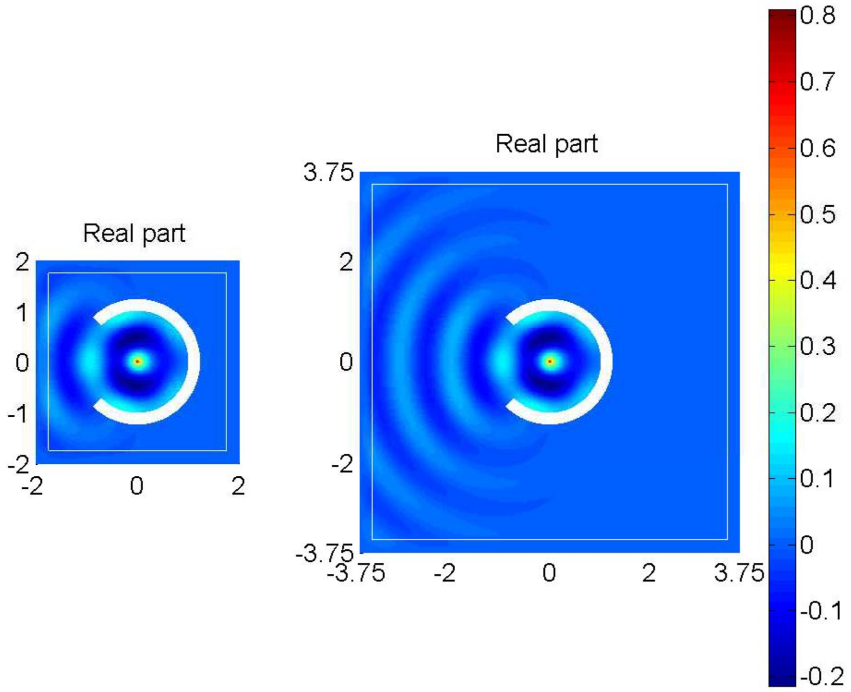

Figure 5.21: Wave field generated by a monopole. Real part.

truncation errors.

As an example of explicit computation, consider the integrals (5.4)–(5.6) over an element K as that shown in Figure 5.4. In this case, we have to compute four different integrals:

$$\int_{a^*-h_1}^{a^*} \gamma_1(x_1)(x_1-a^*)^2\,dx_1, \qquad \int_{a^*-h_1}^{a^*} \frac{dx_1}{\gamma_1(x_1)},$$
$$\int_{b_1}^{b_2} \gamma_2(x_2)(x_2-b_j)(x_2-b_i)\,dx_2, \qquad \int_{b_1}^{b_2} \frac{dx_2}{\gamma_2(x_2)}.$$

All the integrals that appear in the computation of the element matrices for any other element K in Ω_A are essentially equal to one of these four.

The integrals involving γ_1 are computed as follows:

$$\int_{a^*-h_1}^{a^*} \gamma_1(x_1)(x_1-a^*)^2\,dx_1 = \int_{a^*-h_1}^{a^*} \left[1+\frac{i}{\omega}\frac{c}{(a^*-x_1)}\right](x_1-a^*)^2\,dx_1 = \frac{h_1^3}{3} - i\frac{c}{\omega}\frac{h_1^2}{2}$$

and

$$\int_{a^*-h_1}^{a^*} \frac{dx_1}{\gamma_1(x_1)} = \int_{a^*-h_1}^{a^*} \frac{\omega(a^*-x_1)}{\omega(a^*-x_1)+ic}\,dx_1 = h_1 + \frac{ic}{\omega}\log\left(\frac{ic}{\omega h_1 + ic}\right).$$

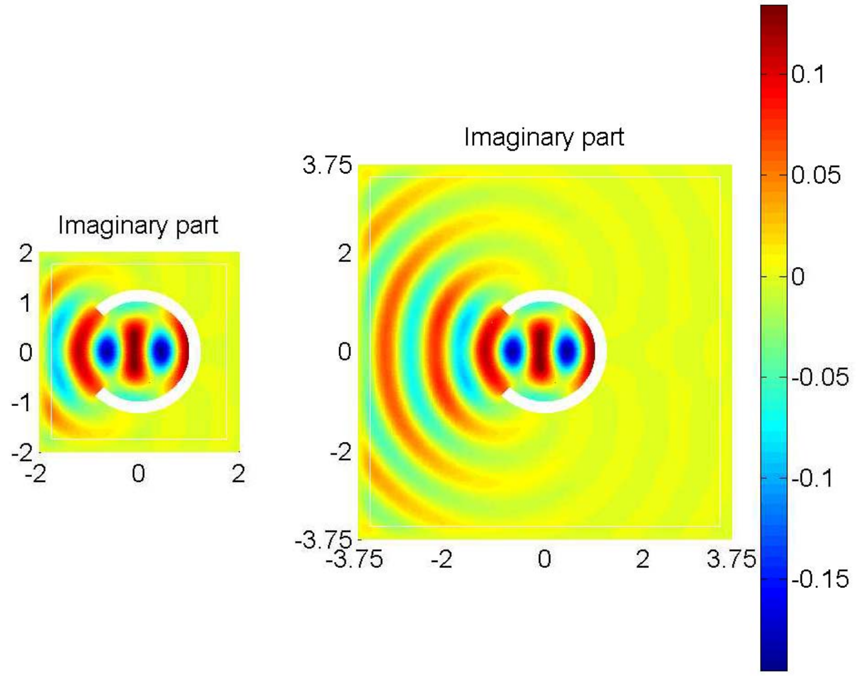

Figure 5.22: Wave field generated by a monopole. Imaginary part.

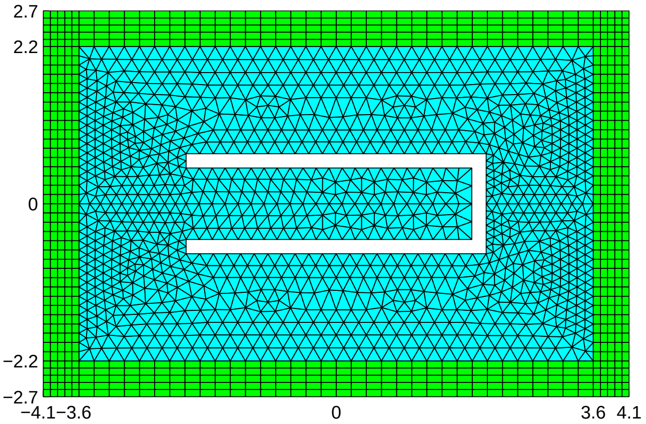

Figure 5.23: Mesh of the fluid domain and PML surrounding the diapason.

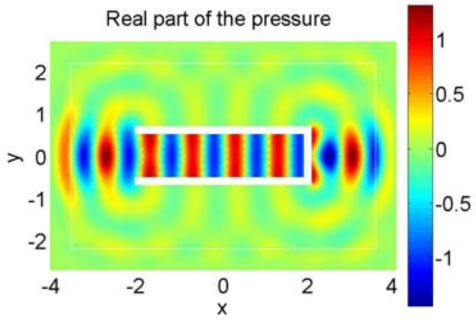

Figure 5.24: Real part of the pressure field generated by an incident plane wave, $k = 2\pi\,\mathrm{m}^{-1}$.

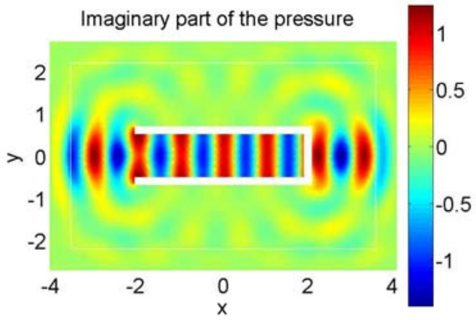

Figure 5.25: Imaginary part of the pressure field generated by an incident plane wave, $k = 2\pi\,\mathrm{m}^{-1}$.

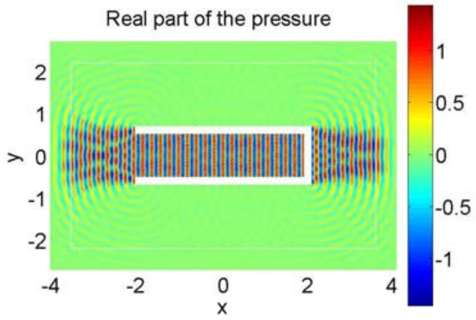

Figure 5.26: Real part of the pressure field generated by an incident plane wave, $k = 10\pi\,\mathrm{m}^{-1}$.

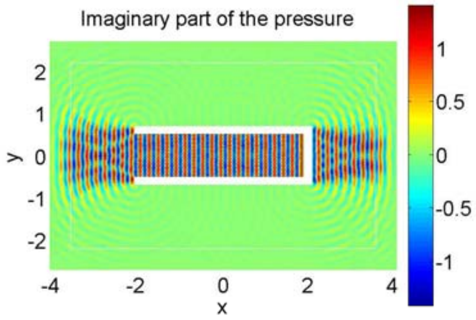

Figure 5.27: Imaginary part of the pressure field generated by an incident plane wave, $k = 10\pi\,\mathrm{m}^{-1}$.

The computation of the integrals involving γ_2 depend on the location of the element K. If $-b \le b_1 < b_2 \le b$, then $\gamma_2 = 1$ and the integrals are trivial. If $b \le b_1 < b_2 \le b^*$, then

$$\int_{b_1}^{b_2} \frac{dx_2}{\gamma_2(x_2)} = \int_{b_1}^{b_2} \frac{\omega(b^* - x_2)}{\omega(b^* - x_2) + ic}\, dx_2 = h_2 + \frac{ic}{\omega} \log\left(\frac{\omega(b^* - b_2) + ic}{\omega(b^* - b_1) + ic}\right)$$

and

$$\int_{b_1}^{b_2} \gamma_2(x_2)(x_2 - b_j)(x_2 - b_i)\, dx_2 = \int_{b_1}^{b_2} (x_2 - b_j)(x_2 - b_i)\, dx_2 + i\frac{\omega}{c} \int_{b_1}^{b_2} \frac{(x_2 - b_j)(x_2 - b_i)}{b^* - x_2}\, dx_2.$$

The first integral above is trivial, whereas for the second one straightforward computations

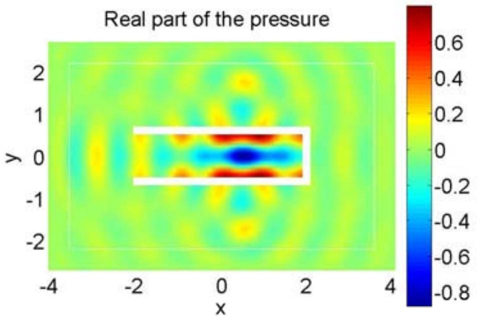

Figure 5.28: Real part of pressure field generated by a monopole, $k = 2\pi\,\mathrm{m}^{-1}$.

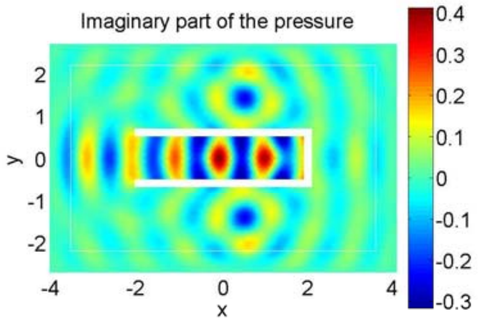

Figure 5.29: Imaginary part of the pressure field generated by a monopole, $k = 2\pi\,\mathrm{m}^{-1}$.

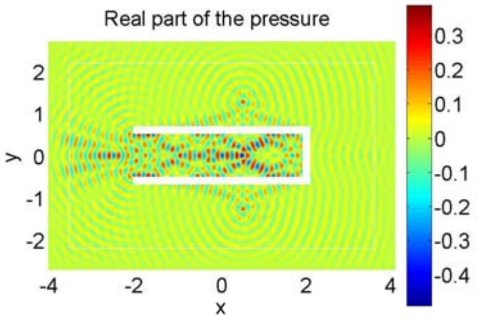

Figure 5.30: Real part of the pressure field generated by a monopole, $k = 10\pi\,\mathrm{m}^{-1}$.

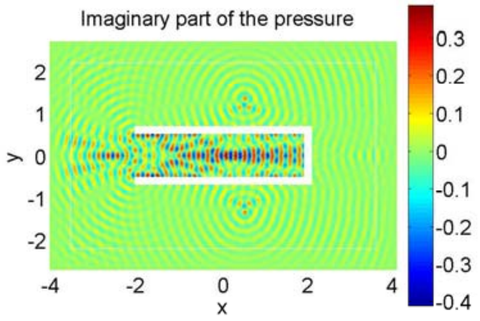

Figure 5.31: Imaginary part of the pressure field generated by a monopole, $k = 10\pi\,\mathrm{m}^{-1}$.

lead to

$$\int_{b_1}^{b_2} \frac{(x_2 - b_j)(x_2 - b_i)}{b^* - x_2}\, dx_2 = \frac{h_2}{2}(2b^* - b_2 - b_1) - h_2(2b^* - b_i - b_j) + (b^* - b_j)(b^* - b_i) \log\left(\frac{b^* - b_1}{b^* - b_2}\right).$$

Similar results are valid if $-b^* \leq b_1 < b_2 \leq -b$.

Alternatively, all these integrals can be computed using standard quadrature rules. In principle, these rules could lead to large truncation errors due to the singular character of the unbounded absorbing functions. However, our preliminary experiments show that the effect of numerical quadrature does not seem to modify significantly the accuracy of the proposed PML method.

To show this we have solved the numerical test from Section 5.4 with the integrals

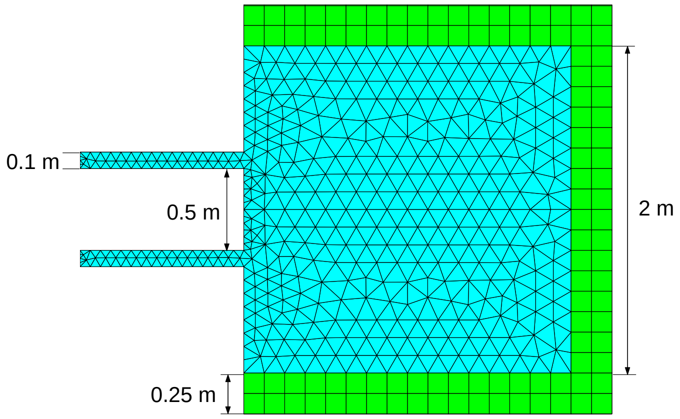

Figure 5.32: Domain and coarse mesh for the double-slit interference test.

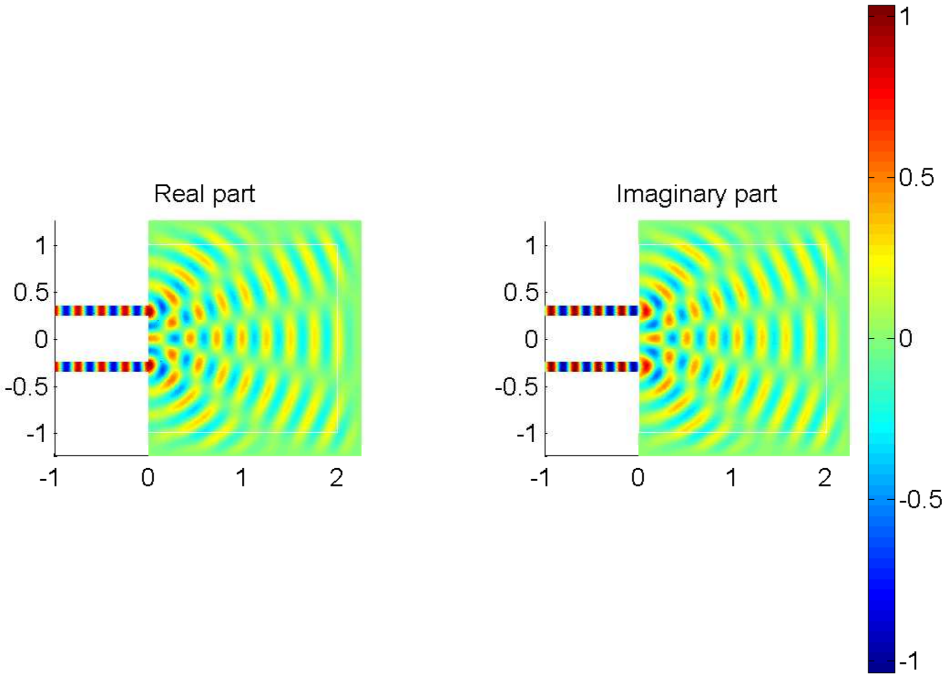

Figure 5.33: Wave field generated by the excitation of the waveguides.

computed by Gauss-Legendre rules with 4 and 9 nodes. We report in Table 5.3 the relative errors of the solutions computed with each rule and with exact integration.

It can be clearly seen that the errors in the numerical integration are negligible. Moreover, for 250 rad/s and 750 rad/s the 4-nodes rule shows a slightly better performance,

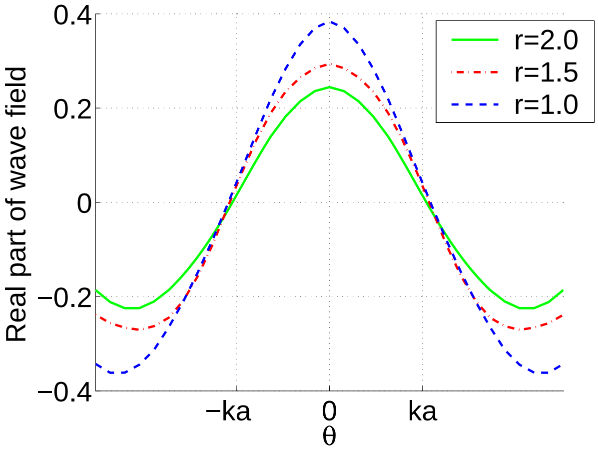

Figure 5.34: Interference pattern at different distances r from the waveguides apertures.

Table 5.3: Comparison of quadrature rules using PML with unbounded absorbing functions.

		Gauss-Legendre		Exact Integration
ω(rad/s)	Mesh	4 nodes	9 nodes	
250	$N = 2$	0.763689	0.770405	0.763485
	$N = 4$	0.130572	0.130413	0.130580
	$N = 8$	0.028858	0.028755	0.028860
750	$N = 2$	1.699869	1.699611	1.699889
	$N = 4$	0.446922	0.446910	0.446922
	$N = 8$	0.109444	0.109467	0.109443
1250	$N = 2$	6.957597	6.958152	6.958012
	$N = 4$	1.946417	1.946320	1.946313
	$N = 8$	0.429920	0.429913	0.429912

which agrees with the fact that low-order integration schemes are preferable for singular integrands.

Chapter 6

An exact bounded PML in radial coordinates

Contents

6.1 Introduction

We have shown in Chapter 5 that the Cartesian PML technique based on singular absorbing functions, leads to accurate numerical results. The aim of this chapter is to analyze mathematically the existence and uniqueness of solution of the corresponding coupled fluid/PML problem.

We also prove that this choice leads to a theoretically exact bounded PML. More precisely, this kind of absorbing function on a circular annular layer allows recovering the exact solution of the time-harmonic scattering problem in the domain of interest, up to discretization errors, even though the thickness of the layer is finite. This is the reason why we call “exact” PML methods to those based on such absorbing functions.

Standard PML techniques based on bounded absorbing function lead to partial differential equations in the PML with bounded coefficients. Thus, the theoretical procedure to prove the well-posedness of the coupled fluid/PML problems is based on the Freedholm alternative in standard Sobolev spaces. However, when a non-integrable absorbing function is used, the coefficients in the PML equation become unbounded, and the natural functional framework involves a non-standard weighted Sobolev space. In this case standard arguments cannot be applied due to the lack of a compactness result. As an alternative, we reproduce the classical steps used for the Helmholtz equation, taking advantage of the series representation of the solution in the PML domain. Thus we prove a result of existence and uniqueness for the coupled fluid/PML problem.

The analysis of the theoretical error for other PML techniques is typically based on the construction of an analogous Dirichlet-to-Neumann operator using the solution in the PML. We also use this approach to prove that the solution in the fluid domain of the coupled fluid/PML problem is *exactly* equal to the solution of the scattering problem in an unbounded domain.

The outline of this chapter is as follows: we recall in Section 6.2 how the classical time-harmonic scattering problem can be stated in a bounded domain by using a DtN operator. Section 6.3 is devoted to settling PML equations based on non-integrable absorbing functions on an annular domain surrounding the physical one. Once the fundamental solution for the PML is calculated in Section 6.4, a integral representation formula is proved in Section 6.5. We rewrite a classical “addition theorem” for the PML fundamental solution in Section 6.6. Using these tools, we prove a characterization theorem for the solution of the radial PML in Section 6.7 and derive a theorem of existence and uniqueness of solution for the PML problem. In Section 6.8, we use this result to recover the classical solution of the scattering problem by means of a coupled fluid/PML problem. We prove existence and uniqueness of solution for this coupled problem and write a weak formulation, as well. Finally, in Section 6.9, we report some numerical results obtained with a standard finite element method.

6.2 Scattering problem

Let Ω be a bounded two-dimensional open set with a Lipschitz boundary Γ. We aim to solve a scattering problem in the unbounded domain $\mathbb{R}^2 \setminus \overline{\Omega}$, which we assume connected (see Figure 6.1). As in Chapter 5, we are going to focus our attention on the time-harmonic scattering problem. More precisely, we consider the following Dirichlet boundary value problem for the Helmholtz equation, which models the wave propagation with frequency $\omega > 0$ and velocity of propagation $c > 0$:

Find $p \in \mathrm{H}^1_{\mathrm{loc}}(\mathbb{R}^2 \setminus \overline{\Omega})$ *such that*

$$-\Delta p - k^2 p = 0 \qquad \text{in } \mathbb{R}^2 \setminus \overline{\Omega}, \tag{6.1}$$

$$p = f \qquad \text{on } \Gamma, \tag{6.2}$$

$$\lim_{r\to\infty} \sqrt{r}\left(\frac{\partial p}{\partial r} - ikp\right) = 0, \tag{6.3}$$

where $r := |\boldsymbol{x}|$ is the radial polar coordinate for $\boldsymbol{x} \in \mathbb{R}^2$, $k := \omega/c$ is the wave number, and $f \in \mathrm{H}^{\frac{1}{2}}(\Gamma)$ is the Dirichlet boundary data. Let us remark that we could analogously consider the corresponding Neumann boundary value problem. The existence of solution to both problems is well known in the literature (see for instance [104]).

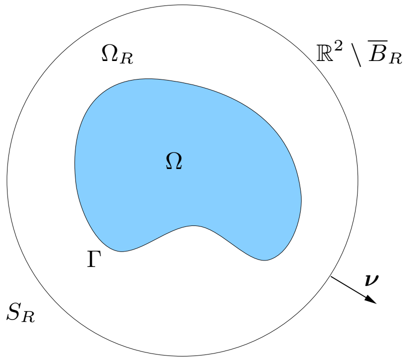

Figure 6.1: Scatterer and artificial circular boundary.

Let $B_R := \{\boldsymbol{x} \in \mathbb{R}^2 : |\boldsymbol{x}| < R\}$ be an open ball of radius R such that $\overline{\Omega} \subset B_R$. Let $S_R := \{\boldsymbol{x} \in \mathbb{R}^2 : |\boldsymbol{x}| = R\}$ be its boundary and $\boldsymbol{\nu}$ its outward unit normal vector (see Figure 6.1). The DtN operator of the problem above is defined as follows:

$$\begin{aligned} G:\ \mathrm{H}^{\frac{1}{2}}(S_R) &\longrightarrow \mathrm{H}^{-\frac{1}{2}}(S_R) \\ g &\longmapsto \left.\frac{\partial \tilde{p}}{\partial \boldsymbol{\nu}}\right|_{S_R} \end{aligned} \tag{6.4}$$

where $\tilde{p} \in \mathrm{H}^1_{\mathrm{loc}}(\mathbb{R}^2 \setminus \overline{B}_R)$ is the unique solution of

$$\begin{aligned} -\Delta\tilde{p} - k^2\tilde{p} &= 0 && \text{in } \mathbb{R}^2 \setminus \overline{B}_R, \\ \tilde{p} &= g && \text{on } S_R, \\ \lim_{r\to\infty} \sqrt{r}\left(\frac{\partial\tilde{p}}{\partial r} - ik\tilde{p}\right) &= 0. \end{aligned}$$

Let us recall that this operator is explicitly given by the following series (see [84, 90]):

$$Gg = \sum_{n=-\infty}^{\infty} g_n k \frac{[\mathrm{H}_n^{(1)}]'(kR)}{\mathrm{H}_n^{(1)}(kR)}\, \mathrm{e}^{in\theta},$$

where θ is the angular polar coordinate of $\boldsymbol{x}$, $g_n := 1/(2\pi R)\int_{S_R} g(\boldsymbol{x})\, \mathrm{e}^{-in\theta}\, dS$ is the n^{th} Fourier coefficient of g, and $\mathrm{H}_n^{(j)}$ denotes the n^{th} Hankel function of j^{th} kind, $j = 1, 2$ (see for instance [103]).

Problem (6.1)–(6.3) can be equivalently settled in the bounded domain

$$\Omega_R := \left\{\boldsymbol{x} \in \mathbb{R}^2 \setminus \overline{\Omega} : |\boldsymbol{x}| < R\right\}$$

by means of this DtN operator as follows:

Find $p \in \mathrm{H}^1(\Omega_R)$ such that

$$-\Delta p - k^2 p = 0 \qquad \text{in } \Omega_R, \tag{6.5}$$

$$p = f \qquad \text{on } \Gamma, \tag{6.6}$$

$$\frac{\partial p}{\partial \boldsymbol{\nu}} = G\left(p|_{S_R}\right) \qquad \text{on } S_R. \tag{6.7}$$

Clearly, if p is the solution of Problem (6.1)–(6.3) (see Figure 6.1), then $p|_{\Omega_R}$ is the unique solution of the problem above.

6.3 Statement of the PML equation

Radial PML methods are based on simulating dissipation in an annular domain, $\mathrm{D} := \{\boldsymbol{x} \in \mathbb{R}^2 : R < |\boldsymbol{x}| < R^\star\}$, surrounding the physical domain of interest (see Figure 6.2).

This can be done by means of a complex-valued radial stretching proposed by Collino and Monk [52], which leads to the following partial differential equation written in polar coordinates:

$$-\frac{1}{r}\left(\frac{\partial}{\partial r}\left(\frac{\hat{\gamma}(r)r}{\gamma(r)}\frac{\partial\hat{p}}{\partial r}\right) + \frac{\gamma(r)}{\hat{\gamma}(r)r}\frac{\partial^2\hat{p}}{\partial\theta^2}\right) - \gamma(r)\hat{\gamma}(r)k^2\hat{p} = 0 \qquad \text{in D}, \tag{6.8}$$

where

$$\gamma(r) := 1 + \frac{i}{\omega}\sigma(r) \qquad \text{and} \qquad \hat{\gamma}(r) := 1 + \frac{i}{\omega r}\int_R^r \sigma(s), \tag{6.9}$$

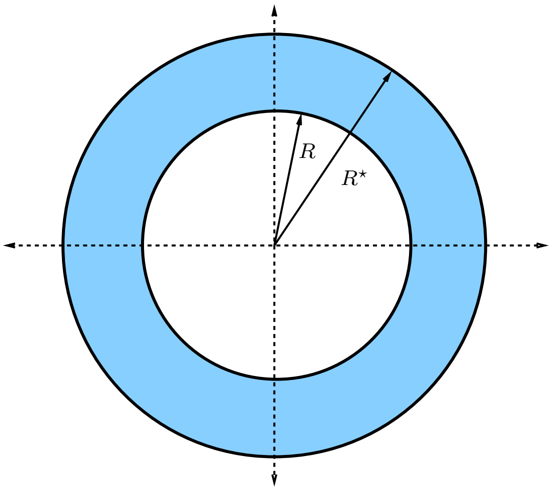

Figure 6.2: Domain D.

with the so-called *absorbing function* $\sigma : [R, R^\star) \longrightarrow [0, \infty)$ being monotonically increasing and smooth. Although in practice σ will be chosen in $\mathcal{C}^\infty([R, R^\star))$, in all what follows it is enough to assume that $\sigma \in \mathcal{C}^{2,1}([R, R'])$ for all $R' \in (R, R^\star)$ (recall that $\mathcal{C}^{2,1}([R, R']) := \{F \in \mathcal{C}^2([R, R'])$; F'' is Lipschitz-continuous in $[R, R']\}$). Notice that we do not assume that $\sigma(R) = 0$. This function has been typically chosen bounded (see [52]). As an alternative, we propose to choose a non-integrable function, i.e., such that

$$\int_R^{R^\star} \sigma(s) = +\infty; \tag{6.10}$$

for example, $\sigma(r) := c/(R^\star - r)$.

Under the previous assumptions on σ, $\lim_{r\to R^\star} |\gamma(r)| = \lim_{r\to R^\star} |\hat{\gamma}(r)| = +\infty$. Moreover, the coefficients of the differential equation (6.8) satisfy

$$\lim_{r\to R^\star} \left| \frac{\hat{\gamma}(r)r}{\gamma(r)} \right| = 0 \qquad \text{and} \qquad \lim_{r\to R^\star} \left| \frac{\gamma(r)}{\hat{\gamma}(r)r} \right| = +\infty. \tag{6.11}$$

Indeed, given $\epsilon > 0$, let $A_\epsilon := \int_R^{R^\star-\epsilon} \sigma(s)$. Because of (6.10), $\exists r \in (R^\star - \epsilon, R^\star)$ such that $\int_{R^\star-\epsilon}^r \sigma(s) \geq A_\epsilon$. Then

$$\int_R^r \sigma(s) = \int_R^{R^\star-\epsilon} \sigma(s) + \int_{R^\star-\epsilon}^r \sigma(s) \leq 2 \int_{R^\star-\epsilon}^r \sigma(s) \leq 2\epsilon\sigma(r).$$

Hence,

$$\lim_{r\to R^\star} \frac{1}{\sigma(r)} \int_R^r \sigma(s) = 0,$$

which together with the definitions of γ and $\hat{\gamma}$, and the fact that $R \leq r \leq R^\star$ yield (6.11).

To end this section, we write the equation (6.8) in a more compact form. Let $\{\boldsymbol{e}_r, \boldsymbol{e}_\theta\}$ be the canonical polar-coordinates basis. Let us recall the expressions of the divergence and gradient operators in this basis:

$$\mathbf{grad}\, q = \frac{\partial q}{\partial r}\boldsymbol{e}_r + \frac{1}{r}\frac{\partial q}{\partial \theta}\boldsymbol{e}_\theta,$$

and, for $\boldsymbol{w} = w_r \boldsymbol{e}_r + w_\theta \boldsymbol{e}_\theta$,

$$\operatorname{div} \boldsymbol{w} = \frac{1}{r}\left(\frac{\partial}{\partial r}(r w_r) + \frac{\partial w_\theta}{\partial \theta}\right).$$

It is straightforward to show that the PML equation (6.8) can be written as follows:

$$-\operatorname{div}(\boldsymbol{A}\,\mathbf{grad}\,\hat{p}) - \gamma(r)\hat{\gamma}(r)k^2\hat{p} = 0 \qquad \text{in D},$$

where

$$\boldsymbol{A} := \begin{pmatrix} a_{rr} & 0 \\ 0 & a_{\theta\theta} \end{pmatrix}, \qquad \text{with} \qquad a_{rr}(r) := \frac{\hat{\gamma}(r)}{\gamma(r)} \qquad \text{and} \qquad a_{\theta\theta}(r) := \frac{\gamma(r)}{\hat{\gamma}(r)}. \tag{6.12}$$

Let us emphasize that matrix $\boldsymbol{A}$ is written in the polar coordinates basis. Therefore, for the concrete evaluation of any expression involving $\boldsymbol{A}$ (like that above), all the vector fields and the differential operators must be written in the same basis.

6.4 PML fundamental solution

We consider the following complex change of variable, proposed by Collino and Monk in [52]:

$$\hat{r}(r) := \hat{\gamma}(r)r = r + \frac{i}{\omega}\int_R^r \sigma(s)ds, \qquad r \in [R, R^\star).$$

The assumed smoothness of σ is more than enough to ensure that $\hat{r} \in \mathcal{C}^2([R, R^\star))$. We also define a complex-valued function $\mathrm{d}(\cdot,\cdot)$ which will be often used instead of the Euclidean distance within the PML: given two points $\boldsymbol{x}$ and $\boldsymbol{y}$ in D, with respective polar coordinates $(r_{\boldsymbol{x}}, \theta_{\boldsymbol{x}})$ and $(r_{\boldsymbol{y}}, \theta_{\boldsymbol{y}})$, let

$$\mathrm{d}(\boldsymbol{x}, \boldsymbol{y}) := \sqrt{\hat{r}_{\boldsymbol{x}}^2 + \hat{r}_{\boldsymbol{y}}^2 - 2\hat{r}_{\boldsymbol{x}}\hat{r}_{\boldsymbol{y}}\cos(\theta_{\boldsymbol{y}} - \theta_{\boldsymbol{x}})}, \tag{6.13}$$

where $\hat{r}_{\boldsymbol{x}} := \hat{r}(r_{\boldsymbol{x}})$, $\hat{r}_{\boldsymbol{y}} := \hat{r}(r_{\boldsymbol{y}})$ and the square root is chosen so that $\mathrm{Re}(\sqrt{z}) > 0$ for $z \neq 0$. The following lemma shows that this definition makes sense, because the radicand in (6.13) is never a negative real number.

Lemma 6.4.1. *For all* $\boldsymbol{x}, \boldsymbol{y} \in \mathrm{D}$, $\boldsymbol{x} \neq \boldsymbol{y}$,

$$\hat{r}_{\boldsymbol{x}}^2 + \hat{r}_{\boldsymbol{y}}^2 - 2\hat{r}_{\boldsymbol{x}}\hat{r}_{\boldsymbol{y}} \cos(\theta_{\boldsymbol{y}} - \theta_{\boldsymbol{x}})$$

either is a positive real number or it has a positive imaginary part. Moreover it vanishes if and only if $\boldsymbol{x} = \boldsymbol{y}$.

Proof. Since $\hat{r}_{\boldsymbol{x}}^2 + \hat{r}_{\boldsymbol{y}}^2 - 2\hat{r}_{\boldsymbol{x}}\hat{r}_{\boldsymbol{y}} \cos(\theta_{\boldsymbol{y}} - \theta_{\boldsymbol{x}})$ is symmetric as a function of $\boldsymbol{x}$ and $\boldsymbol{y}$, it is enough to consider $\hat{r}_{\boldsymbol{x}} \geq \hat{r}_{\boldsymbol{y}}$.

First, consider the trivial case in which σ vanishes in $[R, r_{\boldsymbol{x}}]$. In such a case $\hat{r}_{\boldsymbol{x}} = r_{\boldsymbol{x}}$, $\hat{r}_{\boldsymbol{y}} = r_{\boldsymbol{y}}$, and $\hat{r}_{\boldsymbol{x}}^2 + \hat{r}_{\boldsymbol{y}}^2 - 2\hat{r}_{\boldsymbol{x}}\hat{r}_{\boldsymbol{y}} \cos(\theta_{\boldsymbol{y}} - \theta_{\boldsymbol{x}}) \geq (r_{\boldsymbol{x}} - r_{\boldsymbol{y}})^2 \geq 0$. Moreover $\hat{r}_{\boldsymbol{x}}^2 + \hat{r}_{\boldsymbol{y}}^2 - 2\hat{r}_{\boldsymbol{x}}\hat{r}_{\boldsymbol{y}} \cos(\theta_{\boldsymbol{y}} - \theta_{\boldsymbol{x}})$ vanishes if and only if $r_{\boldsymbol{x}} = r_{\boldsymbol{y}}$ and $\theta_{\boldsymbol{x}} = \theta_{\boldsymbol{y}}$; namely, if and only if $\boldsymbol{x} = \boldsymbol{y}$.

Secondly, consider the case in which σ does not vanishes in $[R, r_{\boldsymbol{x}}]$ and, hence, $\int_R^{r_{\boldsymbol{x}}} \sigma(s)ds > 0$ (recall that σ is monotonically increasing and non-negative). In such a case, there holds

$$\begin{aligned}
&\operatorname{Im}(\hat{r}_{\boldsymbol{x}}^2 + \hat{r}_{\boldsymbol{y}}^2 - 2\hat{r}_{\boldsymbol{x}}\hat{r}_{\boldsymbol{y}} \cos(\theta_{\boldsymbol{y}} - \theta_{\boldsymbol{x}}))\\
=&\frac{2}{\omega}\left(r_{\boldsymbol{x}}\int_R^{r_{\boldsymbol{x}}}\sigma(s)ds + r_{\boldsymbol{y}}\int_R^{r_{\boldsymbol{y}}}\sigma(s)ds - \cos(\theta_{\boldsymbol{y}} - \theta_{\boldsymbol{x}})\left(r_{\boldsymbol{x}}\int_R^{r_{\boldsymbol{y}}}\sigma(s)ds + r_{\boldsymbol{y}}\int_R^{r_{\boldsymbol{x}}}\sigma(s)ds\right)\right)\\
\geq&\frac{2}{\omega}\left(r_{\boldsymbol{x}}\int_R^{r_{\boldsymbol{x}}}\sigma(s)ds + r_{\boldsymbol{y}}\int_R^{r_{\boldsymbol{y}}}\sigma(s)ds - \left(r_{\boldsymbol{x}}\int_R^{r_{\boldsymbol{y}}}\sigma(s)ds + r_{\boldsymbol{y}}\int_R^{r_{\boldsymbol{x}}}\sigma(s)ds\right)\right)\\
=&\frac{2}{\omega}\left(r_{\boldsymbol{x}} - r_{\boldsymbol{y}}\right)\left(\int_R^{r_{\boldsymbol{x}}}\sigma(s)ds - \int_R^{r_{\boldsymbol{y}}}\sigma(s)ds\right) \geq 0,
\end{aligned}$$

the latter because $\int_R^{r_{\boldsymbol{x}}} \sigma(s)ds \geq \int_R^{r_{\boldsymbol{y}}} \sigma(s)ds$, for $r_{\boldsymbol{x}} \geq r_{\boldsymbol{y}}$. Moreover, once more

$$\operatorname{Im}(\hat{r}_{\boldsymbol{x}}^2 + \hat{r}_{\boldsymbol{y}}^2 - 2\hat{r}_{\boldsymbol{x}}\hat{r}_{\boldsymbol{y}} \cos(\theta_{\boldsymbol{y}} - \theta_{\boldsymbol{x}})) = 0$$

if and only if $r_{\boldsymbol{x}} = r_{\boldsymbol{y}}$ and $\theta_{\boldsymbol{x}} = \theta_{\boldsymbol{y}}$; namely, if and only if $\boldsymbol{x} = \boldsymbol{y}$. Thus we conclude the proof. ☐

Corollary 6.4.2. *The complex-valued function* d *takes values in the set*

$$\{z \in \mathbb{C} : \operatorname{Re}(z) > 0,\ \operatorname{Im}(z) \geq 0\} \cup \{0\}.$$

Moreover, $\mathrm{d}(\boldsymbol{x}, \boldsymbol{y})$ *vanishes if and only if* $\boldsymbol{x} = \boldsymbol{y}$.

Remark **6.4.3.** *The usual distance between two points* $\boldsymbol{x}$ *and* $\boldsymbol{y}$ *can be written as follows:*

$$|\boldsymbol{x} - \boldsymbol{y}| = \left|r_{\boldsymbol{x}}\,\mathrm{e}^{i\theta_{\boldsymbol{x}}} - r_{\boldsymbol{y}}\,\mathrm{e}^{i\theta_{\boldsymbol{y}}}\right| = \sqrt{(r_{\boldsymbol{x}}\,\mathrm{e}^{i\theta_{\boldsymbol{x}}} - r_{\boldsymbol{y}}\,\mathrm{e}^{i\theta_{\boldsymbol{y}}})(r_{\boldsymbol{x}}\,\mathrm{e}^{-i\theta_{\boldsymbol{x}}} - r_{\boldsymbol{y}}\,\mathrm{e}^{-i\theta_{\boldsymbol{y}}})}.$$

If we substitute in the previous equation the radial coordinates $r_{\boldsymbol{x}}$ *and* $r_{\boldsymbol{y}}$ *by the complex values* $\hat{r}(r_{\boldsymbol{x}})$ *and* $\hat{r}(r_{\boldsymbol{y}})$*, respectively, we obtain the complex-valued function* $\mathrm{d}(\boldsymbol{x}, \boldsymbol{y})$*. In fact, it is immediate to deduce from (6.13) that*

$$\mathrm{d}(\boldsymbol{x}, \boldsymbol{y}) = \sqrt{(\hat{r}_{\boldsymbol{x}}\,\mathrm{e}^{i\theta_{\boldsymbol{x}}} - \hat{r}_{\boldsymbol{y}}\,\mathrm{e}^{i\theta_{\boldsymbol{y}}})(\hat{r}_{\boldsymbol{x}}\,\mathrm{e}^{-i\theta_{\boldsymbol{x}}} - \hat{r}_{\boldsymbol{y}}\,\mathrm{e}^{-i\theta_{\boldsymbol{y}}})}. \tag{6.14}$$

The following lemma will play a key role in the subsequent analysis. It allows us to compare $|\mathrm{d}(\boldsymbol{x},\boldsymbol{y})|$ with the standard Euclidean distance for $\boldsymbol{x}$ and $\boldsymbol{y}$ sufficiently close.

Lemma 6.4.4. *For fixed $\boldsymbol{x} \in \mathrm{D}$, there exist three positive constants C_1, C_2 and ρ, which depend on $\boldsymbol{x}$, such that,*

$$C_1 |\boldsymbol{x}-\boldsymbol{y}| \le |\mathrm{d}(\boldsymbol{x},\boldsymbol{y})| \le C_2 |\boldsymbol{x}-\boldsymbol{y}|,$$

for all $\boldsymbol{y} \in \mathrm{D}$ such that $|\boldsymbol{y}-\boldsymbol{x}| < \rho$.

Proof. Let $T_\pm : \mathrm{D} \to \mathbb{R}^2$ be defined by $T_\pm \boldsymbol{x} := (\mathrm{Re}(\hat{r}_{\boldsymbol{x}}\,\mathrm{e}^{\pm i\theta_{\boldsymbol{x}}}), \mathrm{Im}(\hat{r}_{\boldsymbol{x}}\,\mathrm{e}^{\pm i\theta_{\boldsymbol{x}}}))$. Because of (6.14) we can write

$$|\mathrm{d}(\boldsymbol{x},\boldsymbol{y})| = \sqrt{|T_+\boldsymbol{x} - T_+\boldsymbol{y}|\,|T_-\boldsymbol{x} - T_-\boldsymbol{y}|}. \tag{6.15}$$

To prove the lemma we will study the smoothness and invertibility of $T_\pm$. For $\boldsymbol{x} = (x_1, x_2) \in \mathrm{D}$, let $r := |\boldsymbol{x}| \in (R, R^\star)$ and $s(r) := \frac{1}{\omega r}\int_R^r \sigma(\xi) d\xi$. Hence

$$\begin{aligned} T_\pm \boldsymbol{x} &= (x_1 \mp x_2 s(r), \pm x_2 + x_1 s(r)), \\ DT_\pm \boldsymbol{x} &= \begin{pmatrix} 1 \mp \frac{x_1 x_2}{r} s'(r) & \mp s(r) \mp \frac{x_2^2}{r} s'(r) \\ s(r) + \frac{x_1^2}{r} s'(r) & \pm 1 + \frac{x_1 x_2}{r} s'(r) \end{pmatrix}, \end{aligned}$$

so that $T_\pm \in \mathcal{C}^1(\mathrm{D})$, and $\det(DT_\pm \boldsymbol{x}) = \pm(1 + s^2(r) + r s(r) s'(r)) \neq 0$, the latter because $s(r) \ge 0$ and

$$s'(r) = \frac{1}{\omega r}\left(\sigma(r) - \frac{1}{r}\int_R^r \sigma(\xi) d\xi\right) \ge \frac{1}{\omega r}\left(\sigma(r) - \frac{1}{r-R}\int_R^r \sigma(\xi) d\xi\right) \ge 0.$$

Therefore, as a consequence of the inverse function theorem, $T_\pm$ is invertible in a neighborhood of $T_\pm \boldsymbol{x}$ and its inverse is $\mathcal{C}^1$ in the same neighborhood. Consequently, $\exists C_1^\pm$, $C_2^\pm$, $\rho_\pm > 0$ such that $\forall \boldsymbol{y} \in \mathrm{D}$, if $|\boldsymbol{x}-\boldsymbol{y}| \le \rho_\pm$, then

$$C_1^\pm |\boldsymbol{x}-\boldsymbol{y}| \le |T_\pm \boldsymbol{x} - T_\pm \boldsymbol{y}| \le C_2^\pm |\boldsymbol{x}-\boldsymbol{y}|;$$

which together with (6.15) allow us to conclude the proof. □

For fixed $\boldsymbol{x} \in \mathrm{D}$, $\mathrm{d}(\boldsymbol{x},\cdot)$ is infinitely differentiable with respect to $\theta_{\boldsymbol{y}}$, but the differentiability with respect to $r_{\boldsymbol{y}}$ depends on the regularity of σ. The assumed smoothness of σ is enough to ensure that $\mathrm{d}(\boldsymbol{x},\cdot) \in \mathcal{C}^2(\mathrm{D} \setminus \{\boldsymbol{x}\})$. The following lemma collects several limits that will be used in the sequel. The corresponding proofs are straightforward. From now on, to simplify the notation, we denote $\gamma_{\boldsymbol{y}} := \gamma(r_{\boldsymbol{y}})$ and $\hat{\gamma}_{\boldsymbol{y}} := \hat{\gamma}(r_{\boldsymbol{y}})$. Accordingly, we denote $\boldsymbol{A}_{\boldsymbol{y}}$ instead of $\boldsymbol{A}$ when $\gamma_{\boldsymbol{y}}$ and $\hat{\gamma}_{\boldsymbol{y}}$ are used in the definition (6.12).

Lemma 6.4.5. *For fixed $\boldsymbol{x} \in \mathrm{D}$, there holds uniformly in $\theta_{\boldsymbol{y}} \in (-\pi, \pi]$:*

$$\boldsymbol{i)} \lim_{r_{\boldsymbol{y}} \to R^\star} \operatorname{Im}(\mathrm{d}(\boldsymbol{x}, \boldsymbol{y})) = +\infty, \tag{6.16}$$

$$\boldsymbol{ii)} \, |\mathrm{d}(\boldsymbol{x}, \boldsymbol{y})| = O\left(\operatorname{Im}(\mathrm{d}(\boldsymbol{x}, \boldsymbol{y}))\right), \qquad \text{as } r_{\boldsymbol{y}} \to R^\star, \tag{6.17}$$

$$\boldsymbol{iii)} \lim_{r_{\boldsymbol{y}} \to R^\star} \frac{\mathrm{d}(\boldsymbol{x}, \boldsymbol{y})}{\hat{r}_{\boldsymbol{y}}} = 1, \tag{6.18}$$

$$\boldsymbol{iv)} \left| \frac{\partial \mathrm{d}(\boldsymbol{x}, \boldsymbol{y})}{\partial \theta_{\boldsymbol{y}}} \right| = 1, \qquad \text{as } r_{\boldsymbol{y}} \to R^\star. \tag{6.19}$$

Proof. ***i)*** We work with the square of the complex 'distance' $\mathrm{d}(\cdot,\cdot)^2$. In fact, we have

$$\begin{aligned}
\mathrm{d}(\boldsymbol{x}, \boldsymbol{y})^2 &= \hat{r}_{\boldsymbol{x}}^2 + \hat{r}_{\boldsymbol{y}}^2 - 2\hat{r}_{\boldsymbol{x}}\hat{r}_{\boldsymbol{y}} \cos(\theta_{\boldsymbol{y}} - \theta_{\boldsymbol{x}}) = \operatorname{Re}(\hat{r}_{\boldsymbol{x}})^2 - \operatorname{Im}(\hat{r}_{\boldsymbol{x}})^2 + 2i \operatorname{Re}(\hat{r}_{\boldsymbol{x}}) \operatorname{Im}(\hat{r}_{\boldsymbol{x}}) \\
&\quad + \operatorname{Re}(\hat{r}_{\boldsymbol{y}})^2 - \operatorname{Im}(\hat{r}_{\boldsymbol{y}})^2 + 2i \operatorname{Re}(\hat{r}_{\boldsymbol{y}}) \operatorname{Im}(\hat{r}_{\boldsymbol{y}}) - 2\cos(\theta_{\boldsymbol{y}} - \theta_{\boldsymbol{x}})[\operatorname{Re}(\hat{r}_{\boldsymbol{x}}) \operatorname{Re}(\hat{r}_{\boldsymbol{y}}) \\
&\quad - \operatorname{Im}(\hat{r}_{\boldsymbol{x}}) \operatorname{Im}(\hat{r}_{\boldsymbol{y}}) + i(\operatorname{Re}(\hat{r}_{\boldsymbol{x}}) \operatorname{Im}(\hat{r}_{\boldsymbol{y}}) + \operatorname{Re}(\hat{r}_{\boldsymbol{y}}) \operatorname{Im}(\hat{r}_{\boldsymbol{x}}))] \\
&= \operatorname{Re}(\hat{r}_{\boldsymbol{x}})^2 + \operatorname{Re}(\hat{r}_{\boldsymbol{y}})^2 - \operatorname{Im}(\hat{r}_{\boldsymbol{x}})^2 - 2\operatorname{Re}(\hat{r}_{\boldsymbol{x}}) \operatorname{Re}(\hat{r}_{\boldsymbol{y}}) \cos(\theta_{\boldsymbol{y}} - \theta_{\boldsymbol{x}}) \\
&\quad + \operatorname{Im}(\hat{r}_{\boldsymbol{y}})(-\operatorname{Im}(\hat{r}_{\boldsymbol{y}}) + 2\operatorname{Im}(\hat{r}_{\boldsymbol{x}}) \cos(\theta_{\boldsymbol{y}} - \theta_{\boldsymbol{x}})) + 2i[\operatorname{Re}(\hat{r}_{\boldsymbol{x}}) \operatorname{Im}(\hat{r}_{\boldsymbol{x}}) \\
&\quad - \operatorname{Re}(\hat{r}_{\boldsymbol{y}}) \operatorname{Im}(\hat{r}_{\boldsymbol{x}}) \cos(\theta_{\boldsymbol{y}} - \theta_{\boldsymbol{x}}) + \operatorname{Im}(\hat{r}_{\boldsymbol{y}})(\operatorname{Re}(\hat{r}_{\boldsymbol{y}}) - \operatorname{Re}(\hat{r}_{\boldsymbol{x}}) \cos(\theta_{\boldsymbol{y}} - \theta_{\boldsymbol{x}}))].
\end{aligned}$$

It is important to remember that, in this case, $\operatorname{Re}(\hat{r}_{\boldsymbol{x}})$, $\operatorname{Re}(\hat{r}_{\boldsymbol{y}})$, and $\operatorname{Im}(\hat{r}_{\boldsymbol{x}})$ remain bounded and only $\operatorname{Im}(\hat{r}_{\boldsymbol{y}})$ tends to infinity when $r_{\boldsymbol{y}}$ goes to $R^\star$. Since the term in the real part of $\mathrm{d}(\cdot,\cdot)^2$ involving $\operatorname{Im}(\hat{r}_{\boldsymbol{y}})$ is $\operatorname{Im}(\hat{r}_{\boldsymbol{y}})(-\operatorname{Im}(\hat{r}_{\boldsymbol{y}}) + 2\operatorname{Im}(\hat{r}_{\boldsymbol{x}}) \cos(\theta_{\boldsymbol{y}} - \theta_{\boldsymbol{x}}))$, then

$$\lim_{r_{\boldsymbol{y}} \to R^\star} \operatorname{Re}(\mathrm{d}(\boldsymbol{x}, \boldsymbol{y})^2) = -\infty,$$

uniformly in all the directions $\theta_{\boldsymbol{y}} \in (-\pi, \pi]$, i.e., for all $A < 0$ there exists $\delta > 0$ such that, if $|r_{\boldsymbol{y}} - R^\star| < \delta$ then $\operatorname{Re}(\mathrm{d}(\boldsymbol{x}, \boldsymbol{y})^2) < A$.

Meanwhile, the term in the imaginary part of $\mathrm{d}(\cdot,\cdot)^2$ involving $\operatorname{Im}(\hat{r}_{\boldsymbol{y}})$ appears multiplied by the factor $(\operatorname{Re}(\hat{r}_{\boldsymbol{y}}) - \operatorname{Re}(\hat{r}_{\boldsymbol{x}}) \cos(\theta_{\boldsymbol{y}} - \theta_{\boldsymbol{x}}))$. Since we can assume that $r_{\boldsymbol{y}} > r_{\boldsymbol{x}}$ (because $r_{\boldsymbol{x}} < R^\star$ is fixed while $r_{\boldsymbol{y}}$ goes to $R^\star$), then $\operatorname{Re}(\hat{r}_{\boldsymbol{y}}) - \operatorname{Re}(\hat{r}_{\boldsymbol{x}}) \cos(\theta_{\boldsymbol{y}} - \theta_{\boldsymbol{x}}) > 0$ and we have

$$\lim_{r_{\boldsymbol{y}} \to R^\star} \operatorname{Im}(\mathrm{d}(\boldsymbol{x}, \boldsymbol{y})^2) = +\infty,$$

uniformly in all the directions $\theta_{\boldsymbol{y}} \in (-\pi, \pi]$.

ii)If $\mathrm{d}(\boldsymbol{x}, \boldsymbol{y}) = a + ib$ with $a, b \in \mathbb{R}$, then $a^2 - b^2 \to -\infty$ and $ab \to +\infty$ when $r_{\boldsymbol{y}} \to R^\star$. Hence $|b| > |a| > 0$ with $|b| \to +\infty$ when $r_{\boldsymbol{y}} \to R^\star$, uniformly in all the directions $\theta_{\boldsymbol{y}} \in (-\pi, \pi]$. Since ab goes to infinity uniformly, for all $A < 0$ there exists $\delta > 0$ such that, if $|r_{\boldsymbol{y}} - R^\star| < \delta$ then $ab > A$ and hence $A < ab < |b|^2$ obtaining that the limit for $|b|$ is also uniform.

Moreover, terms a and b have the same sign, and because of the choice of the positive root in the definition of the complex distance $\mathrm{d}(\cdot,\cdot)$, we can conclude (6.17). On the other hand, since $|b| > |a| > 0$ when $r_{\boldsymbol{y}} \to R^\star$, we have

$$\lim_{r_{\boldsymbol{y}} \to R^\star} \frac{|\mathrm{d}(\boldsymbol{x},\boldsymbol{y})|}{\operatorname{Im}(\mathrm{d}(\boldsymbol{x},\boldsymbol{y}))} \leq \sqrt{2},$$

obviously uniformly with respect to $\theta_{\boldsymbol{y}}$.

iii) Taking again into account that only the term $\operatorname{Im}(\hat{r}_{\boldsymbol{y}})$ is unbounded in $\mathrm{d}(\boldsymbol{x},\boldsymbol{y})^2$ and in $\hat{r}_{\boldsymbol{y}}^2$, we have

$$\begin{aligned} \lim_{r_{\boldsymbol{y}} \to R^\star} \frac{\mathrm{d}(\boldsymbol{x},\boldsymbol{y})^2}{\hat{r}_{\boldsymbol{y}}^2} = {} & \lim_{r_{\boldsymbol{y}} \to R^\star} \frac{\operatorname{Im}(\hat{r}_{\boldsymbol{y}})(-\operatorname{Im}(\hat{r}_{\boldsymbol{y}}) + 2\operatorname{Im}(\hat{r}_{\boldsymbol{x}})\cos(\theta_{\boldsymbol{y}} - \theta_{\boldsymbol{x}}))}{-\operatorname{Im}(\hat{r}_{\boldsymbol{y}})^2 + 2i\operatorname{Re}(\hat{r}_{\boldsymbol{y}})\operatorname{Im}(\hat{r}_{\boldsymbol{y}})} \\ & + \lim_{r_{\boldsymbol{y}} \to R^\star} \frac{2i\operatorname{Im}(\hat{r}_{\boldsymbol{y}})(\operatorname{Re}(\hat{r}_{\boldsymbol{y}}) - \operatorname{Re}(\hat{r}_{\boldsymbol{x}})\cos(\theta_{\boldsymbol{y}} - \theta_{\boldsymbol{x}}))}{-\operatorname{Im}(\hat{r}_{\boldsymbol{y}})^2 + 2i\operatorname{Re}(\hat{r}_{\boldsymbol{y}})\operatorname{Im}(\hat{r}_{\boldsymbol{y}})} = 1. \end{aligned}$$

Hence, the limit in (6.18) is equal to $+1$ or -1. If we take into account that we have chosen the real part of $\mathrm{d}(\boldsymbol{x},\boldsymbol{y})$ to be positive and that the real part of $\hat{r}_{\boldsymbol{y}}$ is also positive, then only 1 is possible. It is immediate to verify that the previous limit is uniform since the dependence of $\mathrm{d}(\boldsymbol{x},\boldsymbol{y})$ with respect to $\theta_{\boldsymbol{y}}$ is continuous in the compact subset $(-\pi,\pi]$ and $\operatorname{Im}(\hat{r}_{\boldsymbol{y}}) \to +\infty$ uniformly in all the directions when r goes to $R^\star$.

iv) It is immediate to prove that $\frac{\partial \hat{r}_{\boldsymbol{y}}}{\partial r_{\boldsymbol{y}}} = \gamma_{\boldsymbol{y}}$. Then, applying the inverse function theorem, we have

$$\lim_{r_{\boldsymbol{y}} \to R^\star} \frac{\partial \mathrm{d}(\boldsymbol{x},\boldsymbol{y})}{\partial r_{\boldsymbol{y}}} \left(\frac{\partial \hat{r}_{\boldsymbol{y}}}{\partial r_{\boldsymbol{y}}}\right)^{-1} = \lim_{r_{\boldsymbol{y}} \to R^\star} \frac{\partial \mathrm{d}(\boldsymbol{x},\boldsymbol{y})}{\partial \hat{r}_{\boldsymbol{y}}} = \lim_{r_{\boldsymbol{y}} \to R^\star} \frac{\hat{r}_{\boldsymbol{y}} - \hat{r}_{\boldsymbol{x}}\cos(\theta_{\boldsymbol{y}} - \theta_{\boldsymbol{x}})}{\mathrm{d}(\boldsymbol{x},\boldsymbol{y})} = 1.$$

Obviously, the uniformity in all the directions of this limit is a direct consequence of the same property proved for (6.18). □

Now we are in a position to compute a fundamental solution of the PML equation, i.e., a solution Φ (in the sense of distributions) of

$$-\operatorname{div}_{\boldsymbol{y}}(\boldsymbol{A}_{\boldsymbol{y}} \,\mathbf{grad}_{\boldsymbol{y}}\, \Phi(\boldsymbol{x},\boldsymbol{y})) - \gamma_{\boldsymbol{y}}\hat{\gamma}_{\boldsymbol{y}} k^2 \Phi(\boldsymbol{x},\boldsymbol{y}) = \delta_{\boldsymbol{x}} \qquad \text{in } \mathcal{D}'(\mathrm{D}), \tag{6.20}$$

$\delta_{\boldsymbol{x}}$ being the Dirac's delta supported at the point $\boldsymbol{x} \in \mathrm{D}$.

Theorem 6.4.6. *For fixed* $\boldsymbol{x} \in \mathrm{D}$*,*

$$\Phi^+(\boldsymbol{x},\boldsymbol{y}) := \frac{i}{4}\,\mathrm{H}_0^{(1)}(k\mathrm{d}(\boldsymbol{x},\boldsymbol{y})), \tag{6.21}$$

and

$$\Phi^-(\boldsymbol{x},\boldsymbol{y}) := -\frac{i}{4}\,\mathrm{H}_0^{(2)}(k\mathrm{d}(\boldsymbol{x},\boldsymbol{y})), \tag{6.22}$$

are solutions of (6.20).

Proof. Let $\boldsymbol{x} \in \mathrm{D}$ be fixed. First, we are going to prove that

$$-\operatorname{div}_{\boldsymbol{y}}(\boldsymbol{A}_{\boldsymbol{y}}\, \mathbf{grad}_{\boldsymbol{y}}\, \Phi^{\pm}(\boldsymbol{x},\boldsymbol{y})) - \gamma_{\boldsymbol{y}}\hat{\gamma}_{\boldsymbol{y}} k^2 \Phi^{\pm}(\boldsymbol{x},\boldsymbol{y}) = 0, \tag{6.23}$$

for all $\boldsymbol{y} \in \mathrm{D} \setminus \{\boldsymbol{x}\}$. With this purpose, (6.23) can be immediately written as follows:

$$-\frac{1}{r_{\boldsymbol{y}}}\left(\frac{\partial}{\partial r_{\boldsymbol{y}}}\left(\frac{\hat{\gamma}_{\boldsymbol{y}} r_{\boldsymbol{y}}}{\gamma_{\boldsymbol{y}}}\frac{\partial \Phi^{\pm}(\boldsymbol{x},\boldsymbol{y})}{\partial r_{\boldsymbol{y}}}\right) + \frac{\gamma_{\boldsymbol{y}}}{\hat{\gamma}_{\boldsymbol{y}} r_{\boldsymbol{y}}}\frac{\partial^2 \Phi^{\pm}(\boldsymbol{x},\boldsymbol{y})}{\partial \theta_{\boldsymbol{y}}^2}\right) - \gamma_{\boldsymbol{y}}\hat{\gamma}_{\boldsymbol{y}} k^2 \Phi^{\pm}(\boldsymbol{x},\boldsymbol{y}) = 0. \tag{6.24}$$

Now $\mathrm{d}(\boldsymbol{x},\cdot) \in \mathcal{C}^2(\mathrm{D} \setminus \{\boldsymbol{x}\})$ and, according to Corollary 6.4.2, it takes values in the half complex plane $\operatorname{Re} z > 0$. Hence $\Phi^{\pm} \in \mathcal{C}^2(\mathrm{D} \setminus \{\boldsymbol{x}\})$, since the Hankel functions are analytical in the whole complex plane except along the negative real axis.

Since $\mathrm{H}_0^{(1)}(z)$ and $\mathrm{H}_0^{(2)}(z)$ are solutions of the following Bessel equation (see [2]):

$$q''(z) + \frac{1}{z} q'(z) + q(z) = 0, \qquad z \neq 0,$$

the change of variable $z = k\mathrm{d}(\boldsymbol{x},\boldsymbol{y})$ allows us to conclude (6.24).

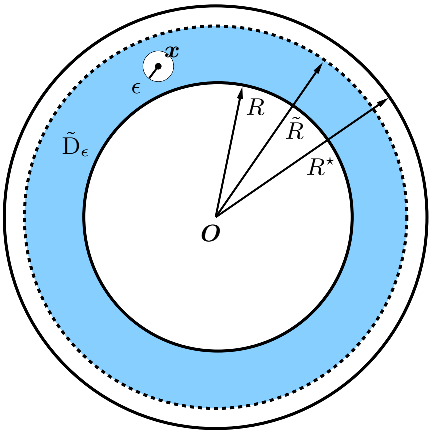

Figure 6.3: Domain $\tilde{\mathrm{D}}_{\epsilon}$.

Next, let $\varphi \in \mathcal{D}(\mathrm{D})$ and $\tilde{R} \in (R, R^{\star})$ be such that $\boldsymbol{x} \in \tilde{\mathrm{D}}$ and $\operatorname{supp} \varphi \subset \tilde{\mathrm{D}}$ with $\tilde{\mathrm{D}} := \{\boldsymbol{x} \in \mathbb{R}^2 : R < |\boldsymbol{x}| < \tilde{R}\}$. Let $\epsilon > 0$ be sufficiently small so that $S(\boldsymbol{x},\epsilon) := \{\boldsymbol{x} \in \mathbb{R}^2 : |\boldsymbol{x} - \boldsymbol{y}| = \epsilon\} \subset \tilde{\mathrm{D}}$. Finally, let $\tilde{\mathrm{D}}_{\epsilon} := \{\boldsymbol{y} \in \tilde{\mathrm{D}} : |\boldsymbol{x} - \boldsymbol{y}| > \epsilon\}$ (see Figure 6.3) and $\boldsymbol{n}$ be its outward unit normal vector. There holds

$$\begin{aligned}
&-\langle \operatorname{div}_{\boldsymbol{y}}(\boldsymbol{A}_{\boldsymbol{y}}\, \mathbf{grad}_{\boldsymbol{y}}\, \Phi^{\pm}(\boldsymbol{x},\boldsymbol{y})) + \gamma_{\boldsymbol{y}}\hat{\gamma}_{\boldsymbol{y}} k^2 \Phi^{\pm}(\boldsymbol{x},\boldsymbol{y}), \varphi\rangle \\
&\quad = -\lim_{\epsilon\to 0}\int_{\tilde{\mathrm{D}}_{\epsilon}} \Phi^{\pm}(\boldsymbol{x},\boldsymbol{y})(\operatorname{div}_{\boldsymbol{y}}(\boldsymbol{A}_{\boldsymbol{y}}\, \mathbf{grad}_{\boldsymbol{y}}\, \varphi(\boldsymbol{y})) + \gamma_{\boldsymbol{y}}\hat{\gamma}_{\boldsymbol{y}} k^2 \varphi(\boldsymbol{y}))\, d\boldsymbol{y} \\
&\quad = \lim_{\epsilon\to 0}\left(\int_{S(\boldsymbol{x},\epsilon)} \boldsymbol{A}_{\boldsymbol{y}}\, \mathbf{grad}_{\boldsymbol{y}}\, \Phi^{\pm}(\boldsymbol{x},\boldsymbol{y}) \cdot \boldsymbol{n}\, \varphi(\boldsymbol{y})\, dS_{\boldsymbol{y}}\right. \\
&\qquad\qquad \left. - \int_{S(\boldsymbol{x},\epsilon)} \boldsymbol{A}_{\boldsymbol{y}}\, \mathbf{grad}_{\boldsymbol{y}}\, \varphi(\boldsymbol{y}) \cdot \boldsymbol{n}\, \Phi^{\pm}(\boldsymbol{x},\boldsymbol{y})\, dS_{\boldsymbol{y}}\right) = \varphi(\boldsymbol{x}) = \langle \delta_{\boldsymbol{x}}, \varphi\rangle,
\end{aligned}$$

where we have used (6.23) and Lemma 6.10.3 (which is proved in Section 6.10 below). Thus we conclude the theorem. ☐

To finish this section, we settle some decay properties of the fundamental solution Φ^+.

Lemma 6.4.7. *For fixed $\boldsymbol{x} \in \mathrm{D}$, there holds uniformly in $\theta_{\boldsymbol{y}} \in (-\pi, \pi]$:*

$$\lim_{r_{\boldsymbol{y}} \to R^\star} \sqrt{\hat{\gamma}_{\boldsymbol{y}} \gamma_{\boldsymbol{y}}} \Phi^+(\boldsymbol{x}, \boldsymbol{y}) = 0,$$

$$\lim_{r_{\boldsymbol{y}} \to R^\star} \sqrt{\frac{\hat{\gamma}_{\boldsymbol{y}}}{\gamma_{\boldsymbol{y}}}} \frac{\partial \Phi^+(\boldsymbol{x}, \boldsymbol{y})}{\partial r_{\boldsymbol{y}}} = 0,$$

$$\lim_{r_{\boldsymbol{y}} \to R^\star} \sqrt{\frac{\gamma_{\boldsymbol{y}}}{\hat{\gamma}_{\boldsymbol{y}}}} \frac{\partial \Phi^+(\boldsymbol{x}, \boldsymbol{y})}{\partial \theta_{\boldsymbol{y}}} = 0.$$

Proof. Let $\boldsymbol{x} \in \mathrm{D}$ fixed. Using the asymptotic classical estimates for Hankel functions (see [103]) and Lemma 6.4.5, we can check that $\Phi^+(\boldsymbol{x}, \cdot)$ and their derivatives go to zero exponentially and uniformly in all the directions, as $r_{\boldsymbol{y}} \to R^\star$. In fact, these three limits are satisfied for each Hankel function of first kind and order n.

From item *i)* of Lemma 6.4.5, $\mathrm{Im}(\mathrm{d}(\boldsymbol{x}, \boldsymbol{y}))$ tends to infinity uniformly in all directions $\theta_{\boldsymbol{y}} \in (-\pi, \pi]$ when $r_{\boldsymbol{y}}$ goes to $R^\star$. Hence, using the asymptotic behavior (6.82) and (6.83), we can check that the first kind Hankel functions and their derivatives go to zero exponentially while those of the second kind (and their derivatives) increase exponentially, in both cases uniformly in all the directions.

Indeed, using the asymptotic behavior (6.82) and the limits (6.17)-(6.19), the outcoming fundamental solution satisfies,

$$\begin{aligned}
&\lim_{r_{\boldsymbol{y}} \to R^\star} \left| \sqrt{\hat{\gamma}_{\boldsymbol{y}} \gamma_{\boldsymbol{y}}}\, \mathrm{H}_n^{(1)}(k \mathrm{d}(\boldsymbol{x}, \boldsymbol{y})) \right| \\
&= \lim_{r_{\boldsymbol{y}} \to R^\star} \left| \sqrt{\frac{2 \hat{\gamma}_{\boldsymbol{y}} \gamma_{\boldsymbol{y}}}{\pi k \mathrm{d}(\boldsymbol{x}, \boldsymbol{y})}}\, \mathrm{e}^{i(k \mathrm{d}(\boldsymbol{x}, \boldsymbol{y}) - \frac{n\pi}{2} - \frac{\pi}{4})} \left(1 + O\left(\frac{1}{|\mathrm{d}(\boldsymbol{x}, \boldsymbol{y})|} \right) \right) \right| \\
&= \sqrt{\frac{2}{\pi k R^\star}} \lim_{r_{\boldsymbol{y}} \to R^\star} \left| \sqrt{\gamma_{\boldsymbol{y}}}\, \mathrm{e}^{i k \hat{r}_{\boldsymbol{y}}} \left(1 + O\left(\frac{1}{|\mathrm{d}(\boldsymbol{x}, \boldsymbol{y})|} \right) \right) \right| = 0,
\end{aligned} \tag{6.25}$$

$$\begin{aligned}
&\lim_{r_{\boldsymbol{y}} \to R^\star} \left| \sqrt{\frac{\hat{\gamma}_{\boldsymbol{y}}}{\gamma_{\boldsymbol{y}}}} \frac{\partial\, \mathrm{H}_n^{(1)}(k \mathrm{d}(\boldsymbol{x}, \boldsymbol{y}))}{\partial r_{\boldsymbol{y}}} \right| \\
&= \lim_{r_{\boldsymbol{y}} \to R^\star} \left| \sqrt{\frac{\hat{\gamma}_{\boldsymbol{y}}}{\gamma_{\boldsymbol{y}}}} \frac{\partial \mathrm{d}(\boldsymbol{x}, \boldsymbol{y})}{\partial r_{\boldsymbol{y}}} i k \sqrt{\frac{2}{\pi k \mathrm{d}(\boldsymbol{x}, \boldsymbol{y})}}\, \mathrm{e}^{i(k \mathrm{d}(\boldsymbol{x}, \boldsymbol{y}) - \frac{n\pi}{2} - \frac{\pi}{4})} \left(1 + O\left(\frac{1}{|\mathrm{d}(\boldsymbol{x}, \boldsymbol{y})|} \right) \right) \right| \\
&= \sqrt{\frac{2k}{\pi R^\star}} \lim_{r_{\boldsymbol{y}} \to R^\star} \left| \sqrt{\gamma_{\boldsymbol{y}}}\, \mathrm{e}^{i k \hat{r}_{\boldsymbol{y}}} \left(1 + O\left(\frac{1}{|\mathrm{d}(\boldsymbol{x}, \boldsymbol{y})|} \right) \right) \right| = 0,
\end{aligned} \tag{6.26}$$

and

$$\begin{aligned}
&\lim_{r_{\boldsymbol{y}}\to R^\star}\left|\sqrt{\frac{\gamma_{\boldsymbol{y}}}{\hat{\gamma}_{\boldsymbol{y}}}}\frac{\partial\,\mathrm{H}_n^{(1)}(k\mathrm{d}(\boldsymbol{x},\boldsymbol{y}))}{\partial\theta_{\boldsymbol{y}}}\right| \\
&= \lim_{r_{\boldsymbol{y}}\to R^\star}\left|\sqrt{\frac{\gamma_{\boldsymbol{y}}}{\hat{\gamma}_{\boldsymbol{y}}}}\frac{\partial\mathrm{d}(\boldsymbol{x},\boldsymbol{y})}{\partial\theta_{\boldsymbol{y}}}ik\sqrt{\frac{2}{\pi k\mathrm{d}(\boldsymbol{x},\boldsymbol{y})}}\,\mathrm{e}^{i(k\mathrm{d}(\boldsymbol{x},\boldsymbol{y})-\frac{n\pi}{2}-\frac{\pi}{4})}\left(1+O\left(\frac{1}{|\mathrm{d}(\boldsymbol{x},\boldsymbol{y})|}\right)\right)\right| \\
&= \sqrt{\frac{2k}{\pi R^\star}}\lim_{r_{\boldsymbol{y}}\to R^\star}\left|\frac{\sqrt{\gamma_{\boldsymbol{y}}}}{\hat{\gamma}_{\boldsymbol{y}}}\,\mathrm{e}^{ik\hat{r}_{\boldsymbol{y}}}\left(1+O\left(\frac{1}{|\mathrm{d}(\boldsymbol{x},\boldsymbol{y})|}\right)\right)\right| = 0, \qquad (6.27)
\end{aligned}$$

In the previous limits we have taken into account that $\lim_{r_{\boldsymbol{y}}\to R^\star}\sqrt{\gamma_{\boldsymbol{y}}}\,\mathrm{e}^{ik\hat{r}_{\boldsymbol{y}}}=0$. In fact,

$$\lim_{r_{\boldsymbol{y}}\to R^\star}\sqrt{\gamma_{\boldsymbol{y}}}\,\mathrm{e}^{ik\hat{r}_{\boldsymbol{y}}} = \left(\frac{1}{2ik}\lim_{r_{\boldsymbol{y}}\to R^\star}\frac{\partial}{\partial r_{\boldsymbol{y}}}(\,\mathrm{e}^{2ik\hat{r}_{\boldsymbol{y}}})\right)^{\frac{1}{2}} = \left(\frac{1}{2ik}\lim_{r_{\boldsymbol{y}}\to R^\star}\frac{\mathrm{e}^{2ik\hat{r}_{\boldsymbol{y}}}}{r_{\boldsymbol{y}}-R^\star}\right)^{\frac{1}{2}} = 0,$$

because of the definition of $\hat{r}$. Moreover, all the previous limits are uniformly in all the directions $\theta_{\boldsymbol{y}}\in(-\pi,\pi]$ since $\theta_{\boldsymbol{y}}$ is not involved in the definition of $\hat{r}_{\boldsymbol{y}}$. $\square$

6.5 PML integral representation formula

The aim of this section is to obtain an integral representation of the solutions of the PML equation (6.8). We search for smooth solutions which, furthermore, belong to the functional space

$$\begin{aligned}
\mathrm{V} := \Bigg\{ q\in\mathrm{H}^1_{\mathrm{loc}}(\mathrm{D}) : \|q\|^2_{\mathrm{V}} &:= \int_R^{R^\star}\int_{-\pi}^{\pi}\left|\frac{\hat{\gamma}(r)r}{\gamma(r)}\right|\left|\frac{\partial q}{\partial r}\right|^2 d\theta\,dr \\
&+ \int_R^{R^\star}\int_{-\pi}^{\pi}\left|\frac{\gamma(r)}{\hat{\gamma}(r)r}\right|\left|\frac{\partial q}{\partial\theta}\right|^2 d\theta\,dr + \int_R^{R^\star}\int_{-\pi}^{\pi}|\hat{\gamma}(r)\gamma(r)r|\,|q|^2\,d\theta\,dr < +\infty\Bigg\}.
\end{aligned}$$

As a first step, we restrict our analysis to solutions of (6.8) in the space

$$\mathrm{W} := V\cap\mathcal{C}^1(\mathrm{D}^\star)\cap\mathcal{C}^2(D),$$

where

$$\mathrm{D}^\star := \mathrm{D}\cup S_R = \{\boldsymbol{x}\in\mathbb{R}^2 : R\le|\boldsymbol{x}|<R^\star\}.$$

Since the weights involved in the definition of V belong to $\mathrm{L}^1_{\mathrm{loc}}(R,R^\star)$ and are positive, V is a Banach space when endowed with the norm $\|\cdot\|_{\mathrm{V}}$ (see Kufner & Sändig [75]) and, moreover, $\mathrm{V}\subset\mathrm{H}^1_{\mathrm{loc}}(\mathrm{D}^\star)$, so that $q\in\mathrm{H}^1(K)$ even for compact sets K intersecting S_R.

First, we prove two preliminary results.

Lemma 6.5.1. *If $q \in \mathrm{V}$, then*

$$\lim_{\tilde{R}\to R^\star} \int_{S_{\tilde{R}}} |\hat{\gamma}|\, |q|^2 \; dS = 0.$$

Proof. For $q \in \mathrm{V}$, we define the complex-valued function F given by

$$F(r) := \int_{S_r} \hat{\gamma}\, |q|^2 \; dS = \int_{-\pi}^{\pi} r\hat{\gamma}(r)\, |q(r,\theta)|^2 \; d\theta.$$

From the definition of V, it is immediate to check that F and γF belong to $\mathrm{L}^1(R, R^\star)$. We also define

$$\begin{aligned} G(r) :&= \int_{-\pi}^{\pi} \frac{\partial}{\partial r}\left(r\hat{\gamma}(r)\, |q(r,\theta)|^2\right) \, d\theta \\ &= \gamma(r) \int_{-\pi}^{\pi} |q(r,\theta)|^2 \, d\theta + 2r\hat{\gamma}(r) \int_{-\pi}^{\pi} \operatorname{Re}\left(\frac{\partial q}{\partial r}(r,\theta)\bar{q}(r,\theta)\right) \, d\theta. \end{aligned}$$

For $q \in \mathrm{V}$, the first term in the above sum is integrable in $(R, R^\star)$. Regarding the second term, we have

$$\begin{aligned} &\int_R^{R^\star} \left| 2r\hat{\gamma}(r) \int_{-\pi}^{\pi} \operatorname{Re}\left(\frac{\partial q}{\partial r}(r,\theta)\bar{q}(r,\theta)\right) \, d\theta \right| \, dr \\ &\qquad \le 2\left(\int_R^{R^\star}\int_{-\pi}^{\pi} \left|\frac{\hat{\gamma}(r) r}{\gamma(r)}\right| \left|\frac{\partial q}{\partial r}\right|^2 \, d\theta\, dr\right)^{\frac{1}{2}} \left(\int_R^{R^\star}\int_{-\pi}^{\pi} |\hat{\gamma}(r)\gamma(r) r|\, |q|^2 \; d\theta\, dr\right)^{\frac{1}{2}}, \end{aligned}$$

which is again finite for $q \in \mathrm{V}$. Thus $G \in \mathrm{L}^1(R, R^\star)$. Moreover, straightforward computations show that G is the distributional derivative of F. Hence $F \in \mathrm{W}^{1,1}(R, R^\star)$ and, consequently, $F \in \mathcal{C}([R, R^\star])$ (see for instance Theorem VIII.2 in [44]).

Now we can conclude the lemma by showing only that $\lim_{r\to R^\star} F(r) = 0$, since $\operatorname{Re}(\gamma)$ and $\operatorname{Im}(\gamma)$ are non negative. We proceed by contradiction. Suppose $\lim_{r\to R^\star} F(r) \neq 0$; in such a case, since $|\gamma| > 1$ and γ is not integrable near $r = R^\star$, $\int_R^{R^\star} |\gamma F| \, dr = \infty$, which would contradict the fact that $\gamma F \in \mathrm{L}^1(R, R^\star)$. □

Lemma 6.5.2. *If $\hat{p} \in \mathrm{W}$ is a solution of (6.8) and $q \in \mathrm{V}$, then*

$$\lim_{\tilde{R}\to R^\star} \int_{S_{\tilde{R}}} \frac{\hat{\gamma}}{\gamma}\frac{\partial \hat{p}}{\partial r} q \, dS = 0.$$

Proof. Let $\tilde{R} \in (R, R^\star)$. Since $q \in \mathrm{V} \subset \mathrm{H}^1_{\mathrm{loc}}(\mathrm{D}^\star)$, if we multiply (6.8) by $q \in \mathrm{V}$ and integrate by parts in $\tilde{\mathrm{D}} := \{\boldsymbol{x} \in \mathbb{R}^2 : R < |\boldsymbol{x}| < \tilde{R}\}$, we obtain

$$\begin{aligned} \int_{S_{\tilde{R}}} \frac{\hat{\gamma}}{\gamma}\frac{\partial \hat{p}}{\partial r} q \, dS &= \int_{\tilde{\mathrm{D}}} \frac{\hat{\gamma}}{\gamma}\frac{\partial \hat{p}}{\partial r}\frac{\partial q}{\partial r} + \int_{\tilde{\mathrm{D}}} \frac{\gamma}{\hat{\gamma} r^2}\frac{\partial \hat{p}}{\partial \theta}\frac{\partial q}{\partial \theta} - k^2 \int_{\tilde{\mathrm{D}}} \gamma\hat{\gamma}\hat{p}q + \int_{S_R} \frac{1}{\gamma}\frac{\partial \hat{p}}{\partial r} q \, dS \\ &= \int_R^{\tilde{R}} \left[\int_{S_r} \left(\frac{\hat{\gamma}}{\gamma}\frac{\partial \hat{p}}{\partial r}\frac{\partial q}{\partial r} + \frac{\gamma}{\hat{\gamma} r^2}\frac{\partial \hat{p}}{\partial \theta}\frac{\partial q}{\partial \theta} - k^2\gamma\hat{\gamma}\hat{p}q\right) dS\right] dr + \int_{S_R} \frac{1}{\gamma}\frac{\partial \hat{p}}{\partial r} q \, dS. \end{aligned} \tag{6.28}$$

Because of the definition of V, the expression between brackets above belongs to $\mathrm{L}^1(R, R^\star)$. Consequently, if we define

$$H(\tilde{R}) := \int_{S_{\tilde{R}}} \frac{\hat{\gamma}}{\gamma} \frac{\partial \hat{p}}{\partial r} q \, dS,$$

then, according to (6.28), from [44] again we have $H \in \mathcal{C}([R, R^\star])$. On the other hand, from the Cauchy-Schwarz inequality, we have

$$\begin{aligned} \int_R^{R^\star} |\gamma(r) H(r)| \, dr &= \int_R^{R^\star} \left| \int_{-\pi}^{\pi} \hat{\gamma}(r) r \frac{\partial \hat{p}}{\partial r} q \, d\theta \right| \, dr \\ &\leq \left(\int_R^{R^\star} \int_{-\pi}^{\pi} \left| \frac{\hat{\gamma}(r) r}{\gamma(r)} \right| \left| \frac{\partial \hat{p}}{\partial r} \right|^2 \, d\theta \, dr \right)^{\frac{1}{2}} \left(\int_R^{R^\star} \int_{-\pi}^{\pi} |\hat{\gamma}(r) \gamma(r) r| \, |q|^2 \, d\theta \, dr \right)^{\frac{1}{2}}. \end{aligned}$$

which is finite for $\hat{p}$, $q \in$ V. Thus, $\gamma H \in \mathrm{L}^1(R, R^\star)$ and, hence, the same argument used to prove the previous lemma, allow us to conclude that $\lim_{r \to R^\star} H(r) = 0$. ☐

Now, the following step is to establish an integral representation of the solution of the PML equation.

Theorem 6.5.3. *If $\hat{p} \in$ W is a solution of (6.8), then the following integral representation formula holds true:*

$$\hat{p}(\boldsymbol{x}) = \frac{1}{\gamma(R)} \int_{S_R} \left(\frac{\partial \Phi^+(\boldsymbol{x}, \boldsymbol{y})}{\partial r_{\boldsymbol{y}}} \hat{p}(\boldsymbol{y}) - \frac{\partial \hat{p}}{\partial r_{\boldsymbol{y}}}(\boldsymbol{y}) \Phi^+(\boldsymbol{x}, \boldsymbol{y}) \right) dS_{\boldsymbol{y}}, \qquad \boldsymbol{x} \in \mathrm{D}. \tag{6.29}$$

Proof. We fix an arbitrary $\boldsymbol{x} \in$ D and use the notation from Figure 6.3. As shown in the proof of Theorem 6.4.6, $\Phi^+(\boldsymbol{x}, \cdot)$ satisfies (6.23). Hence, since $\boldsymbol{A}_{\boldsymbol{y}}$ is diagonal, by using the Green's second theorem and (6.8), we have

$$\begin{aligned} &\int_{\partial \tilde{\mathrm{D}}_\epsilon} \left(\boldsymbol{A}_{\boldsymbol{y}} \, \mathbf{grad}_{\boldsymbol{y}} \, \hat{p}(\boldsymbol{y}) \cdot \boldsymbol{n} \, \Phi^+(\boldsymbol{x}, \boldsymbol{y}) - \boldsymbol{A}_{\boldsymbol{y}} \, \mathbf{grad}_{\boldsymbol{y}} \, \Phi^+(\boldsymbol{x}, \boldsymbol{y}) \cdot \boldsymbol{n} \, \hat{p}(\boldsymbol{y}) \right) dS_{\boldsymbol{y}} \qquad (6.30) \\ = &\int_{\tilde{\mathrm{D}}_\epsilon} \left(\operatorname{div}(\boldsymbol{A}_{\boldsymbol{y}} \, \mathbf{grad}_{\boldsymbol{y}} \, \hat{p}(\boldsymbol{y})) \Phi^+(\boldsymbol{x}, \boldsymbol{y}) - \operatorname{div}(\boldsymbol{A}_{\boldsymbol{y}} \, \mathbf{grad}_{\boldsymbol{y}} \, \Phi^+(\boldsymbol{x}, \boldsymbol{y})) \hat{p}(\boldsymbol{y}) \right) d\boldsymbol{y} = 0, \end{aligned}$$

where $\boldsymbol{n}$ is the outward unit normal vector to $\tilde{\mathrm{D}}_\epsilon$.

By using Lemma 6.10.3 below (see Appendix) and (6.30), we obtain

$$\begin{aligned} \hat{p}(\boldsymbol{x}) = &\lim_{\epsilon \to 0} \left(\int_{S(\boldsymbol{x}, \epsilon)} \boldsymbol{A}_{\boldsymbol{y}} \, \mathbf{grad}_{\boldsymbol{y}} \, \Phi^+(\boldsymbol{x}, \boldsymbol{y}) \cdot \boldsymbol{n} \, \hat{p}(\boldsymbol{y}) \, dS_{\boldsymbol{y}} \right. \\ &\left. - \int_{S(\boldsymbol{x}, \epsilon)} \boldsymbol{A}_{\boldsymbol{y}} \, \mathbf{grad}_{\boldsymbol{y}} \, \hat{p}(\boldsymbol{y}) \cdot \boldsymbol{n} \, \Phi^+(\boldsymbol{x}, \boldsymbol{y}) \, dS_{\boldsymbol{y}} \right) \\ = &\frac{1}{\gamma(R)} \int_{S_R} \left(\frac{\partial \Phi^+(\boldsymbol{x}, \boldsymbol{y})}{\partial r_{\boldsymbol{y}}} \, \hat{p}(\boldsymbol{y}) - \frac{\partial \hat{p}}{\partial r_{\boldsymbol{y}}}(\boldsymbol{y}) \, \Phi^+(\boldsymbol{x}, \boldsymbol{y}) \right) dS_{\boldsymbol{y}} \\ &- \int_{S_{\tilde{R}}} \frac{\hat{\gamma}_{\boldsymbol{y}}}{\gamma_{\boldsymbol{y}}} \frac{\partial \Phi^+(\boldsymbol{x}, \boldsymbol{y})}{\partial r_{\boldsymbol{y}}} \, \hat{p}(\boldsymbol{y}) \, dS_{\boldsymbol{y}} + \int_{S_{\tilde{R}}} \frac{\hat{\gamma}_{\boldsymbol{y}}}{\gamma_{\boldsymbol{y}}} \frac{\partial \hat{p}}{\partial r_{\boldsymbol{y}}}(\boldsymbol{y}) \, \Phi^+(\boldsymbol{x}, \boldsymbol{y}) \, dS_{\boldsymbol{y}}. \end{aligned}$$

To conclude the proof, it is enough to show that the last two integrals go to zero as $\tilde{R} \to R^\star$. For the first one we use Lemmas 6.4.7 and 6.5.1. For the second one, first we replace $\Phi^+(\boldsymbol{x},\boldsymbol{y})$ by $\zeta(\boldsymbol{y})\Phi^+(\boldsymbol{x},\boldsymbol{y})$ where ζ is a smooth cutoff function vanishing in a neighborhood of $\boldsymbol{x}$ and taking the value 1 in $\{\boldsymbol{x} \in \mathbb{R}^2 : \tilde{R} \leq |\boldsymbol{x}| < R^\star\}$. Thus, the value of the integral does not change and $\zeta(\boldsymbol{y})\Phi^+(\boldsymbol{x},\boldsymbol{y}) \in \mathrm{V}$, because of Lemma 6.4.7. Hence, the integral goes to zero as $\tilde{R} \to R^\star$ as a consequence of Lemma 6.5.2. $\square$

6.6 Addition theorem

To characterize the solution of the PML equation, it is useful to write the fundamental solution as a series involving Bessel functions of first kind and order n, which we denote as usual by J_n.

Theorem 6.6.1. *Let $\boldsymbol{x} \in \mathrm{D}$ be fixed. For all $\boldsymbol{y} \in \mathrm{D}$ such that $|\boldsymbol{y}| < |\boldsymbol{x}|$, there holds:*

$$\Phi^+(\boldsymbol{x},\boldsymbol{y}) = \frac{i}{4}\sum_{n=-\infty}^{\infty} \mathrm{H}_n^{(1)}\left(k\hat{r}_{\boldsymbol{x}}\right) \mathrm{J}_n\left(k\hat{r}_{\boldsymbol{y}}\right) \mathrm{e}^{in(\theta_{\boldsymbol{x}}-\theta_{\boldsymbol{y}})}. \tag{6.31}$$

This series and its term by term first derivatives with respect to $r_{\boldsymbol{y}}$ are absolutely and uniformly convergent on compact subsets of the set $\{\boldsymbol{y} \in \mathbb{R}^2 : R \leq |\boldsymbol{y}| < |\boldsymbol{x}|\}$.

Proof. Let $\tilde{R} \in [R, |\boldsymbol{x}|)$. First, we define the following functions:

$$\phi(\boldsymbol{y}) := \begin{cases} \dfrac{i}{4}\,\mathrm{H}_0^{(1)}(k\,|\boldsymbol{x}-\boldsymbol{y}|), & \text{if } 0 \leq |\boldsymbol{y}| < R, \\ \Phi^+(\boldsymbol{x},\boldsymbol{y}), & \text{if } R \leq |\boldsymbol{y}| < R^\star, \end{cases}$$

and, for each $n \in \mathbb{N}$,

$$p_n(\boldsymbol{y}) := \begin{cases} \mathrm{J}_n\left(kr_{\boldsymbol{y}}\right) \mathrm{e}^{in\theta_{\boldsymbol{y}}}, & \text{if } 0 \leq |\boldsymbol{y}| < R, \\ \mathrm{J}_n\left(k\hat{r}_{\boldsymbol{y}}\right) \mathrm{e}^{in\theta_{\boldsymbol{y}}}, & \text{if } R \leq |\boldsymbol{y}| \leq \tilde{R}. \end{cases}$$

All these functions are continuous for $|\boldsymbol{y}| < \tilde{R}$, analytic for $|\boldsymbol{y}| < R$ and $\mathcal{C}^2$ for $R \leq |\boldsymbol{y}| \leq \tilde{R}$. Moreover, they satisfy

$$\lim_{r\to R^+} \frac{1}{\gamma}\frac{\partial\phi}{\partial r} = \lim_{r\to R^-} \frac{\partial\phi}{\partial r} \qquad \text{and} \qquad \lim_{r\to R^+} \frac{1}{\gamma}\frac{\partial p_n}{\partial r} = \lim_{r\to R^-} \frac{\partial p_n}{\partial r},\ n \in \mathbb{N}.$$

Furthermore, straightforward computations allow us to show that ϕ and p_n, $n \in \mathbb{N}$, all are solutions of the PML equation (6.8) in $R \leq |\boldsymbol{y}| < \tilde{R}$ and solutions of the Helmholtz equation in $0 < |\boldsymbol{y}| < R$.

Next, we proceed as in the proof of the addition theorem for the Helmholtz equation (see [54]), taking care of the fact that the Helmholtz equation is substituted by the PML equation for $R \leq |\boldsymbol{y}| < \tilde{R}$. Thus we obtain

$$\int_{S_{\tilde{R}}} \frac{\hat{\gamma}}{\gamma}\left(p_n\frac{\partial\phi}{\partial r} - \frac{\partial p_n}{\partial r}\phi\right) dS = 0. \tag{6.32}$$

On the other hand, straightforward computations allow us to show that, for all $n \in \mathbb{N}$, if we define

$$q_n(\boldsymbol{y}) := \mathrm{H}_n^{(1)}\left(k\hat{r}_{\boldsymbol{y}}\right) \mathrm{e}^{in\theta_{\boldsymbol{y}}}, \qquad \boldsymbol{y} \in \mathrm{D}, \tag{6.33}$$

then q_n are solutions of the PML equation (6.8) and belong to W. By applying the analogous of Theorem 6.5.3 for q_n instead of $\hat{p}$, on the annular domain $\tilde{R} < |\boldsymbol{y}| < R^\star$ instead of D, and taking into account that $\phi = \Phi^+(\boldsymbol{x}, \cdot)$ in this domain, we obtain

$$\int_{S_{\tilde{R}}} \frac{\hat{\gamma}}{\gamma} \left(q_n \frac{\partial \phi}{\partial r} - \frac{\partial q_n}{\partial r} \phi \right) dS = q_n(\boldsymbol{x}). \tag{6.34}$$

Next, multiplying equation (6.32) by $\mathrm{H}_n^{(1)}(k\hat{r}(\tilde{R}))$ and (6.34) by $\mathrm{J}_n(k\hat{r}(\tilde{R}))$, we have

$$\int_{S_{\tilde{R}}} \frac{\hat{\gamma}}{\gamma} \left(\mathrm{H}_n^{(1)}(k\hat{r}(\tilde{R})) p_n \frac{\partial \phi}{\partial r} - \mathrm{H}_n^{(1)}(k\hat{r}(\tilde{R})) \frac{\partial p_n}{\partial r} \phi \right) dS = 0,$$

$$\int_{S_{\tilde{R}}} \frac{\hat{\gamma}}{\gamma} \left(\mathrm{J}_n(k\hat{r}(\tilde{R})) q_n \frac{\partial \phi}{\partial r} - \mathrm{J}_n(k\hat{r}(\tilde{R})) \frac{\partial q_n}{\partial r} \phi \right) dS = \mathrm{J}_n(k\hat{r}(\tilde{R})) q_n(\boldsymbol{x}).$$

If we subtract the first from the second equation, taking into account that $\mathrm{H}_n^{(1)}(k\hat{r}(\tilde{R}))p_n = \mathrm{J}_n(k\hat{r}(\tilde{R}))q_n$ on $S_{\tilde{R}}$, we obtain

$$\begin{aligned} \mathrm{J}_n(k\hat{r}(\tilde{R})) q_n(\boldsymbol{x}) &= \Big(\mathrm{H}_n^{(1)}(k\hat{r}(\tilde{R})) k\gamma(\tilde{R})\, \mathrm{J}'_n(k\hat{r}(\tilde{R})) \\ &\qquad - \mathrm{J}_n(k\hat{r}(\tilde{R})) k\gamma(\tilde{R}) [\mathrm{H}_n^{(1)}]'(k\hat{r}(\tilde{R})) \Big) \frac{\hat{\gamma}(\tilde{R})\tilde{R}}{\gamma(\tilde{R})} \int_{-\pi}^{\pi} \phi \, \mathrm{e}^{in\theta} \, d\theta \\ &= -\frac{2i}{\pi} \int_{-\pi}^{\pi} \phi \, \mathrm{e}^{in\theta} \, d\theta, \end{aligned} \tag{6.35}$$

where we have used the explicit value of the Wronskian $\mathrm{H}_n^{(1)}(z)\, \mathrm{J}'_n(z) - \mathrm{J}_n(z)[\mathrm{H}_n^{(1)}]'(z) = -2i/(\pi z)$ (see [2]).

Since $\phi \in \mathcal{C}(\mathrm{D}^\star)$, $\phi|_{S_{\tilde{R}}}$ admits a Fourier series, i.e.,

$$\phi(\boldsymbol{y}) = \sum_{n=-\infty}^{\infty} \phi_n \, \mathrm{e}^{-in\theta_{\boldsymbol{y}}}, \qquad \boldsymbol{y} \in S_{\tilde{R}}, \tag{6.36}$$

where, from (6.35) and (6.33),

$$\phi_n := \frac{1}{2\pi} \int_{-\pi}^{\pi} \phi \, \mathrm{e}^{in\theta} \, d\theta = \frac{i}{4} \mathrm{H}_n^{(1)}\left(k\hat{r}_{\boldsymbol{x}}\right) \mathrm{J}_n(k\hat{r}(\tilde{R}))\, \mathrm{e}^{in\theta_{\boldsymbol{x}}}. \tag{6.37}$$

Finally, we conclude (6.31) from (6.36) and (6.37), since $\hat{r}(\tilde{R}) = \hat{r}_{\boldsymbol{y}}$, for $\boldsymbol{y} \in S_{\tilde{R}}$.

The uniform convergence of the series (6.31) and its term by term first derivatives on compact subsets of $\{\boldsymbol{y} \in \mathbb{R}^2 : R \le |\boldsymbol{y}| < |\boldsymbol{x}|\}$ is straightforward from the uniform convergence of the analogous series in the addition theorem for the fundamental solution of the Helmholtz equation (see [54]), and the fact that $|\hat{r}(r)|$ is a monotonically increasing function. $\square$

6.7 Existence and uniqueness of solutions for the PML equation

Now we are able to characterize the smooth solutions of the PML equation (6.8):

Theorem 6.7.1. *If $\hat{p} \in \mathrm{W}$ is a solution of (6.8), then there exists a sequence $\{a_n\}$ such that, for all $\boldsymbol{x} \in \mathrm{D}$,*

$$\hat{p}(\boldsymbol{x}) = \sum_{n=-\infty}^{\infty} a_n \, \mathrm{H}_n^{(1)}\left(k\hat{r}_{\boldsymbol{x}}\right) \mathrm{e}^{in\theta_{\boldsymbol{x}}}.$$

Proof. Let $\hat{p} \in \mathrm{W}$ be a solution of (6.8). For fixed $\boldsymbol{x} \in \mathrm{D}$, if we apply the PML integral representation formula (6.29) and Theorem 6.6.1, then we have

$$\begin{aligned}
\hat{p}(\boldsymbol{x}) &= \frac{1}{\gamma(R)} \int_{S_R} \left(\frac{\partial \Phi^+(\boldsymbol{x},\boldsymbol{y})}{\partial r_{\boldsymbol{y}}} \hat{p}(\boldsymbol{y}) - \frac{\partial \hat{p}}{\partial r_{\boldsymbol{y}}}(\boldsymbol{y}) \, \Phi^+(\boldsymbol{x},\boldsymbol{y}) \right) dS_{\boldsymbol{y}} \\
&= \frac{1}{\gamma(R)} \int_{S_R} \Bigg(\frac{i}{4} \sum_{n=-\infty}^{\infty} k\gamma(R) \, \mathrm{H}_n^{(1)}\left(k\hat{r}_{\boldsymbol{x}}\right) \mathrm{J}_n{}'(kR) \, \mathrm{e}^{in(\theta_{\boldsymbol{x}}-\theta_{\boldsymbol{y}})} \, \hat{p}(\boldsymbol{y}) \\
&\qquad\qquad - \frac{\partial \hat{p}}{\partial r_{\boldsymbol{y}}}(\boldsymbol{y}) \, \frac{i}{4} \sum_{n=-\infty}^{\infty} \mathrm{H}_n^{(1)}\left(k\hat{r}_{\boldsymbol{x}}\right) \mathrm{J}_n(kR) \, \mathrm{e}^{in(\theta_{\boldsymbol{x}}-\theta_{\boldsymbol{y}})} \Bigg) \, dS_{\boldsymbol{y}} \\
&= \sum_{n=-\infty}^{\infty} a_n \, \mathrm{H}_n^{(1)}\left(k\hat{r}_{\boldsymbol{x}}\right) \mathrm{e}^{in\theta_{\boldsymbol{x}}},
\end{aligned}$$

where

$$a_n = \frac{i}{4} \frac{1}{\gamma(R)} \int_{S_R} \left(k\gamma(R) \, \mathrm{J}_n{}'(kR) \, \mathrm{e}^{-in\theta_{\boldsymbol{y}}} \, \hat{p}(\boldsymbol{y}) - \frac{\partial \hat{p}}{\partial r_{\boldsymbol{y}}}(\boldsymbol{y}) \; \mathrm{J}_n(kR) \, \mathrm{e}^{-in\theta_{\boldsymbol{y}}} \right) dS_{\boldsymbol{y}}.$$

Now, we prove the existence and uniqueness of smooth solutions of the following problem for the PML equation with Dirichlet data g:

Find $\hat{p} \in \mathrm{W}$ such that

$$-\operatorname{div}(\boldsymbol{A}\, \mathbf{grad}\, \hat{p}) - \gamma\hat{\gamma}k^2\hat{p} = 0 \qquad \text{in } \mathrm{D}, \tag{6.38}$$

$$\hat{p} = g \qquad \text{on } S_R. \tag{6.39}$$

Theorem 6.7.2. *If $g \in \mathrm{H}^s(S_R)$ with $s > 3/2$, then there exists a unique solution $\hat{p} \in \mathrm{W}$ of (6.38)-(6.39). Moreover, this solution is given by*

$$\hat{p}(\boldsymbol{x}) = \sum_{n=-\infty}^{\infty} \frac{g_n}{\mathrm{H}_n^{(1)}(kR)} \, \mathrm{H}_n^{(1)}\left(k\hat{r}_{\boldsymbol{x}}\right) \mathrm{e}^{in\theta_{\boldsymbol{x}}}, \tag{6.40}$$

where $g_n := 1/(2\pi R) \int_{S_R} g(\boldsymbol{x}) \, \mathrm{e}^{-in\theta_{\boldsymbol{x}}} \, dS$ are the Fourier coefficients of g. Moreover the series and its term by term first derivatives converge uniformly on compact subsets of $\mathrm{D}^\star$.

Proof. First, we are going to prove that $\hat{p}$ as defined by (6.40) belongs to W. We split the proof into three steps. The first one consists in proving that $\hat{p} \in \mathcal{C}^2(\mathrm{D})$. This step is essentially identical to what is known for the Helmholtz problem. In fact, taking into account classical estimates of the Hankel functions of first kind for large order (see [103]), for $\boldsymbol{x}$ in any compact subset of D and N large enough, there holds

$$\left(\sum_{|n|\geq N} \left| \frac{g_n}{\mathrm{H}_n^{(1)}(kR)} \mathrm{H}_n^{(1)}(k\hat{r}_{\boldsymbol{x}})\, \mathrm{e}^{in\theta_{\boldsymbol{x}}} \right| \right)^2 \leq \sum_{|n|\geq N} \left| \frac{\mathrm{H}_n^{(1)}(k\hat{r}_{\boldsymbol{x}})}{\mathrm{H}_n^{(1)}(kR)} \right|^2 \sum_{|n|\geq N} |g_n|^2$$
$$\leq C\, \|g\|^2_{\mathrm{L}^2(S_R)} \sum_{|n|\geq N} \left(\frac{R}{|\hat{r}_{\boldsymbol{x}}|} \right)^{2|n|},$$

where we recall that $|\hat{r}_{\boldsymbol{x}}| > R$ (here and thereafter C denotes a generic constant, not necessarily the same at each occurrence). From this, we conclude the uniform and absolute convergence of the series (6.40) on compact subsets of D. Analogous procedures allow us to prove the uniform convergence of the corresponding series for the first and the second derivatives. Since each term in each series is continuous, we conclude that $\hat{p} \in \mathcal{C}^2(\mathrm{D})$.

The second step consists in proving that $\hat{p} \in \mathcal{C}(\mathrm{D}^\star)$. Since $g \in \mathrm{H}^s(S_R)$ with $s > 1/2$, for $\boldsymbol{x}$ in any compact subset of $\mathrm{D}^\star$ we have for N large enough

$$\left(\sum_{|n|\geq N} \left| \frac{g_n}{\mathrm{H}_n^{(1)}(kR)} \mathrm{H}_n^{(1)}(k\hat{r}_{\boldsymbol{x}})\, \mathrm{e}^{in\theta_{\boldsymbol{x}}} \right| \right)^2 \leq \sum_{|n|\geq N} \left| \frac{1}{n^s} \frac{\mathrm{H}_n^{(1)}(k\hat{r}_{\boldsymbol{x}})}{\mathrm{H}_n^{(1)}(kR)} \right|^2 \sum_{|n|\geq N} n^{2s} |g_n|^2$$
$$\leq C \sum_{|n|\geq N} \left| \frac{1}{n^s} \right|^2 \sum_{|n|\geq N} n^{2s} |g_n|^2 \leq C\, \|g\|^2_{\mathrm{H}^s(S_R)} \sum_{|n|\geq N} \frac{1}{n^{2s}},$$

the latter because of the decay behavior of the Fourier coefficients of functions in $\mathrm{H}^s(S_R)$ (see [81]). This allows us to conclude that $\hat{p} \in \mathcal{C}(\mathrm{D}^\star)$.

The same arguments as above applied to the term by term derivatives of the series allow us to show that, for $g \in \mathrm{H}^s(S_R)$ with $s > 3/2$, $\partial\hat{p}/\partial r$ and $\partial\hat{p}/\partial\theta$ belong to $\mathcal{C}(\mathrm{D}^\star)$, too.

From the previous steps, clearly $\hat{p} \in \mathrm{H}^1_{\mathrm{loc}}(\mathrm{D}^\star)$. Hence, since the weights in the norm of V are positive bounded functions in compact subsets of $\mathrm{D}^\star$, in order to prove that $\hat{p} \in \mathrm{V}$ we only need to prove that there exists $\delta > 0$ such that

$$\int_{R^\star-\delta}^{R^\star} \int_{-\pi}^{\pi} \left(\left| \frac{\hat{\gamma}(r) r}{\gamma(r)} \right| \left| \frac{\partial \hat{p}}{\partial r} \right|^2 + \left| \frac{\gamma(r)}{\hat{\gamma}(r) r} \right| \left| \frac{\partial \hat{p}}{\partial \theta} \right|^2 + |\hat{\gamma}(r)\gamma(r) r|\, |\hat{p}|^2 \right) d\theta\, dr < +\infty. \tag{6.41}$$

Since $\mathrm{Im}(\hat{r}_{\boldsymbol{x}}) \to +\infty$, as $r_{\boldsymbol{x}} \to R^\star$, using standard estimates for $\mathrm{H}_0^{(1)}$ and $[\mathrm{H}_0^{(1)}]'$, and for $\mathrm{H}_n^{(1)}$ and $[\mathrm{H}_n^{(1)}]'$, $n \in \mathbb{N}$, the latter uniform in n (see [46]), it is straightforward to prove that the following limits hold uniformly in $\theta_{\boldsymbol{x}} \in (-\pi, \pi]$ and $n \in \mathbb{N}$:

$$\lim_{r_{\boldsymbol{x}} \to R^\star} \sqrt{\hat{\gamma}_{\boldsymbol{x}} \gamma_{\boldsymbol{x}}} \frac{\mathrm{H}_n^{(1)}(k\hat{r}_{\boldsymbol{x}})}{\mathrm{H}_n^{(1)}(kR)} = 0,$$

$$\lim_{r_{\boldsymbol{x}} \to R^\star} \frac{1}{n} \sqrt{\frac{\hat{\gamma}_{\boldsymbol{x}}}{\gamma_{\boldsymbol{x}}}} \frac{\partial}{\partial r_{\boldsymbol{x}}} \left(\frac{\mathrm{H}_n^{(1)}(k\hat{r}_{\boldsymbol{x}})}{\mathrm{H}_n^{(1)}(kR)} \right) = 0,$$

$$\lim_{r_{\boldsymbol{x}} \to R^\star} \frac{1}{n} \sqrt{\frac{\gamma_{\boldsymbol{x}}}{\hat{\gamma}_{\boldsymbol{x}}}} \frac{\mathrm{H}_n^{(1)}(k\hat{r}_{\boldsymbol{x}})}{\mathrm{H}_n^{(1)}(kR)} = 0.$$

Hence, for δ small enough, we have

$$\int_{R^\star-\delta}^{R^\star} \int_{-\pi}^{\pi} |\hat{\gamma}(r)\gamma(r)r| \, |\hat{p}|^2 \, d\theta \, dr \le C\delta \int_{-\pi}^{\pi} \left| \sum_{n=-\infty}^{\infty} g_n \, \mathrm{e}^{in\theta} \right|^2 d\theta = C\delta \, \|g\|^2_{\mathrm{L}^2(S_R)},$$

$$\int_{R^\star-\delta}^{R^\star} \int_{-\pi}^{\pi} \left| \frac{\hat{\gamma}(r)r}{\gamma(r)} \right| \left| \frac{\partial \hat{p}}{\partial r} \right|^2 d\theta \, dr \le C\delta \int_{-\pi}^{\pi} \left| \sum_{n=-\infty}^{\infty} n g_n \, \mathrm{e}^{in\theta} \right|^2 d\theta \le C\delta \, \|g\|^2_{\mathrm{H}^1(S_R)},$$

$$\int_{R^\star-\delta}^{R^\star} \int_{-\pi}^{\pi} \left| \frac{\gamma(r)}{\hat{\gamma}(r)r} \right| \left| \frac{\partial \hat{p}}{\partial \theta} \right|^2 d\theta \, dr \le C\delta \int_{-\pi}^{\pi} \left| \sum_{n=-\infty}^{\infty} n g_n \, \mathrm{e}^{in\theta} \right|^2 d\theta \le C\delta \, \|g\|^2_{\mathrm{H}^1(S_R)},$$

which allow us to conclude that the integral (6.41) is finite. Therefore, from the three previous steps we deduce that $\hat{p} \in \mathrm{W}$.

Next, since $\hat{p}$ is continuous on S_R, evaluating (6.40) for $\boldsymbol{x} \in S_R$ we have $\hat{p}(\boldsymbol{x}) = \sum_{n=-\infty}^{\infty} g_n \, \mathrm{e}^{in\theta}$, so that (6.39) follows from the convergence of the Fourier series of g.

On the other hand, straightforward computations allow us to show that each term in the series (6.40) is a solution of (6.38). Thus, $\hat{p}$ is a solution too, because we have already shown the uniform convergence on compact subsets of D of that series and its term by term first and second derivatives.

Finally, $\hat{p}$ is the unique solution of (6.38)-(6.39) in W because of Theorem 6.7.1 and the uniqueness of the Fourier expansion of g. □

6.8 Coupled fluid/PML problem

Our next goal is to study the coupled fluid/PML problem and to prove that the solution of the classical scattering problem is recovered when the PML is used.

Theorem 6.7.2 allows us to define a "Dirichlet-to-Neumann" PML operator,

$$\hat{G} : \mathrm{H}^{\frac{1}{2}}(S_R) \to \mathrm{H}^{-\frac{1}{2}}(S_R).$$

First we define G for sufficiently smooth data as follows:

$$\hat{G}(g) = \frac{1}{\gamma(R)} \left. \frac{\partial \hat{p}}{\partial r} \right|_{S_R}, \qquad g \in \mathrm{H}^s(S_R), \text{ with } s > 3/2, \tag{6.42}$$

where $\hat{p}$ is the unique solution in W of (6.38)-(6.39). This definition can be extended to $g \in \mathrm{H}^{\frac{1}{2}}(S_R)$ by means of a density argument, because of the following result:

Theorem 6.8.1. *There exists a unique bounded linear operator* $\hat{G} : \mathrm{H}^{\frac{1}{2}}(S_R) \to \mathrm{H}^{-\frac{1}{2}}(S_R)$ *satisfying (6.42), which coincides with* G *as defined by (6.4).*

Proof. If $g \in \mathrm{H}^s(S_R)$, $s > 3/2$, and G is defined by (6.4), then $\hat{G}g = Gg$. Indeed,

$$\begin{aligned}\hat{G}g = \frac{1}{\gamma(R)}\frac{\partial \hat{p}}{\partial r}\bigg|_{S_R} &= \frac{1}{\gamma(R)}\sum_{n=-\infty}^{\infty}\frac{g_n k}{\mathrm{H}_n^{(1)}(kR)}\frac{d\hat{r}}{dr}(R)[\mathrm{H}_n^{(1)}]'(k\hat{r}_{\boldsymbol{x}})\,\mathrm{e}^{in\theta}\\ &= \sum_{n=-\infty}^{\infty}\frac{g_n k}{\mathrm{H}_n^{(1)}(kR)}[\mathrm{H}_n^{(1)}]'(kR)\,\mathrm{e}^{in\theta} = Gg.\end{aligned}$$

Consequently, the definition of $\hat{G}$ extends uniquely to the whole space $\mathrm{H}^{\frac{1}{2}}(S_R)$ and $\hat{G} = G$. ☐

Therefore, $\hat{G}$ can be equivalently used instead of G in the definition of problem (6.5)-(6.7). Moreover we have the following result.

Theorem 6.8.2. *For* $f \in \mathrm{H}^{\frac{1}{2}}(\Gamma)$*, there exists a unique solution* $(p, \hat{p}) \in \mathrm{H}^1(\Omega_R) \times \mathrm{V}$ *of the following problem:*

$$-\Delta p - k^2 p = 0 \qquad \text{in } \Omega_R, \tag{6.43}$$

$$-\operatorname{div}(\boldsymbol{A}\,\mathbf{grad}\,\hat{p}) - \gamma\hat{\gamma}k^2\hat{p} = 0 \qquad \text{in D}, \tag{6.44}$$

$$p = f \qquad \text{on } \Gamma, \tag{6.45}$$

$$\frac{\partial p}{\partial \boldsymbol{\nu}} = \boldsymbol{A}\,\mathbf{grad}\,\hat{p}\cdot\boldsymbol{\nu} \qquad \text{in } \mathrm{H}^{-\frac{1}{2}}(S_R), \tag{6.46}$$

$$p = \hat{p} \qquad \text{on } S_R. \tag{6.47}$$

Moreover, p *coincides with the solution of (6.5)-(6.7) and, hence, it coincides with the solution of the scattering problem (6.1)-(6.3) in* Ω_R.

Proof. Let $p \in \mathrm{H}^1(\Omega_R)$ be the solution of (6.5)-(6.7). Then p is the restriction to Ω_R of the solution of (6.1)-(6.3). Hence $p|_{S_R}$ is arbitrarily smooth. Thus, $\hat{G}(p|_{S_R}) = (1/\gamma(R))\partial\hat{p}/\partial r$, with $\hat{p} \in \mathrm{W}$ being the solution of (6.38)-(6.39). Therefore $(p, \hat{p}) \in \mathrm{H}^1(\Omega_R) \times \mathrm{V}$ is a solution of the coupled fluid/PML problem.

To prove the uniqueness, it is enough to show that the solution $(p_o, \hat{p}_o)$ of problem (6.43)-(6.47) with $f = 0$ vanishes. By applying local regularity up to the boundary results for transmission problems (in particular Theorem 4.20 from [85]), we conclude that $\hat{p}_o \in \mathcal{C}^2(\mathrm{D}^\star)$. Notice that this regularity comes from the assumed smoothness on the absorbing function: $\sigma \in \mathcal{C}^{2,1}([R, R']) \ \forall R' \in (R, R^\star)$. Hence $\hat{p}_o \in \mathrm{W}$ and

$$\boldsymbol{A}\,\mathbf{grad}\,\hat{p}_o\cdot\boldsymbol{\nu} = \frac{1}{\gamma(R)}\frac{\partial\hat{p}_o}{\partial r} \qquad \text{on } S_R.$$

Consequently, (6.44) and (6.47) imply that $\hat{G}(p_o|_{S_R}) = \boldsymbol{A}\,\mathbf{grad}\,\hat{p}_o \cdot \boldsymbol{\nu}$ and, because of (6.46) and Theorem 6.8.1, we have

$$\frac{\partial p_o}{\partial \boldsymbol{\nu}} = \hat{G}(p_o|_{S_R}) = G(p_o|_{S_R}) \qquad \text{on } S_R.$$

Therefore, p_o is the unique solution of (6.5)-(6.7) with $f = 0$ and hence $p_o = 0$. Finally, as a consequence of Theorem 6.7.2, $\hat{p}_o = 0$, too. □

Finally we write a weak formulation of the coupled fluid/PML problem (6.43)-(6.47), which will be used in the following section to introduce a convenient finite element discretization. For this purpose, we introduce the functional space

$$\mathrm{H} := \left\{(q,\hat{q}) \in \mathrm{H}^1(\Omega_R) \times \mathrm{V} : q = \hat{q} \text{ on } S_R\right\},$$

and its subspace

$$\mathrm{H}_0 := \{(q,\hat{q}) \in \mathrm{H} : q = 0 \text{ on } \Gamma\}.$$

Let $(p,\hat{p}) \in \mathrm{H}$ be the solution of problem (6.43)-(6.47) and $(q,\hat{q}) \in \mathrm{H}_0$. Integrating by parts (6.43) in Ω_R and (6.44) in $\tilde{\mathrm{D}} = \{\boldsymbol{x} \in \mathbb{R}^2 : R < |\boldsymbol{x}| < \tilde{R}\}$ with $\tilde{R} \in (R, R^\star)$, since p and $\hat{p}$ are smooth, we obtain

$$\begin{aligned}&\int_{\Omega_R} \mathbf{grad}\,p \cdot \mathbf{grad}\,\overline{q} - k^2 \int_{\Omega_R} p\overline{q} - \int_{S_R} \frac{\partial p}{\partial r}\overline{q}\,dS \\ &+ \int_{\tilde{\mathrm{D}}} \boldsymbol{A}\,\mathbf{grad}\,\hat{p} \cdot \mathbf{grad}\,\overline{\hat{q}} - k^2 \int_{\tilde{\mathrm{D}}} \gamma\hat{\gamma}\hat{p}\overline{\hat{q}} + \int_{S_R} \frac{1}{\gamma}\frac{\partial \hat{p}}{\partial r}\overline{\hat{q}}\,dS - \int_{S_{\tilde{R}}} \frac{\hat{\gamma}}{\gamma}\frac{\partial \hat{p}}{\partial r}\overline{\hat{q}}\,dS = 0.\end{aligned}$$

Since $(q,\hat{q}) \in \mathrm{H}_0 \subset \mathrm{H}$, the boundary terms on S_R cancel out because of (6.46). Moreover, as $\tilde{R}$ goes to $R^\star$, using Lemma 6.5.2 we have

$$\int_{\Omega_R} \mathbf{grad}\,p \cdot \mathbf{grad}\,\overline{q} + \int_{\mathrm{D}} \boldsymbol{A}\,\mathbf{grad}\,\hat{p} \cdot \mathbf{grad}\,\overline{\hat{q}} - k^2 \left(\int_{\Omega_R} p\overline{q} + \int_{\mathrm{D}} \gamma\hat{\gamma}\hat{p}\overline{\hat{q}}\right) = 0.$$

Thus we are led to the following weak formulation of problem (6.43)-(6.47):

For $f \in \mathrm{H}^{\frac{1}{2}}(\Gamma)$*, find* $(p,\hat{p}) \in \mathrm{H}$ *such that* $p = f$ *on* Γ *and*

$$\begin{aligned}&\int_{\Omega_R} \mathbf{grad}\,p \cdot \mathbf{grad}\,\overline{q} + \int_{\mathrm{D}} \boldsymbol{A}\,\mathbf{grad}\,\hat{p} \cdot \mathbf{grad}\,\overline{\hat{q}} \\ &\qquad - k^2 \left(\int_{\Omega_R} p\overline{q} + \int_{\mathrm{D}} \gamma\hat{\gamma}\hat{p}\overline{\hat{q}}\right) = 0 \qquad \forall\,(q,\hat{q}) \in \mathrm{H}_0. \qquad (6.48)\end{aligned}$$

Corollary 6.8.3. *The solution of the coupled fluid/PML problem (6.43)-(6.47) is the unique solution of the weak problem (6.48).*

Proof. We have already shown that the solution of problem (6.43)-(6.47) satisfies (6.48). The converse follows from standard arguments. Hence (6.48) attains a unique solution. □

***Remark* 6.8.4.** *According to Lemma 6.5.1, a kind of homogeneous Dirichlet boundary condition*

$$\hat{p} = 0 \qquad \text{on } S_{R^\star}$$

is implicitly contained in the definition of the space V*. This boundary condition will be actually used in the discretization of Problem (6.48) proposed in the following section.*

6.9 Discretization and numerical results

In this section, we introduce a finite element discretization of problem (6.48). For this purpose, we use meshes $\mathcal{T}_h$ of curved elements which correspond to standard quadrilaterals in polar coordinates. As usual, h denotes the mesh-size. Each element must be completely contained either in $\bar{\Omega}_R$ or in $\bar{\mathrm{D}}$. Moreover, we take advantage of the fact that D is an annular domain by using curved rectangles in D (see Figure 6.4). We use bilinear elements in polar coordinates.Thus, the finite-element space is

$$\begin{aligned}\mathrm{H}_h := \{(q_h, \hat{q}_h) \in \mathcal{C}(\Omega_R) \times \mathcal{C}(\mathrm{D}) :\ & \hat{q}_h = 0 \text{ on } S_{R^\star}, \\ & q_h = \hat{q}_h \text{ on } S_R,\ q_h|_K, \hat{q}_h|_K \text{bilinear in } K\, \forall K \in \mathcal{T}_h\}\,.\end{aligned}$$

As a consequence of Lemma 6.5.1, the boundary condition $\hat{q}_h = 0$ on $S_{R^\star}$ in the definition of H_h turns out necessary for $\mathrm{H}_h \subset \mathrm{H}$. For a non-integrable absorbing function σ in (6.9) as that defined by (6.49) below, this boundary condition is also sufficient (see [30] for other feasible choices of σ for which $\mathrm{H}_h \subset \mathrm{H}$).

Let f_h be a convenient approximation of f in the space of traces on Γ of functions in H_h. The discrete weak problem associated with the coupled fluid/PML problem is the following:

Find $(p_h, \hat{p}_h) \in \mathrm{H}_h$ *such that* $p_h = f_h$ *on* Γ *and*

$$\begin{aligned}\int_{\Omega_R} \mathbf{grad}\, p_h \cdot \mathbf{grad}\, \overline{q}_h + \int_{\mathrm{D}} \boldsymbol{A}\, \mathbf{grad}\, \hat{p}_h \cdot \mathbf{grad}\, \overline{\hat{q}}_h \\ - k^2 \left(\int_{\Omega_R} p_h \overline{q}_h + \int_{\mathrm{D}} \gamma \hat{\gamma} \hat{p}_h \overline{\hat{q}}_h \right) = 0 \qquad \forall\, (q_h, \hat{q}_h) \in \mathrm{H}_h \cap \mathrm{H}_0.\end{aligned}$$

In what follows we report some numerical results obtained with a computer code implementing the perfectly matched layer method with a non-integrable absorbing function σ. In all the numerical tests we have used

$$\sigma(s) := \frac{c}{R^\star - s}; \tag{6.49}$$

let us recall that c is the velocity of propagation in Ω_R.

To illustrate the performance of the PML method with an non-integrable σ, we consider a simple problem for which we have an analytical solution. It is well known that the function

$$p(\boldsymbol{x}) = \frac{i}{4} \mathrm{H}_0^{(1)} \left(k \left| \boldsymbol{x} \right| \right)$$

satisfies the scattering problem (6.1)-(6.3). Therefore, if we take $f := p|_\Gamma$, then p is the component in the fluid domain Ω_R of the unique solution of (6.43)-(6.47).

In this numerical experiment we have taken $k = \omega/c$ with $c = 340\,\mathrm{m/s}$ and $\omega = 750\,\mathrm{rad/s}$. We have used the computational domain shown in Figure 6.4 where $R_\star = 1\,\mathrm{m}$, $R = 2.25\,\mathrm{m}$ and $R^\star = 2.5\,\mathrm{m}$.

Because of the boundary condition $\hat{u}_h = 0$ on $S_{R^\star}$, all the integrals involved in the finite element method are finite (see Chapter 5 for details). To evaluate these integrals we have used a Simpson adaptive rule, to reduce the effect of the numerical errors arising from quadrature as much as possible. However, it is shown in Chapter 5 that standard quadrature rules lead to numerical results essentially of the same accuracy.

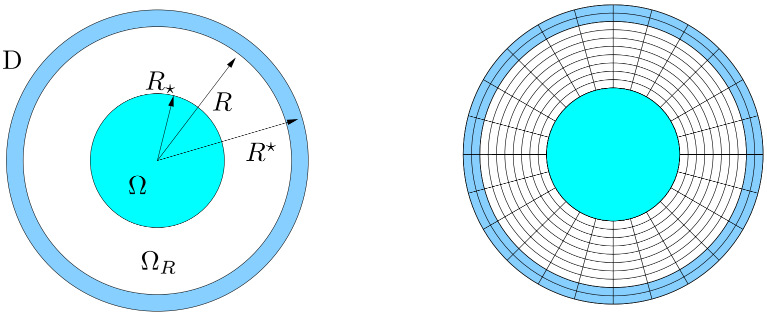

Figure 6.4: Domains and mesh ($N = 2$) in the scattering problem.

We have used uniform refinements of the mesh shown in Figure 6.4; the number N of elements through the thickness of the PML is used to label each mesh. Specifically, meshes corresponding to $N = 2$, 4 and 8 have 264, 1008 and 3936 degrees of freedom, respectively.

We show in Figure 6.5 the real and imaginary parts of the solution computed for the fluid/PML coupled problem with the mesh corresponding to $N = 8$. The solution is plotted in the fluid domain and in the PML as well.

To measure the accuracy we have estimated the relative error in the L^2-norm in Ω_R as follows:

$$\text{Error} := \frac{\|p_h - \Pi_h p\|_{\mathrm{L}^2(\Omega_R)}}{\|\Pi_h p\|_{\mathrm{L}^2(\Omega_R)}},$$

where p_h is the numerical solution in Ω_R and $\Pi_h p$ is the Lagrange interpolant of the exact solution p.

To assess the order of convergence of the proposed numerical method, we show in Figure 6.6 the error curve (log-log plot of error versus mesh-size) computed in the fluid domain Ω_R. It can be seen from this figure that an order of convergence $\mathcal{O}(h^2)$ is achieved. Let us recall that this is the optimal order for the used finite elements in L^2-norm.

To end this section, we compare the numerical performance of this PML technique with

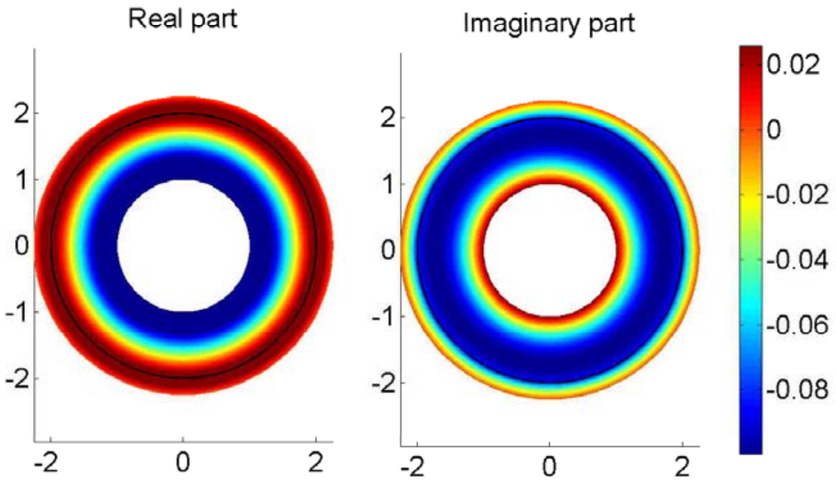

Figure 6.5: Solution of the fluid/PML coupled problem. Mesh $N = 8$

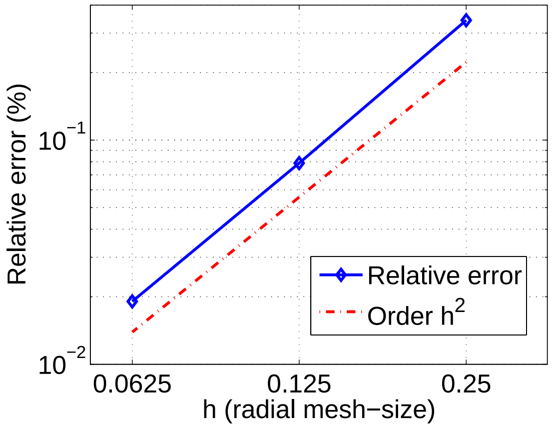

Figure 6.6: Error curve for the fluid/PML coupled problem ($\omega = 750\,\mathrm{rad/s}$).

that of a classical one based on a quadratic function (see for instance [22] or [52]):

$$\sigma_{\mathrm{Q}}(s) := c\sigma^{\star}(s-R)^2. \tag{6.50}$$

As shown in [51], for a given problem and a given mesh there is an optimal value of $\sigma^{\star}$ leading to minimal errors. Such optimal value depends strongly on the problem data as well as on the particular mesh. Thus, in practice, it is necessary to tune it. No theoretical procedure for such a tuning is known to date.

In Table 6.1, we compare the errors of the PML methods with the unbounded absorbing function (6.49) and with the quadratic absorbing function (6.50) applied to the same test problem as above. For the quadratic absorbing function, we have used the optimally tuned value of $\sigma^\star$, which is also reported in the table (and which can be seen that changes significantly from one mesh to the other).

Table 6.1: Comparison of PML methods with non-integrable and quadratic absorbing functions.

	Non-integrable σ (6.49)	Quadratic σ_{Q} (6.50)	
Mesh	Error(%)	Error(%)	$\sigma^\star$
$N=2$	0.342	11.346	415.54
$N=4$	0.079	3.247	565.07
$N=8$	0.019	0.970	702.32

Table 6.1 shows that the errors of the PML method with the non-integrable absorbing function are significantly smaller than those of the classical PML technique. On the other hand, another benefit of our proposed PML method is that there is no need of fitting any non-physical parameter.

Further numerical examples on more complex geometries and with different data have been reported in [30], where we have implemented a Cartesian PML using non-integrable absorbing functions.

6.10 Appendix

For the sake of clarity in the exposition, the more technical results and the fundamental properties of the Hankel functions, which have been used extensively through this chapter, are presented in this Appendix.

6.10.1 Technical results

In this subsection we collect some technical results that have been used through the proof of Theorems 6.4.6 and 6.5.3.

First, we recall some basic results about the relation between polar coordinates centered at different points. For a fixed point $\boldsymbol{x} \in \mathrm{D}$, we introduce $(\rho_{\boldsymbol{y}}, \phi_{\boldsymbol{y}})$ as the coordinates of point $\boldsymbol{y}$ in polar coordinates centered at $\boldsymbol{x}$:

$$\boldsymbol{y} = \boldsymbol{x} + \rho_{\boldsymbol{y}}(\cos\phi_{\boldsymbol{y}}, \sin\phi_{\boldsymbol{y}}).$$

We denote by $\{\boldsymbol{e}_\rho, \boldsymbol{e}_\phi\}$ the canonical basis of the second system of coordinates (see Figure 6.10.1).

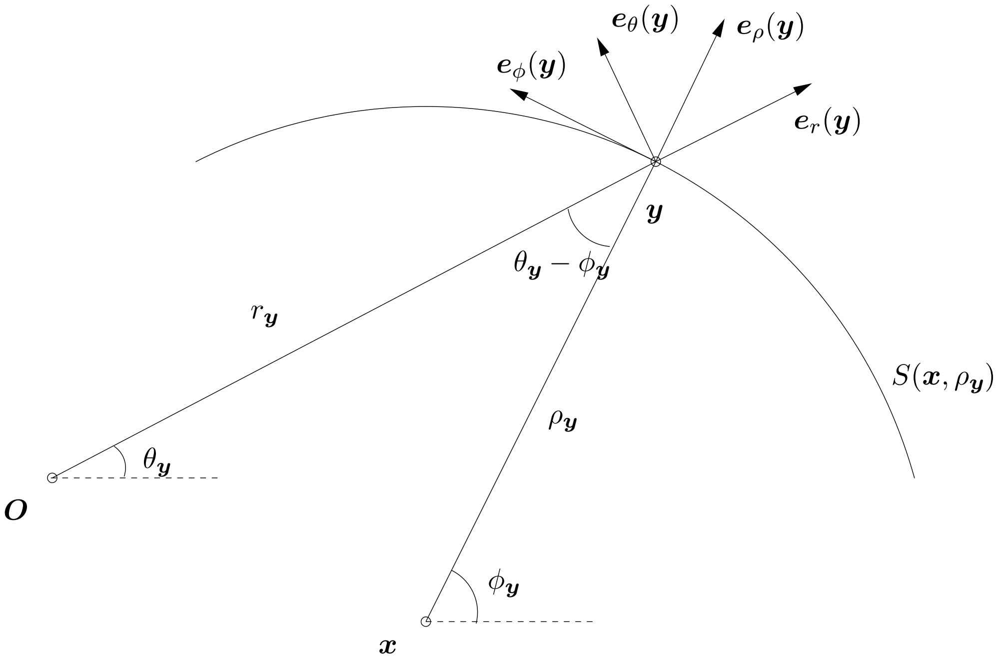

Figure 6.7: Basis of two different polar coordinate system.

For each point $\boldsymbol{y} \in \mathrm{D}$, we have

$$\boldsymbol{e}_r = \cos(\phi_{\boldsymbol{y}} - \theta_{\boldsymbol{y}})\boldsymbol{e}_\rho - \sin(\phi_{\boldsymbol{y}} - \theta_{\boldsymbol{y}})\boldsymbol{e}_\phi, \tag{6.51}$$

$$\boldsymbol{e}_\theta = \sin(\phi_{\boldsymbol{y}} - \theta_{\boldsymbol{y}})\boldsymbol{e}_\rho + \cos(\phi_{\boldsymbol{y}} - \theta_{\boldsymbol{y}})\boldsymbol{e}_\phi. \tag{6.52}$$

Moreover, we compute the partial derivatives of the coordinates in the first system with respect to the second one. Firstly, it is clear that

$$\rho_{\boldsymbol{y}} \cos\phi_{\boldsymbol{y}} = r_{\boldsymbol{y}} \cos\theta_{\boldsymbol{y}} - r(\boldsymbol{x})\cos\theta(\boldsymbol{x}), \tag{6.53}$$

$$\rho_{\boldsymbol{y}} \sin\phi_{\boldsymbol{y}} = r_{\boldsymbol{y}} \sin\theta_{\boldsymbol{y}} - r(\boldsymbol{x})\sin\theta(\boldsymbol{x}). \tag{6.54}$$

Let us introduce the functions ξ_r and ξ_θ be such that $r_{\boldsymbol{y}} = \xi_r(\rho_{\boldsymbol{y}}, \phi_{\boldsymbol{y}})$ and $\theta_{\boldsymbol{y}} = \xi_\theta(\rho_{\boldsymbol{y}}, \phi_{\boldsymbol{y}})$. If we derive both equations with respect to radial coordinate $\rho_{\boldsymbol{y}}$, we obtain the linear system

$$\begin{aligned}
\cos\phi_{\boldsymbol{y}} &= \frac{\partial \xi_r(\rho_{\boldsymbol{y}}, \phi_{\boldsymbol{y}})}{\partial \rho_{\boldsymbol{y}}} \cos\theta_{\boldsymbol{y}} - r_{\boldsymbol{y}} \sin\theta_{\boldsymbol{y}} \frac{\partial \xi_\theta(\rho_{\boldsymbol{y}}, \phi_{\boldsymbol{y}})}{\partial \rho_{\boldsymbol{y}}}, \\
\sin\phi_{\boldsymbol{y}} &= \frac{\partial \xi_r(\rho_{\boldsymbol{y}}, \phi_{\boldsymbol{y}})}{\partial \rho_{\boldsymbol{y}}} \sin\theta_{\boldsymbol{y}} + r_{\boldsymbol{y}} \cos\theta_{\boldsymbol{y}} \frac{\partial \xi_\theta(\rho_{\boldsymbol{y}}, \phi_{\boldsymbol{y}})}{\partial \rho_{\boldsymbol{y}}},
\end{aligned}$$

whose solution is

$$\begin{aligned}
\frac{\partial \xi_r(\rho_{\boldsymbol{y}}, \phi_{\boldsymbol{y}})}{\partial \rho_{\boldsymbol{y}}} &= \cos\phi_{\boldsymbol{y}} \cos\theta_{\boldsymbol{y}} + \sin\phi_{\boldsymbol{y}} \sin\theta_{\boldsymbol{y}} = \cos(\phi_{\boldsymbol{y}} - \theta_{\boldsymbol{y}}), \\
\frac{\partial \xi_\theta(\rho_{\boldsymbol{y}}, \phi_{\boldsymbol{y}})}{\partial \rho_{\boldsymbol{y}}} &= \frac{1}{r_{\boldsymbol{y}}}(\cos\theta_{\boldsymbol{y}} \sin\phi_{\boldsymbol{y}} - \sin\phi_{\boldsymbol{y}} \cos\theta_{\boldsymbol{y}}) = \frac{1}{r_{\boldsymbol{y}}} \sin(\phi_{\boldsymbol{y}} - \theta_{\boldsymbol{y}}).
\end{aligned}$$

Analogously, if we derive with respect to $\phi_{\boldsymbol{y}}$, we have

$$\begin{aligned}-\rho_{\boldsymbol{y}}\sin\phi_{\boldsymbol{y}} &= \frac{\partial\xi_r(\rho_{\boldsymbol{y}},\phi_{\boldsymbol{y}})}{\partial\phi_{\boldsymbol{y}}}\cos\theta_{\boldsymbol{y}} - r_{\boldsymbol{y}}\sin\theta_{\boldsymbol{y}}\frac{\partial\xi_\theta(\rho_{\boldsymbol{y}},\phi_{\boldsymbol{y}})}{\partial\phi_{\boldsymbol{y}}},\\ \rho_{\boldsymbol{y}}\cos\phi_{\boldsymbol{y}} &= \frac{\partial\xi_r(\rho_{\boldsymbol{y}},\phi_{\boldsymbol{y}})}{\partial\phi_{\boldsymbol{y}}}\sin\theta_{\boldsymbol{y}} + r_{\boldsymbol{y}}\cos\theta_{\boldsymbol{y}}\frac{\partial\xi_\theta(\rho_{\boldsymbol{y}},\phi_{\boldsymbol{y}})}{\partial\phi_{\boldsymbol{y}}},\end{aligned}$$

whose solution is

$$\begin{aligned}\frac{\partial\xi_r(\rho_{\boldsymbol{y}},\phi_{\boldsymbol{y}})}{\partial\phi_{\boldsymbol{y}}} &= \rho_{\boldsymbol{y}}(-\sin\phi_{\boldsymbol{y}}\cos\theta_{\boldsymbol{y}} + \cos\phi_{\boldsymbol{y}}\sin\theta_{\boldsymbol{y}}) = -\rho_{\boldsymbol{y}}\sin(\phi_{\boldsymbol{y}}-\theta_{\boldsymbol{y}}),\\ \frac{\partial\xi_\theta(\rho_{\boldsymbol{y}},\phi_{\boldsymbol{y}})}{\partial\phi_{\boldsymbol{y}}} &= \frac{\rho_{\boldsymbol{y}}}{r_{\boldsymbol{y}}}(\cos\theta_{\boldsymbol{y}}\cos\phi_{\boldsymbol{y}} - \sin\theta_{\boldsymbol{y}}\sin\phi_{\boldsymbol{y}}) = \frac{\rho_{\boldsymbol{y}}}{r_{\boldsymbol{y}}}\cos(\phi_{\boldsymbol{y}}-\theta_{\boldsymbol{y}}).\end{aligned}$$

Summarizing we have

$$\frac{\partial r_{\boldsymbol{y}}}{\partial\rho_{\boldsymbol{y}}} = \cos(\phi_{\boldsymbol{y}}-\theta_{\boldsymbol{y}}),\ \frac{\partial\theta_{\boldsymbol{y}}}{\partial\rho_{\boldsymbol{y}}} = \frac{1}{r_{\boldsymbol{y}}}\sin(\phi_{\boldsymbol{y}}-\theta_{\boldsymbol{y}}). \tag{6.55}$$

$$\frac{\partial r_{\boldsymbol{y}}}{\partial\phi_{\boldsymbol{y}}} = -\rho_{\boldsymbol{y}}\sin(\phi_{\boldsymbol{y}}-\theta_{\boldsymbol{y}}),\ \frac{\partial\theta_{\boldsymbol{y}}}{\partial\phi_{\boldsymbol{y}}} = \frac{\rho_{\boldsymbol{y}}}{r_{\boldsymbol{y}}}\cos(\phi_{\boldsymbol{y}}-\theta_{\boldsymbol{y}}). \tag{6.56}$$

Now we are going to study the behavior of the complex distance $\mathrm{d}(\cdot,\cdot)$ between close points and near the circumference $S_{R^\star}$. The following lemma collects several limits that will be used in the proof of Lemma 6.10.3 below.

Lemma 6.10.1. *For fixed $\boldsymbol{x}\in\mathrm{D}$ and $\phi_{\boldsymbol{y}}\in(-\pi,\pi]$,*

$$\lim_{\rho_{\boldsymbol{y}}\to 0}\frac{\partial\hat r_{\boldsymbol{y}}}{\partial\rho_{\boldsymbol{y}}} = \gamma_{\boldsymbol{x}}\cos(\phi_{\boldsymbol{y}}-\theta_{\boldsymbol{x}}), \tag{6.57}$$

$$\lim_{\rho_{\boldsymbol{y}}\to 0}\frac{\partial\mathrm{d}(\boldsymbol{x},\boldsymbol{y})}{\partial\rho_{\boldsymbol{y}}} = \sqrt{\gamma_{\boldsymbol{x}}^2\cos^2(\phi_{\boldsymbol{y}}-\theta_{\boldsymbol{x}}) + \hat\gamma_{\boldsymbol{x}}^2\sin^2(\phi_{\boldsymbol{y}}-\theta_{\boldsymbol{x}})}, \tag{6.58}$$

$$\lim_{\rho_{\boldsymbol{y}}\to 0}\frac{\hat r_{\boldsymbol{y}} - \hat r_{\boldsymbol{x}}\cos(\theta_{\boldsymbol{y}}-\theta_{\boldsymbol{x}})}{r_{\boldsymbol{y}} - r_{\boldsymbol{x}}\cos(\theta_{\boldsymbol{y}}-\theta_{\boldsymbol{x}})} = \gamma_{\boldsymbol{x}}. \tag{6.59}$$

Proof. It is clear that, since $\mathrm{d}(\boldsymbol{x},\cdot)$ and $\hat r(|\cdot|)$ are in $\mathcal{C}^1(\mathrm{D}\setminus\{\boldsymbol{x}\})$, we can compute derivatives at any point of D different form $\boldsymbol{x}$. In order to obtain the first equation, we have

$$\frac{\partial\hat r_{\boldsymbol{y}}}{\partial\rho_{\boldsymbol{y}}} = \frac{\partial\hat r_{\boldsymbol{y}}}{\partial r_{\boldsymbol{y}}}\frac{\partial r_{\boldsymbol{y}}}{\partial\rho_{\boldsymbol{y}}}. \tag{6.60}$$

From the definition of $\hat r_{\boldsymbol{y}}$ it is immediate to check that $\frac{\partial\hat r_{\boldsymbol{y}}}{\partial r_{\boldsymbol{y}}} = \gamma_{\boldsymbol{y}}$. Then, from (6.60) and (6.55) we obtain

$$\frac{\partial\hat r_{\boldsymbol{y}}}{\partial\rho_{\boldsymbol{y}}} = \gamma_{\boldsymbol{y}}\cos(\phi_{\boldsymbol{y}}-\theta_{\boldsymbol{y}}).$$

If $\rho_{\boldsymbol{y}} = 0$, then $\boldsymbol{x} = \boldsymbol{y}$ and (6.57) is obtained. For the second equation, firstly we are going to bound the limit. For $\boldsymbol{x} \in \mathrm{D}$ and a fixed angle $\phi_{\boldsymbol{y}} \in (-\pi, \pi]$, using the Taylor polinomial of first order for function $F(\rho_{\boldsymbol{y}}) = \mathrm{d}(\boldsymbol{x}, \boldsymbol{x} + \rho_{\boldsymbol{y}}(\cos\phi_{\boldsymbol{y}}, \sin\phi_{\boldsymbol{y}}))$, which is smooth in $[0, +\infty)$, we obtain

$$\lim_{\rho_{\boldsymbol{y}}\to 0} \frac{\mathrm{d}(\boldsymbol{x},\boldsymbol{y})}{\rho_{\boldsymbol{y}}} = \lim_{\rho_{\boldsymbol{y}}\to 0} \frac{F(\rho_{\boldsymbol{y}})}{\rho_{\boldsymbol{y}}} = F'(0) = \lim_{\rho_{\boldsymbol{y}}\to 0} \frac{\partial \mathrm{d}(\boldsymbol{x},\boldsymbol{y})}{\partial \rho_{\boldsymbol{y}}}. \tag{6.61}$$

Hence, it is clear that $F'(0) \in [C_1, C_2]$ where the positive constants C_1, C_2 are given by lemma 6.4.4. Therefore,

$$\begin{aligned}
F'(0) &= \lim_{\rho_{\boldsymbol{y}}\to 0} \frac{\partial \mathrm{d}(\boldsymbol{x},\boldsymbol{y})}{\partial \rho_{\boldsymbol{y}}} = \lim_{\rho_{\boldsymbol{y}}\to 0} \left(\frac{\partial \mathrm{d}(\boldsymbol{x},\boldsymbol{y})}{\partial \hat{r}_{\boldsymbol{y}}} \frac{\partial \hat{r}_{\boldsymbol{y}}}{\partial \rho_{\boldsymbol{y}}} + \frac{\partial \mathrm{d}(\boldsymbol{x},\boldsymbol{y})}{\partial \theta_{\boldsymbol{y}}} \frac{\partial \theta_{\boldsymbol{y}}}{\partial \rho_{\boldsymbol{y}}} \right) \\
&= \lim_{\rho_{\boldsymbol{y}}\to 0} \frac{\hat{r}_{\boldsymbol{y}} - \hat{r}_{\boldsymbol{x}} \cos(\theta_{\boldsymbol{y}} - \theta_{\boldsymbol{x}})}{\mathrm{d}(\boldsymbol{x},\boldsymbol{y})} \gamma_{\boldsymbol{y}} \cos(\phi_{\boldsymbol{y}} - \theta_{\boldsymbol{y}}) + \lim_{\rho_{\boldsymbol{y}}\to 0} \frac{\hat{r}_{\boldsymbol{y}} \hat{r}_{\boldsymbol{x}} \sin(\theta_{\boldsymbol{y}} - \theta_{\boldsymbol{x}})}{\mathrm{d}(\boldsymbol{x},\boldsymbol{y})} \frac{\sin(\phi_{\boldsymbol{y}} - \theta_{\boldsymbol{y}})}{r_{\boldsymbol{y}}} \\
&= \gamma_{\boldsymbol{x}} \cos(\phi_{\boldsymbol{y}} - \theta_{\boldsymbol{x}}) \lim_{\rho_{\boldsymbol{y}}\to 0} \frac{\hat{r}_{\boldsymbol{y}} - \hat{r}_{\boldsymbol{x}} \cos(\theta_{\boldsymbol{y}} - \theta_{\boldsymbol{x}})}{\mathrm{d}(\boldsymbol{x},\boldsymbol{y})} + \hat{r}_{\boldsymbol{x}} \hat{\gamma}_{\boldsymbol{x}} \sin(\phi_{\boldsymbol{y}} - \theta_{\boldsymbol{x}}) \lim_{\rho_{\boldsymbol{y}}\to 0} \frac{\sin(\theta_{\boldsymbol{y}} - \theta_{\boldsymbol{x}})}{\mathrm{d}(\boldsymbol{x},\boldsymbol{y})}.
\end{aligned}$$

In the last equality we have used that $\frac{\hat{r}_{\boldsymbol{x}}}{r_{\boldsymbol{x}}} = \hat{\gamma}_{\boldsymbol{x}}$. Now, taking into account that $F'(0) \neq 0$, we have

$$\begin{aligned}
F'(0) =& \gamma_{\boldsymbol{x}} \cos(\phi_{\boldsymbol{y}} - \theta_{\boldsymbol{x}}) \lim_{\rho_{\boldsymbol{y}}\to 0} \frac{\frac{\partial \hat{r}_{\boldsymbol{y}}}{\partial \rho_{\boldsymbol{y}}} + \frac{\hat{r}_{\boldsymbol{x}}}{r_{\boldsymbol{y}}} \sin(\theta_{\boldsymbol{y}} - \theta_{\boldsymbol{x}}) \sin(\phi_{\boldsymbol{y}} - \theta_{\boldsymbol{y}})}{\frac{\partial \mathrm{d}(\boldsymbol{x},\boldsymbol{y})}{\partial \rho_{\boldsymbol{y}}}} \\
&+ \hat{r}_{\boldsymbol{x}} \hat{\gamma}_{\boldsymbol{x}} \sin(\phi_{\boldsymbol{y}} - \theta_{\boldsymbol{x}}) \lim_{\rho_{\boldsymbol{y}}\to 0} \frac{\cos(\theta_{\boldsymbol{y}} - \theta_{\boldsymbol{x}}) \frac{1}{r_{\boldsymbol{y}}} \sin(\phi_{\boldsymbol{y}} - \theta_{\boldsymbol{y}})}{\frac{\partial \mathrm{d}(\boldsymbol{x},\boldsymbol{y})}{\partial \rho_{\boldsymbol{y}}}} \\
=& \gamma_{\boldsymbol{x}} \cos(\phi_{\boldsymbol{y}} - \theta_{\boldsymbol{x}}) \frac{\gamma_{\boldsymbol{x}} \cos(\phi_{\boldsymbol{y}} - \theta_{\boldsymbol{x}})}{F'(0)} + \hat{r}_{\boldsymbol{x}} \hat{\gamma}_{\boldsymbol{x}} \sin(\phi_{\boldsymbol{y}} - \theta_{\boldsymbol{x}}) \frac{1}{r_{\boldsymbol{x}}} \frac{\sin(\phi_{\boldsymbol{y}} - \theta_{\boldsymbol{x}})}{F'(0)} \\
=& F'(0)^{-1} \left(\gamma_{\boldsymbol{x}}^2 \cos^2(\phi_{\boldsymbol{y}} - \theta_{\boldsymbol{x}}) + \hat{\gamma}_{\boldsymbol{x}}^2 \sin^2(\phi_{\boldsymbol{y}} - \theta_{\boldsymbol{x}}) \right).
\end{aligned}$$

Solving the above equation to obtain $F'(0)$, we conclude (6.58). For the last limit (6.59), we can use again an analogous argument involving Taylor polinomial of first order over each factor in the quotient and (6.57), to obtain

$$\lim_{\rho_{\boldsymbol{y}}\to 0} \frac{\hat{r}_{\boldsymbol{y}} - \hat{r}_{\boldsymbol{x}} \cos(\theta_{\boldsymbol{y}} - \theta_{\boldsymbol{x}})}{r_{\boldsymbol{y}} - r_{\boldsymbol{x}} \cos(\theta_{\boldsymbol{y}} - \theta_{\boldsymbol{x}})} = \lim_{\rho_{\boldsymbol{y}}\to 0} \frac{\frac{\partial \hat{r}_{\boldsymbol{y}}}{\partial \rho_{\boldsymbol{y}}} + \hat{r}_{\boldsymbol{x}} \sin(\theta_{\boldsymbol{y}} - \theta_{\boldsymbol{x}}) \frac{\partial \xi_\theta}{\partial \rho_{\boldsymbol{y}}}}{\frac{\partial r_{\boldsymbol{y}}}{\partial \rho_{\boldsymbol{y}}} + r_{\boldsymbol{x}} \sin(\theta_{\boldsymbol{y}} - \theta_{\boldsymbol{x}}) \frac{\partial \xi_\theta}{\partial \rho_{\boldsymbol{y}}}} = \gamma_{\boldsymbol{x}}. \tag{6.62}$$

□

The following integral will be also used below.

Lemma 6.10.2. *For $a \in \mathbb{C}$ with $\mathrm{Re}(a) \neq 0$, there holds*

$$\frac{1}{2\pi} \int_{-\pi}^{\pi} \frac{1}{a \cos^2\theta + a^{-1} \sin^2\theta} \, d\theta = \mathrm{sign}(\mathrm{Re}(a)). \tag{6.63}$$

Proof. Firstly it is easy to see that

$$I = \int_{-\pi}^{\pi} \frac{1}{a\cos^2\theta + a^{-1}\sin^2\theta}\,d\theta = 2a\int_{-\frac{\pi}{2}}^{\frac{\pi}{2}} \frac{1}{\cos^2\theta}\frac{1}{a^2+\tan^2\theta}\,d\theta.$$

Using the change of variable $s = \tan\theta$, we have $\dfrac{ds}{d\theta} = \dfrac{1}{\cos^2\theta}$ and then

$$I = 2a\int_{-\infty}^{\infty}\frac{1}{a^2+s^2}ds = \frac{2}{a}\int_{-\infty}^{\infty}\frac{1}{1+a^{-2}s^2}ds = \lim_{R\to\infty}\frac{2}{a}\int_{-R}^{R}\frac{1}{1+a^{-2}s^2}ds. \tag{6.64}$$

In order to evaluate the previous improper integral, we apply the Residues's theorem. For this purpose we have to calculate the residues of the function $f(\boldsymbol{z}) = \dfrac{1}{1+a^{-2}z^2} = \dfrac{1}{2}\left(\dfrac{1}{1+ia^{-1}z} + \dfrac{1}{1-ia^{-1}z}\right)$ in the poles $\pm ia$. In fact,

$$Res\, f(z) = \begin{cases} \frac{a}{2i} & \text{in } z = ia, \\ \frac{-a}{2i} & \text{in } z = -ia. \end{cases} \tag{6.65}$$

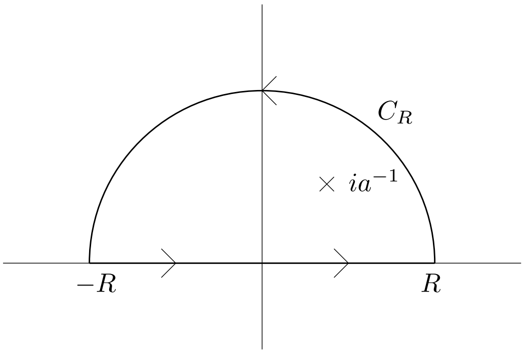

Figure 6.8: Path in the complex plane (when $\mathrm{Im}(ia) > 0$).

Now we have two alternatives to be considered: if $\mathrm{Im}(ia) > 0$ we obtain

$$\int_{-R}^{R}\frac{1}{1+a^{-2}s^2}ds = 2\pi i Res\, f(ia) - \int_{C_R}\frac{1}{1+a^{-2}s^2}ds, \tag{6.66}$$

whereas if $\mathrm{Im}(ia) < 0$,

$$\int_{-R}^{R}\frac{1}{1+a^{-2}s^2}ds = 2\pi i Res\, f(-ia) - \int_{C_R}\frac{1}{1+a^{-2}s^2}ds, \tag{6.67}$$

where $C_r = \{r\,\mathrm{e}^{i\theta} : \theta \in [0,\pi]\}$ with $r = R$ and $r = -R$. When R tends to infinity, the integral on C_R goes to zero and we conclude

$$I = \lim_{R\to\infty} \frac{2}{a} \int_{-R}^{R} \frac{1}{1+a^{-2}s^2} ds = \mathrm{sign}(\mathrm{Im}(ia))2\pi = \mathrm{sign}(\mathrm{Re}(a))2\pi. \tag{6.68}$$

□

Now, we are in a position to prove the next lemma, which has been used in Theorems 6.4.6 and 6.5.3.

Lemma 6.10.3. *For $\boldsymbol{x} \in \mathrm{D}$ fixed, if $\Phi^{\pm}$ are the fundamental solutions given by (6.21) and (6.22), and $\varphi \in \mathcal{C}^1(\mathrm{D})$, then*

$$\lim_{\epsilon\to 0}\left(\int_{S(\boldsymbol{x},\epsilon)} \boldsymbol{A_y}\,\mathbf{grad}_{\boldsymbol{y}}\,\Phi^{\pm}(\boldsymbol{x},\boldsymbol{y})\cdot\boldsymbol{n}\,\varphi(\boldsymbol{y})\,dS_{\boldsymbol{y}} - \int_{S(\boldsymbol{x},\epsilon)} \boldsymbol{A_y}\,\mathbf{grad}_{\boldsymbol{y}}\,\varphi(\boldsymbol{y})\cdot\boldsymbol{n}\,\Phi^{\pm}(\boldsymbol{x},\boldsymbol{y})\,dS_{\boldsymbol{y}}\right) = \varphi(\boldsymbol{x}), \tag{6.69}$$

where $S(\boldsymbol{x},\epsilon) = \{\boldsymbol{y}\in\mathbb{R}^2 : |\boldsymbol{x}-\boldsymbol{y}| = \epsilon\}$ and $\boldsymbol{n}$ is its inward unit normal vector.

Proof. We prove the lemma for Φ^+. An analogous proof is valid for Φ^-.

First, we check that the limit of the second integral in (6.69) is zero. Since $\varphi \in \mathcal{C}^1(\mathrm{D})$ and the coefficients of $\boldsymbol{A_y}$ are bounded for all $\boldsymbol{y}$ such that $|\boldsymbol{x}-\boldsymbol{y}| \leq \epsilon$, we only have to prove that

$$\lim_{\epsilon\to 0}\int_{S(\boldsymbol{x},\epsilon)} \Phi^+(\boldsymbol{x},\boldsymbol{y})\,dS_{\boldsymbol{y}} = 0.$$

The above limit is easy to check by using Lemma 6.4.4 and the following estimate:

$$\left|\Phi^+(\boldsymbol{x},\boldsymbol{y}) - \frac{i}{4}\left(\frac{2i}{\pi}\log\frac{k\mathrm{d}(\boldsymbol{x},\boldsymbol{y})}{2} + \frac{2C_e i}{\pi} + 1\right)\right| \leq C\,|\mathrm{d}(\boldsymbol{x},\boldsymbol{y})|^2\,|\log\mathrm{d}(\boldsymbol{x},\boldsymbol{y})|\,,$$

for $|\boldsymbol{x}-\boldsymbol{y}|$ small enough, which in its turn follows from the asymptotic behavior of Hankel functions (see [103]). In the above expression, C_e is the Euler's constant.

Regarding the first integral in (6.69), since $\boldsymbol{n} = -\boldsymbol{e}_\rho$ on $S(\boldsymbol{x},\epsilon)$, from (6.21), (6.51) and (6.52), we have

$$\begin{aligned}\boldsymbol{A_y}\,\mathbf{grad}_{\boldsymbol{y}}\,\Phi^+(\boldsymbol{x},\boldsymbol{y})\cdot\boldsymbol{n} &= \left(\frac{\hat\gamma_{\boldsymbol{y}}}{\gamma_{\boldsymbol{y}}}\frac{\partial\Phi^+(\boldsymbol{x},\boldsymbol{y})}{\partial r_{\boldsymbol{y}}}\boldsymbol{e}_r + \frac{\gamma_{\boldsymbol{y}}}{\hat r_{\boldsymbol{y}}}\frac{\partial\Phi^+(\boldsymbol{x},\boldsymbol{y})}{\partial\theta_{\boldsymbol{y}}}\boldsymbol{e}_\theta\right)\cdot(-\boldsymbol{e}_\rho)\\ &= -k\frac{i}{4}[\mathrm{H}_0^{(1)}]'(k\mathrm{d}(\boldsymbol{x},\boldsymbol{y}))\left[\frac{\hat\gamma_{\boldsymbol{y}}}{\gamma_{\boldsymbol{y}}}\frac{\partial\mathrm{d}(\boldsymbol{x},\boldsymbol{y})}{\partial r_{\boldsymbol{y}}}\cos(\phi_{\boldsymbol{y}}-\theta_{\boldsymbol{y}}) + \frac{\gamma_{\boldsymbol{y}}}{\hat r_{\boldsymbol{y}}}\frac{\partial\mathrm{d}(\boldsymbol{x},\boldsymbol{y})}{\partial\theta_{\boldsymbol{y}}}\sin(\phi_{\boldsymbol{y}}-\theta_{\boldsymbol{y}})\right]\\ &=: -k\frac{i}{4}[\mathrm{H}_0^{(1)}]'(k\mathrm{d}(\boldsymbol{x},\boldsymbol{y}))M(\boldsymbol{x},\boldsymbol{y}),\end{aligned} \tag{6.70}$$

where $M(\boldsymbol{x},\boldsymbol{y})$ denotes the expression between brackets above. By using the following elementary identities (see Figure 6.9):

$$
\begin{aligned}
|\boldsymbol{x}-\boldsymbol{y}|\cos(\phi_{\boldsymbol{y}}-\theta_{\boldsymbol{y}}) &= r_{\boldsymbol{y}} - r_{\boldsymbol{x}}\cos(\theta_{\boldsymbol{y}}-\theta_{\boldsymbol{x}}),\\
|\boldsymbol{x}-\boldsymbol{y}|\sin(\phi_{\boldsymbol{y}}-\theta_{\boldsymbol{y}}) &= r_{\boldsymbol{x}}\sin(\theta_{\boldsymbol{y}}-\theta_{\boldsymbol{x}}),
\end{aligned}
$$

we obtain

$$
M(\boldsymbol{x},\boldsymbol{y}) = \left(\hat{\gamma}_{\boldsymbol{y}}\frac{\hat{r}_{\boldsymbol{y}}-\hat{r}_{\boldsymbol{x}}\cos(\theta_{\boldsymbol{y}}-\theta_{\boldsymbol{x}})}{r_{\boldsymbol{y}}-r_{\boldsymbol{x}}\cos(\theta_{\boldsymbol{y}}-\theta_{\boldsymbol{x}})}\cos^2(\phi_{\boldsymbol{y}}-\theta_{\boldsymbol{y}}) + \frac{\gamma_{\boldsymbol{y}}\hat{r}_{\boldsymbol{x}}}{r_{\boldsymbol{x}}}\sin^2(\phi_{\boldsymbol{y}}-\theta_{\boldsymbol{y}})\right)\frac{|\boldsymbol{x}-\boldsymbol{y}|}{\mathrm{d}(\boldsymbol{x},\boldsymbol{y})},
$$

which, in particular, together with Lemma 6.4.4 and the third limit from Lemma 6.10.1, show that $M(\boldsymbol{x},\boldsymbol{y})$ is bounded for $|\boldsymbol{x}-\boldsymbol{y}|$ small enough.

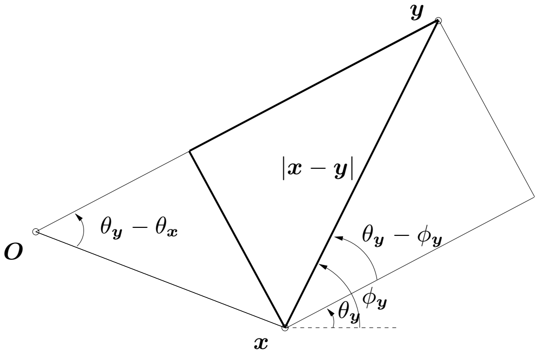

Figure 6.9: Polar coordinates systems centered at the origin $\boldsymbol{O}$ and at a point $\boldsymbol{x}\in\mathbb{R}^2$

On the other hand, by using a classical estimate of $[\mathrm{H}_0^{(1)}]'(z)$ (see [103]) and Lemma 6.4.4, we have

$$
\left|[\mathrm{H}_0^{(1)}]'(k\mathrm{d}(\boldsymbol{x},\boldsymbol{y})) - \frac{2i}{\pi}\frac{1}{k\mathrm{d}(\boldsymbol{x},\boldsymbol{y})}\right| \leq C\,|\boldsymbol{x}-\boldsymbol{y}|\,|\log(k\mathrm{d}(\boldsymbol{x},\boldsymbol{y}))|, \tag{6.71}
$$

for $|\boldsymbol{x}-\boldsymbol{y}|$ small enough. Because of this, we proceed from (6.70) as follows:

$$
\begin{aligned}
\int_{S(\boldsymbol{x},\epsilon)} \boldsymbol{A}_{\boldsymbol{y}}\,\mathbf{grad}_{\boldsymbol{y}}\Phi^+(\boldsymbol{x},\boldsymbol{y})\cdot\boldsymbol{n}\,\varphi(\boldsymbol{y})dS_{\boldsymbol{y}} &= -\int_{-\pi}^{\pi}\epsilon k\frac{i}{4}M(\boldsymbol{x},\boldsymbol{y})\frac{2i}{\pi}\frac{1}{k\mathrm{d}(\boldsymbol{x},\boldsymbol{y})}\varphi(\boldsymbol{y})\,d\phi_{\boldsymbol{y}}\\
&\quad-\int_{-\pi}^{\pi}\epsilon k\frac{i}{4}M(\boldsymbol{x},\boldsymbol{y})\left([\mathrm{H}_0^{(1)}]'(k\mathrm{d}(\boldsymbol{x},\boldsymbol{y})) - \frac{2i}{\pi}\frac{1}{k\mathrm{d}(\boldsymbol{x},\boldsymbol{y})}\right)\varphi(\boldsymbol{y})\,d\phi_{\boldsymbol{y}}.
\end{aligned}\tag{6.72}
$$

Manipulating the second integral from (6.71), we obtain

$$
\begin{aligned}
&\left|\int_{-\pi}^{\pi}\epsilon k\frac{i}{4}M(\boldsymbol{x},\boldsymbol{y})\left([\mathrm{H}_0^{(1)}]'(k\mathrm{d}(\boldsymbol{x},\boldsymbol{y})) - \frac{2i}{\pi}\frac{1}{k\mathrm{d}(\boldsymbol{x},\boldsymbol{y})}\right)\varphi(\boldsymbol{y})\,d\phi_{\boldsymbol{y}}\right|\\
&\qquad\leq C\int_{-\pi}^{\pi}\frac{k}{4}\,|M(\boldsymbol{x},\boldsymbol{y})|\,\epsilon^2\,|\log(k\mathrm{d}(\boldsymbol{x},\boldsymbol{y}))|\,|\varphi(\boldsymbol{y})|\,d\phi_{\boldsymbol{y}} \longrightarrow 0 \qquad \text{as } \epsilon\to 0,
\end{aligned}\tag{6.73}
$$

since $M(\boldsymbol{x},\boldsymbol{y})$ is bounded for $|\boldsymbol{x}-\boldsymbol{y}|\leq\epsilon$ and $|\mathrm{d}(\boldsymbol{x},\boldsymbol{y})|=O(\epsilon)$ uniformly in all directions (see Lemma 6.4.4).

Thus, we only have to calculate the limit of the remaining integral in (6.72). For this purpose, we compute the following limit as $\rho_{\boldsymbol{y}}=|\boldsymbol{x}-\boldsymbol{y}|\to 0$ for fixed $\phi_{\boldsymbol{y}}\in(-\pi,\pi]$:

$$\begin{aligned}\lim_{\rho_{\boldsymbol{y}}\to 0}\frac{\rho_{\boldsymbol{y}}M(\boldsymbol{x},\boldsymbol{y})}{\mathrm{d}(\boldsymbol{x},\boldsymbol{y})}=&\left(\hat{\gamma}_{\boldsymbol{x}}\cos(\phi_{\boldsymbol{y}}-\theta_{\boldsymbol{x}})\lim_{\rho_{\boldsymbol{y}}\to 0}\frac{\dfrac{\partial\hat{r}_{\boldsymbol{y}}}{\partial\rho_{\boldsymbol{y}}}+\hat{r}_{\boldsymbol{x}}\sin(\theta_{\boldsymbol{y}}-\theta_{\boldsymbol{x}})\dfrac{\partial\theta_{\boldsymbol{y}}}{\partial\rho_{\boldsymbol{y}}}}{\dfrac{\partial\mathrm{d}(\boldsymbol{x},\boldsymbol{y})}{\partial\rho_{\boldsymbol{y}}}}\right.\\&\left.+\gamma_{\boldsymbol{x}}\hat{r}_{\boldsymbol{x}}\sin(\phi_{\boldsymbol{y}}-\theta_{\boldsymbol{x}})\lim_{\rho_{\boldsymbol{y}}\to 0}\frac{\cos(\theta_{\boldsymbol{y}}-\theta_{\boldsymbol{x}})\dfrac{\partial\theta_{\boldsymbol{y}}}{\partial\rho_{\boldsymbol{y}}}}{\dfrac{\partial\mathrm{d}(\boldsymbol{x},\boldsymbol{y})}{\partial\rho_{\boldsymbol{y}}}}\right)\lim_{\rho_{\boldsymbol{y}}\to 0}\left(\frac{\partial\mathrm{d}(\boldsymbol{x},\boldsymbol{y})}{\partial\rho_{\boldsymbol{y}}}\right)^{-1}\\=&\gamma_{\boldsymbol{x}}\hat{\gamma}_{\boldsymbol{x}}\lim_{\rho_{\boldsymbol{y}}\to 0}\left(\frac{\partial\mathrm{d}(\boldsymbol{x},\boldsymbol{y})}{\partial\rho_{\boldsymbol{y}}}\right)^{-2}=\frac{\gamma_{\boldsymbol{x}}\hat{\gamma}_{\boldsymbol{x}}}{\gamma_{\boldsymbol{x}}^2\cos^2(\phi_{\boldsymbol{y}}-\theta_{\boldsymbol{x}})+\hat{\gamma}_{\boldsymbol{x}}^2\sin^2(\phi_{\boldsymbol{y}}-\theta_{\boldsymbol{x}})},\end{aligned}$$

where we have used L'Hôpital's rule, Lemma 6.10.1 and (6.55).

Therefore, since $\rho_{\boldsymbol{y}}=\epsilon$ on $S(\boldsymbol{x},\epsilon)$, by using the above limit, the boundedness of $M(\boldsymbol{x},\boldsymbol{y})$ and Lemma 6.4.4, we have from (6.72) and (6.73)

$$\begin{aligned}&\lim_{\epsilon\to 0}\int_{S(\boldsymbol{x},\epsilon)}\boldsymbol{A}_{\boldsymbol{y}}\,\mathbf{grad}_{\boldsymbol{y}}\,\Phi^{+}(\boldsymbol{x},\boldsymbol{y})\cdot\boldsymbol{n}\,\varphi(\boldsymbol{y})dS_{\boldsymbol{y}}\\&\quad=\varphi(\boldsymbol{x})\frac{1}{2\pi}\int_{-\pi}^{\pi}\frac{\gamma_{\boldsymbol{x}}\hat{\gamma}_{\boldsymbol{x}}}{\gamma_{\boldsymbol{x}}^2\cos^2(\phi_{\boldsymbol{y}}-\theta_{\boldsymbol{x}})+\hat{\gamma}_{\boldsymbol{x}}^2\sin^2(\phi_{\boldsymbol{y}}-\theta_{\boldsymbol{x}})}\,d\phi_{\boldsymbol{y}}\\&\quad=\operatorname{sign}\left(\operatorname{Re}\left(\frac{\gamma_{\boldsymbol{x}}}{\hat{\gamma}_{\boldsymbol{x}}}\right)\right)\varphi(\boldsymbol{x})\\&\quad=\varphi(\boldsymbol{x}),\end{aligned}$$

because of Lemma 6.10.2 with $a=\gamma_{\boldsymbol{x}}/\hat{\gamma}_{\boldsymbol{x}}$, which can be shown that has a positive real part. ☐

6.10.2 Some classical results about the Hankel functions

In the two dimensional case, the elementary solutions of Helmholtz equation are the Hankel functions of first and second kind of order n, which are denoted by $\mathrm{H}_n^{(1)}$ and $\mathrm{H}_n^{(2)}$, respectively. In this appendix, we focus our attention on some simple asymptotic properties of the Hankel functions. For a more detailed analysis we refer to Lebedev [80] or Watson [103].

Firstly, we can write the Hankel functions using Bessel functions as

$$\begin{aligned}\mathrm{H}_n^{(1)}(z)&:=\mathrm{J}_n(z)+i\,Y_n(z),\\\mathrm{H}_n^{(2)}(z)&:=\mathrm{J}_n(z)-i\,Y_n(z),\end{aligned}$$

where J_n and Y_n are the Bessel functions of first and second kind of order n.

The following series expansions for the Bessel functions are known:

$$\mathrm{J}_n(z) =\sum_{k=0}^{\infty} \frac{(-1)^k}{k!(n+k)!}\left(\frac{z}{2}\right)^{n+2k}, \tag{6.74}$$

$$\begin{aligned} Y_n(z) =& \frac{2}{\pi}\,\mathrm{J}_n(z)\log\frac{z}{2} - \frac{1}{\pi}\sum_{k=0}^{n-1}\frac{(n-k-1)!}{k!}\left(\frac{z}{2}\right)^{2k-n} \\ &- \frac{1}{\pi}\sum_{k=0}^{\infty}\frac{(-1)^k}{k!(n+k)!}\left(\frac{z}{2}\right)^{n+2k}(\psi(k+1)+\psi(k+n+1)), \end{aligned} \tag{6.75}$$

where $\psi(k+1) = -C_e + 1 + \cdots + \frac{1}{k}$, $k \in \mathbb{N}$ and C_e is the Euler's constant. The sum of the series (6.74) and (6.75) are analytic functions of z in the complex plane cut along $(-\infty, 0]$.

Lemma 6.10.4. *The Hankel functions of order 0 verify the following asymptotic behavior when the modulus of the argument is small, i. e., when* $|z| \to 0$

$$\mathrm{H}_0^{(1)}(z) = \frac{2i}{\pi}\log\frac{z}{2}\frac{2C_e i}{\pi} + 1 + O(|z|^2\,|\log z|), \tag{6.76}$$

$$\frac{d\,\mathrm{H}_0^{(1)}}{dz}(z) = \frac{2i}{\pi}\frac{1}{z} + O(|z|\,|\log z|). \tag{6.77}$$

Proof. For $n = 0$, using (6.74) and (6.75) it is immediate to conclude that

$$\begin{aligned} \mathrm{H}_0^{(1)}(z) &= \mathrm{J}_0(z) + i\,Y_0(z) \\ &= 1 + O(|z^2|) + i\left(\frac{2}{\pi}\left(1 + O(|z|^2)\right)\log\frac{z}{2} + \frac{2C_e}{\pi} + O(|z|^2)\right) \\ &= \frac{2i}{\pi}\log\frac{z}{2} + \frac{2C_e i}{\pi} + 1 + O(|z|^2\,|\log z|), \end{aligned}$$

when $|z| \to 0$.

On the other hand, taking into account (6.74) and (6.75) for $n = 1$,

$$\begin{aligned} \frac{d\,\mathrm{H}_0^{(1)}}{dz}(z) &= -\,\mathrm{H}_1^{(1)}(z) = -\,\mathrm{J}_1(z) - i\,Y_1(z) \\ &= O(|z|) - i\left(\frac{2}{\pi}O(|z|)\log\frac{z}{2} - \frac{1}{\pi}\frac{2}{z} + O(|z|)\right) \\ &= \frac{2i}{\pi}\frac{1}{z} + O(|z|\,|\log z|) + O(|z|) = \frac{2i}{\pi}\frac{1}{z} + O(|z|\,|\log z|), \end{aligned}$$

when $|z| \to 0$.

Analogously, using the definition of $\mathrm{H}_n^{(2)}$, (6.74) and (6.75) we obtain the results for the Hankel functions of second kind. □

Lemma 6.10.5. *The following asymptotic behavior with respect to the order n is verified*

$$\mathrm{J}_n(z) = \frac{z^n}{2^n n!}\left(1 + O\left(\frac{1}{n}\right)\right), \tag{6.78}$$

$$\mathrm{H}_n^{(1)}(z) = \frac{2^n (n-1)!}{i\pi z^n}\left(1 + O\left(\frac{1}{n}\right)\right), \tag{6.79}$$

when $n \to \infty$. Moreover, analogous asymtotic behaviour is obtained for their derivatives:

$$\frac{d\,\mathrm{J}_n}{dz}(z) = \frac{z^{n-1}}{2^n (n-1)!}\left(1 + O\left(\frac{1}{n}\right)\right), \tag{6.80}$$

$$\frac{d\,\mathrm{H}_n^{(1)}}{dz}(z) = \frac{-2^n n!}{i\pi z^{n+1}}\left(1 + O\left(\frac{1}{n}\right)\right), \tag{6.81}$$

when $n \to \infty$.

Proof. Firstly, from (6.74) we have

$$\begin{aligned}\mathrm{J}_n(z) &= \sum_{k=0}^{\infty} \frac{(-1)^k}{k!(n+k)!}\left(\frac{z}{2}\right)^{n+2k} = \frac{z^n}{2^n n!}\sum_{k=0}^{\infty}\frac{(-1)^k n!}{k!(n+k)!}\left(\frac{z}{2}\right)^{2k} \\ &= \frac{z^n}{2^n n!}\left(1 + O\left(\frac{1}{n}\right)\right) = O\left(\frac{1}{n}\right),\end{aligned}$$

when $n \to \infty$.

In a similar way,

$$\begin{aligned}Y_n(z) &= -\frac{(n-1)!}{\pi}\left(\frac{2}{z}\right)^n\left(1 + O\left(\frac{1}{n}\right)\right) + O\left(\frac{1}{n}\right) + O\left(\frac{1}{n!}\right) \\ &= -\frac{(n-1)!}{\pi}\left(\frac{2}{z}\right)^n\left(1 + O\left(\frac{1}{n}\right)\right),\end{aligned}$$

when $n \to \infty$. Then, from the definition of $\mathrm{H}_n^{(1)}$, we obtain the asymptotic behavior (6.79). Finally, we can obtain estimates (6.80) and (6.81) again taking into account the series expansions of the Bessel and Hankel functions. ☐

***Remark* 6.10.6.** *We must remark how the expressions (6.78)-(6.81) must be understood. For instance, (6.78) implies that there exists $C > 0$ and $N \in \mathbb{N}$ such that for all $n > N$, if $n > N$ then*

$$1 - \frac{C}{n} \leq \left|\frac{\mathrm{J}_n(z)}{\dfrac{z^n}{2^n n!}}\right| \leq 1 + \frac{C}{n}.$$

We finish this section with a more technical and classical lemma proved, for example, in [103].

Lemma 6.10.7. *For large argument, we have the following asymptotic behavior of the Hankel functions*

$$\mathrm{H}_n^{(1)}(z) = \sqrt{\frac{2}{\pi z}}\, \mathrm{e}^{i(z-\frac{n\pi}{2}-\frac{\pi}{4})} \left(1 + O\left(\frac{1}{|z|}\right)\right), \tag{6.82}$$

$$\frac{d\,\mathrm{H}_n^{(1)}}{dz}(z) = \pm i\sqrt{\frac{2}{\pi z}}\, \mathrm{e}^{i(z-\frac{n\pi}{2}-\frac{\pi}{4})} \left(1 + O\left(\frac{1}{|z|}\right)\right), \tag{6.83}$$

when $|z| \to \infty$ *and* $|\arg(z)| < \pi - \delta$*, where* δ *is an arbitrary small positive number.*

Part III

Computational applications on dissipative acoustics

Chapter 7

Validation of acoustic dissipative models

Contents

7.1 Introduction

One of the most used techniques in passive control of noise consists of covering the reflecting surfaces with porous materials.

From a microscopic point of view, these materials consist of a solid skeleton, rigid or elastic, completely saturated by an acoustic fluid. This kind of absorbing materials are widely used because of its capability to dissipate acoustic waves, specially at high range frequencies.

There are several alternatives to derive models governing the vibrations of porous media; an overview can be found in Allard's book [3] and in Chapter 1.

If the solid skeleton is assumed to be rigid, the porous material can be considered as an equivalent fluid with dynamical density and bulk modulus coefficients depending on the frequency (see Section 1.2). These parameters can be obtained by empirical laws. In this setting, the equations introduced by Delany and Bazley [56] in 1970 have been widely used to describe sound propagation in fibrous materials. This model was subsequently improved by Morse and Ingard [88], Attenborough [12], and, more recently, by Allard and Champoux [5], among others.

On the other hand, when the elastic deformation of the skeleton is taken into account, the theoretical basis for the mechanical behavior of the porous material was established by Biot [38, 39]. This theory describes the propagation of elastic waves in fluid-saturated porous media. The adaptation of this theory to acoustics can be found, for example, in the work of Allard *et al.* [4].

Furthermore, under the assumptions of rigid or elastic skeleton, it is also possible to obtain models for the motion of porous materials from a rigorous mathematical point of view by homogenization techniques [49, 28], (see Section 1.3).

The use of all these models can be inadequate when modelling the propagation of sound in an enclosure including porous media, since the thickness of the porous layer coating the reflecting surfaces is often much smaller than the characteristic dimensions of the physical domain of interest. This difference in size is typically a serious drawback to create a mesh of the domain in order to compute the acoustic field with, for instance, a finite-element method.

If we assume that the porous layers are thin, this numerical difficulty can be overcome by substituting the partial differential equations governing the porous medium by a wall impedance condition on the coated boundaries. This boundary condition involves frequency dependent coefficients which can be theoretically computed from the dynamic density and bulk modulus of the coating porous material in the case of incident plane waves on a plane surface (see Subsection 7.2.3 below). Let us remark that the two models do not necessarily lead to the same solution for more general geometric conditions.

We compare in this chapter a fluid-porous model with an approximation obtained by replacing the porous media by a wall impedance condition. We study the dependence of both models with respect to the thickness of the porous layer, the frequency, the acoustic source and the geometry of the problem domain. More precisely, we study the accuracy of the wall impedance model versus the Allard-Champoux model for time-harmonic scattering problems in unbounded three-dimensional domains. Many problems with practical interest fall in this framework, as for instance the numerical simulation of real experiments involving absorbing materials in an anechoic or semi-anechoic room [21].

The fluid-porous scattering problems can be solved analytically only for some geometrically simple domains. However, in general, it is necessary to use numerical techniques. Because of its easy implementation and its effectiveness in handling complex geometries, the finite-element method has become popular to solve such problems. Some examples of the finite element method applied to sound propagation in porous media are the papers by Easwaran *et al.* [58], Panneton and Atalla [92], and Bermúdez *et al.* [27]. All of them consider acoustic propagation inside rigid cavities and, hence, the problems are posed in bounded domains.

For problems posed on unbounded domains, finite-element methods require first to truncate the computational domain without perturbing too much the solution of the original problem. Several techniques are available to do this: absorbing boundary conditions [60], boundary elements [72], infinite elements [9], etc. In the present chapter, we will use the PML (*Perfectly Matched Layer*) method, introduced in Chapter 4.

The PML method is based on simulating an absorbing layer of damping material surrounding the domain of interest, like a thin sponge which absorbs the scattered field radiated to the exterior of this domain. This method is known as 'perfectly matched' because the interface between the physical domain and the absorbing layer does not produce spurious reflections.

In practice, since the PML has to be truncated at a finite distance of the domain of interest, its external boundary produces artificial reflections. Theoretically, these reflections are of minor importance because of the exponential decay of the acoustic waves inside the PML, but the approximation error typically becomes larger once the problem is discretized. Increasing the thickness of the PML may be a remedy, although not always available because of its computational cost. An alternative usual choice to achieve low error levels is to take larger values of the absorption coefficients in the layer. However, Collino and Monk [51] showed that this methodology may produce an increasing error in the discretized problem.

We will use the alternative procedure to avoid this numerical drawback, which has been proposed and analyzed in Chapter 5. It consists of using an absorbing function with unbounded integral on the PML. In such a case, the exact solution of the original time-harmonic scattering problem in the domain of interest is recovered, even though the thickness of the layer is finite (see Chapter 6).

The outline of this chapter is as follows: In Section 7.2, we state the scattering problems in a three-dimensional unbounded domain with a porous layer surrounding a rigid obstacle. We introduce the Allard-Champoux equations, governing the motion in the porous layer, and the wall impedance model. Then we compute the frequency dependent impedance which yields the equivalence between both models under the assumption of plane waves with normal incidence. In Section 7.3, we study the particular case where the obstacle is planar and unbounded. For this simple geometry we obtain the exact solution for the scattering problem assuming plane waves of oblique incidence or spherical waves. In both cases we compare the pressure fields computed from the two models. In Section 7.4, under the hypothesis of spherical geometry, both models are numerically solved by using an optimal bounded PML technique combined with a finite-element method. Finally, we report the numerical results obtained with this approach, when the obstacle is a sphere covered by a porous material.

7.2 Statement of the problem. Mathematical modeling

We consider in this section a time-harmonic scattering problem for a coupled system formed by an acoustic fluid and a porous medium.

Let Ω be a domain (bounded or unbounded) occupied by an obstacle to the propagation of acoustic waves, with a totally reflecting boundary Γ and outward unit normal vector $\boldsymbol{\nu}$. We consider a set of coordinates with its origin lying inside the obstacle.

Let Ω_{A} be another domain surrounding the obstacle and occupied by a porous material, with outer boundary Γ_{I} and outward normal unit vector $\boldsymbol{n}$. The rest of the space, Ω_{F}, is filled with an acoustic fluid (i.e., compressible, barotropic and inviscid). Figure 7.1 shows a two-dimensional section of the domains.

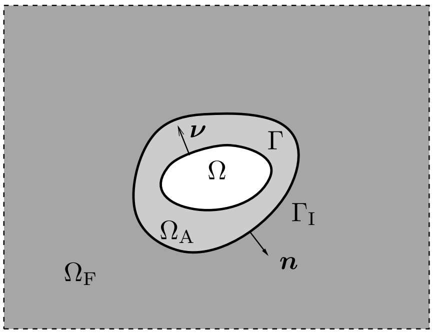

Figure 7.1: Two-dimensional vertical section of the domains.

In what follows we introduce the equations of the time-harmonic scattering problem with two different models for the porous medium.

7.2.1 The Allard-Champoux model

The first model consists of using directly the Allard-Champoux equations governing the porous material. Consider a periodic acoustic source with angular frequency ω and amplitude g acting inside Ω_{F}. The amplitudes of the pressure fields in Ω_{F} and Ω_{A} are, respectively, the solutions p_1 and p_{A} of the following equations:

$$\frac{1}{\rho_{\mathrm{F}}}\Delta p_1 + \frac{\omega^2}{\mu_{\mathrm{F}}} p_1 = g \qquad \text{in } \Omega_{\mathrm{F}}, \tag{7.1}$$

$$\frac{1}{\rho_{\mathrm{A}}}\Delta p_{\mathrm{A}} + \frac{\omega^2}{\mu_{\mathrm{A}}} p_{\mathrm{A}} = 0 \qquad \text{in } \Omega_{\mathrm{A}}, \tag{7.2}$$

$$p_1 = p_{\mathrm{A}} \qquad \text{on } \Gamma_{\mathrm{I}}, \tag{7.3}$$

$$\frac{1}{\rho_{\mathrm{F}}}\frac{\partial p_1}{\partial \boldsymbol{n}} = \frac{1}{\rho_{\mathrm{A}}}\frac{\partial p_{\mathrm{A}}}{\partial \boldsymbol{n}} \qquad \text{on } \Gamma_{\mathrm{I}}, \tag{7.4}$$

$$\frac{1}{\rho_{\mathrm{A}}}\frac{\partial p_{\mathrm{A}}}{\partial \boldsymbol{\nu}} = 0 \qquad \text{on } \Gamma, \tag{7.5}$$

$$\lim_{r\to+\infty} r\left(\frac{1}{ik_{\mathrm{F}}}\frac{\partial p_1}{\partial r} - p_1\right) = 0 \qquad \text{in } \Omega_{\mathrm{F}}, \tag{7.6}$$

$$\lim_{r\to+\infty} r\left(\frac{1}{ik_{\mathrm{A}}}\frac{\partial p_{\mathrm{A}}}{\partial r} - p_{\mathrm{A}}\right) = 0 \qquad \text{in } \Omega_{\mathrm{A}}. \tag{7.7}$$

Eq. (7.1) is the standard Helmholtz equation for an acoustic fluid, where ρ_{F} is the mass density of the fluid at rest and μ_{F} its bulk modulus which, for an acoustic fluid, is given by $\mu_{\mathrm{F}} = \rho_{\mathrm{F}} c_{\mathrm{F}}^2$, with c_{F} being the sound speed in the fluid.

Eq. (7.2) corresponds to the Allard-Champoux [5] model for the vibrations in Ω_{A}. This model assumes that the skeleton of the porous medium is rigid. In fact, it considers that the medium consists of a fluid-saturated rigid fibrous material. It also assumes that the thermal exchange between the fluid and the fibers of the porous medium is not negligible. If the porous material is assumed to be isotropic from a macroscopic point of view, then the pressure in the porous medium satisfies Eq. (7.2), where ρ_{A} and μ_{A} are the so called dynamic density and dynamic bulk modulus, respectively, which depend on the frequency. These coefficients are given by the expressions given by the Allard-Champoux model Eqs. (1.29)-(1.30), described in Chapter 1. Let us remark that we are using the pressure as the unknown field to write the equations of the model.

Eq. (7.3) and (7.4) are the usual kinematic and kinetic interface conditions, which preserve continuity of pressure and velocity fields, respectively, whereas Eq. (7.5) is the standard reflecting condition on a rigid obstacle. Finally, Eq. (7.6) and (7.7) are the radiation Sommerfeld conditions in fluid and porous domains, with k_{F} and k_{A} being the respective wave numbers

$$k_{\mathrm{F}} = \omega\sqrt{\frac{\rho_{\mathrm{F}}}{\mu_{\mathrm{F}}}} = \frac{\omega}{c_{\mathrm{F}}} \qquad \text{and} \qquad k_{\mathrm{A}} = \omega\sqrt{\frac{\rho_{\mathrm{A}}}{\mu_{\mathrm{A}}}}. \tag{7.8}$$

Let us remark that Eq. (7.7) only holds if the porous medium domain is unbounded.

7.2.2 The wall impedance model

An alternative to model the effect of the porous medium, valid in principle when the thickness of the porous layer is negligible, consists of replacing the equation in Ω_{A} by a complex-valued frequency-dependent wall impedance condition on Γ_{I}. This condition is defined as to recover the exact pressure field in problems involving plane waves with normal incidence, as will be shown in the next subsection.

Consider again the notation shown in Figure 7.1 and the same periodic acoustic source as above. The amplitude of the pressure field in Ω_{F} is now the solution p_2 of the following exterior Helmholtz problem:

$$\frac{1}{\rho_{\mathrm{F}}}\Delta p_2 + \frac{\omega^2}{\mu_{\mathrm{F}}} p_2 = g \qquad \text{in } \Omega_{\mathrm{F}}, \tag{7.9}$$

$$p_2 - \frac{Z}{i\omega\rho_{\mathrm{F}}}\frac{\partial p_2}{\partial \boldsymbol{n}} = 0 \qquad \text{on } \Gamma_{\mathrm{I}}, \tag{7.10}$$

$$\lim_{r\to+\infty} r\left(\frac{1}{ik_{\mathrm{F}}}\frac{\partial p_2}{\partial r} - p_2\right) = 0 \qquad \text{in } \Omega_{\mathrm{F}}. \tag{7.11}$$

Eq. (7.10) is the wall impedance condition which models the layer of porous material covering the obstacle and involves the frequency-dependent wall impedance coefficient Z. Since the fluid is assumed to be inviscid, this condition only involves the normal derivative of the pressure.

7.2.3 Computing the wall impedance

In what follows we compute the complex frequency-dependent wall impedance coefficient Z, in such a way that the solutions p_1 and p_2 of problems (7.1)-(7.7) and (7.9)-(7.11), respectively, coincide under the assumption of plane waves with normal incidence. Let us recall that this is the standard assumption for a Kundt's tube.

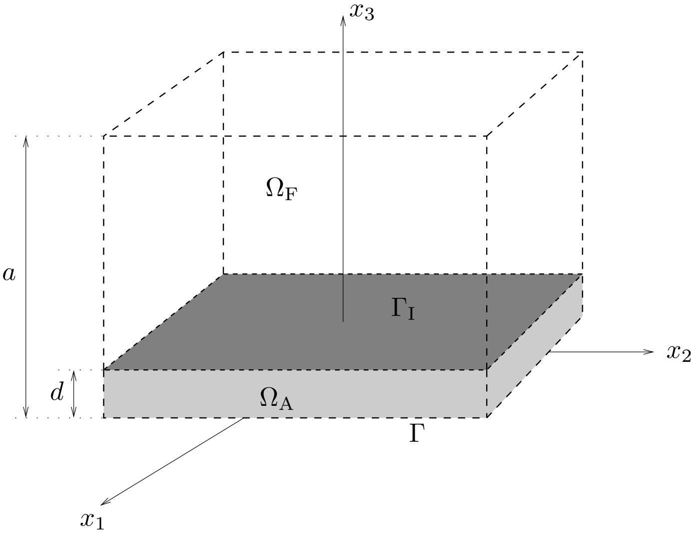

Figure 7.2: Unbounded obstacle with planar boundary. 3D domains.

Consider fluid and porous medium domains Ω_F and Ω_A, respectively, as in Figure 7.2. Assume that the source term is now a plane wave with normal incidence to Γ_I with amplitude p_inc. Assume also that this plane wave has a zero phase on the plane $x_3 = a$. We introduce this source in both problems through the following boundary condition:

$$-\frac{1}{2}\left(\frac{1}{ik_\mathrm{F}}\frac{\partial p_j}{\partial x_3} - p_j\right)\bigg|_{x_3=a} = p_\mathrm{inc}, \qquad j = 1, 2.$$

It is clear that with this boundary condition and without any other source term in the fluid domain, the solution is composed of different plane waves with normal incidence.

Eq. (7.1)-(7.7) reduce in this case to the following one-dimensional problem:

$$\left\{\begin{aligned}
\frac{1}{\rho_\mathrm{F}}\frac{d^2 p_1}{dx_3^2} + \frac{\omega^2}{\mu_\mathrm{F}} p_1 &= 0, && d < x_3 < a,\\
\frac{1}{\rho_\mathrm{A}}\frac{d^2 p_\mathrm{A}}{dx_3^2} + \frac{\omega^2}{\mu_\mathrm{A}} p_\mathrm{A} &= 0, && 0 > x_3 > d,\\
-\frac{1}{2}\left(\frac{1}{ik_\mathrm{F}}\frac{dp_1}{dx_3} - p_1\right) &= p_\mathrm{inc}, && x_3 = a,\\
p_1 &= p_\mathrm{A} && x_3 = d,\\
\frac{1}{\rho_\mathrm{F}}\frac{dp_1}{dx_3} &= \frac{1}{\rho_\mathrm{A}}\frac{dp_\mathrm{A}}{dx_3}, && x_3 = d,\\
\frac{1}{\rho_\mathrm{A}}\frac{dp_\mathrm{A}}{dx_3} &= 0, && x_3 = 0.
\end{aligned}\right. \tag{7.12}$$

Straightforward computations lead to

$$p_1(x_1, x_2, x_3) = p_\mathrm{inc}\left[\mathrm{e}^{-ik_\mathrm{F}(x_3-a)} + R_1\,\mathrm{e}^{ik_\mathrm{F}(x_3+a)}\right],$$

where the reflection coefficient R_1 is given by

$$R_1 = \mathrm{e}^{-2ik_\mathrm{F}d}\,\frac{Z_\mathrm{A}\cos(k_\mathrm{A}d) + iZ_\mathrm{F}\sin(k_\mathrm{A}d)}{Z_\mathrm{A}\cos(k_\mathrm{A}d) - iZ_\mathrm{F}\sin(k_\mathrm{A}d)},$$

with

$$Z_\mathrm{F} = \frac{\omega\rho_\mathrm{F}}{k_\mathrm{F}} = \rho_\mathrm{F} c_\mathrm{F} \qquad \text{and} \qquad Z_\mathrm{A} = \frac{\omega\rho_\mathrm{A}}{k_\mathrm{A}}$$

being the characteristic impedances of the fluid and the porous medium, respectively.

Analogously, Eq. (7.9)-(7.11) yield in this case the following one-dimensional problem:

$$\left\{\begin{aligned}
\frac{1}{\rho_\mathrm{F}}\frac{d^2 p_2}{dx_3^2} + \frac{\omega^2}{\mu_\mathrm{F}} p_2 &= 0, && d < x_3 < a,\\
-\frac{1}{2}\left(\frac{1}{ik_\mathrm{F}}\frac{dp_2}{dx_3} - p_2\right) &= p_\mathrm{inc}, && x_3 = a,\\
p_2 - \frac{Z}{i\omega\rho_\mathrm{F}}\frac{dp_2}{dx_3} &= 0, && x_3 = d.
\end{aligned}\right. \tag{7.13}$$

In this case, it is simple to show that

$$p_2(x_1, x_2, x_3) = p_{\text{inc}} \left[\mathrm{e}^{-ik_{\text{F}}(x_3-a)} + R_2\, \mathrm{e}^{ik_{\text{F}}(x_3+a)} \right],$$

with

$$R_2 = \mathrm{e}^{-2ik_{\text{F}}d}\, \frac{Z + Z_{\text{F}}}{Z - Z_{\text{F}}}.$$

Thus, it is possible to define a particular complex-valued coefficient Z so that its solution coincides with that of problem (7.12). Therefore we obtain the following result:

Proposition 7.2.1. *Let p_1 and p_2 be the solutions of problems (7.12) and (7.13), respectively. If*

$$Z = Z_{\text{A}} \coth(ik_{\text{A}}d), \tag{7.14}$$

then $p_1(x_1, x_2, x_3) = p_2(x_1, x_2, x_3)$, for $d < x_3 < a$.

This is a classical result [43]. Eq. (7.14) is nothing but the well-known expression of the input impedance to a rigidly backed porous layer with thickness d.

7.3 Planar unbounded wall

In this section we will deal with other particular problems in which the obstacle and the absorbing layer are unbounded and have a planar boundary as in Figure 7.2. We will consider two simple source terms: plane waves with oblique incidence and spherical waves. In both cases, we will deduce explicit formulas for the solutions of problems (7.1)-(7.7) and (7.9)-(7.11), which will allow us to compare both models.

In spite of the fact that the assumption of an unbounded absorbing layer is not realistic, it allows us to avoid the diffraction effects due to the borders of the porous sample. This assumption is usually made, even from an experimental point of view, when the size of the sample is much larger than the length wave of the acoustic source.

7.3.1 Plane waves with oblique incidence

Consider now as a source term a plane wave of amplitude p_{inc} with oblique incidence on the interface Γ_{I}, the incidence angle being α. We assume again that this plane wave has a zero phase with respect to the variable x_3 on the plane $x_3 = a$, so that we introduce the source term by means of the following boundary condition:

$$-\frac{1}{2}\left(\frac{1}{ik_{\text{F}}\cos\alpha} \frac{\partial p_j}{\partial x_3} - p_j \right)\bigg|_{x_3=a} = p_{\text{inc}}\, \mathrm{e}^{-ik_{\text{F}}x_2 \sin\alpha}, \qquad j = 1, 2.$$

In this case, Eq. (7.1)-(7.7) reduce to the following two-dimensional problem:

$$\left\{\begin{array}{rl} \dfrac{1}{\rho_\mathrm{F}}\dfrac{\partial^2 p_1}{\partial x_2^2}+\dfrac{1}{\rho_\mathrm{F}}\dfrac{\partial^2 p_1}{\partial x_3^2}+\dfrac{\omega^2}{\mu_\mathrm{F}}p_1=0, & d<x_3<a,\\ \dfrac{1}{\rho_\mathrm{A}}\dfrac{\partial^2 p_\mathrm{A}}{\partial x_2^2}+\dfrac{1}{\rho_\mathrm{A}}\dfrac{\partial^2 p_\mathrm{A}}{\partial x_3^2}+\dfrac{\omega^2}{\mu_\mathrm{A}}p_\mathrm{A}=0, & 0<x_3<d,\\ -\dfrac{1}{2}\left(\dfrac{1}{ik_\mathrm{F}\cos\alpha}\dfrac{\partial p_1}{\partial x_3}-p_1\right)=p_\mathrm{inc}\,\mathrm{e}^{-ik_\mathrm{F}x_2\sin\alpha}, & x_3=a,\\ p_1=p_\mathrm{A}, & x_3=d,\\ \dfrac{1}{\rho_\mathrm{F}}\dfrac{\partial p_1}{\partial x_3}=\dfrac{1}{\rho_\mathrm{A}}\dfrac{\partial p_\mathrm{A}}{\partial x_3}, & x_3=d,\\ \dfrac{1}{\rho_\mathrm{A}}\dfrac{\partial p_\mathrm{A}}{\partial x_3}=0, & x_3=0. \end{array}\right. \tag{7.15}$$

Straightforward computations lead now to the following expression for p_1:

$$p_1(x_1,x_2,x_3)=p_\mathrm{inc}\,\mathrm{e}^{-ik_\mathrm{F}x_2\sin\alpha}\left[\mathrm{e}^{-ik_\mathrm{F}(x_3-a)\cos\alpha}+R_1\,\mathrm{e}^{ik_\mathrm{F}(x_3+a)\cos\alpha}\right], \tag{7.16}$$

where the reflection coefficient R_1, which depends on the frequency and the incidence angle, is given by

$$R_1=\mathrm{e}^{-2ik_\mathrm{F}d\cos\alpha}\,\frac{Z_\mathrm{A}^*\cos\alpha\,\cos(k_\mathrm{A}^*d)+iZ_\mathrm{F}\sin(k_\mathrm{A}^*d)}{Z_\mathrm{A}^*\cos\alpha\,\cos(k_\mathrm{A}^*d)-iZ_\mathrm{F}\sin(k_\mathrm{A}^*d)},$$

with

$$k_\mathrm{A}^*=\sqrt{k_\mathrm{A}^2-k_\mathrm{F}^2\sin^2\alpha}\qquad\text{and}\qquad Z_\mathrm{A}^*=\omega\rho_\mathrm{A}/k_\mathrm{A}^*,$$

whereas $Z_\mathrm{F}=\omega\rho_\mathrm{F}/k_\mathrm{F}=\rho_\mathrm{F}c_\mathrm{F}$, as above.

Analogously, under the assumption of plane waves with oblique incidence, problem (7.9)-(7.11) can be written as follows:

$$\left\{\begin{array}{rl} \dfrac{1}{\rho_\mathrm{F}}\dfrac{\partial^2 p_2}{\partial x_2^2}+\dfrac{1}{\rho_\mathrm{F}}\dfrac{\partial^2 p_2}{\partial x_3^2}+\dfrac{\omega^2}{\mu_\mathrm{F}}p_2=0, & d<x_3<a,\\ -\dfrac{1}{2}\left(\dfrac{1}{ik_\mathrm{F}\cos\alpha}\dfrac{\partial p_2}{\partial x_3}-p_2\right)=p_\mathrm{inc}\,\mathrm{e}^{-ik_\mathrm{F}x_2\sin\alpha}, & x_3=a,\\ p_2-\dfrac{Z}{i\omega\rho_\mathrm{F}}\dfrac{\partial p_2}{\partial x_3}=0, & x_3=d. \end{array}\right. \tag{7.17}$$

Proceeding as above, it is easy to show that the pressure field is given by

$$p_2(x_1,x_2,x_3)=p_\mathrm{inc}\,\mathrm{e}^{-ik_\mathrm{F}x_2\sin\alpha}\left[\mathrm{e}^{-ik_\mathrm{F}(x_3-a)\cos\alpha}+R_2\,\mathrm{e}^{ik_\mathrm{F}(x_3+a)\cos\alpha}\right], \tag{7.18}$$

where the reflection coefficient is now

$$R_2=\mathrm{e}^{-2ik_\mathrm{F}d\cos\alpha}\,\frac{Z\cos\alpha+Z_\mathrm{F}}{Z\cos\alpha-Z_\mathrm{F}}.$$

The expression of the input impedance for plane waves with oblique incidence in a multilayered media is also well known [43]. In principle, we could use it to define Z so that we recover the equivalence between the solutions of problems (7.15) and (7.17). However, this value of Z would depend on the incidence angle α.

Our aim is to characterize the behavior of a porous layer by a wall impedance depending only on the thickness and the physical properties of the porous material, but not on the particular acoustic source. Because of this, we propose to use the wall impedance (7.14) computed for plane waves with normal incidence. In what follows, we compare the solutions (7.16) and (7.18) of problems (7.15) and (7.17), respectively, as a first validation of this proposal.

For the fluid parameters we have used $\rho_{\mathrm{F}} = 1.2\,\mathrm{kg/m^3}$ and $c_{\mathrm{F}} = 343\,\mathrm{m/s}$, whereas, for the porous layer, $\mathrm{Pr} = 0.702$, $\gamma = 1.4$, $\sigma = 20000\,\mathrm{rays\ mks}$ and $P_0 = 101320\,\mathrm{N/m^2}$, the thickness of the layer being $d = 0.05\,\mathrm{m}$.

Figure 7.3 shows the real and the imaginary parts of the wall impedance defined in (7.14) for a range of frequencies $f = \omega/(2\pi)$ between 100 and 2000 Hz.

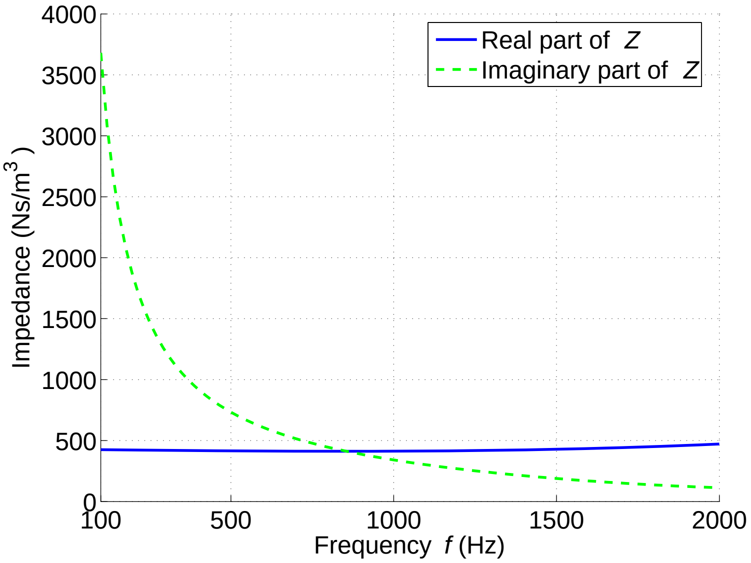

Figure 7.3: Wall impedance Z as defined by Eq. (7.14) for different values of $f = \omega/(2\pi)$.

We consider an incoming plane wave of oblique incidence with angle $\alpha = \pi/3\,\mathrm{rad}$, amplitude $p_{\mathrm{inc}} = 1\,\mathrm{N/m^2}$ and null x_3-phase on the plane $x_3 = 1\,\mathrm{m}$.

As a first test, we compute the solutions p_1 and p_2 provided by each model at different observation points on the x_3-axis that we call $\boldsymbol{m}_1$, $\boldsymbol{m}_2$, $\boldsymbol{m}_3$ and $\boldsymbol{m}_4$ (see Figure 7.4), for a wide range of frequencies.

We show the real parts of the results in Figure 7.5, where the agreement of both models can be clearly appreciated. Indeed, the agreement is so good that, for each of the observation points, the curves corresponding to each model almost coincide, making it very hard to

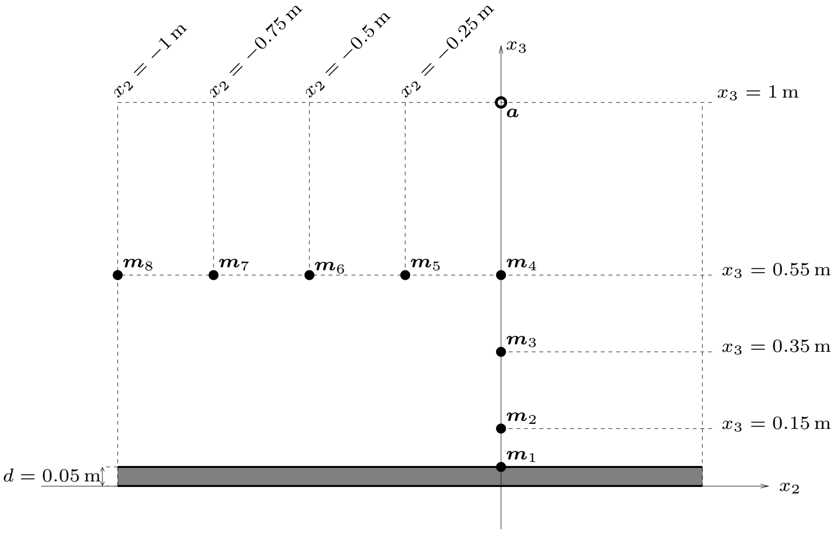

Figure 7.4: Observation points for the pressure field.

distinguish one from the other.

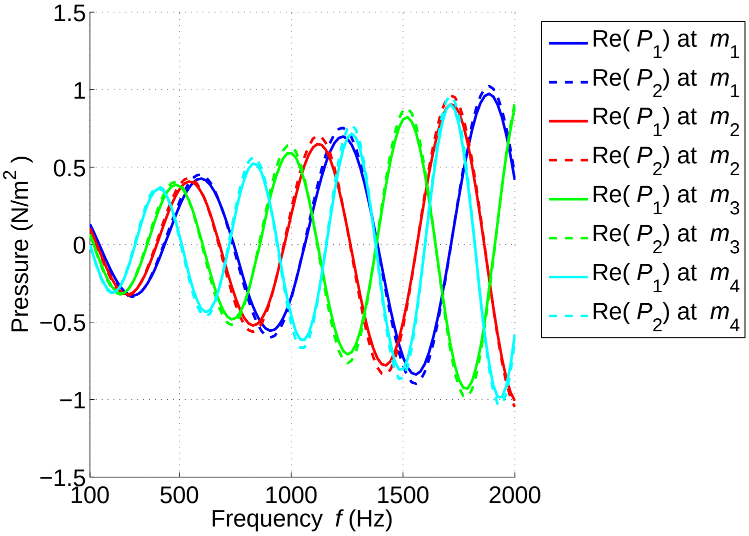

Figure 7.5: Plane waves with oblique incidence. Real part of the pressure fields at different points.

For plane waves, there is no need of comparing the solution provided by both models at points with the same coordinate z, as $\boldsymbol{m}_5, \ldots, \boldsymbol{m}_8$ in Figure 7.4. Indeed, $p_1(\boldsymbol{m}_j)$, $j = 4, \ldots, 8$, only differ in phase, and the same happens with $p_2(\boldsymbol{m}_j)$ (see Eq. (7.16) and (7.18)). Clearly, this is not the case for more general waves as will be shown in the next section.

Finally, we check the agreement between both models for different values of the thickness of the porous material. In Figure 7.6 we show the relative difference between both solutions, $|p_1 - p_2| / |p_{\mathrm{inc}}|$, at the points $\boldsymbol{m}_3$ and $\boldsymbol{m}_8$ (see Figure 7.4), for a couple of frequencies and a wide range of values of the thickness.

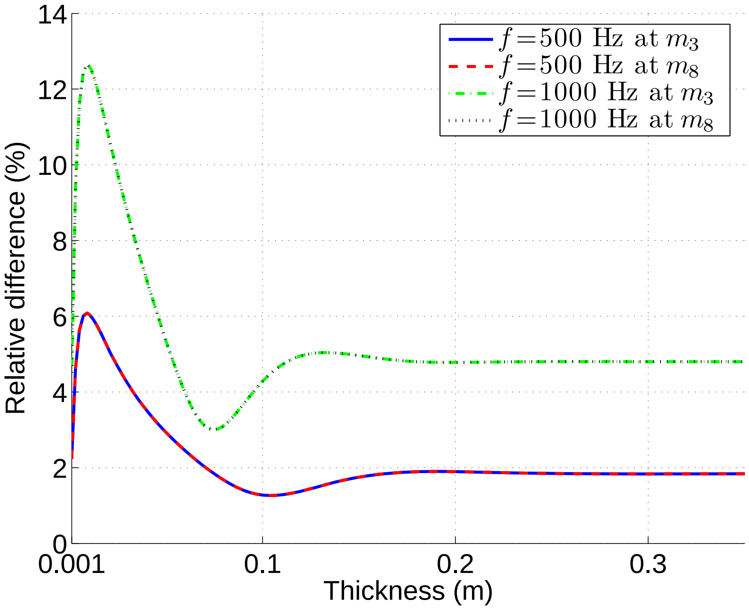

Figure 7.6: Plane waves with oblique incidence. $|p_1 - p_2| / |p_{\mathrm{inc}}|$ versus thickness of the porous layer.

We observe that the agreement between both models is essentially independent of the point where we compute the pressure field. Moreover, the relative difference between both models does not increase with frequency. On the other hand, even for a thick porous layer and moderate values of the angle of incidence ($\alpha = \pi/3\,\mathrm{rad}$), the agreement does not degenerate. Indeed each curve shows only one small error peak for very small values of the thickness d ($\approx 12\%$ for 1000 Hz and $\approx 6\%$ for 500 Hz).

7.3.2 Spherical waves

Next we consider a new source term: a monopole acting inside the fluid domain. In this case, the technique to obtain the solutions of the scattering problems is classical [55]. For completeness, we detail the computations for the Allard-Champoux model.

For a monopole at the point $\boldsymbol{a} = (0, 0, a)$, with constant volume velocity Q [22], the acoustic source term in (7.1) is $g = i\omega Q \delta_{\boldsymbol{a}}$, with $\delta_{\boldsymbol{a}}$ being the Dirac's delta with support at $\boldsymbol{a}$.

Since the source term depends neither on x_1 nor on x_2, and the interfaces Γ_{I} and Γ are orthogonal to the x_3-axis, we take advantage of the symmetry of the problem. We use the two-dimensional Fourier transform [42] in the space variables x_1 and x_2:

$$\widetilde{P}_1(\widetilde{x}_1, \widetilde{x}_2, x_3) = \int_{-\infty}^{+\infty} \int_{-\infty}^{+\infty} p_1(x_1, x_2, x_3)\, \mathrm{e}^{-i\widetilde{x}_1 x_1}\, \mathrm{e}^{-i\widetilde{x}_2 x_2}\, dx_1\, dx_2.$$

Let us remark that we use tildes to denote Fourier variables because hats have already been used for variables related to the PML.

Taking Fourier transform of Eq. (7.1) and (7.2), we obtain:

$$\begin{cases} \dfrac{1}{\rho_{\mathrm{F}}} \left[-(\widetilde{x}_1^2 + \widetilde{x}_2^2)\widetilde{P}_1 + \dfrac{\partial^2 \widetilde{P}_1}{\partial x_3^2} \right] + \omega^2 \dfrac{1}{\mu_{\mathrm{F}}} \widetilde{P}_1 = i\omega Q \widetilde{\delta}_{\boldsymbol{a}} & \text{in } \Omega_{\mathrm{F}}, \\ \dfrac{1}{\rho_{\mathrm{A}}} \left[-(\widetilde{x}_1^2 + \widetilde{x}_2^2)\widetilde{P}_{\mathrm{A}} + \dfrac{\partial^2 \widetilde{P}_{\mathrm{A}}}{\partial x_3^2} \right] + \omega^2 \dfrac{1}{\mu_{\mathrm{A}}} \widetilde{P}_{\mathrm{A}} = 0 & \text{in } \Omega_{\mathrm{A}}. \end{cases}$$

Notice that $\widetilde{\delta}_{\boldsymbol{a}}$ coincides with the one-variable Dirac's delta with support at the point $x_3 = a$. Hence, by using the Sommerfeld radiation conditions (7.6) and (7.7), we obtain:

$$\widetilde{P}_1(\widetilde{x}_1, \widetilde{x}_2, x_3) = \frac{\omega \rho_{\mathrm{F}} Q\, \mathrm{e}^{i\sqrt{k_{\mathrm{F}}^2 - \widetilde{r}^2}\, |x_3 - a|}}{2\sqrt{k_{\mathrm{F}}^2 - \widetilde{r}^2}} + \widetilde{R}_1\, \mathrm{e}^{i\sqrt{k_{\mathrm{F}}^2 - \widetilde{r}^2}\, x_3}, \tag{7.19}$$

$$\widetilde{P}_{\mathrm{A}}(\widetilde{x}_1, \widetilde{x}_2, x_3) = T_{\mathrm{A}}\, \mathrm{e}^{-i\sqrt{k_{\mathrm{A}}^2 - \widetilde{r}^2}\, x_3} + R_{\mathrm{A}}\, \mathrm{e}^{i\sqrt{k_{\mathrm{A}}^2 - \widetilde{r}^2}\, x_3}, \tag{7.20}$$

where $\widetilde{r} = \sqrt{\widetilde{x}_1^2 + \widetilde{x}_2^2}$, and k_{F} and k_{A} are the wave numbers in the fluid and in the porous media, respectively, as defined in (7.8).

We introduce the following notation:

$$\widetilde{k}_{\mathrm{F}} = \sqrt{k_{\mathrm{F}}^2 - \widetilde{r}^2}, \qquad \widetilde{k}_{\mathrm{A}} = \sqrt{k_{\mathrm{A}}^2 - \widetilde{r}^2}, \qquad \widetilde{Z}_{\mathrm{F}} = \frac{\omega \rho_{\mathrm{F}}}{\widetilde{k}_{\mathrm{F}}}, \qquad \widetilde{Z}_{\mathrm{A}} = \frac{\omega \rho_{\mathrm{A}}}{\widetilde{k}_{\mathrm{A}}}.$$

The interface conditions (7.3)-(7.5) lead to the following system of equations for the coefficients R_{A}, $\widetilde{R}_1$ and T_{A}:

$$\begin{cases} \dfrac{\widetilde{Z}_{\mathrm{F}} Q}{2}\, \mathrm{e}^{i\widetilde{k}_{\mathrm{F}}(d-a)} + \widetilde{R}_1\, \mathrm{e}^{i\widetilde{k}_{\mathrm{F}} d} = T_{\mathrm{A}}\, \mathrm{e}^{-i\widetilde{k}_{\mathrm{A}} d} + R_{\mathrm{A}}\, \mathrm{e}^{i\widetilde{k}_{\mathrm{A}} d}, \\ -\dfrac{Q}{2}\, \mathrm{e}^{i\widetilde{k}_{\mathrm{F}}(d-a)} + \dfrac{\widetilde{R}_1}{\widetilde{Z}_{\mathrm{F}}}\, \mathrm{e}^{i\widetilde{k}_{\mathrm{F}} d} = -\dfrac{T_{\mathrm{A}}}{\widetilde{Z}_{\mathrm{A}}}\, \mathrm{e}^{-i\widetilde{k}_{\mathrm{A}} d} + \dfrac{R_{\mathrm{A}}}{\widetilde{Z}_{\mathrm{A}}}\, \mathrm{e}^{i\widetilde{k}_{\mathrm{A}} d}, \\ -T_{\mathrm{A}} + R_{\mathrm{A}} = 0. \end{cases}$$

Notice that since $\widetilde{k}_{\mathrm{F}}$ and $\widetilde{k}_{\mathrm{A}}$ depend on $\widetilde{x}_1$ and $\widetilde{x}_2$ through $\widetilde{r}$, so do R_{A}, $\widetilde{R}_1$ and T_{A}.

By solving this linear system, we obtain

$$\widetilde{R}_1 = \mathrm{e}^{-2i\widetilde{k}_{\mathrm{F}} d}\, \frac{\widetilde{Z}_{\mathrm{A}} \cos(\widetilde{k}_{\mathrm{A}} d) + i\widetilde{Z}_{\mathrm{F}} \sin(\widetilde{k}_{\mathrm{A}} d)}{\widetilde{Z}_{\mathrm{A}} \cos(\widetilde{k}_{\mathrm{A}} d) - i\widetilde{Z}_{\mathrm{F}} \sin(\widetilde{k}_{\mathrm{A}} d)}\, \frac{\widetilde{Z}_{\mathrm{F}} Q}{2}\, \mathrm{e}^{i\widetilde{k}_{\mathrm{F}} a}.$$

Using now (7.19) and the inverse Fourier transform, we have

$$p_1(\boldsymbol{x}) = \frac{i\omega\rho_{\mathrm{F}}Q}{4\pi}\,\frac{\mathrm{e}^{ik_{\mathrm{F}}|\boldsymbol{x}-\boldsymbol{a}|}}{|\boldsymbol{x}-\boldsymbol{a}|} + p_1^R(\boldsymbol{x}),$$

where

$$p_1^R(\boldsymbol{x}) = \frac{1}{(2\pi)^2}\int_{-\infty}^{+\infty}\int_{-\infty}^{+\infty}\widetilde{R}_1(\widetilde{x}_1,\widetilde{x}_2)\,\mathrm{e}^{i\widetilde{k}_{\mathrm{F}}x_3}\,\mathrm{e}^{i\widetilde{x}_1x_1}\,\mathrm{e}^{i\widetilde{x}_2x_2}\,d\widetilde{x}_1\,d\widetilde{x}_2.$$

Since $\widetilde{R}_1$ depends on $\widetilde{x}_1$ and $\widetilde{x}_2$ only through $\widetilde{r}$, by using the Hankel transform[42] we can rewrite the pressure field in Ω_{F} as follows:

$$p_1(\boldsymbol{x}) = \frac{i\omega\rho_{\mathrm{F}}Q}{4\pi}\,\frac{\mathrm{e}^{ik_{\mathrm{F}}|\boldsymbol{x}-\boldsymbol{a}|}}{|\boldsymbol{x}-\boldsymbol{a}|} + \frac{1}{2\pi}\int_0^{+\infty}\widetilde{R}_1(\widetilde{r})\,\mathrm{e}^{i\widetilde{k}_{\mathrm{F}}x_3}\,\mathrm{J}_0\left(\widetilde{r}\sqrt{x_1^2+x_2^2}\right)\widetilde{r}\,d\hat{r}, \tag{7.21}$$

where J_0 denotes the Bessel function of first kind and order zero.

The above integral can be computed exactly only if the geometry is very simple. Otherwise, some quadrature rule has to be used. In such case, numerical problems should be expected because the function $\widetilde{R}_1(\widetilde{r})$ has a singularity at $\widetilde{r} = k_{\mathrm{F}}$.

By applying similar techniques to the wall impedance model, we can also write explicitly the solution of (7.9)-(7.11) as follows:

$$p_2(\boldsymbol{x}) = \frac{i\omega\rho_{\mathrm{F}}Q}{4\pi}\,\frac{\mathrm{e}^{ik_{\mathrm{F}}|\boldsymbol{x}-\boldsymbol{a}|}}{|\boldsymbol{x}-\boldsymbol{a}|} + \frac{1}{2\pi}\int_0^{+\infty}\widetilde{R}_2(\widetilde{r})\,\mathrm{e}^{i\widetilde{k}_{\mathrm{F}}x_3}\,\mathrm{J}_0\left(\widetilde{r}\sqrt{x_1^2+x_2^2}\right)\widetilde{r}\,d\hat{r}, \tag{7.22}$$

where $\widetilde{R}_2$ is given by

$$\widetilde{R}_2 = \mathrm{e}^{-2i\widetilde{k}_{\mathrm{F}}d}\,\frac{Z+\widetilde{Z}_{\mathrm{F}}}{Z-\widetilde{Z}_{\mathrm{F}}}\,\frac{\widetilde{Z}_{\mathrm{F}}Q}{2}\,\mathrm{e}^{i\widetilde{k}_{\mathrm{F}}a}.$$

Our next goal is to compare the solutions (7.21) and (7.22) when the wall impedance Z is taken according to (7.14).

We have used the same values for the physical and geometrical parameters as in the previous test. The integrals in (7.21) and (7.22) have been computed by using recursive adaptive Lobatto quadrature [64] with a tolerance error of 10^{-8} and truncating the integration domain at a distance 10^{-7} from the singular point $\widetilde{r} = k_{\mathrm{F}}$.

We have computed p_1 and p_2 at the same points as in the previous test for different frequencies. The real parts of the results are shown in Figure 7.7, where an excellent agreement between both models can be clearly observed again for a wide range of frequencies. Once more, the agreement is so good that it is very hard to distinguish the curves corresponding to each model.

We have also computed p_1 and p_2 at points $\boldsymbol{m}_5$, $\boldsymbol{m}_6$, $\boldsymbol{m}_7$ and $\boldsymbol{m}_8$, not lying on the x_3-axis (see Figure 7.4) for different frequencies. The real parts of the results, are shown in Figure 7.8. Once more, for each of the observation points, the curves corresponding to each model almost coincide because of the excellent agreement.

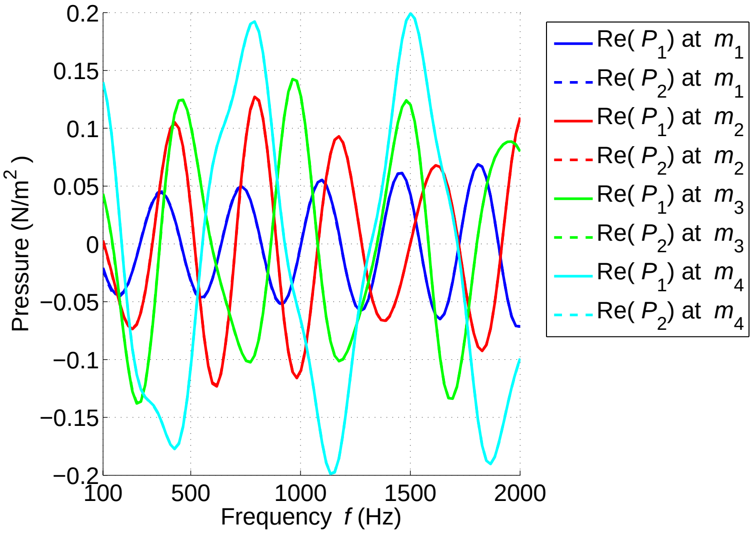

Figure 7.7: Spherical waves. Real part of the pressure fields at different points lying on the x_3-axis.

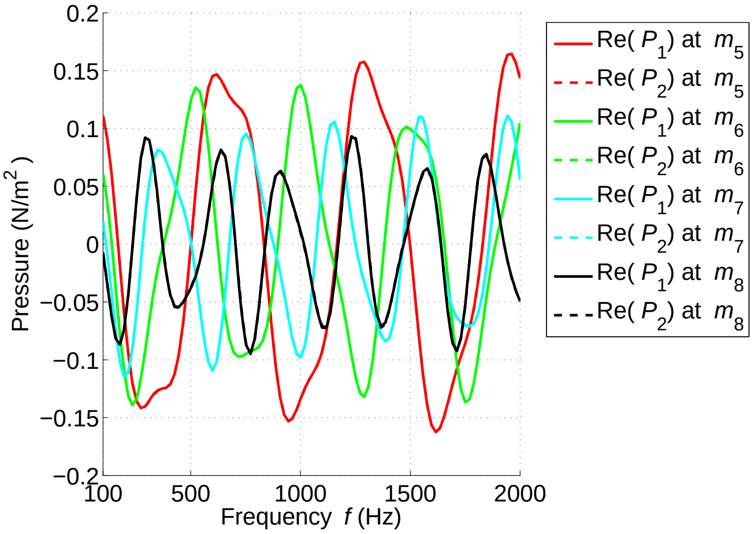

Figure 7.8: Spherical waves. Real part of the pressure fields at different points lying on the line $x_3 = 0.55$.

Finally, Figure 7.9 shows the relative difference between both solutions, $|p_1 - p_2| \,/\, |p_{\text{inc}}|$, at points $\boldsymbol{m}_3$, $\boldsymbol{m}_4$ and $\boldsymbol{m}_8$, for a couple of frequencies and a range of values of the thickness. The incidence pressure p_{inc} is now the first term in the right hand sides of Eq. (7.21) and

(7.22), namely,

$$p_{\mathrm{inc}} = \frac{i\omega\rho_{\mathrm{F}}Q}{4\pi}\,\frac{\mathrm{e}^{ik_{\mathrm{F}}|\boldsymbol{x}-\boldsymbol{a}|}}{|\boldsymbol{x}-\boldsymbol{a}|}. \tag{7.23}$$

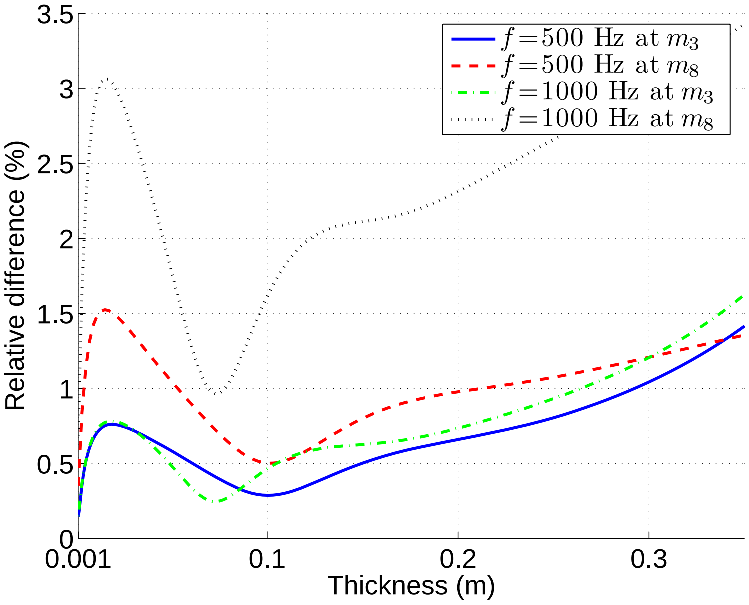

Figure 7.9: Spherical waves. $|p_1 - p_2| \,/\, |p_{\mathrm{inc}}|$ versus thickness of the porous layer.

It can be checked that the agreement between both models gets worse for large values of d. Anyway, for rather thick porous media layers and moderate values of the frequency, the agreement is excellent, the relative difference remaining smaller than 3%.

7.4 Curved wall

In the previous section, we have solved analytically the Allard-Champoux and the wall impedance models in two particular cases, taking advantage of the special geometric configuration of the domains (planar interfaces and unbounded fluid and porous media). However, in real problems, the obstacle and the porous layer are bounded and have arbitrary shapes, usually with non-planar boundaries.

In this framework, we are going to focus our attention on the comparison of both models in the case of non-planar geometries. Since in such case it is not possible to compute the exact solutions using analytical techniques, it is necessary to introduce a computational method. This is the aim of the rest of the chapter.

From a computational point of view, we have to deal with two main difficulties:

- the fluid domain is unbounded,

- the thickness of the porous layer is much smaller than the other dimensions.

We overcome the first difficulty by using the Perfectly Matched Layer technique [22] with optimal choice of the absorbing function, [32] as described in Subsection 7.4.1 below.

The second difficulty becomes relevant when we try to solve numerically problem (7.1)-(7.7) in three-dimensional domains by applying a finite-element method. Indeed, because of the different scales in the dimensions of the porous layer, it is necessary to use meshes with a large number of degrees of freedom to obtain a good accuracy of the results, which in its turn implies to solve large linear systems of equations.

For simplicity, we restrict our analysis to axisymmetric problems. Let (r, θ, φ) denote the standard spherical coordinates of a point $\boldsymbol{x} \in \mathbb{R}^3$ (see Figure 7.10) and $\{\boldsymbol{e}_r, \boldsymbol{e}_\theta, \boldsymbol{e}_\varphi\}$ the canonical basis associated to this system of coordinates. We consider problems such that the porous and fluid domains as well as the external source are independent of the azimuthal angle φ. In such case Eqs. (7.1)-(7.7) and (7.9)-(7.11) can be rewritten in terms of r and θ, and, hence, reduced to two dimensions.

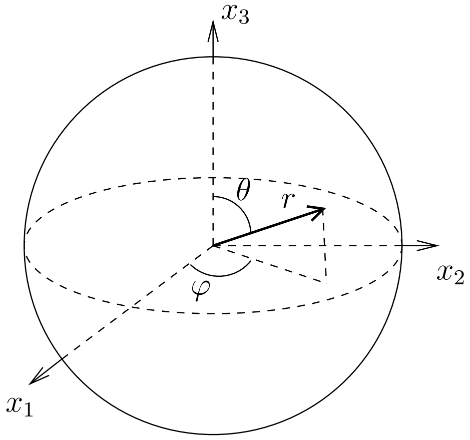

$$x_1 = r \sin\theta \cos\varphi,$$
$$x_2 = r \sin\theta \sin\varphi,$$
$$x_3 = r \cos\theta.$$

Figure 7.10: Spherical coordinates.

7.4.1 The Perfectly Matched Layer

Analogously to the derivation of the two-dimensional PML technique in polar polar coordinates in Chapter 6, we are going to introduce a PML technique in spherical coordinates [93] to truncate the unbounded fluid domain.

For this purpose, we surround the domain of interest (i.e., the part of the domain where we want to compute the pressure field) with a spherical PML. We consider a ball of radius R containing the domain of interest, the porous layer and the scatterer. The PML occupies the "annular" domain $\widehat{\Omega}_{\mathrm{F}} = \{\boldsymbol{x} \in \Omega_{\mathrm{F}} : R < |\boldsymbol{x}| < R^\star\}$ and we denote by Γ_{M} and Γ_{D} the spherical surfaces of radius R and $R^\star$, respectively, so that the boundary of $\widehat{\Omega}_{\mathrm{F}}$ is $\Gamma_{\mathrm{M}} \cup \Gamma_{\mathrm{D}}$, as shown in Figure 7.11 (left). Notice that $\boldsymbol{e}_r$ is a unit normal vector for both surfaces.

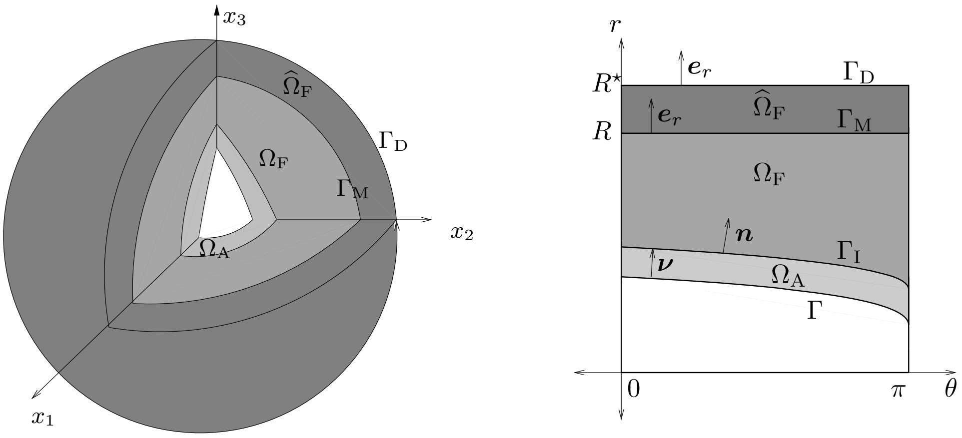

Figure 7.11: Original axisymmetric (cut) domains and spherical coordinates domains.

From now on, we make an abuse of notation: we denote with the same names the original three-dimensional domains and the corresponding two-dimensional projections, namely,

$$\Omega_{\mathrm{F}} = \{(r,\theta) : \boldsymbol{x} = (r,\theta,\varphi) \in \Omega_{\mathrm{F}}\}, \qquad \Gamma_{\mathrm{I}} = \{(r,\theta) : \boldsymbol{x} = (r,\theta,\varphi) \in \Gamma_{\mathrm{I}}\}, \qquad \text{etc.}$$

See Figure 7.11 for a better understanding of this notation.

Problems (7.1)-(7.7) and (7.9)-(7.11) are respectively written in this two-dimensional spherical coordinates setting as follows, where $\hat{p}_j$ $(j = 1,2)$ denote the pressure fields in $\widehat{\Omega}_{\mathrm{F}}$:

$$\left\{\begin{aligned}
\frac{1}{\rho_{\mathrm{F}}}\operatorname{div}(\mathbf{grad}\, p_1) + \frac{\omega^2}{\mu_{\mathrm{F}}} p_1 &= g && \text{in } \Omega_{\mathrm{F}},\\
\frac{1}{\rho_{\mathrm{A}}}\operatorname{div}(\mathbf{grad}\, p_{\mathrm{A}}) + \frac{\omega^2}{\mu_{\mathrm{A}}} p_{\mathrm{A}} &= 0 && \text{in } \Omega_{\mathrm{A}},\\
\frac{1}{\rho_{\mathrm{F}}}\widehat{\operatorname{div}}\left(\widehat{\mathbf{grad}}\, \hat{p}_1\right) + \frac{\omega^2}{\mu_{\mathrm{F}}} \hat{p}_1 &= 0 && \text{in } \widehat{\Omega}_{\mathrm{F}},\\
p_1 &= p_{\mathrm{A}} && \text{on } \Gamma_{\mathrm{I}},\\
\frac{1}{\rho_{\mathrm{F}}}\frac{\partial p_1}{\partial \boldsymbol{n}} &= \frac{1}{\rho_{\mathrm{A}}}\frac{\partial p_{\mathrm{A}}}{\partial \boldsymbol{n}} && \text{on } \Gamma_{\mathrm{I}},\\
\frac{1}{\rho_{\mathrm{A}}}\frac{\partial p_{\mathrm{A}}}{\partial \boldsymbol{\nu}} &= 0 && \text{on } \Gamma,\\
p_1 &= \hat{p}_1 && \text{on } \Gamma_{\mathrm{M}},\\
\frac{1}{\rho_{\mathrm{F}}}\frac{\partial p_1}{\partial r} &= \frac{1}{\rho_{\mathrm{F}}}\widehat{\mathbf{grad}}\, \hat{p}_1 \cdot \boldsymbol{e}_r && \text{on } \Gamma_{\mathrm{M}},\\
\hat{p}_1 &= 0 && \text{on } \Gamma_{\mathrm{D}}.
\end{aligned}\right. \tag{7.24}$$

$$\left\{\begin{aligned} \frac{1}{\rho_{\mathrm{F}}}\operatorname{div}(\mathbf{grad}\,p_2)+\frac{\omega^2}{\mu_{\mathrm{F}}}p_2&=g && \text{in } \Omega_{\mathrm{F}},\\ \frac{1}{\rho_{\mathrm{F}}}\widehat{\operatorname{div}}\left(\widehat{\mathbf{grad}}\,\hat{p}_2\right)+\frac{\omega^2}{\mu_{\mathrm{F}}}\hat{p}_2&=0 && \text{in } \widehat{\Omega}_{\mathrm{F}},\\ p_2-\frac{Z}{i\omega\rho_{\mathrm{F}}}\frac{\partial p_2}{\partial\boldsymbol{\nu}}&=0 && \text{on } \Gamma_{\mathrm{I}},\\ p_2&=\hat{p}_2 && \text{on } \Gamma_{\mathrm{M}},\\ \frac{1}{\rho_{\mathrm{F}}}\frac{\partial p_2}{\partial r}=\frac{1}{\rho_{\mathrm{F}}}&\widehat{\mathbf{grad}}\,\hat{p}_2\cdot\boldsymbol{e}_r && \text{on } \Gamma_{\mathrm{M}},\\ \hat{p}_2&=0 && \text{on } \Gamma_{\mathrm{D}}. \end{aligned}\right. \tag{7.25}$$

In the previous systems, the differential operators div and **grad** are, respectively, the divergence and gradient differential operators in spherical coordinates for axisymmetric problems (i.e., with vanishing partial derivatives with respect to φ):

$$\begin{aligned} \mathbf{grad}\,Q=&\frac{\partial Q}{\partial r}\boldsymbol{e}_r+\frac{1}{r}\frac{\partial Q}{\partial\theta}\boldsymbol{e}_\theta,\\ \operatorname{div}\boldsymbol{w}=&\frac{1}{r^2}\frac{\partial}{\partial r}(r^2w_r)+\frac{1}{r\sin\theta}\frac{\partial}{\partial\theta}(\sin\theta w_\theta), \end{aligned}$$

where $\boldsymbol{w}=w_r\boldsymbol{e}_r+w_\theta\boldsymbol{e}_\theta$. On the other hand, $\widehat{\operatorname{div}}$ and $\widehat{\mathbf{grad}}$ are the differential operators associated to the specific complex change of coordinates typical of the PML technique [47]:

$$\begin{aligned} \widehat{\mathbf{grad}}\,Q=&\frac{1}{\gamma_r}\frac{\partial Q}{\partial r}\boldsymbol{e}_r+\frac{1}{r\widehat{\gamma}_r}\frac{\partial Q}{\partial\theta}\boldsymbol{e}_\theta,\\ \widehat{\operatorname{div}}\,\boldsymbol{w}=&\frac{1}{r^2\gamma_r\widehat{\gamma}_r^2}\frac{\partial}{\partial r}(r^2\widehat{\gamma}_r^2w_r)+\frac{1}{r\widehat{\gamma}_r\sin\theta}\frac{\partial}{\partial\theta}(\sin\theta w_\theta), \end{aligned}$$

where

$$\gamma_r(r)=1+\frac{i}{\omega}\sigma_r(r)\qquad\text{and}\qquad\widehat{\gamma}_r(r)=1+\frac{i}{r\omega}\int_R^r\sigma_r(s)\,ds,\qquad R<r<R^\star,$$

with σ_r being the variable absorption coefficient in the PML.

The typical choices for σ_r are constant, linear or parabolic functions [22, 52]. Instead, we use a non-integrable absorbing function σ_r, which allows us to recover the exact solution of the original scattering problem in the domain of interest [32]. In particular we use

$$\sigma_r(s)=\frac{c_{\mathrm{F}}}{R^\star-s},\qquad R<s<R^\star, \tag{7.26}$$

which has been shown to be an optimal choice in Chapters 5 and 6.

7.4.2 Finite-element discretization

In this section we introduce a standard finite-element method to solve numerically the variational formulations of problems (7.24) and (7.25).

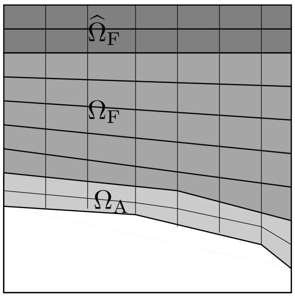

Figure 7.12: Quadrilateral finite elements for the domains in spherical coordinates.

Consider a quadrilateral mesh of the domains Ω_{A}, Ω_{F} and $\widehat{\Omega}_{\mathrm{F}}$, matching on the common interfaces, Γ_{I} and Γ_{M} (see Figure 7.12).

Regarding problem (7.24), we will compute approximations $p_{\mathrm{A}h}$, p_{1h} and $\hat{p}_{1h}$ of the pressure amplitude in Ω_{A}, Ω_{F} and $\widehat{\Omega}_{\mathrm{F}}$, respectively, by using continuous piecewise bilinear quadrilateral finite elements. The degrees of freedom defining the finite-element solution are the values of $p_{\mathrm{A}h}$, p_{1h} and $\hat{p}_{1h}$ at the vertices of the elements. Notice that, because of the transmission conditions, $p_{\mathrm{A}h} = p_{1h}$ on Γ_{I} and $p_{1h} = \hat{p}_{1h}$ on Γ_{M}, and, hence, the values of these functions must coincide at the vertices on the interfaces. Moreover, because of the boundary condition, $p_{1h} = 0$ on Γ_{D}.

Standard arguments lead to the following discrete problem from the variational formulation of problem (7.24):

$$\begin{aligned}\int_{\Omega_{\mathrm{F}}} \left(\mathbf{grad}\, p_{1h} \cdot \mathbf{grad}\, \overline{q}_h - k_{\mathrm{F}}^2 p_{1h}\overline{q}_h\right) dS + \int_{\Omega_{\mathrm{A}}} \left(\mathbf{grad}\, p_{\mathrm{A}h} \cdot \mathbf{grad}\, \overline{q}_h - k_{\mathrm{A}}^2 p_{\mathrm{A}h}\overline{q}_h\right) dS \\ + \int_{\widehat{\Omega}_{\mathrm{F}}} \left(\frac{\widehat{\gamma}_r^2}{\gamma_r}\frac{\partial \hat{p}_{1h}}{\partial r}\frac{\partial \overline{q}_h}{\partial r} + \frac{\gamma_r}{r^2}\frac{\partial \hat{p}_{1h}}{\partial \theta}\frac{\partial \overline{q}_h}{\partial \theta} - k_{\mathrm{F}}^2 \widehat{\gamma}_r^2 \gamma_r \hat{p}_{1h}\overline{q}_h\right) dS = \int_{\Omega_{\mathrm{F}}} \rho_{\mathrm{F}} g \overline{q}_h \, dS,\end{aligned}$$

for all discrete test pressure field q_h in the corresponding finite-element space. Recall that the surface element $dS = r \sin\theta \, dr \, d\theta$. Let us remark that the integrals in the above problem are well defined, in spite of the non-integrable character of the absorbing function (7.26) (for more details, see [30] or Chapter 6).

Analogously, the following is the discrete problem corresponding to (7.25):

$$\begin{aligned}\int_{\Omega_{\mathrm{F}}} \left(\mathbf{grad}\, p_{2h} \cdot \mathbf{grad}\, \overline{q}_h - k_{\mathrm{F}}^2 p_{2h}\overline{q}_h\right) dS - \int_{\Gamma_{\mathrm{I}}} \frac{i\omega\rho_{\mathrm{F}}}{Z} p_{2h}\overline{q}_h \, dL \\ + \int_{\widehat{\Omega}_{\mathrm{F}}} \left(\frac{\widehat{\gamma}_r^2}{\gamma_r}\frac{\partial \hat{p}_{2h}}{\partial r}\frac{\partial \overline{q}_h}{\partial r} + \frac{\gamma_r}{r^2}\frac{\partial \hat{p}_{2h}}{\partial \theta}\frac{\partial \overline{q}_h}{\partial \theta} - k_{\mathrm{F}}^2 \widehat{\gamma}_r^2 \gamma_r \hat{p}_{2h}\overline{q}_h\right) dS = \int_{\Omega_{\mathrm{F}}} \rho_{\mathrm{F}} g \overline{q}_h \, dS,\end{aligned}$$

for all discrete test pressure field q_h in the corresponding finite-element space; dL stands for the arc-length element. Notice that, once more, $p_{2h} = \hat{p}_{2h}$ on Γ_{M} and $p_{2h} = 0$ on Γ_{D}.

7.4.3 Verification of the numerical methods

In this section we verify the numerical methods that we have introduced in Section 7.4.2; namely, the PML model with a singular absorbing function and the finite element methods in spherical coordinates to approximate each model: Allard-Champoux and wall impedance. With this purpose, we have solved two simple problems, one for each model, both of them with known analytical solutions.

Verification of the numerical method for the Allard-Champoux model

In the first test, we check the accuracy of the numerical approximation of the Allard-Champoux model. Let Ω be a sphere centered at the origin of coordinates (see Figure 7.13). We consider problem (7.1)-(7.7) with $g = 0$ and Eq. (7.5) substituted by the following one: $\dfrac{\partial p_{\mathrm{A}}}{\partial \boldsymbol{\nu}} = 1$ on Γ. In this case, the solution is a superposition of two spherical waves:

$$\begin{aligned} p_{\mathrm{A}}(\boldsymbol{x}) &= A_{\mathrm{A}} \frac{\mathrm{e}^{ik_{\mathrm{A}}r}}{r} + B_{\mathrm{A}} \frac{\mathrm{e}^{-ik_{\mathrm{A}}r}}{r}, \\ p_1(\boldsymbol{x}) &= A_1 \frac{\mathrm{e}^{ik_{\mathrm{F}}r}}{r} + B_1 \frac{\mathrm{e}^{-ik_{\mathrm{F}}r}}{r}. \end{aligned}$$

The pairs of complex constants A_{A}, A_1 and B_{A}, B_1 are, respectively, the amplitudes of the ingoing and outgoing spherical waves in the porous media and the fluid. They are determined by the transmission and boundary conditions of the problem.

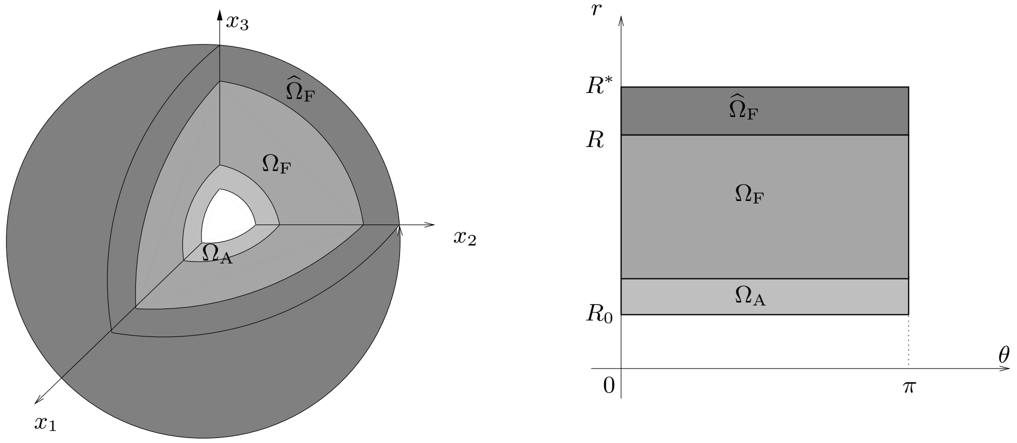

Figure 7.13: Three-dimensional cut of the spherical geometry and spherical coordinates domains.

We have taken an inner sphere of radius $R_0 = 0.5\,\mathrm{m}$, $R = 1.6\,\mathrm{m}$ and $R^\star = 1.8\,\mathrm{m}$. We have used the same values for the physical parameters as in Section 7.3: $\rho_{\mathrm{F}} = 1.2\,\mathrm{kg/m^3}$, $c_{\mathrm{F}} = 343\,\mathrm{m/s}$, $\mathrm{Pr} = 0.702$, $\gamma = 1.4$, $\sigma = 20000\,\mathrm{rays\ mks}$, $P_0 = 101320\,\mathrm{N/m^2}$ and $d = 0.05\,\mathrm{m}$.

We have used uniform refinements of the mesh shown in Figure 7.15. The number N of elements through the thickness of the PML is used to label each mesh.

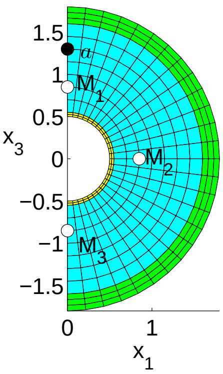

Figure 7.14: Coarse mesh for Allard-Champoux model in Cartesian coordinates ($N = 3$).

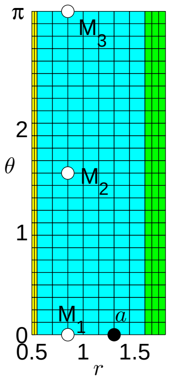

Figure 7.15: Coarse mesh for Allard-Champoux model in spherical coordinates ($N = 3$).

We compare in Figure 7.16 the exact and the computed solution of the Allard-Champoux model along the x_3-axis, for a frequency $f = 1000\,\mathrm{Hz}$. The computed solution was obtained with the mesh corresponding to $N = 12$, which has 5145 degrees of freedom. The solution is plotted in the physical domain and in the PML.

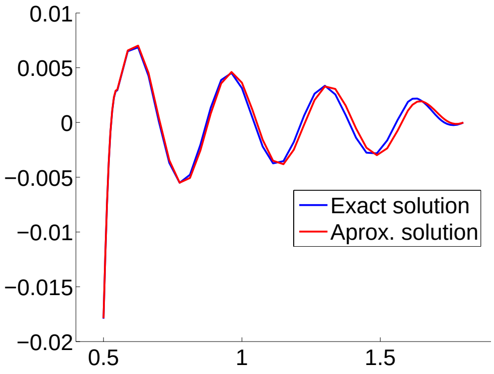

Figure 7.16: Real part of the pressure field computed with Allard-Champoux model. Mesh: $N = 12$ (5145 degrees of freedom); frequency: $f = 1000\,\mathrm{Hz}$.

To measure the accuracy of the numerical solution we have computed the relative error in L^2-norm:

$$\frac{\left(\displaystyle\int_{\Omega_{\rm F}} |p_{1h} - p_1|^2 \, dS\right)^{1/2}}{\left(\displaystyle\int_{\Omega_{\rm F}} |p_1|^2 \, dS\right)^{1/2}}.$$

We report in Figure 7.17 the error curves (log-log plot of errors versus degrees of freedom) for a couple of frequencies. For instance, in the case of Figure 7.16, the relative error is 18.15%.

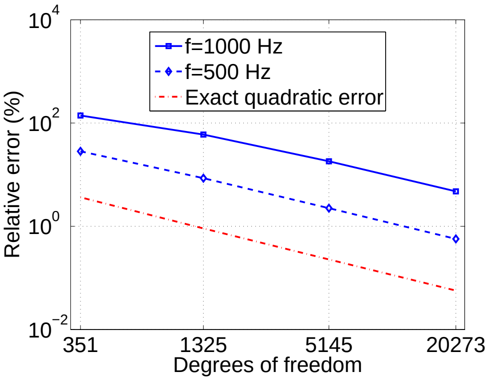

Figure 7.17: Error curve for Allard-Champoux model.

Figure 7.17 allow us to asses the order of convergence of the method. It can be seen that a quadratic order of convergence is achieved in all cases. Let us recall that this is the optimal order for the finite elements we have used.

Verification of the numerical method for the wall impedance model

In the second test, we check the accuracy of the numerical approximation of the wall impedance model. We use the same values for the physical and geometrical parameters as in the previous test. We consider now problem (7.9)-(7.11) with $g = 0$ and the boundary condition $p_2 = \dfrac{Z}{i\omega\rho_{\rm F}} \dfrac{\partial p_2}{\partial \boldsymbol{n}} + 1$ on $\Gamma_{\rm I}$, instead of Eq. (7.10). The solution is a spherical wave

$$p_2(\boldsymbol{x}) = A_2 \frac{\mathrm{e}^{ik_{\rm F} r}}{r} + B_2 \frac{\mathrm{e}^{-ik_{\rm F} r}}{r},$$

whose complex coefficients, A_2 and B_2, can be explicitly determined from the boundary conditions of the problem.

We have used the same meshes as in the previous test, excluding the elements in $\Omega_{\rm A}$.

We compare in Figure 7.18 the exact and the computed solution of the wall impedance model along the x_3-axis, for a frequency $f = 1000$ Hz. The computed solution was obtained with the mesh corresponding to $N = 12$ (5145 degrees of freedom).

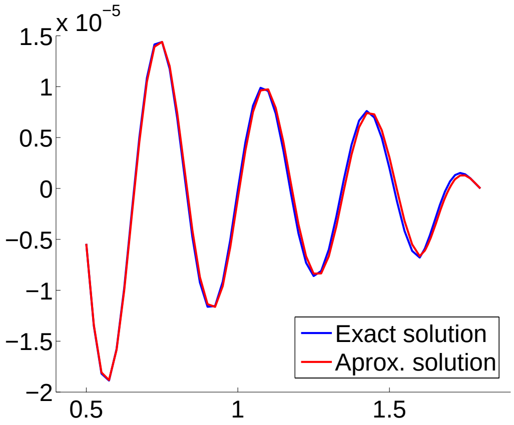

Figure 7.18: Real part of the pressure field computed with the wall impedance model. Mesh: $N = 12$ (5145 degrees of freedom); frequency: $f = 1000\,\mathrm{Hz}$.

Figure 7.19 shows the error curves for a couple of frequencies. For instance, in the case of Figure 7.18, the relative error is 9.83%. The order of convergence is again optimal (quadratic).

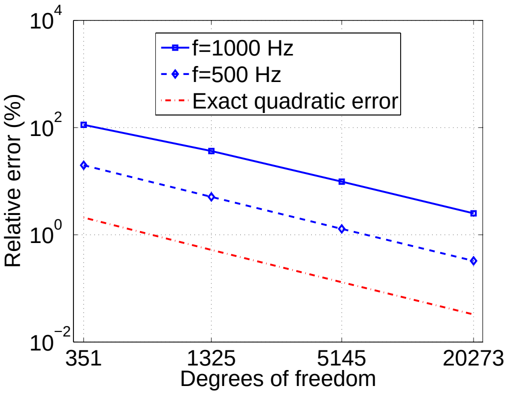

Figure 7.19: Error curves for wall impedance model.

7.4.4 Numerical validation of the wall impedance model for non-planar geometries

In this section we validate the wall impedance model by means of a test involving non-planar geometries. With this purpose, we compare the results of this model with those obtained with Allard-Champoux model. We will show that the geometry and the data of the problem are essential factors which can affect the agreement shown in Section 7.3.

We study the reflection of a spherical wave scattered by a non-concentric spherical obstacle. The solution of this problem has been broadly studied in the literature and an exact solution can be obtained via a series representation [7, 87].

We have used the physical parameters and the geometry described in Section 7.4.3. We have taken as external source a monopole with volume velocity $Q = 1\,\mathrm{m}^3/\mathrm{s}$ acting at the point $\boldsymbol{a} = (0, 0, a)$, with $a = 1.3\,\mathrm{m}$ (see Figures 7.14 and 7.15).

Figures 7.20 and 7.21 show the real parts of the pressure fields computed with each model on the mesh corresponding to $N = 12$, for a frequency $f = 500\,\mathrm{Hz}$ and a thickness of the porous layer $d = 0.05\,\mathrm{m}$. In all cases, the solution is plotted in the physical domain and in the PML. The pressure field has not been plotted around the monopole location to avoid scale distortions due to excessively large pressure values arising from the singularity.

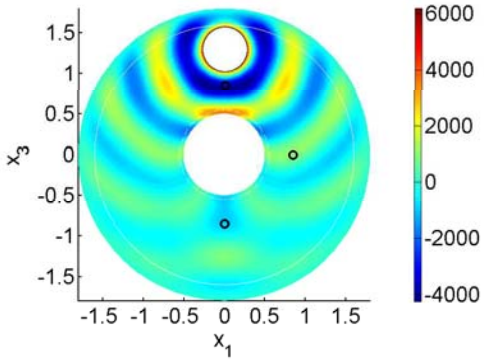

Figure 7.20: Real part of the pressure field computed with Allard-Champoux model. Mesh: $N = 12$; frequency: $f = 500\,\mathrm{Hz}$; thickness $d = 0.05\,\mathrm{m}$.

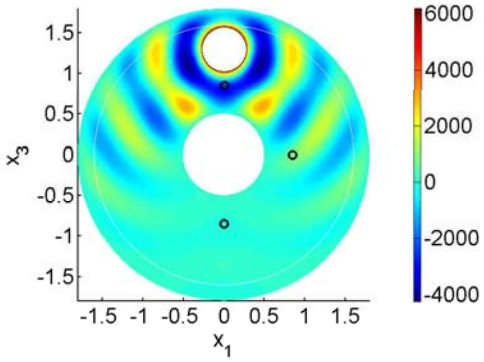

Figure 7.21: Real part of the pressure field computed with the wall impedance model. Mesh: $N = 12$; frequency: $f = 500\,\mathrm{Hz}$; thickness $d = 0.05\,\mathrm{m}$.

We have checked the agreement between both models by comparing the values of the pressure field computed with each model at three points in the fluid domain: $\boldsymbol{M}_1 = (0, 0, b)$, $\boldsymbol{M}_2 = (0, b, 0)$ and $\boldsymbol{M}_3 = (0, 0, -b)$, with $b = 0.85\,\mathrm{m}$ (see Figures 7.14 and 7.15). For each of these points, we have plotted the relative difference between both models, $|p_{1h} - p_{2h}| \,/\, |p_{\mathrm{inc}}|$, versus the frequency. In this expression, p_{1h} and p_{2h} are the values computed with Allard-Champoux and the wall impedance model, respectively, whereas p_{inc} is the incidence pressure as given by Eq. (7.23), which is the standard for spherical waves. Figures 7.22 and 7.23 shows these plots for two values of the thickness: $d = 0.05\,\mathrm{m}$ and $d = 0.2\,\mathrm{m}$, respectively.

We observe large differences between the solutions obtained with both models in many cases. For instance, the curves corresponding to points $\boldsymbol{M}_1$ and $\boldsymbol{M}_2$ have peaks of around 100% at very low frequencies, although they show a reasonable agreement in the middle frequencies range. This behavior is essentially independent of the layer thickness.

Finally, we show in Figures 7.24 and 7.25 the real parts of the pressure field computed with each model for a larger frequency, $f = 6000\,\mathrm{Hz}$, and a thickness $d = 0.05\,\mathrm{m}$. We have

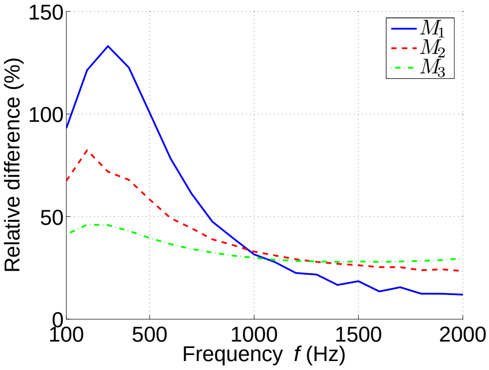

Figure 7.22: $|p_{1h} - p_{2h}| / |p_{\rm inc}|$ versus frequency. Mesh: $N = 12$; thickness: $d = 0.05$ m.

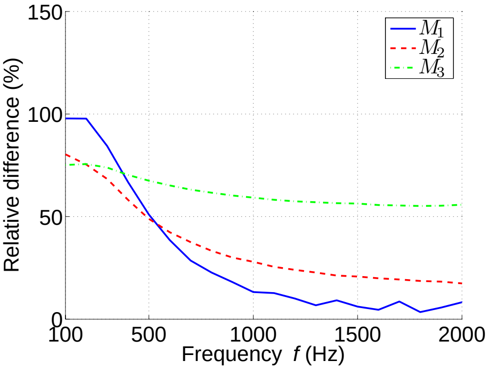

Figure 7.23: $|p_{1h} - p_{2h}| / |p_{\rm inc}|$ versus frequency. Mesh: $N = 12$; thickness: $d = 0.2$ m.

used in this case a very refined mesh corresponding to $N = 48$ in order to preserve the six elements per wave-length rule. A much better agreement can be observed in this case.

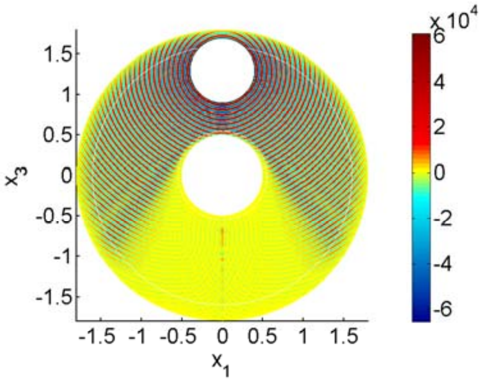

Figure 7.24: Real part of the pressure field computed with Allard-Champoux model. Mesh: $N = 48$; frequency: $f = 6000$ Hz; thickness: $d = 0.05$ m.

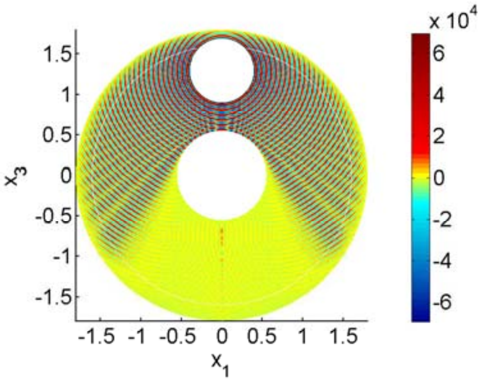

Figure 7.25: Real part of the pressure field computed with the wall impedance model. Mesh: $N = 48$; frequency: $f = 6000$ Hz; thickness: $d = 0.05$ m.

7.5 Conclusions

We have studied the agreement between two models for porous media in acoustic scattering problems: Allard-Champoux and a wall impedance model. We have shown that both provide almost identical results in planar geometries, even in the case of oblique incidence or spherical waves. This agreement holds for a wide range of frequencies, even for a non negligible thickness.

To be able to deal with non-planar geometries, we have introduced a finite-element method combined with an optimal bounded PML technique. We have applied this numerical strategy to compute the pressure field scattered by a sphere. This numerical example has shown that the agreement between the model for non-planar geometries may be very poor.

From these results, we conclude that the simplified wall impedance model is suitable to model porous media in planar geometries, but not so reliable in more general cases.

Chapter 8

Numerical simulation of locally reacting panels

Contents

8.1 Introduction

This final chapter is devoted to describe other computational application of the Perfectly Matched Layer technique in the context of dissipative acoustics. In particular, the main goal of this chapter is the numerical simulation of locally reacting panels in free field.

More precisely, we compute the acoustic field associated to a thin panels surrounded by an unbounded cavity of fluid, which is excited by a time-harmonic source. With this purpose, we apply the Cartesian PML technique with the singular absorbing functions introduced in Chapter 5, combined with a standard finite element code, in the three space dimensions.

First, we focus our attention on panels of dissipative materials modelled as locally reacting surfaces inside a cavity filled with an inviscid, barotropic and compressible fluid. If we consider a three-dimensional problem, it can be useful to take into account the normal specific impedance associated to a surface (see [21]), since this physical quantity gives us information about the ratio between the pressure and the normal velocity on this surface.

In the framework of acoustic propagation of plane waves, when we deal with an interface between two different media, the normal specific impedance depends on the angle of incidence of the wave. But, in some cases, this normal specific impedance can be considered independent of this angle. In these cases, we say that it is a locally reacting surface (see [43]). The interesting feature is that acoustic propagation through this kind of surfaces is determined by its impedance at each point on the surface.

If we consider a locally reacting surface, the normal component of the velocity at each point of the surface is completely determined by the pressure at that point. This fact makes possible that several thin layers of dissipative materials can be modelled by boundary conditions. This happens, for instance, in the case of impedance walls, porous veils, and microperforated or rigid plates.

To model the panel, it is considered as a layer with negligible thickness which reacts locally. According to this simplification, we study several possible boundary conditions to model the panel which can be used for classical porous veils, thin layers of porous materials, etc.

Secondly, to deal with the unbounded domain where the problem is stated, we use the PML technique in Cartesian coordinates described in Chapter 5, to truncate the domain of physical interest.

The outline of this chapter is as follows. In Section 8.2 we study different boundary conditions that can be used to model a panel of dissipative material surrounded by an unbounded fluid domain. In Section 8.3, we describe the variational formulation of each of the problems stated in the previous sections. Finally, in Sections 8.4 and 8.5 we describe a finite element method for numerical discretization of each of the acoustic problems. Finally, some numerical results in a more realistic case are shown in Section 8.6.

8.2 Modelling the panel

Since the PML technique has already been widely used through the present work, we are going to state directly the fluid/PML coupled problem (see Chapter 4 and 5 for details). In this chapter, the unique new feature of the PML technique is that the equations are written in three space dimensions.

We consider a coupled system consisting of an acoustic fluid in the physical domain of interest

$$\Omega_{\mathrm{F}} = (-a, a) \times (-b, b) \times (-d, d).$$

Since we need to simulate numerically a problem in an unbounded fluid domain, we surround this fluid domain by a cartesian PML layer, which occupies the domain

$$\Omega_{\mathrm{A}} = (-a^*, a^*) \times (-b^*, b^*) \times (-d^*, d^*) \setminus \overline{\Omega_{\mathrm{F}}}.$$

In the sequel we assume that the locally reacting panel is included in the physical domain of interest. Ω_{F} (see Figure 8.1).

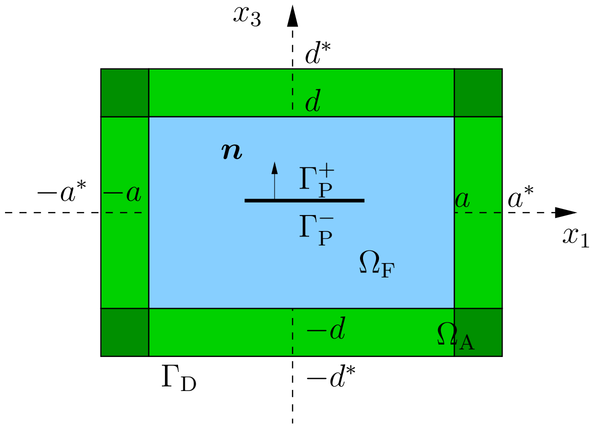

Figure 8.1: Vertical cut of the fluid/PML domain and the locally reacting panel.

We denote the exterior boundary of the PML by Γ_{D} and we assume that the absorbing panel is placed on the surface Γ_{P}, inside Ω_{F}. We denote by Γ_{P}^+ and Γ_{P}^- each of the sides of the panel, with $\boldsymbol{n}$ the unit normal vector which is chosen as shown in Figure 8.1.

Through the next section, we consider four types of locally reacting panels:

- an absorbing panel modelled by a wall impedance condition which preserves the continuity of the pressure,
- an absorbing panel which preserves the continuity of the displacements,
- an absorbing panel that preserves neither the continuity of the pressure nor that of the displacements,

- an absorbing panel with a rigid back.

In every case we focus our attention on the description of the boundary conditions and on the complex impedance value associated to the panels.

8.2.1 Wall-like impedance

First, we assume that the absorbing panel can be modelled by a wall-like impedance condition. If we denote by $p^+, \boldsymbol{u}^+$ the pressure and the displacement, respectively, on the positive side of the absorbing panel, Γ_{P}^+, and by $p^-, \boldsymbol{u}^-$ those on the negative side, Γ_{P}^-, then the equations governing the behavior of the absorbing panel are

$$\begin{aligned} p^+ &= p^- && \text{on } \Gamma_{\mathrm{P}}, \\ p^+ &= -i\omega Z(\boldsymbol{u}^+ \cdot \boldsymbol{n} - \boldsymbol{u}^- \cdot \boldsymbol{n}) && \text{on } \Gamma_{\mathrm{P}}, \end{aligned}$$

where Z is the surface impedance of the panel.

Taking into account the motion equation in the frequency domain, the fluid normal displacement can be written in terms of the normal derivative of the pressure field as

$$\begin{aligned} \boldsymbol{u}^+ \cdot \boldsymbol{n} &= \frac{1}{\omega^2 \rho_0} \frac{\partial p^+}{\partial \boldsymbol{n}} && \text{on } \Gamma_{\mathrm{P}}, \\ \boldsymbol{u}^- \cdot \boldsymbol{n} &= \frac{1}{\omega^2 \rho_0} \frac{\partial p^-}{\partial \boldsymbol{n}} && \text{on } \Gamma_{\mathrm{P}}. \end{aligned}$$

Then, in this case, the pressure field is solution of the following problem:

For a given acoustic source f with compact support in Ω_{F} and a fixed angular frequency ω, find the pressure field p satisfying

$$-k^2 p - \sum_{j=1}^{3} \frac{1}{\gamma_j} \frac{\partial}{\partial x_j} \left[\frac{1}{\gamma_j} \frac{\partial p}{\partial x_j} \right] = f \qquad \text{in } \Omega_{\mathrm{A}} \cup \Omega_{\mathrm{F}}, \tag{8.1}$$

$$p^+ = p^- = -\frac{iZ}{\omega \rho_0} \left(\frac{\partial p^+}{\partial \boldsymbol{n}} - \frac{\partial p^-}{\partial \boldsymbol{n}} \right) \qquad \text{on } \Gamma_{\mathrm{P}}, \tag{8.2}$$

$$p = 0 \qquad \text{on } \Gamma_{\mathrm{D}}, \tag{8.3}$$

where $k = \dfrac{\omega}{c}$ is the wave number.

In summary, the acoustic behavior of the locally reacting panel depends on the value of the complex impedance $Z(\omega)$. To determine this quantity we can either use experimental measures (see [21]) or try to obtain an explicit mathematical expression. For instance, if we assume that the panel consists of a unique thin layer of porous material, the surface impedance of the panel can be considered as the input impedance to a multilayered media formed with a porous medium and an unbounded layer of fluid. In this case, the surface impedance of the panel is given by (see [43])

$$Z = Z_p \frac{Z_0 \cos(k_p d) - iZ_p \sin(k_p d)}{Z_p \cos(k_p d) - iZ_0 \sin(k_p d)},$$

where d is the thickness of the panel, Z_0 the fluid characteristic impedance, k_p the wave number of the porous medium and Z_p the characteristic impedance of the porous material. If we compute the impedance and the wave number with the Darcy's like model, introduced in Chapter 2, then we have

$$Z_p = \rho_0 c \left(1 - i\frac{\sigma}{\rho_0 \omega}\right), \qquad k_p = \frac{\omega}{c}\left(1 - i\frac{\sigma}{\rho_0 \omega}\right),$$

where we recall that σ is the flow resistivity of the porous medium.

8.2.2 Porous veil and micro-perforated plates

Now we assume that the displacement is continuous through the panel, whereas the pressure has a jump. This is the case of porous veils or rigid or microperforated plates. Then, in the frequency domain, the equations governing the motion of the absorbing panel are given by

$$\begin{aligned} \frac{\partial p^+}{\partial \boldsymbol{n}} &= \frac{\partial p^-}{\partial \boldsymbol{n}} && \text{on } \Gamma_\mathrm{P}, \\ p^+ - p^- = -i\omega Z \boldsymbol{u}^+ \cdot \boldsymbol{n} &= -\frac{iZ}{\omega\rho_0}\frac{\partial p^+}{\partial \boldsymbol{n}} && \text{on } \Gamma_\mathrm{P}. \end{aligned}$$

Let us remark that the first boundary condition implies that $\boldsymbol{u}^+ \cdot \boldsymbol{n} = \boldsymbol{u}^- \cdot \boldsymbol{n}$. Taking into account these transmission conditions, the pressure field is solution of the following problem:

For a given acoustic source f with compact support in Ω_F and a fixed angular frequency ω, find the pressure field p satisfying

$$-k^2 p - \sum_{j=1}^{3} \frac{1}{\gamma_j}\frac{\partial}{\partial x_j}\left[\frac{1}{\gamma_j}\frac{\partial p}{\partial x_j}\right] = f \qquad \text{in } \Omega_\mathrm{A} \cup \Omega_\mathrm{F}, \tag{8.4}$$

$$\frac{\partial p^+}{\partial \boldsymbol{n}} = \frac{\partial p^-}{\partial \boldsymbol{n}} \qquad \text{on } \Gamma_\mathrm{P}, \tag{8.5}$$

$$p^+ - p^- = -\frac{iZ}{\omega\rho_0}\frac{\partial p^+}{\partial \boldsymbol{n}} \qquad \text{on } \Gamma_\mathrm{P}, \tag{8.6}$$

$$p = 0 \qquad \text{on } \Gamma_\mathrm{D}. \tag{8.7}$$

As in the case of the wall impedance model, we should know the value of the complex impedance $Z(\omega)$ via experimental or theoretical analysis. For instance, in the case of a microperforated plate, the impedance can be computed by using the Maa's formula (see [83]).

8.2.3 Thin porous layer

In the previous subsections, we have modelled a panel as a locally reacting surface preserving the continuity of the pressure (in the case of the wall-like impedance condition) or the continuity of the normal displacements (in the case of porous veils or microperforated plates). Nevertheless, it is also possible to model the absorbing panel as a locally reacting surface where neither the continuity of the pressure field nor the continuity of the normal displacement are preserved.

This is the case when we consider a panel formed by a thin layer of porous material, with a negligible thickness as it is compared to the rest of the dimensions of the panel.

In fact, if the porous layer is thin enough, we can approximate the solution of the acoustic propagation problem inside the layer in terms of plane waves with normal incidence. Hence, we can use a simple one-dimensional model to write the pressure and the normal displacements fields as

$$\begin{aligned} \boldsymbol{u}(x_3)\cdot\boldsymbol{n} &= Ae^{-ik_px_3}+Be^{ik_px_3},\\ p(x_3) &= -i\omega Z_p(-Ae^{-ik_px_3}+Be^{ik_px_3}), \end{aligned}$$

where k_p and Z_p are the wave number and the characteristic impedance in the porous material, respectively. Taking these considerations into account, we write the pressure field and the normal displacement on the two faces of the absorbing panel in terms of the amplitudes of the plane waves,

$$\boldsymbol{u}^-\cdot\boldsymbol{n} = A+B, \qquad p^- = -i\omega Z_p(-A+B) \qquad \text{on } x_3=0, \tag{8.8}$$

$$\boldsymbol{u}^+\cdot\boldsymbol{n} = Ae^{-ik_pd}+Be^{ik_pd}, \qquad p^+ = -i\omega Z_p(-Ae^{-ik_pd}+Be^{ik_pd}) \qquad \text{on } x_3=d, \tag{8.9}$$

where d is the thickness of the panel. From (8.8), we write the amplitudes A and B in terms of p^- and $\boldsymbol{u}^-\cdot\boldsymbol{n}$. Substituting them in (8.9), we obtain

$$\boldsymbol{u}^+\cdot\boldsymbol{n} = \cos(k_pd)\boldsymbol{u}^-\cdot\boldsymbol{n} - \frac{1}{\omega Z_p}\sin(k_pd)p^- \qquad \text{on } \Gamma_{\mathrm{P}}, \tag{8.10}$$

$$p^+ = \omega Z_p\sin(k_pd)\boldsymbol{u}^-\cdot\boldsymbol{n} + \cos(k_pd)p^- \qquad \text{on } \Gamma_{\mathrm{P}}. \tag{8.11}$$

Finally, if we write the normal displacements in terms of the normal derivatives of the pressure field, from (8.10)-(8.11), we have

$$\begin{aligned} \frac{\partial p^+}{\partial \boldsymbol{n}} &= \frac{\omega\rho_0}{Z_p\sin(k_pd)}\left(p^+\cos(k_pd)-p^-\right) \qquad \text{on } \Gamma_{\mathrm{P}},\\ \frac{\partial p^-}{\partial \boldsymbol{n}} &= -\frac{\omega\rho_0}{Z_p\sin(k_pd)}\left(p^-\cos(k_pd)-p^+\right) \qquad \text{on } \Gamma_{\mathrm{P}}. \end{aligned}$$

Hence, the pressure field is solution of the following problem:
For a given acoustic source f with compact support in Ω_{F}, and a fixed angular frequency ω,

find the pressure field p which satisfies

$$-k^2p-\sum_{j=1}^{3}\frac{1}{\gamma_j}\frac{\partial}{\partial x_j}\left[\frac{1}{\gamma_j}\frac{\partial p}{\partial x_j}\right]=f \qquad \textit{in } \Omega_{\mathrm{A}}\cup\Omega_{\mathrm{F}}, \tag{8.12}$$

$$\frac{\partial p^+}{\partial \boldsymbol{n}}=\frac{\omega\rho_0}{Z_p\sin(k_pd)}\left(p^+\cos(k_pd)-p^-\right) \qquad \textit{on } \Gamma_{\mathrm{P}}, \tag{8.13}$$

$$\frac{\partial p^-}{\partial \boldsymbol{n}}=-\frac{\omega\rho_0}{Z_p\sin(k_pd)}\left(p^-\cos(k_pd)-p^+\right) \qquad \textit{on } \Gamma_{\mathrm{P}}, \tag{8.14}$$

$$p=0 \qquad \textit{on } \Gamma_{\mathrm{D}}. \tag{8.15}$$

8.2.4 Multilayer panel with a rigid back

Now we analyze the acoustic behavior of a locally reacting multilayer panel surrounded by an unbounded fluid. In fact, we focus our attention on a multilayer panel constituted by three media: a porous material, a fluid cavity and a rigid wall (see Figure 8.2).

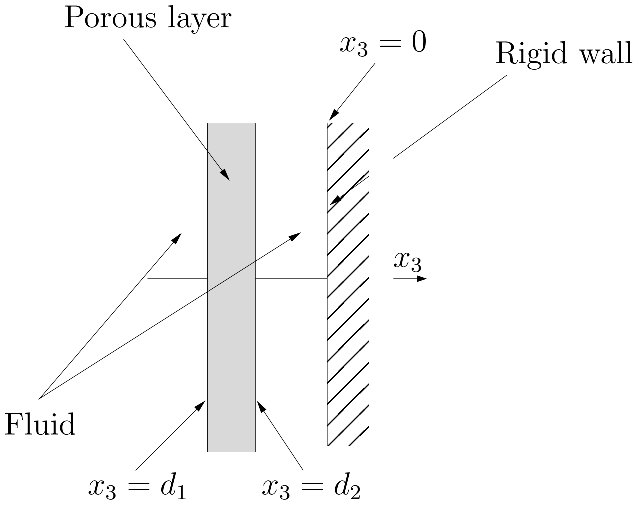

Figure 8.2: Multilayer panel formed by a porous layer and a fluid cavity with rigid back.

We again consider that the thickness of the multilayer is small enough as to model it by using the one-dimensional equations of acoustic propagation of plane waves with normal incidence.

Following the same technique as the one used in the case of the thin porous layer model, we can compute the input impedance of the multilayer as (see [43])

$$Z=\frac{p^-}{-i\omega\boldsymbol{u}^-\cdot\boldsymbol{n}}=Z_p\frac{Z_T\cos(k_pd_1)-iZ_p\sin(k_pd_1)}{Z_p\cos(k_pd_1)-iZ_T\sin(k_pd_1)},$$

where $Z_T = iZ_0\text{cotan}(k_pd_2)$, and $x_3 = d_1$ and $x_3 = d_2$ are the planes where the coupling interfaces between the porous material and the fluid domains are located (see Figure 8.2).

Moreover, we must take into account that the rigid wall condition imposes a homogeneous condition on the normal derivative of the pressure on the back of the panel (Γ_{P}^{+}),

$$\boldsymbol{u}^{+}\cdot\boldsymbol{n}=\frac{1}{\omega^{2}\rho_{0}}\frac{\partial p^{+}}{\partial\boldsymbol{n}}=0.$$

Hence, the pressure field is solution of the following problem:

For a given acoustic source f with compact support in Ω_{F}, and a fixed angular frequency ω, find the pressure field p which satisfies

$$-k^{2}p-\sum_{j=1}^{3}\frac{1}{\gamma_{j}}\frac{\partial}{\partial x_{j}}\left[\frac{1}{\gamma_{j}}\frac{\partial p}{\partial x_{j}}\right]=f\qquad in\ \Omega_{\mathrm{A}}\cup\Omega_{\mathrm{F}},\tag{8.16}$$

$$\frac{\partial p^{+}}{\partial\boldsymbol{n}}=0\qquad on\ \Gamma_{\mathrm{P}}^{+},\tag{8.17}$$

$$p^{-}=\frac{iZ}{\omega\rho_{0}}\frac{\partial p^{-}}{\partial\boldsymbol{n}}\qquad on\ \Gamma_{\mathrm{P}}^{-},\tag{8.18}$$

$$p=0\qquad on\ \Gamma_{\mathrm{D}}.\tag{8.19}$$

8.3 Variational formulation

As a previous step to their numerical solution, we write down the variational formulation of the problems stated in the previous section. With this purpose, first we introduce the adequate functional spaces. To simplify the notation, we denote $\Omega=(\Omega_{\mathrm{A}}\cup\Omega_{\mathrm{F}})\setminus\Gamma_{\mathrm{P}}$ and the boundary of this domain Ω by $\partial\Omega=\Gamma_{\mathrm{D}}\cup\Gamma_{\mathrm{P}}^{+}\cup\Gamma_{\mathrm{P}}^{-}$.

Let H be the Hilbert space defined by

$$\mathrm{H}=\{q\in\mathrm{H}^{1}_{\mathrm{loc}}(\Omega):\ q|_{\Omega_{\mathrm{F}}}\in\mathrm{H}^{1}(\Omega_{\mathrm{F}}\setminus\Gamma_{\mathrm{P}}),\ q|_{\Omega_{\mathrm{A}}}\in\mathrm{W}\},\tag{8.20}$$

where the Hilbert space W is a weighted Sobolev space endowed with the norm

$$\|q\|_{\mathrm{W}}^{2}=\int_{\Omega_{\mathrm{A}}}\left|\frac{\gamma_{2}\gamma_{3}}{\gamma_{1}}\right|\left|\frac{\partial q}{\partial x_{1}}\right|^{2}+\int_{\Omega_{\mathrm{A}}}\left|\frac{\gamma_{1}\gamma_{3}}{\gamma_{2}}\right|\left|\frac{\partial q}{\partial x_{2}}\right|^{2}+\int_{\Omega_{\mathrm{A}}}\left|\frac{\gamma_{1}\gamma_{2}}{\gamma_{3}}\right|\left|\frac{\partial q}{\partial x_{3}}\right|^{2}+\int_{\Omega_{\mathrm{A}}}|\gamma_{1}\gamma_{2}\gamma_{3}|\,|q|^{2}.$$

In fact, a kind of homogeneous Dirichlet boundary condition on the exterior boundary of the PML domain,

$$q=0\qquad\text{on }\Gamma_{\mathrm{D}},$$

is contained implicitly in the definition of space W. This boundary condition will be actually used in the discretization of weak problems proposed in the following section.

In order to obtain a variational formulation of the four source problems, first we multiply the PML equation by $\gamma_{1}\gamma_{2}\gamma_{3}$ with γ_{j}, $j=1,2,3$, analogous to those defined for the two-dimensional case in Chapter 4. Thus we obtain symmetric bilinear forms in all cases. So we have

$$-k^2\gamma_1\gamma_2\gamma_3 p - \frac{\partial}{\partial x_1}\left(\frac{\gamma_2\gamma_3}{\gamma_1}\frac{\partial p}{\partial x_1}\right) - \frac{\partial}{\partial x_2}\left(\frac{\gamma_1\gamma_3}{\gamma_2}\frac{\partial p}{\partial x_2}\right) - \frac{\partial}{\partial x_3}\left(\frac{\gamma_1\gamma_2}{\gamma_3}\frac{\partial p}{\partial x_3}\right) = f.$$

To obtain the previous expression we have used that f has compact support contained in Ω_{F} and that each coefficient γ_j only depends on the variable x_j.

Now if we multiply this expression by the complex conjugate of the virtual pressure $q \in \mathrm{H}$, integrate in Ω and use the first Green formula, then we have

$$\begin{aligned}-\int_\Omega k^2\gamma_1\gamma_2\gamma_3 p\bar{q} + \int_\Omega \frac{\gamma_2\gamma_3}{\gamma_1}\frac{\partial p}{\partial x_1}\frac{\partial \bar{q}}{\partial x_1} + \int_\Omega \frac{\gamma_1\gamma_3}{\gamma_2}\frac{\partial p}{\partial x_2}\frac{\partial \bar{q}}{\partial x_2}& \\ + \int_\Omega \frac{\gamma_1\gamma_2}{\gamma_3}\frac{\partial p}{\partial x_3}\frac{\partial \bar{q}}{\partial x_3} - \int_{\Gamma_{\mathrm{P}}^+}\frac{\partial p^+}{\partial \boldsymbol{n}}\bar{q}^+ + \int_{\Gamma_{\mathrm{P}}^-}\frac{\partial p^-}{\partial \boldsymbol{n}}\bar{q}^- &= \int_{\Omega_{\mathrm{F}}} f\bar{q}, \qquad (8.21)\end{aligned}$$

where p^+, q^+ and p^-, q^- are the restrictions of the pressure fields p, q to the boundaries Γ_{P}^+ and Γ_{P}^-, respectively.

Taking into account each one of the different boundary conditions stated for each type of panel, we write four different variational problems.

8.3.1 Wall-like impedance

Since, in the case of the wall impedance condition, the pressure field is continuous through the panel, the functional space of the virtual pressure is given by

$$\mathrm{V} = \{q \in \mathrm{H}^1_{\mathrm{loc}}(\Omega_{\mathrm{F}} \cup \Omega_{\mathrm{A}}) : \ q|_{\Omega_{\mathrm{F}}} \in \mathrm{H}^1(\Omega_{\mathrm{F}}),\ q|_{\Omega_{\mathrm{A}}} \in \mathrm{W}\}, \qquad (8.22)$$

and hence, by identifying Γ_{P}^+ and Γ_{P}^-, the boundary integrals that arise in (8.21) are reduced to

$$\int_{\Gamma_{\mathrm{P}}^+}\frac{\partial p^+}{\partial \boldsymbol{n}}\bar{q}^+ - \int_{\Gamma_{\mathrm{P}}^-}\frac{\partial p^-}{\partial \boldsymbol{n}}\bar{q}^- = \int_{\Gamma_{\mathrm{P}}}\left(\frac{\partial p^+}{\partial \boldsymbol{n}} - \frac{\partial p^-}{\partial \boldsymbol{n}}\right)\bar{q} = -\int_{\Gamma_{\mathrm{P}}}\frac{\omega\rho_0}{iZ}p\bar{q}.$$

Consequently, the variational formulation of problem (8.1)-(8.3) can be written as follows:

For a fixed frequency ω, find $p \in \mathrm{V}$ such that

$$\begin{aligned}-\int_\Omega k^2\gamma_1\gamma_2\gamma_3 p\bar{q} + \int_\Omega \frac{\gamma_2\gamma_3}{\gamma_1}\frac{\partial p}{\partial x_1}\frac{\partial \bar{q}}{\partial x_1} + \int_\Omega \frac{\gamma_1\gamma_3}{\gamma_2}\frac{\partial p}{\partial x_2}\frac{\partial \bar{q}}{\partial x_2}& \\ + \int_\Omega \frac{\gamma_1\gamma_2}{\gamma_3}\frac{\partial p}{\partial x_3}\frac{\partial \bar{q}}{\partial x_3} + \int_{\Gamma_{\mathrm{P}}}\frac{\omega\rho_0}{iZ}p\bar{q} &= \int_{\Omega_{\mathrm{F}}} f\bar{q}, \qquad (8.23)\end{aligned}$$

for all $q \in \mathrm{V}$.

8.3.2 Porous veil

In the case of the porous veil or a rigid or microperforated plate the normal derivative of the pressure field is continuous through the panel. Hence, by identifying Γ_{P}^{+} and Γ_{P}^{-}, the boundary integrals that arise in (8.21) are reduced to

$$\int_{\Gamma_{\mathrm{P}}^{+}} \frac{\partial p^{+}}{\partial \boldsymbol{n}} \bar{q}^{+} - \int_{\Gamma_{\mathrm{P}}^{-}} \frac{\partial p^{-}}{\partial \boldsymbol{n}} \bar{q}^{-} = \int_{\Gamma_{\mathrm{P}}} \frac{\partial p^{+}}{\partial \boldsymbol{n}} (\bar{q}^{+} - \bar{q}^{-}) = - \int_{\Gamma_{\mathrm{P}}} \frac{\omega \rho_0}{iZ} (p^{+} - p^{-})(\bar{q}^{+} - \bar{q}^{-}).$$

Consequently, the variational formulation of problem (8.4)-(8.7) can be written as follows:

For a fixed frequency ω, *find* $p \in \mathrm{H}$ *such that*

$$- \int_{\Omega} k^2 \gamma_1 \gamma_2 \gamma_3 p \bar{q} + \int_{\Omega} \frac{\gamma_2 \gamma_3}{\gamma_1} \frac{\partial p}{\partial x_1} \frac{\partial \bar{q}}{\partial x_1} + \int_{\Omega} \frac{\gamma_1 \gamma_3}{\gamma_2} \frac{\partial p}{\partial x_2} \frac{\partial \bar{q}}{\partial x_2} + \int_{\Omega} \frac{\gamma_1 \gamma_2}{\gamma_3} \frac{\partial p}{\partial x_3} \frac{\partial \bar{q}}{\partial x_3} + \int_{\Gamma_{\mathrm{P}}} \frac{\omega \rho_0}{iZ} (p^{+} - p^{-})(\bar{q}^{+} - \bar{q}^{-}) = \int_{\Omega_{\mathrm{F}}} f \bar{q}, \quad (8.24)$$

for all $q \in \mathrm{H}$.

8.3.3 Thin porous layer

If the panel preserves neither the continuity of the pressure nor that of the displacement, then, taking into account (8.13)-(8.14), the boundary integrals that arise in (8.21) can be rewritten as

$$\begin{aligned} &\int_{\Gamma_{\mathrm{P}}^{+}} \frac{\partial p^{+}}{\partial \boldsymbol{n}} \bar{q}^{+} - \int_{\Gamma_{\mathrm{P}}^{-}} \frac{\partial p^{-}}{\partial \boldsymbol{n}} \bar{q}^{-} \\ &\quad = \int_{\Gamma_{\mathrm{P}}^{+}} \frac{\omega \rho_0}{Z_p \sin(k_p d)} \left(p^{+} \cos(k_p d) - p^{-}\right) \bar{q}^{+} + \int_{\Gamma_{\mathrm{P}}^{-}} \frac{\omega \rho_0}{Z_p \sin(k_p d)} \left(p^{-} \cos(k_p d) - p^{+}\right) \bar{q}^{-} \\ &\quad = \int_{\Gamma_{\mathrm{P}}} \frac{\omega \rho_0}{Z_p \sin(k_p d)} \left((p^{+} \bar{q}^{+} + p^{-} \bar{q}^{-}) \cos(k_p d) - (p^{+} \bar{q}^{-} + p^{-} \bar{q}^{+})\right). \end{aligned}$$

Hence, the variational formulation of problem (8.12)-(8.15) can be written as follows:

For a fixed frequency ω, *find* $p \in \mathrm{H}$ *such that*

$$- \int_{\Omega} k^2 \gamma_1 \gamma_2 \gamma_3 p \bar{q} + \int_{\Omega} \frac{\gamma_2 \gamma_3}{\gamma_1} \frac{\partial p}{\partial x_1} \frac{\partial \bar{q}}{\partial x_1} + \int_{\Omega} \frac{\gamma_1 \gamma_3}{\gamma_2} \frac{\partial p}{\partial x_2} \frac{\partial \bar{q}}{\partial x_2} + \int_{\Omega} \frac{\gamma_1 \gamma_2}{\gamma_3} \frac{\partial p}{\partial x_3} \frac{\partial \bar{q}}{\partial x_3} - \int_{\Gamma_{\mathrm{P}}} \frac{\omega \rho_0}{Z_p \sin(k_p d)} \left((p^{+} \bar{q}^{+} + p^{-} \bar{q}^{-}) \cos(k_p d) - (p^{+} \bar{q}^{-} + p^{-} \bar{q}^{+})\right) = \int_{\Omega_{\mathrm{F}}} f \bar{q}, \quad (8.25)$$

for all $q \in \mathrm{H}$.

8.3.4 Multilayer panel with a rigid back

Finally, if we assume that the panel is a multilayer formed by two media in contact with a rigid wall, then, taking into account (8.17)-(8.18), the substraction of boundary integrals that arises in (8.21) is given by

$$\int_{\Gamma_\mathrm{P}^+} \frac{\partial p^+}{\partial \boldsymbol{n}} \bar{q}^+ - \int_{\Gamma_\mathrm{P}^-} \frac{\partial p^-}{\partial \boldsymbol{n}} \bar{q}^- = -\int_{\Gamma_\mathrm{P}^-} \frac{\partial p^-}{\partial \boldsymbol{n}} \bar{q}^- = -\int_{\Gamma_\mathrm{P}} \frac{\omega \rho_0}{iZ} p^- \bar{q}^-.$$

Hence, the variational formulation of problem (8.16)-(8.19) can be written as follows:

For a fixed frequency ω, find $p \in \mathrm{H}$ such that

$$-\int_\Omega k^2 \gamma_1\gamma_2\gamma_3 p\bar{q} + \int_\Omega \frac{\gamma_2\gamma_3}{\gamma_1}\frac{\partial p}{\partial x_1}\frac{\partial \bar{q}}{\partial x_1} + \int_\Omega \frac{\gamma_1\gamma_3}{\gamma_2}\frac{\partial p}{\partial x_2}\frac{\partial \bar{q}}{\partial x_2} + \int_\Omega \frac{\gamma_1\gamma_2}{\gamma_3}\frac{\partial p}{\partial x_3}\frac{\partial \bar{q}}{\partial x_3} + \int_{\Gamma_\mathrm{P}} \frac{\omega\rho_0}{iZ} p^- \bar{q}^- = \int_{\Omega_\mathrm{F}} f\bar{q}, \quad (8.26)$$

for all $q \in \mathrm{H}$.

8.4 Finite element discretization

In order to solve the variational problems (8.23)-(8.26) stated in the previous section, we discretize them by using a finite element method.

Let $\mathcal{T}_h$ be a structure partition of the three-dimensional domain Ω in parallelepipedic elements, such that each parallelepiped is completely contained either in Ω_F or in Ω_A (see Figure 8.11). We also assume the if a finite element in $\mathcal{T}_h$ has a face on the boundary of Ω, this face is completely contained in Γ_D, Γ_P^- or Γ_P^+.

To approximate the pressure field p, we use piecewise continuous bilinear elements. Hence, in the variational problems (8.24), (8.25) and (8.26), the pressure field is approximated in the discrete space of finite elements

$$\mathrm{H}_h := \{q_h \in \mathcal{C}(\Omega_\mathrm{F} \cup \Omega_\mathrm{A}) : \ q_h = 0 \text{ on } \Gamma_\mathrm{D},\ q_h|_K \text{ bilinear in } K,\ \forall K \in \mathcal{T}_h\} \subset \mathrm{H},$$

and, analogously, in the problem (8.23) the discrete space of finite elements is

$$\mathrm{V}_h := \{q_h \in \mathcal{C}(\Omega) : \ q_h = 0 \text{ on } \Gamma_\mathrm{D},\ q_h|_K \text{ bilinear in } K,\ \forall K \in \mathcal{T}_h\} \subset \mathrm{V},$$

where H and V are defined by (8.20) and (8.22), respectively.

Then, we define the following approximate problems:

- Discrete problem associated to (8.23):
  For a fixed frequency ω, find $p_h \in \mathrm{V}_h$ such that

$$-\int_\Omega k^2 \gamma_1\gamma_2\gamma_3 p_h\bar{q}_h + \int_\Omega \frac{\gamma_2\gamma_3}{\gamma_1}\frac{\partial p_h}{\partial x_1}\frac{\partial \bar{q}_h}{\partial x_1} + \int_\Omega \frac{\gamma_1\gamma_3}{\gamma_2}\frac{\partial p_h}{\partial x_2}\frac{\partial \bar{q}_h}{\partial x_2} + \int_\Omega \frac{\gamma_1\gamma_2}{\gamma_3}\frac{\partial p_h}{\partial x_3}\frac{\partial \bar{q}_h}{\partial x_3} + \int_{\Gamma_\mathrm{P}} \frac{\omega\rho_0}{iZ} p_h \bar{q}_h = \int_{\Omega_\mathrm{F}} f\bar{q}_h, \quad (8.27)$$

for all $q_h \in \mathrm{V}_h$.

- Discrete problem associated to (8.24):
  For a fixed frequency ω*, find* $p_h \in \mathrm{H}_h$ *such that*

$$-\int_\Omega k^2\gamma_1\gamma_2\gamma_3 p_h\bar{q}_h + \int_\Omega \frac{\gamma_2\gamma_3}{\gamma_1}\frac{\partial p_h}{\partial x_1}\frac{\partial \bar{q}_h}{\partial x_1} + \int_\Omega \frac{\gamma_1\gamma_3}{\gamma_2}\frac{\partial p_h}{\partial x_2}\frac{\partial \bar{q}_h}{\partial x_2} + \int_\Omega \frac{\gamma_1\gamma_2}{\gamma_3}\frac{\partial p_h}{\partial x_3}\frac{\partial \bar{q}_h}{\partial x_3} \\ + \int_{\Gamma_\mathrm{P}} \frac{\omega\rho_0}{iZ}(p_h^+ - p_h^-)(\bar{q}_h^+ - \bar{q}_h^-) = \int_{\Omega_\mathrm{F}} f\bar{q}_h, \quad (8.28)$$

for all $q_h \in \mathrm{H}_h$.

- Discrete problem associated to (8.25):
  For a fixed frequency ω*, find* $p_h \in \mathrm{H}_h$ *such that*

$$-\int_\Omega k^2\gamma_1\gamma_2\gamma_3 p_h\bar{q}_h + \int_\Omega \frac{\gamma_2\gamma_3}{\gamma_1}\frac{\partial p_h}{\partial x_1}\frac{\partial \bar{q}_h}{\partial x_1} + \int_\Omega \frac{\gamma_1\gamma_3}{\gamma_2}\frac{\partial p_h}{\partial x_2}\frac{\partial \bar{q}_h}{\partial x_2} + \int_\Omega \frac{\gamma_1\gamma_2}{\gamma_3}\frac{\partial p_h}{\partial x_3}\frac{\partial \bar{q}_h}{\partial x_3} \\ - \int_{\Gamma_\mathrm{P}} \frac{\omega\rho_0}{Z_p\sin(k_p d)}\left((p_h^+\bar{q}_h^+ + p_h^-\bar{q}_h^-)\cos(k_p d) - (p_h^+\bar{q}_h^- + p_h^-\bar{q}_h^+)\right) = \int_{\Omega_\mathrm{F}} f\bar{q}_h, \quad (8.29)$$

for all $q_h \in \mathrm{H}_h$.

- Discrete problem associated to (8.26):
  For a fixed frequency ω*, find* $p_h \in \mathrm{H}_h$ *such that*

$$-\int_\Omega k^2\gamma_1\gamma_2\gamma_3 p_h\bar{q}_h + \int_\Omega \frac{\gamma_2\gamma_3}{\gamma_1}\frac{\partial p_h}{\partial x_1}\frac{\partial \bar{q}_h}{\partial x_1} + \int_\Omega \frac{\gamma_1\gamma_3}{\gamma_2}\frac{\partial p_h}{\partial x_2}\frac{\partial \bar{q}_h}{\partial x_2} + \int_\Omega \frac{\gamma_1\gamma_2}{\gamma_3}\frac{\partial p_h}{\partial x_3}\frac{\partial \bar{q}_h}{\partial x_3} \\ + \int_{\Gamma_\mathrm{P}} \frac{\omega\rho_0}{iZ}p_h^-\bar{q}_h^- = \int_{\Omega_\mathrm{F}} f\bar{q}_h, \quad (8.30)$$

for all $q_h \in \mathrm{H}_h$.

8.5 Numerical validation

In this section we present a validation of the numerical codes implementing the FE methods that we have described in the previous section. To perform such validation, we have chosen five problems whose exact solution are well-known, since they can reduce to one-dimensional problems.

With this purpose, we assume that the cavities containing the fluid and the PML layer is situated are $\Omega_\mathrm{F} = (-a,a)\times(-b,b)\times(-d,d)$ and $\Omega_\mathrm{A} = (-a,a)\times(-b,b)\times(-d^*,d^*)\setminus\Omega_\mathrm{F}$ respectively. The boundary $\partial(\Omega_\mathrm{F}\cup\Omega_\mathrm{A})$, is divided in three parts: $\partial(\Omega_\mathrm{F}\cup\Omega_\mathrm{A}) = \Gamma_\mathrm{D}^0\cup\Gamma_\mathrm{D}^1\cup\Gamma_\mathrm{N}$, where

$$\Gamma_\mathrm{D}^1 = \{(x_1,x_2,x_3)\in\mathbb{R}^3 : x_3 = d\},$$
$$\Gamma_\mathrm{D}^0 = \{(x_1,x_2,x_3)\in\mathbb{R}^3 : x_3 = -d^*\},$$
$$\Gamma_\mathrm{N} = \{(x_1,x_2,x_3)\in\mathbb{R}^3 : |x_1| = a \text{ or } |x_2| = b\}.$$

The panel is inside the fluid cavity on a plane centered at the origin, i.e., $\Gamma_{\mathrm{P}} = \{(x_1, x_2, x_3) \in \Omega_{\mathrm{F}} : x_3 = 0\}$. Figure 8.3 shows the vertical cut of the domain for all the tests. In all of them we have used the following geometrical data: $a = 0.5\,\mathrm{m}$, $b = 0.5\,\mathrm{m}$, $d = 0.5\,\mathrm{m}$, $d^* = 0.75\,\mathrm{m}$. In every case, we have excited the acoustic system on Γ_{D}^1 by using a non homogeneous Dirichlet condition $p = p_0$, with $p_0 = 1\ \mathrm{N/m^2}$. The physical data of the problem are $\omega = 1000\,\mathrm{rad/s}$, $c = 340\,\mathrm{m/s}$, $\rho_0 = 1\,\mathrm{m/s}$, and $\sigma = 25000\ \mathrm{Ns/m^4}$.

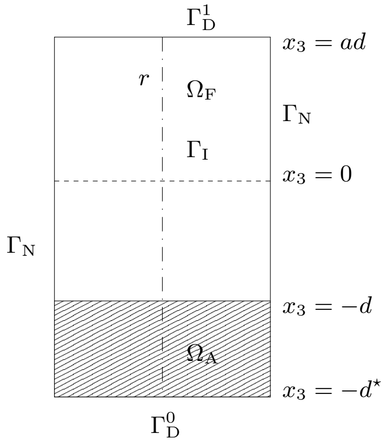

Figure 8.3: Vertical cut of the three-dimensional domain $\Omega_{\mathrm{A}} \cup \Omega_{\mathrm{F}}$.

To solve numerically all the problems, we have used two successive refinements of the mesh in Figure 8.4, which are labelled by the numbers 2 and 4, with 1440 and 11520 elements, respectively.

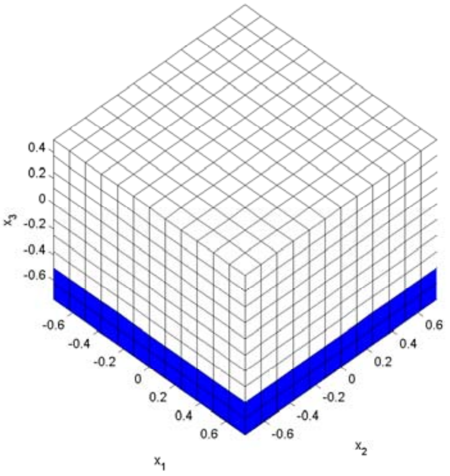

Figure 8.4: Mesh 2 used in the numerical validation problems.

Problem 1: In the first test no panel has been included. The boundary conditions for this problem are

$$
\begin{aligned}
p &= 0 && \text{on } \Gamma_{\mathrm{D}}^{0},\\
p &= p_0 && \text{on } \Gamma_{\mathrm{D}}^{1},\\
\frac{\partial p}{\partial \boldsymbol{n}} &= 0 && \text{on } \Gamma_{\mathrm{N}}.
\end{aligned}
$$

The plots of Figure 8.5 show the exact and approximate pressure fields of the problem on the line $x_1 = x_2 = 0$ (line r in Figure 8.3).

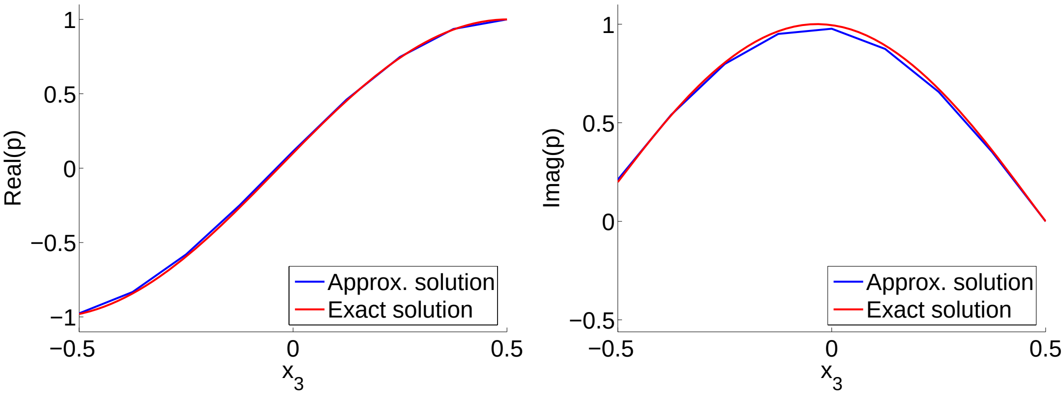

Figure 8.5: Problem without panel. Pressure field on the line r.

Problem 2: A wall impedance panel has been included on Γ_{P}. The boundary conditions for this problem are

$$
\begin{aligned}
p &= 0 && \text{on } \Gamma_{\mathrm{D}}^{0},\\
p &= p_0 && \text{on } \Gamma_{\mathrm{D}}^{1},\\
\frac{\partial p}{\partial \boldsymbol{n}} &= 0 && \text{on } \Gamma_{\mathrm{N}},\\
p^{+} &= p^{-} && \text{on } \Gamma_{\mathrm{P}},\\
p^{+} &= -i\omega Z(\boldsymbol{u}^{+}\cdot\boldsymbol{n} - \boldsymbol{u}^{-}\cdot\boldsymbol{n}) && \text{on } \Gamma_{\mathrm{P}},
\end{aligned}
$$

where we have taken $Z = 340 - i8500\,\mathrm{Ns/m^3}$. In Figure 8.6, we show the exact and approximate pressure fields for this problem on the line $x_1 = x_2 = 0$.

Problem 3: A porous veil panel has been included on Γ_{P}. In this case, The boundary

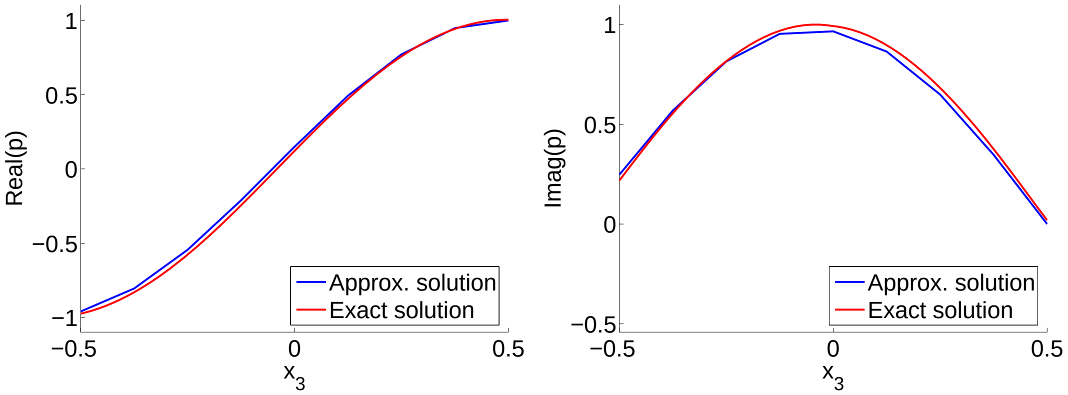

Figure 8.6: Wall impedance panel. Pressure field on the line r.

conditions are

$$\begin{aligned} p &= 0 && \text{on } \Gamma_{\mathrm{D}}^{0}, \\ p &= p_0 && \text{on } \Gamma_{\mathrm{D}}^{1}, \\ \frac{\partial p}{\partial \boldsymbol{n}} &= 0 && \text{on } \Gamma_{\mathrm{N}}, \\ \frac{\partial p^+}{\partial \boldsymbol{n}} &= \frac{\partial p^-}{\partial \boldsymbol{n}} && \text{on } \Gamma_{\mathrm{P}}, \\ p^+ - p^- = -i\omega Z \boldsymbol{u}^+ \cdot \boldsymbol{n} &= -\frac{iZ}{\omega\rho_0}\frac{\partial p^+}{\partial \boldsymbol{n}} && \text{on } \Gamma_{\mathrm{P}}. \end{aligned}$$

Now, we have considered $Z = i1000\,\mathrm{Ns/m}^3$. In Figure 8.7 we show the exact and approximate pressure fields for this problem on the line $x_1 = x_2 = 0$.

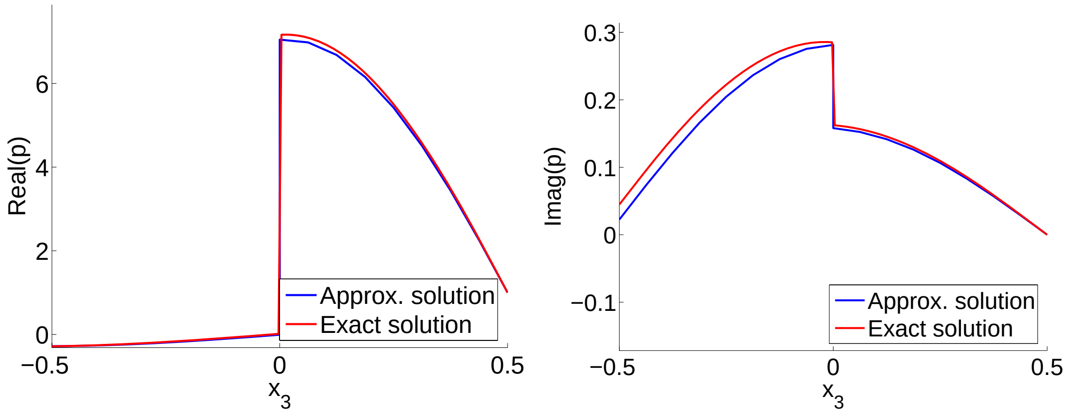

Figure 8.7: Porous veil panel. Pressure field on the line r.

Problem 4: A locally reacting porous layer has been included on Γ_{P}. The boundary conditions for this problem are

$$\begin{aligned} p &= 0 && \text{on } \Gamma_{\mathrm{D}}^{0}, \\ p &= p_0 && \text{on } \Gamma_{\mathrm{D}}^{1}, \\ \frac{\partial p}{\partial \boldsymbol{n}} &= 0 && \text{on } \Gamma_{\mathrm{N}}, \\ \frac{\partial p^+}{\partial \boldsymbol{n}} &= \frac{\omega\rho_0}{Z_p \sin(k_p d)}\left(p^+ \cos(k_p d) - p^-\right) && \text{on } \Gamma_{\mathrm{P}}, \\ \frac{\partial p^-}{\partial \boldsymbol{n}} &= -\frac{\omega\rho_0}{Z_p \sin(k_p d)}\left(p^- \cos(k_p d) - p^+\right) && \text{on } \Gamma_{\mathrm{P}}. \end{aligned}$$

In Figure 8.8 we show the exact and approximate pressure fields for this problem on the line $x_1 = x_2 = 0$.

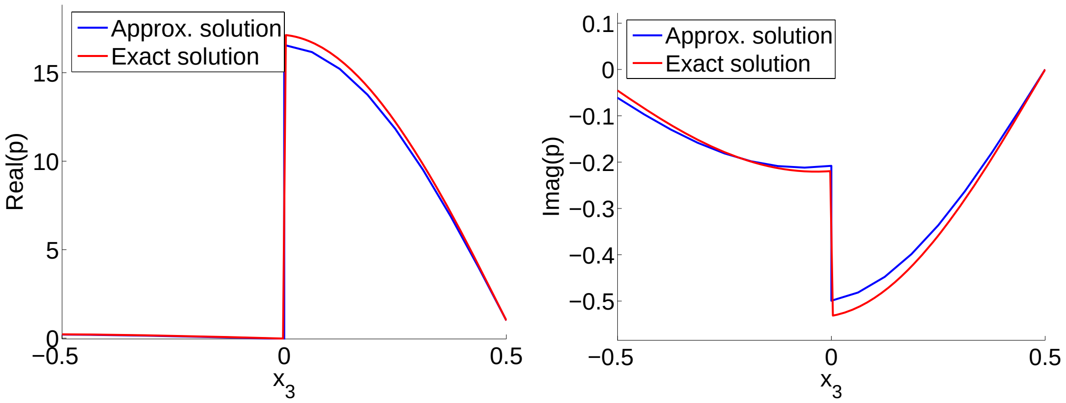

Figure 8.8: Locally reacting porous layer. Pressure field on the line r.

Problem 5: A wall impedance panel in contact with a rigid wall has been included on Γ_{P}. The boundary conditions for this problem are

$$\begin{aligned} p &= 0 && \text{on } \Gamma_{\mathrm{D}}^{0}, \\ p &= p_0 && \text{on } \Gamma_{\mathrm{D}}^{1}, \\ \frac{\partial p}{\partial \boldsymbol{n}} &= 0 && \text{on } \Gamma_{\mathrm{N}}, \\ \frac{\partial p^+}{\partial \boldsymbol{n}} &= 0 && \text{on } \Gamma_{\mathrm{P}}, \\ p^- &= \frac{iZ}{\omega\rho_0}\frac{\partial p^-}{\partial \boldsymbol{n}} && \text{on } \Gamma_{\mathrm{P}}, \end{aligned}$$

where $Z = 340 - i8500\,\mathrm{Ns/m^3}$. The corresponding pressure fields are drawn in Figure 8.9.

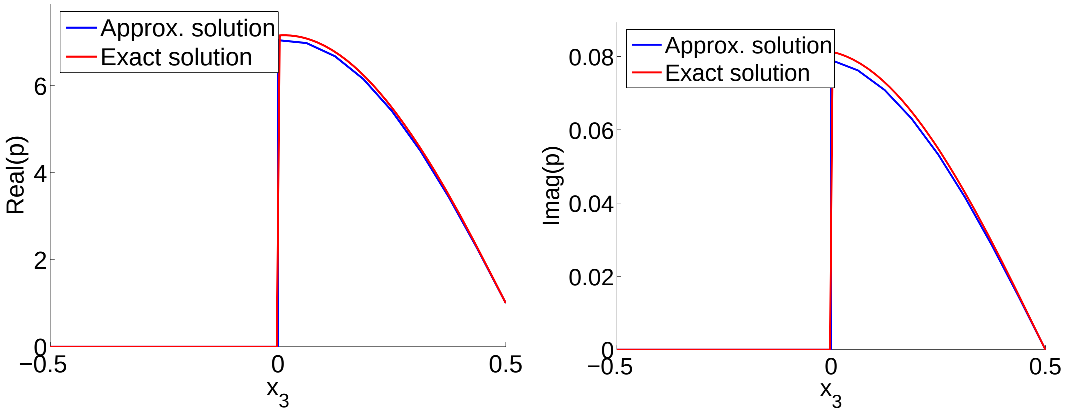

Figure 8.9: Wall impedance panel in contact with a rigid wall. Pressure field on the line r.

In Table 8.1, we show the relative errors in L^2-norm for the solution of each discrete problem. The last column in this table shows the orders of convergence, which are very close to the optimal one for all the problems.

Table 8.1: Relative errors for the numerical test examples.

	Mesh 2	Mesh 4	Order
Problem 1	0.015995	0.003694	2.081
Problem 2	0.016010	0.003696	2.081
Problem 3	0.071112	0.017137	2.037
Problem 4	0.116677	0.032372	1.898
Problem 5	0.053719	0.014156	1.948

8.6 Numerical results for an absorbing box for reducing noise in rooms

In this section we present some numerical results in a real-life experiment. We consider a box which has a micro-perforated plate in one of its faces and the rest of them are rigid. This box is filled and surrounded with a fluid of the same physical characteristics (see Figure 8.10).

Since five of the box faces are rigid, the unique boundary term in the weak formulation is that computing on Γ_P, where the micro-perforated panel is situated. Hence, the weak formulation (8.24) and consequently, its discrete formulation (8.28) remain valid.

In all the numerical results which are showed below, we have chosen the following data: the dimensions of the box are $a = b = 0.6\,\mathrm{m}$, $h = 0.15\,\mathrm{m}$, the data of the fluid are

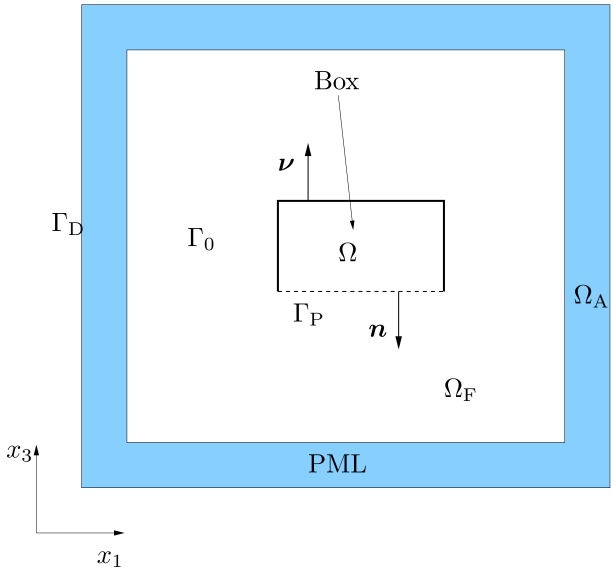

Figure 8.10: Cut of the three-dimensional domain: a rigid box with a micro-perforated plate on a face.

$c = 343\,\mathrm{m/s}$, $\rho_0 = 1\,\mathrm{kg/m^3}$. The geometrical dimensions of the PML domain and the fluid cavity which surrounds the box are the following (in meters):

$$\Omega_F = [-0.5, 0.5] \times [-0.5, 0.5] \times [-0.925, 0.925],$$
$$\Omega_A = [-0.7, 0.7] \times [-0.7, 0.7] \times [-1.125, 1.125] \setminus \Omega_F.$$

We have used a refinement of the parallelepiped meshes showed in Figure 8.11. Let us remark that the mesh is refined in the neighborhood the faces of the locally reacting panel to capture accurately the discontinuities of the pressure field.

The acoustic source that we have considered is a monopole supported at the point $\boldsymbol{a}$ =(0,0,-0.725) m and a pure complex amplitude depending linearly on the angular frequency and on the fluid density at rest, i.e., we have considered $f = i\omega\rho_0 Q\delta_{\boldsymbol{a}}$, where $Q = 1\,\mathrm{m^3/s}$ is the volume velocity of the monopole, and $\delta_{\boldsymbol{a}}$ is the Dirac's delta supported at the point $\boldsymbol{a}$.

To model the acoustic behavior of the micro-perforated plate, we have used the approximated Maa's formula (see [83]) to compute its impedance,

$$Z = \frac{1}{\phi}\left(\frac{32\eta s}{4r_0^2}\sqrt{1+\frac{x(\omega)^2}{32}} + i\omega\rho_F s\left(1+\frac{1}{\sqrt{9+\frac{x(\omega)^2}{2}}}\right)\right) \tag{8.31}$$

where $x(\omega) = r_0\sqrt{\omega\rho_0/\eta}$ being $\eta = 1.789 \times 10^{-5}\,\mathrm{kg/ms}$ the fluid viscosity, $s = 10^{-3}\,\mathrm{m}$ the thickness of the plate, $\phi = 0.1$ the rate of its perforation, and $r_0 = 4 \times 10^{-3}\,\mathrm{m}$ the radius of its holes.

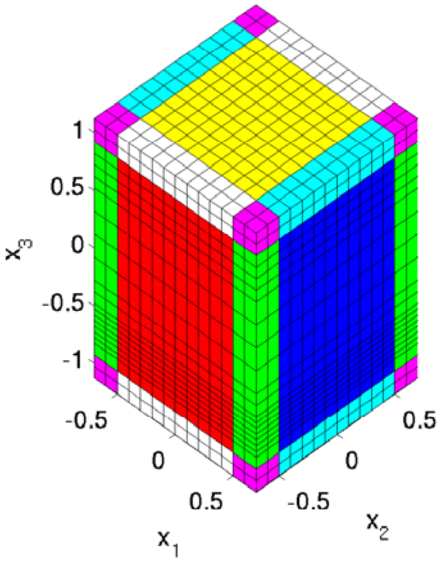

Figure 8.11: Parallelepiped mesh of the fluid and PML domains, refined in the neighborhood of the panel.

Figures 8.12, 8.13 and 8.14 show the real part (plots on the left side) and the imaginary part (plots on the right side) of the pressure field associated respectively to the angular frequencies $\omega = 800\,\mathrm{rad/s}$, $\omega = 1330\,\mathrm{rad/s}$, and $\omega = 2500\,\mathrm{rad/s}$.

In all cases, the pressure field have been plotted on the plane $x_2 = 0$. In order to avoid that the singularity of the pressure field in the support of the monopole modifies the color scale of the figures, a white circle has been drawn centered at the point (0,0,-0.725) m.

Let us remark that in each of the three examples the discontinuity of the pressure fields between the faces of the boundary, where the micro-perforated plate is situated, is small because of the scale used in the plots. In fact, in each of the numeric examples the pressure jump is close to $3\,\mathrm{N/m^2}$.

8.7 Conclusions

Different mathematical models have been considered for modelling locally reacting absorbing panels in an acoustic propagation problem in an unbounded domain. The PML technique has been used to reduce the problem to a computational bounded domain. Several different models, attending to the different coupling conditions between pressure and normal displacement on the faces of the panel, have been analyzed to write four variational problems depending on the type of locally reacting panel. Finally, the discrete coupled problems fluid/locally reacting panel have been solved by a finite element method with the PML technique. Finally a more complex real-life experiment has been solved numerically with the same code.

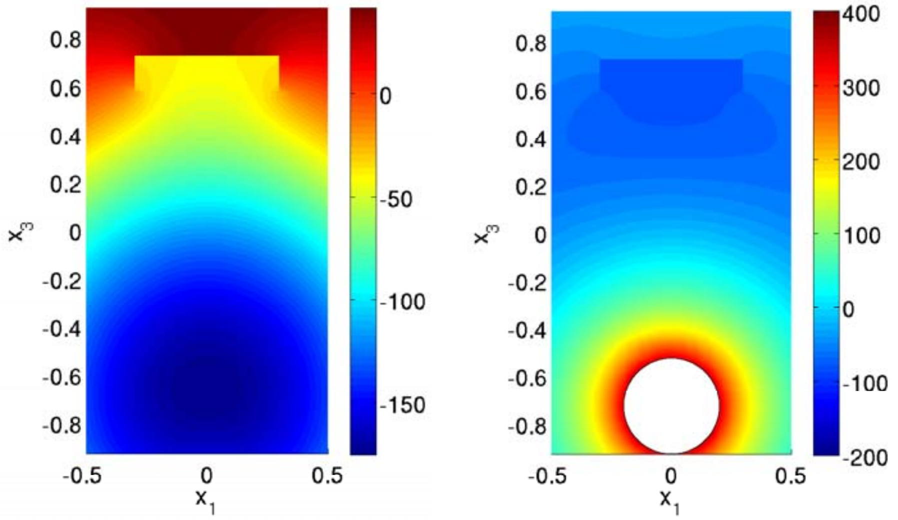

Figure 8.12: Real part (left) and imaginary part (right) of the pressure field for $\omega = 800\,\text{rad/s}$.

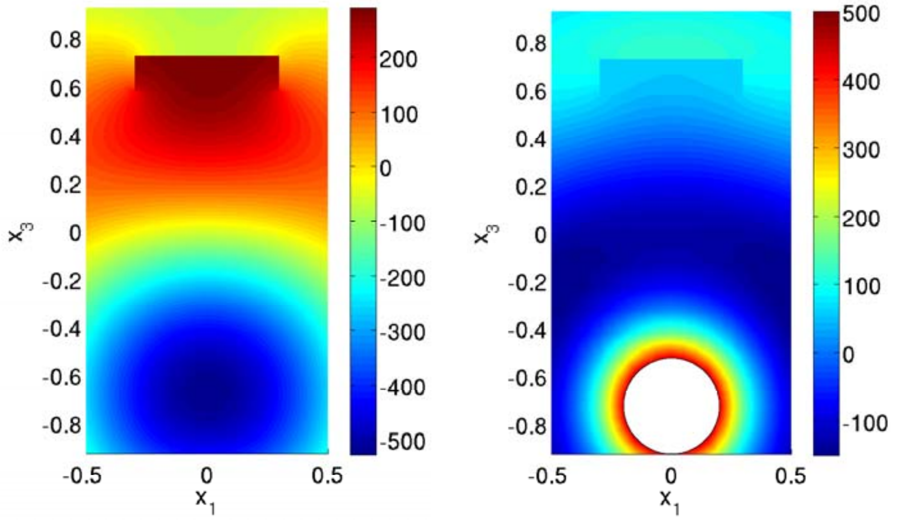

Figure 8.13: Real part (left) and imaginary part (right) of the pressure field for $\omega = 1330\,\text{rad/s}$.

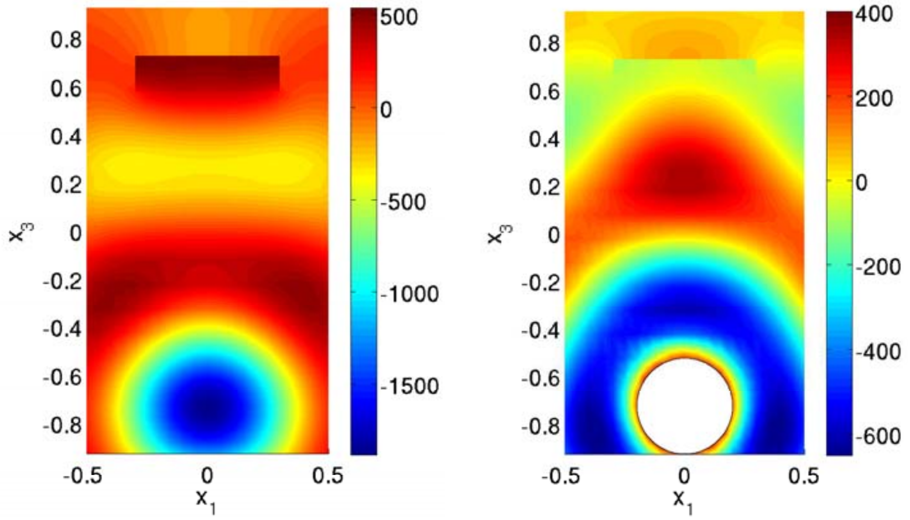

Figure 8.14: Real part (left) and imaginary part (right) of the pressure field for $\omega = 2500\,\mathrm{rad/s}$.

Further research

To finish this memory, we describe briefly some of the research lines we are starting to explore. We can divide them in two large blocks, attending to the aims of each one: the study of new dissipative models and the analysis of new aspects of the PMLs.

- The first future research line is devoted to the analysis of new models for the dissipative materials. More precisely, we have started to study new models for new dissipative panels *Micro-perforated panels* (MPP).

  In the literature, this kind of panels is modelled by the Maa's equations (see [83]), which give a semi-empirical expression for the input impedance of the panel. However, this model is not completely satisfactory from a mathematical point of view, since it is a local reacting model and, moreover, in the simplest plane wave analysis, the equations do not take into account the angle of incidence of the waves.

  The first stage of this research line is currently being done. From a numerical point of view, a preliminary approach by using a finite element method (based on the Raviart-Thomas elements described in Chapter 2) is being used to validate the Maa's equations in a periodic micro-perforated panel when the angle of incidence of the plane waves is not null. At the same time, in order to fix the Maa's model drawbacks, a derivation of a new system of equations is being done by using homogenization techniques.

  In the context of the comparison of local and extended reacting models, there are also some forthcoming open problems. For instance, in the validation of models presented in Chapter 7, the implementation of models without axisymmetric assumptions, and the study of the accuracy of both models in relation with the length-wave and the size of the obstacle should be done.

  Finally, we have always kept through this dissertation, the hypothesis of time-harmonic motions related with porous models. Obviously, the mathematical study of the models in the time domain, and their forthcoming implementation in a computer code, are also challenging future objectives. In particular, to derive a time domain model associated to Allard-Champoux model, which seems to require the introduction of time derivatives of fractional order.

- The second block of open problems arises around the Perfectly Matched Layer technique.

  Among the technical issues in the context of the time-harmonic problems, we distinguish the proof of error estimates for the discrete finite solution. This kind of estimates have an inherent difficulty, since they involve the non-standard weighted Sobolev spaces presented in Chapter 5.

  We can also mention some future computational challenges such as fluid/structure problems stated in unbounded domains, where the elastic solid and the coupling interfaces between fluid and solid domains are unbounded and, so, they have to be truncated by the PML domain. The implementation of this problem in a computer code is currently being done and some preliminar results have been presented in [34].

  Moreover, through this dissertation, every finite element implementation use a quadrilateral (or parallelepipedic) partition in the PML domain (in Cartesian, polar or spherical coordinates). Other open problem consists of studying if the finite element implementation with triangular meshes and numerical integration using a non-integrable absorbing function is so accurate as those with quadrilaterals.

  On the other hand, in the context of the study of the PML technique there are several open problems that could be tackled in the framework of the time domain. Problems so basic as energy estimates for the time domain PML equations (even for classical choices of the bounded absorbing functions) remain open for non constant absorbing functions. Moreover, some numerical aspects of the stability of finite difference schemes starts to be well understood only recently (see for instance [20]).

  Obviously, the mathematical analysis of the PML technique in the time domain using the non-integrable absorbing function is also a future line of work in order to asses the performance of this strategy to deal with the scattering problems in the time domain as well as in the frequency domain.

  The preliminary studies about the existence and uniqueness of solution for the coupled fluid/PML problem with the singular absorbing function, its time domain implementation, by a finite difference scheme, and the numerical comparison between the classical choices and the singular absorbing function, are by now in progress (see [19]), in a work jointly with Eliane Bécache, researcher of the Poems team at INRIA (*Institut National de Recherche en Informatique et Automatique*).

  In this context, the first results show that the exact solution of the time domain scattering problem is recovered by using the non-integrable absorbing function. The existence and uniqueness is also proved by using the retarding potential technique and the Fourier-Laplace transform. Moreover, the time domain implementation is also standard and it does not require any extra computational cost to obtain better numerical results than the classical PML technique with bounded absorbing functions.

Acknowledgments

I would like to thank my advisors, Prof. Alfredo Bermúdez de Castro, Prof. Luis María Hervella Nieto, and Prof. Rodolfo Rodríguez for their work and support during these years. I would also like to acknowledge Prof. José Luis Ferrín for his help in my first steps on porous media, to Prof. Rodolfo Rodríguez for his huge work, support and, hospitality during my two stages in Chile, and to Prof. Eliane Bécache for her friendly and deeper sight on PMLs during my two stages at INRIA.

The first part of this work was partially supported by Ministerio de Ciencia y Tecnología (Spain) through project No. DPI2001-1613-C02-02 and Xunta de Galicia project No. PGIDT02PXIC20701PN. For obtaining the numerical results, a Compaq HPC 320 computer from CESGA (Centro de Supercomputación de Galicia) has been used. The second and third part of this work was partially supported by Ministerio de Ciencia y Tecnología (Spain) through project No. DPI2001-1613-C02-02 and No. DPI2004-05504-C02-02, and Xunta de Galicia project No. PGIDIT05PXIC20705PN. Futhermore, during these years I have been funded by Ministerio de Ciencia y Tecnología (Spain) through grant No. AP2003-1092.

Resumo en galego

Os métodos numéricos están a adquirir un papel cada vez máis importante como ferramenta para reducir os tempos e custos no deseño e desenvolvemento de produtos en moitos dos ámbitos da enxeñaría (aeronáutica, mecánica, naval, telecomunicacións, etc.). Neste sentido a rápida evolución dos computadores non é suficiente en todos os casos para resolver de xeito eficiente e en tempos razonables problemas da enxeñaría con interese práctico e polo tanto ten que ser complementado con algoritmos e métodos de resolución numéricos eficientes.

Un dos problemas que cobra maior importancia social é a reducción da contaminación acústica producida por coches, avións, sistemas de aires acondicionados etc, como queda reflexado nas lexislacións autonómicas, estatais e europeas cada vez máis esixentes. Neste contexto, xurde a necesidade de resolver problemas de propagación acústica cada vez máis complexos que non poden ser resoltos por técnicas baseadas en métodos matemáticos clásicos. Por suposto, as probas sobre prototipos son fundamentais para asegurarse do bon funcionamento das tecnoloxías propostas. Sen embargo, o alto custo da fabricación de prototipos, fai necesario que estas probas se realicen nunha etapa xa avanzada do deseño, cunha proposta próxima á solución final. Estes dous factores fan que a acústica computacional se convirta nunha disciplina cada vez de maior importancia e que a simulación numérica sexa unha técnica determinante para realizar análises e deseños de sistemas acústicamente confortabeis en tempos e con custos competitivos.

A riqueza matemática dos problemas relacionados coa acústica orixina que os modelos numéricos que se deben utilizar na súa resolución abrangan un espectro moi amplo, requerindo a utilización de moitas das técnicas máis avanzadas da computación numérica actual. Entre estes modelos debemos destacar a ecuación de Helmholtz, como a ecuación fundamental que modela a propagación harmónica das ondas acústicas no dominio da frecuencia. Ademais, todos estes modelos poden aplicarse a problemas en dominios limitados, o que non involucra novas dificultades, pero tamén en dominios non limitados. Esta última posibilidade é moi frecuente en acústica e esixe técnicas específicas de resolución.

Como xa adiantamos, a complexidade destes modelos matemáticos demandan a súa resolución mediante métodos numéricos, como, por exemplo, o método de elementos finitos. Cando se presentan dominios non limitados, estes métodos teñen que ser complementados con condicións de non reflexión como, por exemplo, as técnicas de capas absorbentes perfectamente adaptadas, ou, seguindo o seu acrónimo inglés, PML (*Perfecty Matched Layers*).

O traballo presentado ao longo da tese enmarcase no dominio da frecuencia, é dicir, baixo a hipótese de dependencia harmónica da variable do tempo. De feito, a nosa atención centrarase en problemas de propagación acústica no réxime de baixas frecuencias, no que a discretización mediante un método de elementos finitos é ainda viable e non costosa, dende un punto de vista computacional. De feito, todos os métodos propostos para a resolución numérica dos problemas de propagación acústica ao longo da tese, teñen en común o uso dos elementos finitos.

Pódense distinguir tres parte ben diferenciadas ainda que cunha temática común: o estudio de problemas de propagación acústica tanto en dominios limitados como non limitados que involucran materias disipativos. Nuns casos a materia de estudio serán o comportamento acústico dos materias porosos, mentras que noutros, ditos materiais usaranse como ferramenta numérica para tentar resolver outros problemas, como pode ser o truncamento de dominios computacionais non limitados. Na primeira parte, centramos a nosa atención no cálculo das frecuencias de resonancia e da resposta en frecuencia de materias porosos acoplados a fluidos acústicos en recintos limitados. Mentras a segunda parte adícase á análise matemática e numérica da técnica das PML , a cal tamén pode ser considerado como un caso especial de medio disipativo. Finalmente, a última parte deste traballo mostra algunas aplicacións computacionais que involucran medios porosos e que usan a técnica das PML para truncar o dominio non limitado que involucra o problema de propagación acústica. Vexamos cada unha das partes máis polo miudo.

A primeira parte MATERIAIS POROSOS está dedicada ao estudio da propagación acústica en réxime harmónico a través de materiais porosos. Esta clase de materiais é amplamente usada en diferentes aplicacións do control pasivo do ruido. Estes materiais son ben coñecidos pola súa habilidade para disipar as ondas acústicas. Polo tanto, dende un punto de vista acústico, os materiais porosos posuen vantaxes relevantes fronte a outra clase de materiais xa que son lixeiros e absorbentes ao mesmo tempo, dúas características que os convirten en fundamentais nas aplicacións acústicas á vida real. Esta primeira parte ten dous obxectivos fundamentais. Por unha parte, facer unha revisión dos modelos de medios porosos atendendo ás características físicas dos materias, xa sexan de parte sólida ríxida ou elástica, remarcando a diferencia entre os modelos clásicos e aqueles que apareceron recentemente, obtidos mediante as técnicas de homoxeneización. Por outra parte, a nosa atención tamén se centra na resolución numérica dalgún destes modelos, proporcionando ferramentas numéricas capaces de calcular as frecuencias de resonancia e a resposta en frecuencia de sistemas acústicos que involucran a estes materias porosos. A primeira parte da tese está organizada como segue:

Capítulo 1. Modelos para medio porosos. Ao longo deste capítulo se consideran diferentes modelos cos que describir o movemento no interior de un medio poroso. A principal diferencia entre todos estes modelos radica na suposición feita sobre a parte solida do esquelete dos materiais. Primeiro, os modelos de Darcy e de Allard-Champoux son descritos como o máis simple e o máis amplamente empregado en canto a medios poroso con parte sólida ríxida se refire. Despois, faise unha revisión exhaustiva dos modelos de medio porosos con parte sólida elástica. Esta revisión se comeza presentando o modelo clásico de Biot e logo se describe unha colección de modelos obtidos mediante técnicas de homoxeneización atendendo ás diferentes xeometrías que poden ter os poros do material, xa sexan de poros abertos (parte fluida conexa) ou poros pechados (parte fluida aillada), ou ben se se tratan de modelos disipativos ou non disipativos. Neste últimos casos, faise unha breve exposición de cal é o procedemento de obtención de ditos modelos macroscopicos e de cales son os problemas, enunciados sobre a parte fluida e sólida de un único poro do mateiral, que definen os coeficientes que aparecen nas ecuacións do movemento macroscópico.

Capítulo 2. Resolución numérica mediante un método de elementos finitos da propagación acústica en medios porosos con parte sólida ríxida. Este capítulo se enfrenta co comportamento acústico dun material poroso de matriz sólida ríxida. Primeiro se enuncia o problema de propagación no dominio da frecuencia tendo en conta os modelos de Darcy e de Allard-Champoux que governan o movemento no interior do medio poroso, no que se usa o campo de desplazamentos como a incógnita do problema a determinar. Para o caso do modelo de Darcy, estúdiase de forma analítica os autovalores sobreamortiguados (frecuencias de resonancia complexas puras) no caso dun problema acoplado fluido/medio poroso no interior dunha cavidade rectangular limitada. Como ferramenta numérica, implementouse un método de elementos finitos para calcular a resposta do sistema acústico a unha excitación harmónica e tamén para calcular as vibracións libres dun sistema multicapa tridimensional formado por un fluido acústico e un material poroso acoplados. O elemento finito usado é o elemento de cara de orde máis baixo introducido por Raviart e Thomas, o cal elimina os modos espureos de circulación que non teñen significado físico e no que os graos de liberdade son os desplazamentos normais a cada unha das caras dos tetraedros que forman a malla de discretización. Os resultados numéricos mostran que o método de elementos finitos permítenos calcular a curva de resposta en frecuencia do sistema acoplado fluido/medio poroso e os autovalores complexos do sistema acústico. Tamén se pode apreciar que algúns destes autovalores posuen unha pequena parte imaxinaria mentras que outros son sobreamortiguados. Parte destes resultados contidos neste capítulo foron presentados en [27].

Capítulo 3. Resolución numérica mediante un método de elementos finitos dun novo modelo desplazamento/presión de medios poroelásticos. O comportamento acústico de materiais porosos con un esquelete sólido elástico é tido en conta neste capítulo. Primeiro, centramos a nosa atención nun novo modelo en particular que emprega un único campo de desplazamento e presións como incógnitas que aparecen nas ecuacións en derivadas parcias que describen o movemento no interior do material poroso non disipativo e que posue poros abertos. Se supoñemos unha estructura periódica no material entón podemos calcular os coeficientes no modelo usando técnicas de homoxeneización que requiren resolver problemas na celda unidade coa que se construe cada un dos poros que forman o medio poroso. Despois proponse un método de elementos finitos para calcular a resposta a unha excitación harmónica nunha cavidade tridimensional limitada que contén a un fluido acústico acoplado cun medio poroelástico. O elemento usado para o fluido é o elemento de cara de orde máis baixo introducido por Raviart e Thomas, o cal elimina os modos espureos de circulación que non teñen significado físico e no que os graos de liberdade son os desplazamentos normais a cada unha das caras dos tetraedros que forman a malla de discretización. Mentras, o elemento finito usado para o desplazamento no medio poroso é denominado “mini elemento”, no que os graos de liberdade son ademais dos desplazamentos en cada vértice dos tetraedros da malla, un novo grao de liberdade que depende dunha función burbulla asociada a cada tetraedro. Este tipo de elementos é usado para garantir a estabilidade numérica do método. O resultados numéricos mostran a orde óptima de converxencia e a capacidade da ferramenta numérica para calcular a resposta en frecuencia do sistema acústico. Parte destes resultados contidos neste capítulo foron presentados en [28].

A segunda parte da tese CAPAS PERFECTAMENTE ADAPTADAS está dedicada ao estudio da técnica das PML (*Perfectly Matched Layers*). Primeiro introdúcense as ecuacións en derivadas parcias que definen o seu comportamento como orixinalmente fixo Berenger en [22] empregando o argumento da separación artificial das variables do problema (tamén coñecido como “splitting”) para despois darlle unha interpretación física como medio disipativo que non produce reflexións espureas ao acoplarse cun fluido acústico. De feito a técnica das PML é ferramenta numérica que se usa ao longo deste traballo para truncar a dominio computacional dos problemas de dispersión acústica enunciados sobre dominios non limitados. Esta técnica permite reducir o dominio de ditos problemas sen perturbar demasiado a solución do problema orixinal. Sen embargo, o estudio das PML non se reduce á simple utilización da técnica senon que ao longo desta parte da tese se propón unha modificación que optimiza os resultados numéricos acadados nos problemas discretizados. Máis precisamente, ata o de agora para construir as capas PML usábase unha función absorbente limitada,que ainda que teoricamente adecuados, non producía un resultados numéricos óptimos nos problemas discretizados. Ao longo desta parte ademais de presentar esta técnica, se analizan dende un punto de vista teórico e numérico a solución destes inconvintes empregando unha función absorbente non integrable. A segunda parte da tese está organizada como segue:

Capítulo 4: Un material poroso non reflectante: as capas perfectamente adaptadas (PML). Neste capítulo introdúcese a técnica das capas perfectamente adaptadas, primeiro, como un remedio que modifica o comportamento das ecuacións do modelo de Darcy para medios porosos ríxidos e que convirte o material disipativo nun medio que non xenera reflexións espureas e artificiais cando se acopla cun fluido acústico. De feito, se escribimos as ecuacións da PML en función do desplazamento pódese interpretar a PML como un matetial viscoelástico con memoria longa. A continuación se enuncia cales son as ecuacións en derivadas parciais do modelo no caso tridimensional e usando coordenadas cartesianas. O que é máis, tamén se fai unha analise preliminar nunha dimensión para ilustrar as vantaxes de usar unha función absorbente singular (non integrable) en vez de escoller unha función limitada, como pode ser a elección clásica dunha función cuadrática.

Capítulo 5: Unha PML exacta e limitada en coordenadas radiais. O obxectivo deste capítulo é introducir unha capa perfectamente adaptada (PML) cun espesor limitado e ao mesmo tempo "exacta" para a ecuación escalar de Helmholtz. Esta PML está basada no uso dunha función absorbente non integrable. A "exactitude" debe ser entendida no sentido de que esta técnica permite recuperar a solución do problema harmónico de dispersión acústica en dominios non limitados. A pesar da singularidade da función absorbente, o problema acoplado fluido/PML está ben posto cando a solución se busca no adecuado espacio de Sobolev con pesos non standar. A existencia e unicidade de solución do problema acoplado fluido/PML é demostrada para o caso das PML definidas en coordenadas radiais. Posto que o problema variacional asociado non é de Fredholm, os pasos a seguir na demostración centranse na representación dun novo operador Dirichet-to-Neumman asociado á capa PML e máis á posibilidade de definir dito operador mediante unha representación en serie do operador cando a función é suficientemente regular. Por último, a formulación variacional resultante pode ser manexada numéricamente mediante unha discretización por elementos finitos standar. A alta precisión de está técnica é demostrada numéricamente cando se compara coa técnica PML clásica. Parte destes resultados contidos neste capítulo foron presentados en [32] e [33].

Capítulo 6: Unha PML óptima en coordenadas cartesianas. Introducimos en coordenadas cartesianas unha técnica de capas perfectamente adaptadas (PML) óptima e cun espesor limitado escollendo como función absorbente unha función de integral non limitada. Con esta escolla, as reflexións espúreas son evitadas, a pesar de que o espesor da capa é finita. Ademais probamos que tal elección é sinxela de implementar usando un método de elementos finitos. O escoller unha función absorbente singular permítenos evitar a dependencia de parámetros que as funcións absorbentes limitadas teñen respecto da xeometría ou dos datos físicos no problema discretizado. Por último, a eficiencia e a precisión desta técnica PML son ilustradas mediante algúns exemplos numéricos. Parte destes resultados contidos neste capítulo foron presentados en [30].

Na terceira parte Aplicacións computacionais na acústica de medios disipativos, preséntanse algunas aplicacións numéricas da técnica das PML e dos modelos de medios porosos que foron estudiados nas dúas primeiras partes. Primeiro, comparamos dous modelos diferentes que tratan de modelar medios disipativos: o modelo de Allard-Champoux, que se pode entender como un medio de reacción extensa (entendendo que o campo de presión nun punto espacial depende dos valores da presión que hai ao seu redor) e o modelo de impedancia de parede que se clasifica como un modelo de reacción local (xa que a presión na impedancia de parede depende unicamente do que ocorre nese punto espacial concreto). Os dous modelos son comparados en varios problemas de dispersión acústica enunciados en dominios non limitados. Despois, o cálculo do coeficiente de absorción é analizado para os modelos de medios porosos de parte sólida ríxida e para diferentes tipos de paneis de reacción local. En todos os casos, lévase a cabo unha análise preliminar con ondas planas e, ademais, a técnica das PML é usada para truncar o dominio computacional de interese físico en todos os problemas. A terceira parte da tese está organizada como segue:

Capítulo 7: Validación de dous modelos acústicos de medios disipativos. O obxectivo deste capítulo é o estudio no dominio da frecuencia dos problemas de propagación acústica que involucran un sistema acoplado fluido/medio poroso. Nos consideramos dous modelos diferentes para o tratamento dos materiais porosos: o modelo de Allard-Champoux e un modelo aproximado basado no condición de impedancia de parede. Ambolos dous modelos son comparados calculando analiticamente as súas respectivas solucións en tres problemas nos que as xeometrías son planas, considerando sucesivamente ondas planas con incidencia normal e oblicúa e, por outra, banda ondas esféricas. Un método numérico que combina a técnica óptima das capas perfectamente adaptadas (PML), que usan unha función de absorción singular, cun método de elementos finitos é tamén presentado para calcular as solucións de problemas que empregan os dous modelos no caso máis xeral das xeometrías axisimétricas. Este método é usado para comparar as solucións do campo de presións para unha estructura esférica absorbente. Parte destes resultados contidos neste capítulo foron presentados en [31].

Capítulo 8: Simulación numérica de paneis de reacción local. Como unha alternativa aos modelos de medios porosos presentados na primeira parte da tese, nos que a propagación acústica viña determinada por diferentes ecuacións en derivadas parciais en dominios que podían ter pequenas dimensións e que conlevarían difilcultades computacionais na discretización dos problemas, preséntanse outro tipo de modelos baixo a simplificación de consideralos de reacción local. Máis precisamente, introdúcense catro condicións de contorno: a impedancia de parede, o velo poroso, unha panel poroso de reacción local e unha multicapa de reacción local en contacto cunha parede ríxida, coas que se escriben canda seu problema variacional enunciado nun dominio non limitado recheo dun fluido acústico. Como en capítulos previos, úsase un método de elementos finitos combinado coa técnica das capas perfectamente adaptadas (PML) en coordenadas cartesianas para calcular o campo de presións en problemas tridimensionais nunha batería de problemas test onde a solución exacta coecida. Por último, unha vez validado o programa, móstranse algúns resultados numéricos nun exemplo máis realista. Parte destes resultados contidos neste capítulo foron presentados no informe técnico [29].

Agradecementos.
A primeira parte deste traballo foi finaciada parcialmente polo Ministerio de Ciencia y Tecnología (Spain) a través do proxecto DPI2001-1613-C02-02 e polo proxecto da Xunta de Galicia PGIDT02PXIC20701PN. Para obter os resultados numéricos desta parte usouse o ordenador Compaq HPC 320 do CESGA (Centro de Supercomputación de Galicia). A redacción da segunda e a terceira parte deste traballo foi parcialmente financiada polo Ministerio de Ciencia y Tecnología (Spain) a través dos proxectos DPI2001-1613-C02-02 e DPI2004-05504-C02-02, e polo proxecto da Xunta de Galicia PGIDIT05PXIC20705PN.

Ademais, durante os últimos anos de estudante de doutorado estiven financiado polo Ministerio de Ciencia y Tecnología (Spain) a través da bolsa predoutoral de Formación de Profesorado Universitario AP2003-1092.

Bibliography

[1] S. Abarbanel, D. Gottlieb, and J. S. Hesthaven. Well-posed perfectly matched layers for advective acoustics. *J. Comp. Phys.*, 154(2):266–283, 1999.

[2] M. Abramowitz and I. A. Stegun. *Handbook of Mathematical Functions, With Formulas, Graphs, and Mathematical Tables.* Dover Publications, Inc., 1965.

[3] J.-F. Allard. *Propagation of sound in porous media: modelling sound absorbing materials.* Elsevier, New York, 1993.

[4] J.-F. Allard, A. Aknine, and C. Depollier. Acoustical properties of partially reticulated foams with high and medium flow resistance. *J. Acoust. Soc. Am.*, 79:1734–1740, 1986.

[5] J.-F. Allard and Y. Champoux. New empirical equations for sound propagation in rigid frame fibrous materials. *J. Acoust. Soc. Am.*, 91:3346–3353, 1992.

[6] J.-F. Allard, C. Depollier, J. Nicolas, W. Lauriks, and A. Cops. Propiétés acoustiques des matériaux poreux saturés d'air et théorie de Biot. *J. Acoust.*, 3:29–38, 1990.

[7] Y. Arnaoudov, G. Dassios, and V. Kostopoulos. The soft and the hard coated sphere within a point source wave field. *J. Acoust. Soc. Am.*, 104:1929–1942, 1998.

[8] D. N. Arnold, F. Brezzi, and M. Fortin. A stable finite element method for the Stokes equations. *Calcolo*, 21:337–344, 1984.

[9] R. J. Astley. Infinite elements for wave problems: A review of current formulations and an assessment of accuracy. *Int. J. Numer. Methods Eng.*, 49:951–976, 2000.

[10] S. Asvadurov, V. Druskin, M. N. Guddati, and L. Knizhnerman. On optimal finite-difference approximation of PML. *SIAM J. Numer. Anal.*, 41(1):287–305.

[11] N. Atalla, R. Panneton, and P. Debergue. A mixed displacement pressure formulation for poroelastic materials. *J. Acoust. Soc. Am.*, 104(3):1444–1452, 1998.

[12] K. Attenborough. Acoustical characteristics of porous materials. *Physics Reports*, 82(3):179–227, 1982.

[13] K. Attenborough. Acoustical characteristics of rigid fibrous absorbents and granular materials. *J. Acoust. Soc. Am.*, 73(3):785–799, 1983.

[14] U. Basu and A. K. Chopra. Perfectly matched layers for time-harmonic elastodynamics of unbounded domains: theory and finite-element implementation. *Comput. Methods Appl. Mech. Engrg.*, 192(11):1337–1375, 2003.

[15] A. Bayliss and E. Turkel. Radiation boundary conditions for wave-like equations. *Comm. Pure Appl. Math.*, 33:707–725, 1980.

[16] E. Bécache, A.-S. Bonnet-Benn Dhia, and G. Legendre. Perfectly matched layers for the convected Helmholtz equation. *SIAM J. Numer. Anal.*, 42(1):409–433.

[17] E. Bécache, A.-S. Bonnet-Benn Dhia, and G. Legendre. Perfectly matched layers for time-harmonic acoustics in the presence of a uniform flow. *SIAM J. Numer. Anal.*, 44(3):1191–1217.

[18] E. Bécache and P. Joly. On the analysis of Berenger's perfectly matched layers for Maxwell's equations. *M2AN Math. Model. Numer. Anal.*, 36(1):87–119, 2002.

[19] E. Bécache and A. Prieto. Exact perfectly matched layers of bounded thickness in the time domain. 2007. In preparation.

[20] E. Bécache and A. Prieto. Some remarks on stability of cartesian perfectly matched layers. 2007. In preparation.

[21] L. L. Beranek and I. L. Vér. *Noise and Vibration Control Engineering: Principles and Applications.* Wiley-Interscience, 1992.

[22] J. P. Berenger. A perfectly matched layer for the absortion of electromagnetics waves. *J. Comp. Phys.*, 114(1):185–200, 1994.

[23] J. P. Berenger. Perfectly matched layer for the FDTD solution of wave-structureinteraction problems. *IEEE Trans. Antennas Propag.*, 44(1):110–117, 1996.

[24] J. P. Berenger. Three-dimensional perfectly matched layer for the absorption of electromagnetic waves. *J. Comput. Phys.*, 127(2):363–379, 1996.

[25] A. Bermúdez. *Continuum Thermomechanics.* Birkhäuser, 2005.

[26] A. Bermúdez, R. Durán, M. A. Muschietti, R. Rodríguez, and J. Solomin. Finite element vibration analysis of fluid-solid systems without spurious modes. *SIAM J. Numer. Anal.*, 32(4):1280–1295, 1995.

[27] A. Bermúdez, J. L. Ferrín, and A. Prieto. A finite element solution of acoustic propagation in rigid porous media. *Int. J. Numer. Meth. Engng.*, 62(10):1295–1314, 2005.

[28] A. Bermúdez, J. L. Ferrín, and A. Prieto. Finite element solution of new displacement/pressure poroelastic models in acoustics. *Comput. Methods Appl. Mech. Engrg.*, 195(17-18):1914–1932, 2006.

[29] A. Bermúdez, L. Hervella-Nieto, and A. Prieto. Simulación numérica del coeficiente de absorción de un medio poroso. Technical report, 2005. Project DPI2001-1613-C02-01.

[30] A. Bermúdez, L. Hervella-Nieto, A. Prieto, and R. Rodríguez. An optimal perfectly matched layer with unbounded absorbing function for time-harmonic acoustic scattering problems. *J. Comput. Phys.* To appear.

[31] A. Bermúdez, L. Hervella-Nieto, A. Prieto, and R. Rodríguez. Validation of acoustic models for time harmonic dissipative scattering problems. *J. Comput. Acous.* To appear.

[32] A. Bermúdez, L. Hervella-Nieto, A. Prieto, and R. Rodríguez. An exact bounded PML for the Helmholtz equation. *C. R. Math. Acad. Sci. Paris*, 339(11):803–808, 2004.

[33] A. Bermúdez, L. Hervella-Nieto, A. Prieto, and R. Rodríguez. An exact bounded perfectly matched layer for time-harmonic scattering problems. 2006. Submmited.

[34] A. Bermúdez, L. Hervella-Nieto, A. Prieto, and R. Rodríguez. Numerical simulation of unbounded elastoacoustic problems applying the optimal PML technique. In *Conference on the Mathematics of Finite Elements and Applications. Book of abstracts*, pages 29–30, 2006.

[35] A. Bermúdez, L. Hervella-Nieto, and R. Rodríguez. Finite element computation of three-dimensional elastoacoustic vibrations. *J. Sound Vibration*, 219(2):279–306, 1999.

[36] A. Bermúdez, L. Hervella-Nieto, and R. Rodríguez. Finite element computation of the vibrations of a plate-fluid system with interface damping. *Comput. Methods Appl. Mech. Engrg*, 190:3021–3038, 2001.

[37] A. Bermúdez and R. Rodríguez. Finite element computation of the vibration modes of a fluid-solid system. *Comput. Methods Appl. Mech. Engrg.*, 119(3-4):355–370, 1994.

[38] M. A. Biot. Theory of propagation of elastic waves in a fluid-saturated porous solid. I. Low-frequency range. *J. Acoust. Soc. Am.*, 28:168–178, 1956.

[39] M. A. Biot. Theory of propagation of elastic waves in a fluid-saturated porous solid. II. Higher frequency range. *J. Acoust. Soc. Am.*, 28:179–191, 1956.

[40] M. A. Biot and D. G. Willis. The elastic coefficients of the theory of consolidation. *J. Appl. Mech.*, 24:594–601, 1957.

[41] M. Born and E. Wolf. *Principles of Optics.* Pergamon Press, 1980.

[42] R. N. Bracewell. The Fourier transform and its applications. 2000.

[43] L. M. Brekhovskikh and O. Godin. *Acoustics of Layered Media I: Plane and Quasi-Plane Waves.* Springer, 1999.

[44] H. Brezis. *Analyse fonctionnelle. Theorie et Applications.* Mason, 1983.

[45] Y. Champoux and M. R. Stinson. On acoustical models for sound propagation in rigid frame porous materials and the influence of shape factors. *J. Acoust. Soc. Am.*, 92:1120–1131, 1992.

[46] Z. Chen and X. Liu. An adaptive perfectly matched layer technique for time-harmonic scattering problems. *SIAM J. Numer. Anal.*, 43(2):645–671.

[47] W. C. Chew and W. H. Weedon. A 3D perfectly matched medium from modified Maxwell's equations with stretched coordinates. *IEEE Microwave Opt. Technol. Lett.*, 7(13):599–604, 1994.

[48] T. Clopeau and A. Mikelić. Nonstationary flows with viscous heating effects. In *Élasticité, viscoélasticité et contrôle optimal (Lyon, 1995)*, pages 55–63 (electronic). Soc. Math. Appl. Indust., Paris, 1997.

[49] Th. Clopeau, J. L. Ferrín, R. P. Gilbert, and A. Mikelić. Homogenizing the acoustic properties of the seabed. Part II. *Math. Comput. Modelling*, 33(8-9):821–841, 2001.

[50] Th. Clopeau, J. L. Ferrín, and A. Mikelić. Derivation of the diphasic Biot's law for an elastic solid matrix containing isolated fluid drops. In *Multiscale problems in science and technology (Dubrovnik, 2000)*, pages 151–160. Springer, Berlin, 2002.

[51] F. Collino and P. Monk. Optimizing the perfectly matched layer. *Comput. Methods Appl. Mech. Engrg.*, 164(1):157–171, 1998.

[52] F. Collino and P. Monk. The Perfectly Matched Layer in Curvilinear Coordinates. *SIAM J. Sci. Comput.*, 19(6):2061–2090, 1998.

[53] F. Collino and C. Tsogka. Application of the PML absorbing layer model to the linear elastodynamic problem in anisotropic heterogeneous media. *Geophysics*, 66(1):294–307, 2001.

[54] D. Colton and R. Kress. *Inverse Acoustic and Electromagnetic Scattering Theory.* Springer Verlag, 1992.

[55] D. G. Crighton, A. P. Dowling, J. E. Ffowcs-Williams, M. Heckl, F.G. Leppington, and J. F. Bartram. *Modern Methods in Analytical Acoustics. Lecture Notes.* Springer Verlag, 1992.

[56] M. A. Delany and E. N. Bazley. Acoustic properties of fibrous absorbent materials. *Appl. Acoust.*, 3:105–116, 1970.

[57] L. Demkowicz and F. Ihlenburg. Analysis of a coupled finite-infinite element method for exterior Helmholtz problems. *Numer. Math.*, 88(1):43–73, 2001.

[58] V. Easwaran, W. Lauriks, and J. P. Coyette. Displacement-based finite element method for guided wave propagation problems: application to poroelastic media. *J. Acoust. Soc. Am.*, 100(5):2989–3002, 1996.

[59] H. I. Ene and E. Sánchez-Palencia. Équations et phénomènes de surface pour l'écoulement dans un modèle de milieu poreux. *J. Mécanique*, 14:73–108, 1975.

[60] B. Engquist and A. Majda. Absorbing boundary conditions for numerical simulation of waves. *Math. Comput.*, 31:629–651, 1977.

[61] K. Feng. Finite element method and natural boundary reduction. In *Proc. Int. Congress of Mathematicians*, pages 1439–1453, 1983.

[62] J. L. Ferrín and A. Mikelić. Homogenizing the acoustic properties of a porous matrix containing an incompressible inviscid fluid. *Math. Methods Appl. Sci.*, 26(10):831–859, 2003.

[63] P. Gamallo. *Contribución ao estudo de problemas de simulación elastoacústica e control activo do ruido.* PhD thesis, Departamento de Matemática Aplicada, Universidade de Santiago de Compostela, 2000.

[64] W. Gander and W. Gautschi. Adaptive Quadrature – revisited. *BIT Numerical Mathematics*, 40(1):84–101, 2000.

[65] R. P. Gilbert and A. Mikelić. Homogenizing the acoustic properties of the seabed. Part I. *Nonlinear Anal.*, 40(1-8, Ser. A: Theory Methods):185–212, 2000.

[66] D. Givoli. *Numerical Methods for Problems in Infinite Domains.* Elsevier, 1992.

[67] D. Givoli and B. Neta. High-order non-reflecting boundary scheme for time-dependent waves. *J. Comput. Phys.*, 186(1):24–46, 2004.

[68] P. Göransson. A 3-D, simmetric, finite element formulation of the Biot equations with application to acoustic wave propagation through an elastic porous medium. *Int. J. Numer. Meth. Engng.*, 41:167–192, 1998.

[69] I. Harari, M. Slavutin, and E. Turkel. Analytical and numerical studies of a finite element PML for the Helmholtz equation. *J. Comput. Acoust*, 8(1):121–137, 2000.

[70] T. Hohage, F. Schmidt, and L. Zschiedrich. Solving time-harmonic scattering problems based on the pole condition. II: Convergence of the PML method. *SIAM J. Math. Anal.*, 35(3):547–560, 2004.

[71] F. Q. Hu. A stable, perfectly matched layer for linearized euler equations in unsplit physical variables. *J. Comput. Phys.*, 173(2):455–480, 2001.

[72] F. Ihlenburg. *Finite Element Analysis of Acoustic Scattering.* Springer Verlag, 1998.

[73] D. L. Johnson, J. Koplik, and R. Dashen. Theory of dynamic permeability and tortuosity in fluid-saturated porous media. *J. Fluid Mech*, 176:379–402, 2006.

[74] L. Kiefling and G. C. Feng. Fluid-structure finite element vibrational analysis. *AIAA J.*, 14(2):199–203, 1976.

[75] A. Kufner and A.-M. Sändig. *Some applications of weighted Sobolev spaces*, volume 100 of *Teubner-Texte zur Mathematik.* Teubner, 1987.

[76] D. Lafarge and B. Brouard. Présentation générale des modèles de propagation du son dans les matériaux poreux et illustration dans des cas simples. *Publications du LMA (Marseille)*, pages 147–165.

[77] M. Lassas, J. Liukkonen, and E. Somersalo. Complex Riemannian metric and absorbing boundary conditions. *J. Math. Pures Appl*, 80(7):739–768, 2001.

[78] M. Lassas and E. Somersalo. On the existence and convergence of the solution of PML equations. *Computing*, 60(3):229–242, 1998.

[79] M. Lassas and E. Somersalo. Analysis of the PML equations in general convex geometry. *Proc. Roy. Soc. Edinburgh Sect. A*, 131(5):1183–1207, 2001.

[80] N. N. Lebedev. *Special Functions and Their Applications.* Dover Publications, 1972.

[81] J. L. Lions and E. Magenes. *Problèmes aux limites non homogènes et applications*, volume 1. Dunod, 1968.

[82] J. L. Lions, J. Métral, and O. Vacus. Well-posed absorbing layer for hyperbolic problems. *Numer. Math.*, 92(3):535–562, 2002.

[83] D.Y. Maa. Microperforated-panel wideband absorbers. *Noise Control Eng. J*, 29(3):77–84, 1987.

[84] M. Masmoudi. Numerical solution for exterior problems. *Numer. Math.*, 51(1):87–101, 1987.

[85] W. McLean. *Strongly Elliptic Systems and Boundary Integral Equations.* Cambridge University Press, 2000.

[86] A. Mikelić. Homogenization theory and applications to filtration through porous media. In *Filtration in porous media and industrial application (Cetraro, 1998)*, pages 127–214. Springer, Berlin, 2000.

[87] P. J. Morris. Scattering of sound from a spatially distributed, spherically symmetric source by a sphere. *J. Acoust. Soc. Amer.*, 98:3536–3539, 1995.

[88] P. M. Morse and K. U. Ingard. *Theoretical acoustics*. McGraw-Hill, New York, 1978.

[89] I. M. Navon, B. Neta, and M. Y. Hussaini. A perfectly matched layer approach to the linearized shallow water equations models. *Monthly Weather Review*, 132(6):1369–1378, 2004.

[90] J.-C. Nédélec. *Acoustic and Electromagnetic Equations. Integral Representations for Harmonic Problems*. Springer Verlag, 2000.

[91] D.A. Nield and A. Bejan. *Convection in Porous Media*. Springer, 1998.

[92] R. Panneton and N. Atalla. An efficient finite element scheme for solving the three-dimensional poroelasticiey problem in acoustics. *J. Acoust. Soc. Am.*, 101(6):3287–3298, 1997.

[93] P. G. Petropoulos. Reflectionless sponge layers as absorbing boundary conditions for the numerical solution of Maxwell equations in rectangular, cylindrical, and spherical coordinates. *SIAM J. Appl. Math.*, 60(3):1037–1058, 2000.

[94] Q. Qi and T. L. Geers. Evaluation of the Perfectly Matched Layer for Computational Acoustics. *J. Computat. Phys.*, 139(1):166–183, 1998.

[95] C. M. Rappaport. Interpreting and Improving the PML Absorbing Boundary Condition Using Anisotropic Lossy Mapping of Space. *IEEE Trans. Magn.*, 32(3):968–974, 1996.

[96] P. A. Raviart and J. M. Thomas. A mixed finite element method for 2nd order elliptic problems. In *Mathematical aspects of finite element methods (Proc. Conf., Consiglio Naz. delle Ricerche (C.N.R.), Rome, 1975)*, pages 292–315. Lecture Notes in Math., Vol. 606. Springer, Berlin, 1977.

[97] E. Sanchez-Palencia. *Non-homogeneous media and vibration theory*, volume 127 of *Lecture Notes in Physics*. Springer Verlag, 1980.

[98] N.-M. Shiau. *Multi-dimensional wave propagation in elastic porous materials*. PhD thesis, School of Mechanical Engineering, Purdue University, 1991.

[99] J. J. Shirron and I. Babuska. A comparison of approximate boundary conditions and infinite element methods for exterior Helmholtz problems. *Comput. Methods Appl. Mech. Engrg.*, 164(1):121–139, 1998.

[100] B. Sjögreen and N.A. Petersson. Perfectly matched layers for Maxwells equations in second order formulation. *J. Comput. Phys.*, 209(1):19–46, 2005.

[101] E. Turkel and A. Yefet. Absorbing PML boundary layers for wave-like equations. *Appl. Numer. Math*, 27(4):533–557, 1998.

[102] V. J. van Joolen, B. Neta, and D. Givoli. High-order Higdon-like boundary conditions for exterior transient wave problems. *Int. J. Numer. Methods. Eng.*, 63(7):1041–1068, 2005.

[103] G. N. Watson. *A Treatise on the Theory of Bessel Functions.* Cambridge University Press, 1966.

[104] C. H. Wilcox. *Scattering theory for the d'Alambert equation in exterior domains.* Springer Verlag, 1975.

[105] Y. Q. Zeng, J. Q. He, and Q. H. Liu. The application of the perfectly matched layer in numerical modeling of wave propagation in poroelastic media. *Geophysics*, 66(4):1258–1266, 2006.